Université catholique de Louvain

Louvain School of Engineering

Institute of Information and Communication Technologies, Electronics and Applied Mathematics

Royal Military Academy

Polytechnic Faculty

Signal and Image Centre

Analysis of Environmental Effects on Electromagnetic Induction Sensors

Pascal DRUYTS

Thesis presented for the Ph.D. degree in engineering sciences

PhD committee

Marc ACHEROY	RMA/SIC – Supervisor
Christophe CRAEYE	UCL/ICTEAM – Supervisor
Danielle VANHOENACKER-JANVIER	UCL/ICTEAM – President
Xavier NEYT	RMA/SIC, Belgium – Secretary
Yogadhish DAS	DRDC, Canada
Ali KHENCHAF	ENSTA Bretagne, France
Philippe LATAIRE	VUB/ETEC, Belgium

Belgium

October 2011

Abstract

Electromagnetic induction sensors are widely used in a number of applications, such as mine clearance, improvised explosive detection, treasure hunting and geophysical survey. Our focus is on pulse induction metal detectors used in the scope of humanitarian demining to detect anti-personnel mines, but most developments remain valid for other applications and for other types of electromagnetic induction sensors. The detection performance of metal detectors may significantly be affected by the environment. In this thesis, we consider the effect of a magnetic soil, the effect of a water layer on the head of the detector and the effect of the electromagnetic background.

The analysis is based on a detailed model of the detector, including the coil and the fast time electronics. Classically, the voltage induced in a coil is assumed to be equal to the time derivative of the linked flux. We show, by resorting to the quasi-static approximation of the reciprocity expression, that an additional contribution, related to the incident electro quasi-static field, must be taken into account. In many applications this contribution is negligible but in some cases, for example when using some metal detectors over dew grass, the additional term is required to explain the observed phenomena.

Regarding the soil, a general model is developed, which is valid in the presence of inhomogeneities or soil relief and for an arbitrary head geometry. Then the *volume of influence* is rigorously defined and computed for typical head geometries.

Regarding the effect of water, important losses of sensitivity were reported from the field when scanning over dew grass with some detectors. The problem was investigated in the nineties. The effect could be reproduced and the conditions under which it occurs were well understood but the underlying physics could not be explained. Circuit and field level models are developed to explain the various phenomena observed. We show that the loss of sensitivity is due to an electro quasi-static interaction between the water layer and the coil.

Finally, we show that the electromagnetic background may affect the detector for frequencies from below 1 Hz to about 20 MHz, with a sensitivity peak around 100 kHz. For the maximum allowed background fields, the effect may be very severe, significantly lowering the sensitivity or even preventing the normal functioning of the detector.

La pensée ne doit jamais se soumettre,
ni à un dogme, ni à un parti, ni à une passion,
ni à un intérêt, ni à une idée préconçue,
ni à quoi que ce soit, si ce n'est aux faits eux-mêmes,
parce que, pour elle, se soumettre,
ce serait cesser d'être.

Henri Poincaré

Acknowledgments

Ce travail représente une étape importante dans ma vie professionnelle et il n'aurait pas pu être mené à bien sans le soutien de nombreuses personnes.

Je voudrais d'abord remercier mon promoteur, Marc Acheroy, pour m'avoir permis de réaliser ce travail. Notamment en ayant obtenu les financements nécessaires mais aussi en m'ayant soutenu dans les moments de doute. Ceci s'applique d'ailleurs plus largement aux près de vingt années de recherche que j'ai eu la chance de faire sous sa supervision.

Merci aussi à mon promoteur, Christophe Craeye, pour les nombreuses discussions, notamment celles relatives aux deux articles de journaux qu'il m'a aidé à publier dans le cadre de cette recherche. Les discussions furent parfois animées mais son expérience m'a clairement été bénéfique.

Toute ma gratitude s'adresse également à Yogadhish Das qui a accepté de faire partie de mon comité d'encadrement et à ce titre m'a prodigué de nombreux conseils judicieux. Malgré sa notoriété, il a su rester simple et abordable, comme j'ai pu m'en rendre compte lors de réunions et d'essais auxquels nous avons participé ensemble.

Merci aussi à mes collègues pour les discussions techniques ou plus superficielles que nous avons pu avoir, au département ou autour d'un verre. Il serait trop long de tous les citer et je sais qu'ils ne m'en tiendront pas rigueur si je ne mentionne que ceux qui ont directement contribué à ce travail, que ce soit au niveau théorique ou en m'aidant pour la partie expérimentale. Je pense à Xavier Neyt, Christo Tsigros, Idesbald Van den Bosch et Yann Yvinec, sans oublier le soutien des techniciens, Pascal De Kimpe, Marie-Christine Vrijens et Frédéric Moustier.

Un merci tout particulier à Marc Acheroy, Christophe Craeye, Yogadhish Das et Xavier Neyt pour avoir relu attentivement les différentes versions de ce document, sans oublier les autres membres du jury, Ali Khenchaf, Philippe Lataire, et Danielle Vanhoenacker pour avoir également formulé des remarques constructives et proposé des améliorations judicieuses. Sans ces contributions, cette thèse serait très certainement moins agréable à lire.

Il m'est impossible de terminer sans exprimer ma profonde reconnaissance à ma maman et à ma compagne Isabelle pour leur soutien et leur confiance inaltérables. La rédaction d'une thèse demande des sacrifices qui peuvent déteindre sur ses proches. En espérant ne pas leur avoir rendu la vie trop impossible dans les moments de stress, c'est tout naturellement que je leur dédie cette thèse.

$\sim$

This work was funded by the Belgian Ministry of Defence, the Belgian Federal Science Policy Office, the Federal Public Service Foreign Affairs and the Belgian Secretariat of State for Development Cooperation in the scope of two humanitarian demining projects: HUmanitarian DEMining (HUDEM) and Belgian Mine Action Technology (BEMAT).

Contents

Symbols and notations

Abbreviations

AP Anti-Personnel

BFO Beat Frequency Oscillator

CW Continuous Wave

DRDC Defence Research and Development Canada

EM Electromagnetic

EMI Electromagnetic Induction

EQS Electro Quasi-Static

FW Full Wave

GPR Ground Penetrating Radars

HS Half-Space

HSH Half-Space with Holes

ICNIRP International Commission on Non-Ionizing Radiation Protection

IED Improvised Explosive Device

l.h.s. left hand side

LMS Least Mean Square

MAS Method of Auxiliary Sources

MD Metal Detector

MOD Ministry of Defence

MoM Method of Moments

MQS Magneto Quasi-Static

PEC Perfect Electric Conductor

PI Pulse Induction

PQS Potential Quasi-Static

PRF Pulse Repetition Frequency

QS Quasi-Static

r.h.s. right hand side

RMS Root Mean Square

RX Receive

TEM Transverse Electromagnetic

TX Transmit

VoI Volume of Influence

Symbols

$\boldsymbol{A}$	Magnetic vector potential.
$\boldsymbol{B}$	Magnetic induction.
$\mathcal{C}_{\mathrm{RX}}$	Contour describing Receive (RX) coil shape.
$\mathcal{C}_{\mathrm{TX}}$	Contour describing Transmit (TX) coil shape.
$\mathcal{C}_{\mathrm{x}}$	Contour x. if $\mathcal{S}_{\mathrm{x}}$ is also defined, $\mathcal{C}_{\mathrm{x}}$ is the boundary of $\mathcal{S}_{\mathrm{x}}$ and positive tangent is related to positive normal of the surface by the right hand rule.
(d)	environment including the detector.
$\mathrm{d}V$	Volume element at $\boldsymbol{r}$ ($\mathrm{d}V'$ is volume element at $\boldsymbol{r}'$).
$\mathrm{d}S$	Surface element at $\boldsymbol{r}$.
$\mathrm{d}\boldsymbol{S}$	Vectorial surface element at $\boldsymbol{r}$: $\mathrm{d}\boldsymbol{S} = \hat{\boldsymbol{n}}\mathrm{d}S$.
$\mathrm{d}\ell$	Contour element at $\boldsymbol{r}$.
$\mathrm{d}\boldsymbol{\ell}$	Vectorial contour element at $\boldsymbol{r}$: $\mathrm{d}\boldsymbol{\ell} = \hat{\boldsymbol{\ell}}\mathrm{d}\ell$.
$\boldsymbol{D}$	Electric displacement.
e	Voltage induced in the coil.
e_{C}	Contribution of a capacitor to e.
e_{E}	Electric contribution to e.
e_{L}	Contribution of an inductor to e.
e_{M}	Magnetic contribution to e.
$\boldsymbol{E}$	Electric field.
ϵ	Electric permittivity.
ϵ_0	Free space electric permittivity.
ϵ_{r}	Relative electric permittivity.
ϵ_σ	Effective electric permittivity (including conductivity).

(fs)	free space environment.
ϕ	Electric scalar potential.
$\boldsymbol{H}$	Magnetic field.
j	Complex number $j = \sqrt{-1}$.
I	Electric current.
I_{RX}	Fictive current injected in the RX coil. Used to compute the coil induced voltage by resorting to reciprocity.
$\boldsymbol{J}$	Electric current distribution.
$\hat{\boldsymbol{\ell}}$	Positive unitary tangent to contour.
λ	Linear electric charge distribution.
$\boldsymbol{m}$	Magnetic dipole moment.
$\boldsymbol{M}$	Magnetic current distribution.
$\overline{\boldsymbol{M}}$	Magnetic polarizability tensor.
μ	Magnetic permeability.
μ_0	Free space magnetic permeability.
μ_{r}	Relative magnetic permeability.
$\hat{\boldsymbol{n}}$	Positive unitary normal to surface.
ν	Frequency
ω	Angular frequency.
$\boldsymbol{p}$	Electric dipole moment.
$\overline{\boldsymbol{P}}$	Electric polarizability tensor.
q	Electric point charge.
$\boldsymbol{r}$	Position vector.
$\boldsymbol{r}'$	Source position vector (when field and source position vector must be distinguished).

ρ	Electric charge distribution.
S_{head}	Head sensitivity. By default, the magnetic sensitivity $S^{\mathrm{M}}_{\mathrm{head}}$ is considered.
$S^{\mathrm{E}}_{\mathrm{head}}$	Electric head sensitivity.
$S^{\mathrm{M}}_{\mathrm{head}}$	Magnetic head sensitivity.
$\mathcal{S}_{\mathrm{x}}$	Surface x. If $\mathcal{V}_{\mathrm{x}}$ is also defined, $\mathcal{S}_{\mathrm{x}}$ is the boundary of $\mathcal{V}_{\mathrm{x}}$ and the positive normal points outside.
$\mathcal{S}_{\mathrm{x}\cap\mathrm{y}}$	Boundary of $\mathcal{V}_{\mathrm{x}\cap\mathrm{y}}$. This is usually an open surface and its positive normal coincides with that of $\mathcal{S}_{\mathrm{x}}$.
$\mathcal{S}_{\overline{\mathrm{x}}}$	Boundary of $\mathcal{V}_{\overline{\mathrm{x}}}$. It is composed of $\mathcal{S}_{\mathrm{x}}$ (but the positive normal is opposite to that of $\mathcal{S}_{\mathrm{x}}$) and the infinite sphere $\mathcal{S}_{\infty}$.
$\mathcal{S}_{\infty}$	Infinite sphere bounding $\mathcal{V}_{\infty}$.
σ	Electric conductivity.
$\Sigma^{(\mathrm{env})}_{\mathrm{x}}$	State used when resorting to reciprocity in which the source is characterized by 'x' and the environment by '(env)'.
V	Voltage.
$V^{\mathrm{RX}}_{\mathrm{amp}}$	Voltage at the output of the RX amplifier.
$V^{\mathrm{RX}}_{\mathrm{filt}}$	Voltage at the output of the RX filter network.
$V^{\mathrm{RX}}_{\mathrm{slow}}$	Slow-time voltage. Obtained by integrating the output of the RX amplifier $V^{\mathrm{RX}}_{\mathrm{amp}}$ in the evaluation window.
$V^{\mathrm{RX}}_{\mathrm{coil}}$	Voltage at the RX coil terminals.
$V^{\mathrm{TX}}_{\mathrm{coil}}$	Voltage at the TX coil terminals.
$\mathcal{V}_{\mathrm{x}}$	Volume x.
$\mathcal{V}_{\infty}$	Whole space.

$\mathcal{V}_{\overline{\mathrm{x}}}$	Volume complement of $\mathcal{V}_{\mathrm{x}}$: $\mathcal{V}_{\infty} \setminus \mathcal{V}_{\mathrm{x}}$.
$\lvert\mathcal{V}_{\mathrm{x}}\rvert$	Volume of $\mathcal{V}_{\mathrm{x}}$. A scalar with units $[\mathrm{m}^3]$.
$\mathcal{V}_{\mathrm{x}\cap\mathrm{y}}$	Intersection of volumes $\mathcal{V}_{\mathrm{x}} \cap \mathcal{V}_{\mathrm{y}}$
$\lvert x\rvert$	Absolute value of x.
$\lvert\boldsymbol{x}\rvert$	Norm of vector x.
x	Scalar.
x^*	Complex conjugate of x.
$\boldsymbol{x}$	Vector.
$\hat{\boldsymbol{x}}$	Unitary vector.
$\underline{\underline{X}}$	Matrix of order 2.
$\overline{\overline{\boldsymbol{X}}}$	Tensor of order 2.
$\underline{X}$	Column vector[1].
x	Dimensionless scalar (sans serif font).
$\boldsymbol{\mathsf{x}}$	Dimensionless vector (sans serif font).
χ	Magnetic susceptibility $\mu = \mu_0(1 + \chi)$.
$\boldsymbol{Y}_{\mathrm{x}}^{(\mathrm{env})}$	Where $\boldsymbol{Y}$ stands for the fields $\boldsymbol{E}$, $\boldsymbol{D}$, $\boldsymbol{H}$ or $\boldsymbol{B}$ or the potentials $\boldsymbol{A}$ or ϕ. Field or potential produced by source 'x' (in general an electric current distribution $\boldsymbol{J}_{\mathrm{x}}$ but may also include a magnetic current distribution $\boldsymbol{M}_{\mathrm{x}}$) when it radiates in an environment characterized by '(env)'.

[1]In contrast with $\boldsymbol{x}$ that is a physical vector, usually defined in a three-dimensional space, they may have any dimension. Furthermore, to have a physical meaning, vectors and tensors must obey the tensor transformation when changing axis system. This is not the case for general vectors and matrices, for which such transformation usually has no meaning.

$\check{\boldsymbol{Y}}_{\mathrm{x}}^{(\mathrm{env})}$ Where $\boldsymbol{Y}$ stands for the fields $\boldsymbol{E}$, $\boldsymbol{D}$, $\boldsymbol{H}$ or $\boldsymbol{B}$ or the potentials $\boldsymbol{A}$ or ϕ. Field or potential normalized by the current source source $\check{\boldsymbol{Y}}_{\mathrm{x}}^{(\mathrm{env})} = \boldsymbol{Y}_{\mathrm{x}}^{(\mathrm{env})}/I_{\mathrm{x}}$, assuming that the source can be characterized by a current I_{x} through an access port.

$\check{\boldsymbol{Y}}_{\mathrm{x,Q}}^{(\mathrm{env})}$ Same as $\check{\boldsymbol{Y}}_{\mathrm{x}}^{(\mathrm{env})}$ but the normalization is performed on the source charge (typically a capacitor) Q_{x}: $\check{\boldsymbol{Y}}_{\mathrm{x,Q}}^{(\mathrm{env})} = \boldsymbol{Y}_{\mathrm{x}}^{(\mathrm{env})}/Q_{\mathrm{x}}$.

$\cup$ Union of sets, volumes or surfaces.

$\cap$ Intersection of sets, volumes or surfaces.

$\setminus$ Difference of sets, volumes or surfaces.

Conventions

When the same label is used for a volume $\mathcal{V}_{\mathrm{x}}$ and a surface $\mathcal{S}_{\mathrm{x}}$, the surface is defined as the boundary of the volume and its positive normal points outside $\mathcal{V}_{\mathrm{x}}$. When the same label is used for a (open) surface $\mathcal{S}_{\mathrm{x}}$ and a (closed) contour $\mathcal{C}_{\mathrm{x}}$, the contour is defined as the boundary of the surface and the positive normal of $\mathcal{S}_{\mathrm{x}}$ and the positive tangent of $\mathcal{C}_{\mathrm{x}}$ are related by the right-hand rule.

Fields are in general denoted in a way that the source and environment is apparent from the notation. A source is identified by its label 's' and the corresponding current distribution is denoted $\boldsymbol{J}_{\mathrm{s}}$. When such a source is radiating in an environment defined as 'env' the corresponding magnetic field is denoted by $\boldsymbol{H}_{\mathrm{s}}^{(\mathrm{env})}$. For example, the magnetic field generated by the TX coil in the free space (fs) is denoted by $\boldsymbol{H}_{\mathrm{TX}}^{(\mathrm{fs})}$. A similar notation is used for the corresponding magnetic induction $\boldsymbol{B}_{\mathrm{s}}^{(\mathrm{env})}$ and magnetic vector potential $\boldsymbol{A}_{\mathrm{s}}^{(\mathrm{env})}$. When reciprocity is used, states are denoted $\Sigma_{\mathrm{s}}^{(\mathrm{env})}$ where 's' is the source and '(env)' the environment characterizing these states.

Unless otherwise specified, harmonic sources and fields are considered with an $e^{j\omega t}$ time variation assumed and suppressed.

CHAPTER 1

Introduction

This work addresses the effect of the environment on Electromagnetic Induction (EMI) sensors. As introduction, the research is put into context and a number of typical applications in which EMI sensors are used are briefly reviewed. Thereafter, the environmental effects considered are briefly described. Then, an overview of the working principles of an Pulse Induction (PI) metal detector is provided and the Schiebel AN-19/2 detector that will be used as an example when detailed specifications are required to perform the modeling is briefly described. Finally, the structure of this document is presented and the original contributions are highlighted.

Contents

1.1 Work context

EMI sensors are widely used in a number of applications, such as mine clearance [1], Improvised Explosive Device (IED) detection, treasure hunting [2], geophysical survey [3], security screening, industrial metal detectors, and civil engineering. Depending on the application, various sensor names are used, such as a *metal detector*, *wire detector* or *susceptibility meter*. All EMI sensors are based on the principle of electromagnetic induction, according to which a varying magnetic field will produce an induced voltage. More specifically, a Transmit (TX) coil is used to generate a time-varying magnetic field which will induce eddy currents in metallic objects and magnetic dipoles in magnetic objects. Those currents and magnetic dipoles will in turn generate a secondary magnetic field which generate a voltage in a Receive (RX) coil. This voltage can then be used to trigger an alarm in presence of a metallic object, as is the case in a *metal detector*, or to characterize the soil magnetic susceptibility, as is the case in a *susceptibility meter*.

All sensors work on the same basic principle but each application has its specificities and, when looking to the details, significant differences may exist. Our focus is on pulse induction metal detectors used in the scope of humanitarian demining to detect anti-personnel mines, but most developments remain valid for other applications and for other types of electromagnetic induction sensors.

A good review of the history of metal detectors can be found in [4]. One of the first reported usage of a metal detector is attributed to Alexander Graham Bell who used a crude device in 1881 to locate a bullet lodged in the chest of American President James Garfield [5]. Gerhard Fisher filed the first patent for a metal detectors, the ‘Metallascope’ in 1925. During the early years of World War II, experimental detectors were developed by Britain’s Ministry of Supply but it was finally a detector developed independently by the Polish forces that was retained for production. The detector was heavy, ran on vacuum tubes, and needed separate battery packs. It was extensively used during World War II to clear German mine fields [6]. With the apparition of the transistors, the detectors were significantly improved and miniaturized. Modern detectors still work on the same principles but their sensitivity has significantly been increased and they provide new features such as soil compensation, electromagnetic background filtering, automatic tuning, visual displays.

Humanitarian demining also called mine action began in the 1980s when civilian organizations started to clear the soil from landmines and other explosive remnants of war in Afghanistan and Cambodia [1]. Humanitarian demining has a number of specificities when compared to military demining. All explosive items must be removed or destroyed to a recorded depth whereas in military demining one often clear only a route in the minefield. Further in military demining, speed is an important factor and some losses may be accepted if it allows to move forward faster. In contrast, in humanitarian demining the main requirement is a level of clearance close to 100% and speed is less an issue.

Metal detectors can be split in two classes: the Continuous Wave (CW) and the PI detectors [7]. CW detectors generate fields at one or several frequencies in the VLF spectrum or slightly above (say 1 to 50kHz). The magnetic field generated by PI detectors exhibits a triangular variation in time with a rather slow increase and a fast decay (a few μs) of the magnetic field. The bandwidth of those detectors typically extends to about 100kHz. In all cases propagation does not play any significant role at the frequencies used by metal detectors. The propagation time can thus not be used to estimate the distance to the target. This is a major difference with Ground Penetrating Radars (GPR). On the other hand energy dissipation in the soil and large reflection at the air-soil interface are major problems for GPRs but not for Metal Detectors (MDs).

The simplest CW detectors use the Beat Frequency Oscillator (BFO) principle [7]. The search coil together with a capacitor form a resonant circuit called the search oscillator. When a metallic object interacts with the coil, the resonance frequency changes and this is detected by mixing the signal of the search oscillator with that of a reference oscillator. The resulting beat frequency is then be fed to a loudspeaker. The sound emitted is directly related to the frequency shift produced by the metallic object. Such a detector uses a single coil. Soil compensation is however impossible. More sophisticated CW detectors use two coils, one for transmission and another for reception. The coils are arranged in a way to minimize the direct coupling between the coil. The target response is then directly accessible in the RX coil. By synchronous demodulation, the magnitude and phase of the response can be obtained. This allows for some discrimination and for soil compensation. Better discrimination can be obtained by using more than one frequency.

With a PI detector, the transmit and receive phases are separated in time and a single coil can therefore be used. Further the complete impulse response of the target can in principle be recovered from the response. However, most detectors don't sample the full target response. Instead they use a single value obtained by averaging the response in a so-called evaluation window. Yet, by adapting the window, efficient soil compensation is possible. Further the newest detectors are digital and this makes more complex analysis of the target response possible. This may allow for discrimination as confirmed by the recent marketing of PI detectors with discrimination features. Those new features should however be evaluated with care, especially in the scope of humanitarian demining, where the level of detection required is very high. Until recently, the sensitivity of PI detectors was lower than that of PI detectors but nowadays, the most sensitive detectors, especially in difficult soils, are PI detectors [8].

A critical parameter affecting the detector performances is the signal-to-noise ratio in which the signal corresponds to the target response. Further, the noise not only includes the electronic noise but also any signal produced by the environment. Many authors [9, 10, 11, 12, 13, 14, 15, 16] have proposed methods to assess the target response but the influence of the environment on the detector has received less attention.

This thesis will therefore focus on a number of important effects that the environment may have on the detector:

- The effect of a magnetic soil.
- The effect of water on the head.
- The effect of the electromagnetic background.

The existence of those effects is well known and the MD manufacturers have developed practical solutions to mitigate them. However, the interaction with the detector was not fully understood or, in any case, little open literature exists on the subject.

1.2 Application of EMI sensors

As mentioned above, EMI detectors are widely used in a number of applications. In the scope of security screening, they are typically used in airport to detect weapons such as knives and guns. In the scope of civil engineering, they are used to detect steel reinforcing bars in concrete or to detect pipes and wires buried in walls and floors. Industrial metal detectors are used to detect foreign bodies in food. In this Section, we further briefly review a number of typical applications: mine clearance, IED detection, treasure hunting and geophysical survey.

In the scope of mine action, the EMI sensor is used to detect mines during the mine clearance or during the earlier area reduction phase. The sensor is then called a MD because it is the metallic part of the mine that is actually detected. The most challenging mines to detect are the minimum metal Anti-Personnel (AP) mines such as the type 72 anti-personnel blast mine [17]. Those mines are sometimes called plastic mines though, in most cases, they still contain some metal pieces as a spring or the firing pin. The amount of metal may however be quite small and the metal detectors used must be very sensitive, especially in the scope of humanitarian demining, where detection rates close to 100% are required. Many detectors used in the scope of humanitarian demining can be found in [18].

In the scope of treasure hunting, many hobbyists are using metal detectors to locate gold ore, coins, or jewels. The detectors used are similar to those used in humanitarian demining but they are often less sensitive. To make the distinction between precious and other metals, they may include discriminating features to classify a metal piece as ferrous or nonferrous or even to identify the type of metal. Discriminating features are also appearing in the scope of demining, to distinguish between mines and other scrap metal. Those features should be carefully evaluated before using them, especially in the scope of humanitarian demining, where detection rates close to 100% are required. They might be more suited to military demining, where in some conditions, missed detections may be accepted if the discrimination feature allows for faster movement.

In the scope of IED detection, wire detectors such as the Guartel WD 100 [19] or the Ebinger EBEX 420-DR [20] are appearing on the market. These detectors work on the same principle as CW metal detectors but are typically working at higher frequencies. Wire detectors are useful to detect IEDs operated at a distance by means of a command wire.

In the scope of geophysical survey, EMI detectors are used to measure the soil conductivity or magnetic susceptibility [3]. The depth of investigation is a function of the application. For deep exploration, large loops are used to increase sensitivity. Changing the size of the loop may significantly change the behavior of the sensor. For example, heads used in the scope of humanitarian demining have sizes in the order of 20cm.

This is much smaller than the skin depth for most soil conductivities encountered in practice, and, therefore, the soil conductivity has little effect on PI detectors. On the contrary, for large loops, the soil conductivity may have a significant effect on PI detectors and this is exploited to map the soil electric conductivity [21, 22].

1.3 Environmental effects considered

1.3.1 Effect of a magnetic soil

It is well-known that the soil can produce false alarms, as confirmed by the fact that most manufacturers provide high-end MDs with soil compensation capabilities. Unfortunately, due to competition among manufacturers, details of the soil compensation techniques implemented are often proprietary, although some information is available in patents [23]. Until recently, there was a lot of confusion about the exact origin of the problem. This is highlighted by the number of fuzzy terms used for the problematic soils. For example, references to 'noisy', 'uncooperative', 'lateritic', 'red' or 'mineral' soils are often found. The problem has recently received more attention from the scientific community and several publications [24, 25, 26] suggest that for most soils of interest the response is due to the frequency variation of the soil magnetic susceptibility. In most cases, however, a uniform soil and simple coil shapes were considered. We will extend the analysis by developing a model allowing for a general coil configuration and for arbitrary soil inhomogeneities and relief. This will lead us to a rigorous definition of the Volume of Influence (VoI) which is a very important concept for MDs. In simple terms, the VoI is the volume from which most of the soil response originates.

1.3.2 Effect of water

Several sources such as the Belgian Ministry of Defence (MOD), the Canadian forces and others, have reported serious degradation in sensitivity with the Schiebel AN-19/2 in some moisture conditions. The problem was investigated in the nineties by the Defence Research and Development Canada (DRDC) Suffield. The problem could be reproduced in the laboratory but the physics was not understood and no model explaining the observed phenomena was developed. It was however speculated that the effect was likely due to coupling of the electric field which is usually ignored in the analysis of metal detectors and it was suggested that shielding the coils should reduce the effect. Most modern detectors have shielded coils and this indeed solves the problem. We nevertheless investigated this problem again to understand the underlying physics. A better understanding of the interaction mechanism may have practical applications. Indeed, the shield increases the coil capacitance and this may have some negative effect on the detector sensitivity. Hence, to further improve the detector performance, it may become necessary to optimize the shield and this may require us to better understand what the shield exactly has to shield against.

1.3.3 Effect of the EM background

It is well-known that the Electromagnetic (EM) background may affect a MD. Operators are well aware that a detector may become unusable under a power line. Some detectors proposes filters to mitigate the effect of fields at 50Hz or 60Hz. Other sources of EM fields may also affect the detector but the specific sources that may affect the detector are not documented. Problems were reported with detectors in presence of jammers, though the frequencies used by jammers seem large when compared to the frequency band of the detectors. An in-depth analysis of the EM background on the detectors is therefore performed.

1.4 PI MD general description

Most of the new MDs are PI detectors because they allow for better soil compensation [8]. We therefore focus on such a detector for which the functional diagram is illustrated in Fig. 1.1. The TX pulse generation module generates current pulses in the TX coil (typically many pulses per second are generated). Each pulse yields a time varying current in the TX coil which in good approximation has a triangular shape with a slow increase and a fast decay. This current will generate a varying magnetic field that in turn will induce eddy-currents in metallic targets and/or magnetic dipoles in magnetic targets. Those induced currents and magnetic dipoles will generate a secondary field that in turn will generate an induced voltage in the RX coil. This induced voltage is first filtered to reduce the effect of the EM background and then highly amplified. A strong amplification is needed because the response of the targets of interest is typically quite small. We call the signal at the

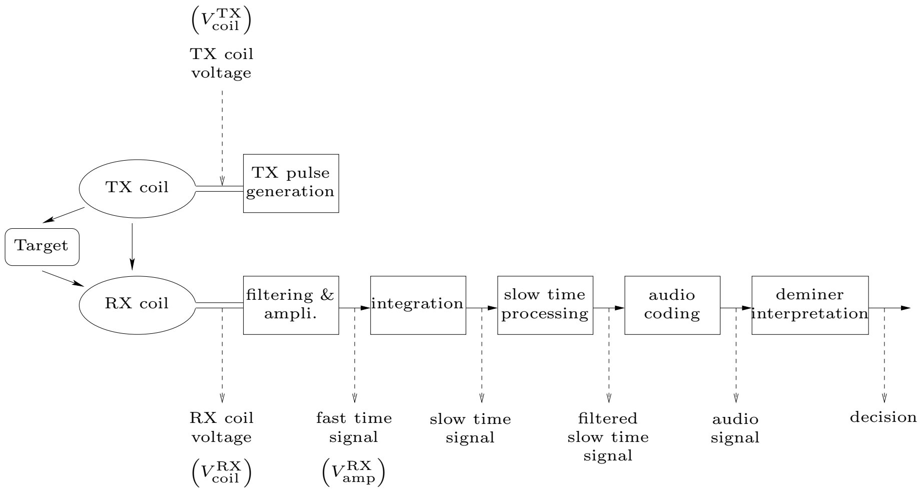

Figure 1.1: *MD functional diagram.*

output of the amplifier the *fast-time* signal. It is related to the impulse response of the target. Typically, and in first approximation, this is an exponential decay and the corresponding time constant is a function of the object. The fast-time signal is then integrated on an evaluation window to obtain a single value per pulse which we call the *slow-time* signal. This signal remains approximatively constant as long as the detector is not moved. It will thus vary on time scales of about $1s$, according to the movement of the detector. Comparing this time scale to the time scale of about $100\mu s$ on which the output of the amplifier vanishes explains why this latter is called the fast-time signal whereas the output of the integrator is called the slow-time signal.

The slow-time signal may be further filtered to remove the background signal from the soil and the resulting signal is then used to generate an audio alarm.

1.5 Example detector

As example detector we will use the AN-19/2 detector manufactured by Schiebel. It was chosen because we could access[1] such a detector to make measurements and we could also get useful information on the coil

[1]Thanks to DRDC that we want to acknowledge.

(a) (b)

Figure 1.2: *Schiebel AN-19/2 (a) detector head and (b) electronic box and headphone.*

winding and on the electronic circuit[27]. The Schiebel AN-19/2 is a rather old detector but it still has many features in common with the new detectors. Hence, most of our results should be relevant for other detectors. Newer detectors include new features and this will be highlighted whenever relevant. Note that Schiebel has now developed several new detectors such as the all-terrain mine detector (ATMID)[2]. We will nevertheless refer to the Schiebel AN-19/2 simply as 'the Schiebel detector' for conciseness and this should not bring any confusion.

Although the detector is relatively old, it still has many features in common with the new PI detectors. The developed model should thus be easily adaptable to other PI detectors and with some additional work to CW detectors. For example the coil model is generic and can easily be adapted to any detector (CW or PI) by computing the circuit parameters for the head geometry of the considered detector. Newer detectors include new features such as soil compensation that will be discussed when relevant.

The Schiebel AN-19/2 is illustrated in Fig. 1.2. It is composed of a head and an electronic box. The head is composed of two circular concentric coils. The outer coil has a radius of 13cm and is used for transmission and the inner coil has a radius of 9.5cm and is used for reception.

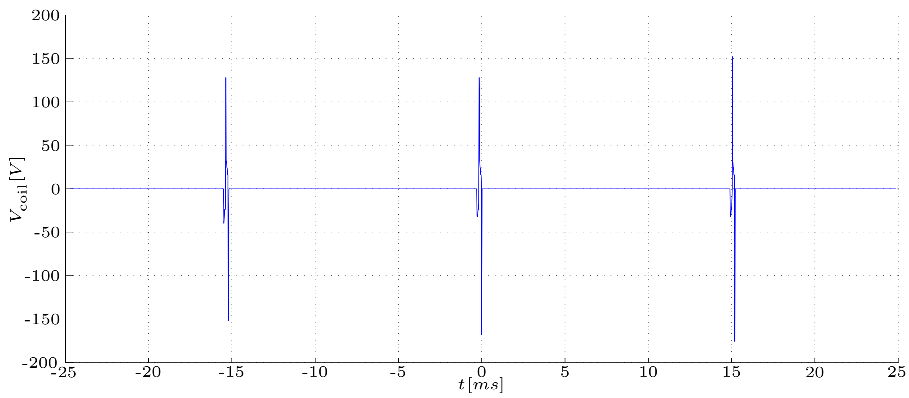

Figure 1.3: *Schiebel TX coil voltage.*

The voltage and current wave forms generated by the Schiebel have been measured by introducing a home-made connector between the elec-

[2]see `http://www.schiebel.net/`

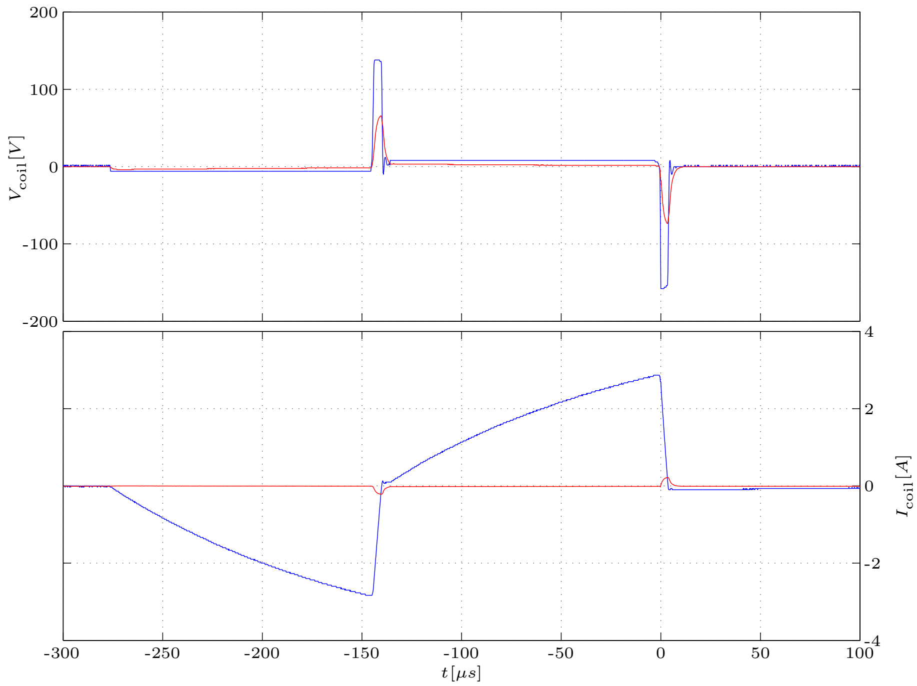

Figure 1.4: *Schiebel TX (blue) and RX (red) coil voltages (top) and currents (bottom).*

tronics and the coil cable connectors. This yields access to the coils terminals allowing measurement of the TX and RX voltages. Furthermore, a 1Ω resistor has been put in series with each coil which allows us to measure the coil current[3]. The output of the amplifier and the timing signals can also be measured on test pins located on the printed circuit board.

The measured TX coil voltage is shown in Fig. 1.3 where one sees that a pulse is sent every 15ms. This yields a Pulse Repetition Frequency (PRF) of 66 Hertz. A close view on one pulse is shown in Fig. 1.4 where the measured TX and RX coil voltages and currents are shown. In simple terms, the detector generates triangular current pulses that last for about $140\mu s$. The voltage waveform is in first approximation a rectangular pulse that lasts for about $4\mu s$ and that occurs during the current fall off. One therefore speaks of a pulsed detector. Going into more details, one sees that a bipolar pulse, which is composed of two successive pulses with opposite polarity, is used. The motivation for using such a double pulse is to prevent the triggering of magnetic mines. The response is only sensed after the second pulse. Hence, as will be further discussed below, apart from the mine anti-triggering feature, the detector can be further analyzed by considering only the second pulse. During that pulse, one sees that the TX coil is first energized for about $140\mu s$ on a voltage of 8V. The current reaches about 3A and is then decreased to zero in a much shorter time (about $4\mu s$). For this, a voltage of about 140V is applied to the coil.

Note that a current is induced in the RX coil and this current remains some time after the TX pulse. The RX voltage therefore needs some time to reach a small value when compared to the target response. This transient phenomenon is better visible on Fig. 3.2. Important parameters that govern the transient are the coils parasitic capacitances, which together with the coils inductances yield oscillating systems, on both the TX and the RX side. A resistor is connected in parallel with each coil to damp the oscillations but the voltage at the RX coil terminals still remains significant for several tens of micro seconds. As a consequence of this and because the amplifier needs some time to recover

[3]This resistor is not negligible with respect to the coil resistance; especially for the TX coil. It will therefore affect the shape of the current pulse as will be shown in Chapter 3 (Figs. 3.3 and 3.4). This is however not an issue because the measurements are made to validate the model and the resistor may be added in the model for this comparison. It may then be removed from the model to simulate the detector in its normal state.

from saturation, the evaluation window can only start a few μs after the pulse.

For the Schiebel detector, the window starts when $V_{\text{amp}}^{\text{RX}}$ goes below 1V and lasts for $10\mu s$. The fast-time signal is integrated in that window to yield the slow-time signal. Finally, an alarm is generated if the slow-time signal is above a threshold. This threshold can be set by the operator by turning the sensitivity knob.

One also sees that some current is induced in the RX coil. Rigorously, this current must be taken into account to compute the magnetic field generated by the head. However, this current is much smaller than the TX current and it can in general be neglected to compute the magnetic field.

1.6 Thesis structure

This thesis is divided in two parts. In the first part, a model of the detector, including the coils and the electronics, is developed. In the second part, this model is used to assess the effect of the environment on the detector.

In part 1, Chapter 2 presents the coil and electronics model. Regarding the coil, this model takes into account the coil parasitic capacitances. Two models are be developed and compared; a simple model in which the coil is represented by a single inductor and a single capacitor and a detailed model in which each turn is modeled by an inductor and a capacitor is introduced between each pair of turns. The various parameters appearing in those circuit models are computed, which requires the use of a detailed coil description. In addition, to estimate the turn-to-turn capacitance, a numerical method is needed. Here we make use of the Method of Auxiliary Sources (MAS). An in-depth study of the voltage induced in the coil is performed. Therefore, we resort to reciprocity to establish an accurate expression for this voltage. We show that the resulting voltage is more complex than the derivative of the magnetic flux through the coil, as often used. An additional electrical term due to the parasitic capacitances appears. This additional term is required to explain the effect of water on the detector (see Chapter 6). Regarding the electronics, the fast-time and the slow-time electronics are described. The fast-time electronics includes the TX pulse generation and the RX signal filtering and amplification circuits as well as the conversion from the fast-time signal to the slow-time signal by integration in the evaluation window. The slow-time electronics, which includes the slow-time filtering and the audio alarm generation, is briefly described.

Chapter 3, develops a state-space model of the detector, that combines the coil and the fast-time electronics. It allows us to simulate and better understand the fast-time signals. This model is further extended to include typical targets. Simple small and first order targets are considered and the distinction is made between three target types: an electric, a magnetic and a conducting target. We show that the response may then be characterized by a geometric and a dynamic factor. The geometric factor is called the head *geometrical sensitivity*[4] and includes the effect of head geometry and target location with respect to the head. The dynamic factor is called the detector *dynamic sensitivity* and includes the effect of the shape of the TX pulse and the RX electronics dynamics (filter and amplifier, integration in the evaluation window) and the target dynamics. For the first order targets considered, the target dynamics is characterized by a gain and a time constant. The detector dynamic sensitivity map for such targets is thus a two-dimensional image that can easily be visualized. This is illustrated for the three target types considered and the possibility to distinguish the various types of targets based on the target response shape or polarity is discussed.

In part 2, the response of a magnetic soil is investigated in Chapter 4. Using the Magneto Quasi-Static (MQS) reciprocity expression, we show that for the *weakly* magnetic soils often encountered, the soil response can be expressed in the frequency domain as a simple integral on the soil volume. The integrand is the product of the magnetic susceptibility with the *head sensitivity*. The *head sensitivity* used to compute the response of an extended soil is identical to that used to compute the response of a localized target. This head sensitivity is computed for a number of typical head geometries, which allows us to better understand important head characteristics such as the intrinsic soil compensation. With the model proposed, the soil response can be computed for arbitrary soil inhomogeneities and for an arbitrary soil relief. This is a significant advantage of the method because realistic soils can be taken into account. For a PI detector, it is the time-domain response that is of interest and the critical part of the response is due to the frequency variation of the magnetic susceptibility. For a general inhomogeneity, the time-domain

[4]For conciseness, most of the time, we simply refer to this factor as the *head sensitivity*. This should not bring any confusion with the detector *dynamic sensitivity* because the latter is related to the detector as a whole and not only to the head.

response can be obtained by first computing the response at a number of frequencies and then performing an inverse Fourier transform. If the frequency dependency is the same everywhere (this does not imply a homogeneous soil and might be representative of a soil with the same magnetic constituents everywhere, but in different concentration), the computation of the time domain response can be simplified significantly. Indeed, we show that in this case, the response is again (as for small targets) characterized by a geometric and a dynamic factor which can be computed independently.

In Chapter 5, the above mentioned general magnetic soil model is used to rigorously define the concept of VoI. It enables us to better understand the response of a magnetic soil to an electromagnetic induction sensor, as well as the effect of soil inhomogeneities on soil compensation. The volume of influence is first defined as the volume producing a fraction α of the total response of a homogeneous Half-Space (HS). As this basic definition is not appropriate for sensor heads with intrinsic soil compensation, a generalized definition is then proposed. These definitions still do not yield a unique VoI and a constraint must be introduced to reach uniqueness. Two constraints are investigated: one yielding the *smallest VoI* and the other one the *layer of influence*. Those two specific VoI have a number of practical applications which are discussed. The *smallest VoI* is illustrated for typical head geometries and we prove that, apart from differential heads such as the quad head, the shape of the *smallest VoI* is independent of the head geometry and can be computed from the far-field approximation. In addition, quantitative head characteristics are provided and show –among others– that double-D heads allow for a good soil compensation, assuming however approximate homogeneity over a larger volume of soil. The effect of soil inhomogeneity is further discussed and a worst-case VoI is defined for inhomogeneous soils.

In Chapter 6, the effect of water on the detector head is investigated. The effect is more complex than a simple capacitive coupling as illustrated by the variety of phenomena observed. If the head is fully immersed in the water, no effect is observed. When the head is lifted out of the water, a large response, similar to that of a metallic object, is observed while large quantities of water are dripping from the head. Finally, when enough water has dripped and only a thin water layer remains on the head, a response with opposite polarity is observed. This latter case is the most important from a practical point of view because similar conditions can occur when the detector head is swept over wet grass and the effect observed is at the origin of a reduction of the detector sensitivity. Indeed, the water produces a negative background signal and, therefore, a metallic target must produce a larger positive signal to reach the detection threshold. The effect of water conductivity is also investigated and this yields additional insight in the underlying physic phenomena. For the three observed phenomena, a circuit model is proposed and for the most critical phenomenon (the reduction of sensitivity) a more detailed field-level model is also proposed. The latter model could only be developed using the rigorous expression for the induced voltage that is developed in Chapter 2. Indeed, the water response is due to the Electro Quasi-Static (EQS) fields backscattered by the water layer and, according to the simple coil model classically used, such fields have no effect on a coil.

Finally, in Chapter 7, the effect of the EM background is investigated. First the relation between an (harmonic) external field and the slow-time response is established as a function of the field frequency and amplitude. The result is more complex than might be expected at first sight because the evaluation window starts when the fast-time signal reaches a given threshold. As a result, the external field influences the location of the evaluation window and, therefore, two contributions to the response must be considered: a steady-state one and a transient one. A simple analysis would neglect the transient contribution, which we prove to be inaccurate as the transient contribution dominates the response for frequencies larger than about 50kHz. We also show that even more complex phenomena may occur for large external fields, when nonlinear effects come into play. The magnitude of EM fields is restricted by national or international norms which are often based on the International Commission on Non-Ionizing Radiation Protection (ICNIRP) guidelines. We therefore use these guidelines to compute the critical frequency band, which is defined as the part of the electromagnetic spectrum that may significantly affect the detector, when the maximum allowed fields are considered. Finally, two important test-cases are investigated in more detail: the effect of a high voltage power line and the effect of fluorescent lamp with a high-frequency electronic ballast.

1.7 Original contributions

Our main contributions are as follows:

- A coherent development of various low-frequency approximations (EQS, MQS and Quasi-Static (QS)) of the Full Wave (FW) reciprocity expression, highlighting the relation between the various approximations. The validity of the various approximations is also discussed.

- A detailed coil model, in which each turn is represented by an inductor and in which the parasitic capacitances between each pair of turns are considered. Those capacitances are estimated using the MAS. The detailed coil model is related to a simpler model in which a single inductor and a single capacitance are used. The output of both models is also compared with measurements.

- A rigorous expression for the voltage induced in the coil is obtained using the QS approximation of the reciprocity expression that we have derived. We show that a real coil does not only respond to magnetic fields but also to an EQS field. This latter contribution is not taken into account in the classical coil models but it may significantly affect the detector. It is this contribution that may explain the reduction of sensitivity observed when the head is wet.

- A state-space model of a complete detector, including the coils and the electronics as well as the interconnection between this detector model and simple target models.

- The concept of (geometrical) head sensitivity is reviewed and sensitivity maps are computed for various head geometries. Beside the geometrical head sensitivity, the concept of dynamic sensitivity maps is also defined. It allows us to highlight the sensitivity of the detector to various target types as a function of their dynamics (gain and time constant).

- A model was developed to compute the response of a detector composed of coils with an arbitrary geometry to a magnetic soil with an arbitrary relief and with arbitrary inhomogeneities.

- A rigorous definition of the soil VoI was proposed. We show that a constraint must be introduced to obtain a unique VoI. Two constraints are proposed. One leading to the smallest VoI and the other leading to the layer of influence. The practical usefulness of those VoIs are highlighted and they are further computed for a number of typical detector head geometries. The effect of soil inhomogeneities on the VoIs is also discussed.

- A novel method has been developed to analyze the effect of water on the detector head to provide insight into previously unexplained field observations.

- An analysis of the effect of the EM background on the detector.

Part I

Model of the detector

CHAPTER 2

Coil and electronics model

This chapter presents the coil and the electronics model. First, a detailed coil model including a capacitance between each turn pairs is developed and the corresponding capacitances are computed numerically, using the MAS. A simple circuit model including a single capacitor is also reviewed and the relation between the two models is investigated. The dynamics of the coil is then discussed.

Regarding the voltage induced in the coil by incident fields, one usually assumes that it is equal to the time derivative of the flux linked by the coil. We show, by resorting to the quasi-static approximation of the reciprocity expression, that an additional contribution, related to the incident electro quasi-static field, must be taken into account. Then, the effect of coil shielding is discussed in that context.

Regarding the electronics, the fast-time electronics is first described. This includes the TX pulse generation and the RX signal filtering and amplification circuits as well as the conversion from the fast-time signal to the slow-time signal by integration in the evaluation window. Then, the slow-time electronics, which includes the slow-time filtering and the audio alarm generation, is briefly described.

Contents

2.1 Head geometry

Figure 2.1: *Schiebel head.*

The general Schiebel head geometry is shown on Fig. 2.1. The head is composed of two concentric coils. The outer coil has a radius of 13cm and is used for transmission and the inner coil has a radius of 9.5cm and is used for reception. To develop a detailed model of the head, the details of the coil windings are needed. Those details are not publicly available. Fortunately, we could obtain a drawing of the detector head which was converted into a numerical model as illustrated in Fig. 2.2, which shows a transverse cut across the TX and RX coils. Note that the figure is for illustration only as the turn layout drawing has been modified to avoid confidentiality issues. The TX and RX coils are made of 20 and 33 turns respectively. The turns are numbered according to their winding order. A current flowing into the coil first goes through turn 1, then through turn 2 and so on. This turn numbering was not provided but could be guessed taking into account practical constraints for the winding. An alternative valid numbering can be obtained by starting from the upper left wire instead of the lower left. Each turn is represented by two circles; the inner circle being the boundary of the conductor and the outer circle being the boundary of the insulator. According to the available drawings, we have estimated that, for the TX coil, the diameter of the conductor is 1.3mm and the insulator thickness is 0.13mm whereas for the RX coil, the diameter of the conductor is 0.9mm and the insulator thickness is 0.10mm. Note that 16x0.2 and 18x0.1 Litz[1] wires are used respectively for the TX and RX coils.

[1]Litz wire is a stranded wire where the individual strands are insulated and twisted

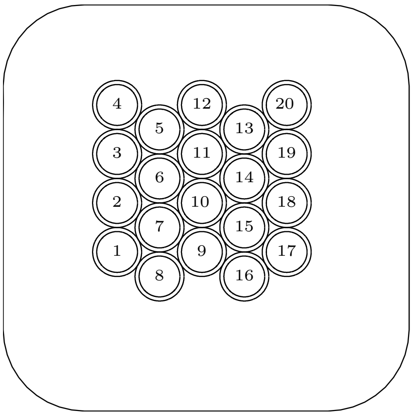

(a)

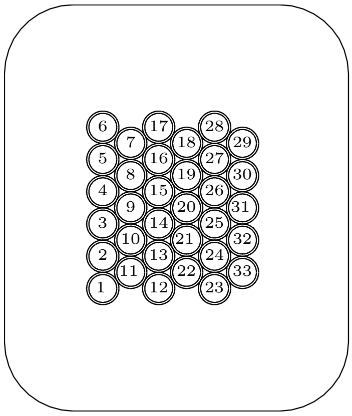

(b)

Figure 2.2: *Detail of the Schiebel coil winding. (a) TX coil and (b) RX coil with turn numbering. Coil center is on the left of the cuts. Turn layout has been modified and is for illustration only.*

2.2 Coil circuit model

Following [29, 30], we have modeled the coil by a lumped equivalent circuit. A simple model and a detailed model have been used as illustrated in Fig. 2.3. In the simple model, charge accumulation along the coil is taken into account by introducing a capacitance branch parallel to the RL branch. The current is thus assumed constant along the whole coil. In the detailed model, this assumption is relaxed by representing each turn with a separate RL branch. Charge accumulation is then taken into account by introducing a capacitance between each pair of turns.

As will be shown in Section 2.3, in the frequency band of interest, which remains far below the first coil resonance frequency, the simple model is a good approximation of the detailed one. Therefore, the simple coil model may be used in most cases. The detailed model is still useful because it allows us to estimate the parasitic coil capacitance instead of measuring it, which may be useful, for example to evaluate a new coil design without having to build a prototype. Furthermore, the detailed

(so that each strand tends to take all possible positions in the cross-section of the entire conductor) to limit skin and proximity effect [28]. They are characterized by the number of strands (n) and the diameter of an individual strand (D, expressed in mm) and this is denoted nxD.

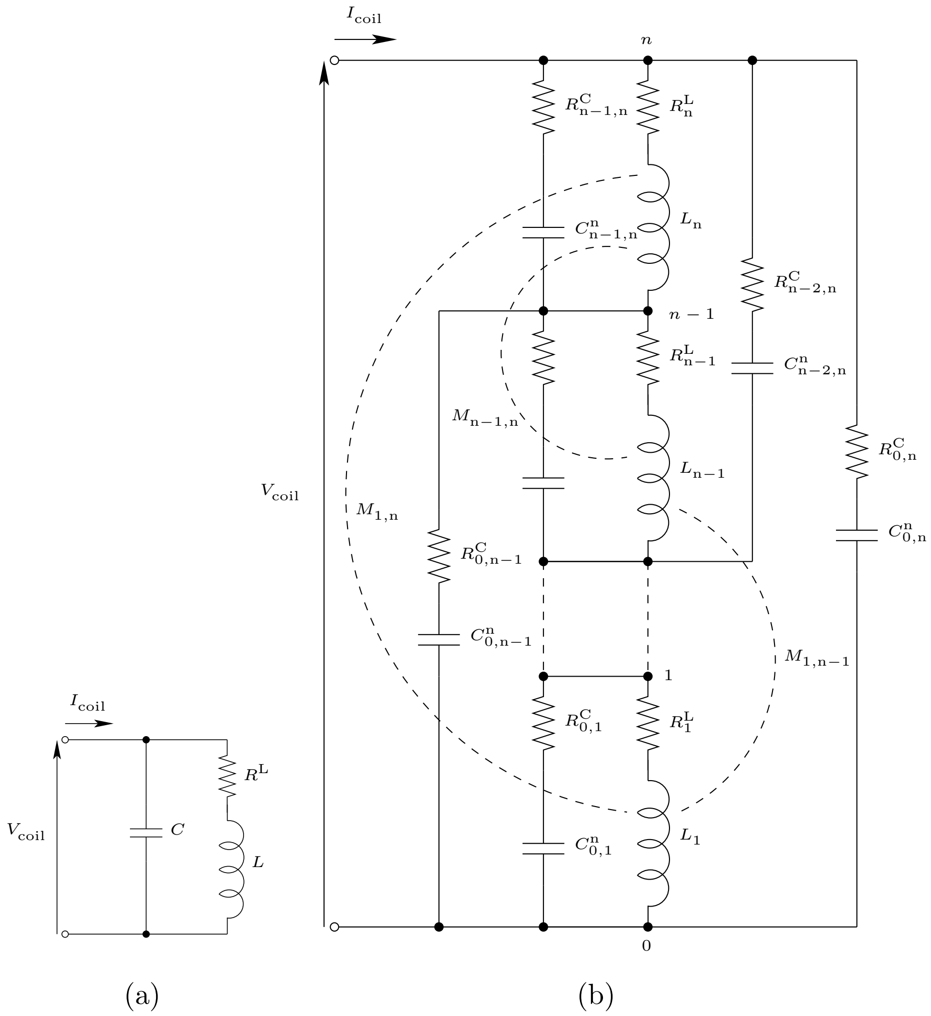

Figure 2.3: *Coil model (a) simple and (b) detailed.*

one allows us to assess the capacitance of the head in the presence of a shield or when the head is put in water and this will be useful to understand the effect of water on the head as discussed in Chapter 6. In addition, the detailed model allows estimation of the charge distribution along the coil. This charge distribution will also be useful to understand the effect of water on the detector head.

The detailed model is more precisely described as follows: turn i extends between nodes $i-1$ and i. It is represented by an inductor L_{i} and a resistor $R^{\mathrm{L}}_{\mathrm{i}}$. Between turn i and turn j, there exists a magnetic coupling represented by $M_{\mathrm{i,j}}$ and a capacitive coupling represented by $C^{\mathrm{t}}_{\mathrm{ij}}$. This turn-to-turn capacitance $C^{\mathrm{t}}_{\mathrm{ij}}$ is further transformed into a node-to-node capacitance by putting half of it to each side of the turns as illustrated in Fig. 2.4. Two turn-to-turn capacitance contribute to each node-to-node capacitance and the resulting node-to-node capacitance matrix is:

$$C^{\mathrm{n}}_{\mathrm{ij}} = (C^{\mathrm{t}}_{\mathrm{ij}} + C^{\mathrm{t}}_{\mathrm{i-1,j-1}})/2 \tag{2.1}$$

Resistors $R^{\mathrm{C}}_{\mathrm{ij}}$ have been introduced in the capacitance branches to avoid loops containing only capacitors because such loops lead to circuit equations that have no solution (similar to a loop containing only voltage sources). Those resistors exist physically but they are very small. Their exact value is not important as long as they are small enough. Indeed, for small resistors, the time constant of the RC branch will be very small and will have no visible effect on the coil dynamics in the frequency band of interest.

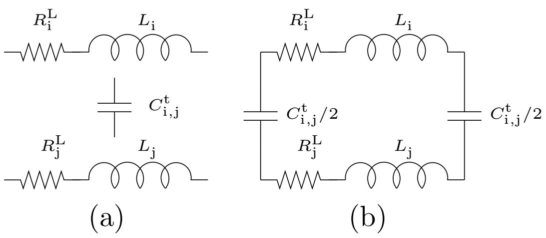

Figure 2.4: *Capacitance (a) turn-to-turn and (b) node-to-node.*

The self and mutual induction coefficients L_{i} and $M_{\mathrm{i,j}}$ can be computed by resorting to the analytic solution available for concentric circular loops [31, Equ. 9 p. 264 and Equ. 7 p. 263]:

$$L = \mu_0 a \left\{ \ln\left(\frac{8a}{r}\right) - \frac{3}{4} \right\} \tag{2.2}$$

with a the radius of the circular loop and r the cross-section radius of the wire. The expression for the mutual coupling coefficient is :

$$M = \mu_0 \frac{2\sqrt{ab}}{k} \left[\left(1 - \frac{k^2}{2} \right) K(k) - E(k) \right] \tag{2.3}$$

where K, E are the complete elliptic integrals of first and second kinds, $k^2 = 4ab/[(a+b)^2 + d^2]$, with a and b the radii of the coils and d the distance between the centers.

Note that strictly speaking (2.2) and (2.3) are not valid in the presence of additional loops. The presence of the other loops in the coil may change the magnetic field distribution and therefore the induction coefficients. This so called proximity effect is expected to be small because the wires are thin and the current induced in the neighboring open-loop[2] wires is expected to be small and have little effect on the magnetic field. The MQS proximity effect is further reduced by the use of Litz wires [28].

Neglecting the skin effect, the resistance of a turn can be expressed as [31, Equ. 17 p. 15]:

$$R = \frac{2\pi a}{S\sigma} \tag{2.4}$$

with a the radius of the circular loop, S the area of the conductor cross-section and σ the conductivity of the wire. We assumed that the coil wire is composed of copper and we therefore used $\sigma = 5.8 \times 10^7 S/m$. Recall that for the Schiebel coil, multi-strand Litz wire is used and therefore, the copper cross-section to consider (S) is smaller than the overall wire cross-section (S_{w}). The wire used has an overall diameter if 1.3mm and is composed of 16 strands of 0.2mm diameter. This yields a copper cross-section of $S = 0.5\mathrm{mm}^2$ and an overall wire cross-section of $S_{\mathrm{w}} = 1.3\mathrm{mm}^2$

The skin effect can be neglected if the radius of the wire is small compared to the skin depth. The skin depth can be computed using [31, Equ. 66 p. 504]

$$\delta = \sqrt{\frac{2}{\omega \mu_0 \sigma}} \tag{2.5}$$

For copper, this yields $660\mu m$ at 10kHz. The radius of the wire strand is $100\mu m$ and $50\mu m$ respectively for the TX and the RX coil. Therefore

[2]To assess the proximity effect, the neighboring loops are open. Indeed, when computing one element of the mutual coupling matrix, current is injected only in the considered source coil; all other loops do not carry any loop current; they may only carry local eddy-currents.

skin effect is negligible at the strand level. In contrast, the total wire radius is $650\mu m$ and $450\mu m$ respectively for the TX and the RX coil. Hence for a solid wire, skin effect would be significant at the highest frequencies used by the detector. With the Litz wire used, the skin effect should remain negligible.

The last parameter to estimate is the turn-to-turn capacitance. In [30], this capacitance is computed for a single-layer coil by neglecting the curvature of the coil wire and using the analytic expression available for the capacitance of two infinite parallel wires. For multi-layer coils, as the Schiebel coils, this expression is inaccurate because the EQS proximity effects[3] are strong. For such coils, a semi-empirical approximation is proposed in [29] and a numerical approach based on the Method of Moments (MoM) is used in [32]. As the accuracy of the approximate formula is unknown, especially for the Schiebel coil which also includes a dielectric casing, and as we also need the charge distribution on the wire to analyze the effect of water on the head (see Chapter 6) we implemented a numerical method to estimate the capacitances. This is discussed in more details in the next section.

2.2.1 MAS Capacitance matrix

Both the MoM [33] and the MAS [34] can be used for problems where the space can be split in a number of homogeneous regions, with discontinuities between the regions. In both cases, the field is computed in each homogeneous region as if the whole space was homogeneous; that is using the full-space Green's function with permittivity and permeability of the considered region. This is possible according to the equivalence principle [35, Section 3.5] by introducing fictious sources on the boundary of the considered surface. Those sources radiate in a homogeneous space and the corresponding fields are thus easy to compute. The problem is then solved numerically by imposing that the boundary conditions are fulfilled at the discontinuity interfaces. For the MoM, the fictious sources are put on the surface and this comes with a number of numerical problems because, to impose the boundary condition, the fields must also be estimated at the boundary. The coincidence of the source and field points may yield discontinuities or even singularities in the field. The solution may also be ill-conditioned at low frequency

[3] It is the EQS proximity effect that is considered here, which is related to induced charge. It is different from the above mentioned MQS proximity effect which was said to be negligible.

(the low-frequency breakdown). Solutions have been found to perform the computations properly [36, 37, 38, 39, 40]. Nevertheless, the presence of those singularities makes the implementation of a numerical code significantly more complex.

In most cases, the fields may be computed in good approximation by using sources at some distance from the boundary. This alleviates the problems related to the presence of singularities. Furthermore, as there exists some distance between the source and field points, a number of discrete point sources may be adequate. Using such point sources at some distance from the boundaries is the idea underlying the MAS and this renders the implementation of a numerical code almost straightforward.

At frequencies of interest for a MD (up to 100kHz), the EQS approximation can be used to compute the charge distribution on the coil. Furthermore, neglecting the curvature of the coil, the problem can be reduced to a 2D problem, using line charge sources. For an EQS problem, it is simpler to solve the problem in terms of the scalar potential (ϕ) rather than in terms of the fields. The boundary conditions are then expressed in terms of the potential and its normal derivative $E_{\mathrm{n}} = \boldsymbol{E} \cdot \hat{\boldsymbol{n}} = -\dfrac{\mathrm{d}\phi}{\mathrm{d}n}$ which can be computed from the sources, using the full-space Green's function, as follows [31, p. 219]:

$$\phi(\boldsymbol{r}) = -\frac{\ln(R)}{2\pi\epsilon}\lambda(\boldsymbol{r}') \tag{2.6}$$

$$\boldsymbol{E}(\boldsymbol{r}) = \frac{\hat{\boldsymbol{R}}}{2\pi\epsilon R}\lambda(\boldsymbol{r}') \tag{2.7}$$

with λ the charge per unit length and $R = |\boldsymbol{r} - \boldsymbol{r}'|$ the distance between the source and field point and $\hat{\boldsymbol{R}} = (\boldsymbol{r} - \boldsymbol{r}')/R$ the unit vector along the line joining the source to the field point.

At dielectric interfaces the boundary conditions are the continuity of the potential and of the normal displacement field ($D_{\mathrm{n}} = \epsilon\dfrac{\mathrm{d}\phi}{\mathrm{d}n}$). On conductors the potential is constant. Hence, no external sources are required to compute the potential inside the conductors; only internal sources are required to compute the potential outside the conductors.

When the conductors are connected through a voltage source, the potential difference between the two conductors is imposed. Note that one often chooses a reference conductor and assigns to it by convention a null potential. This is not possible here because with the chosen Green's function (2.6), the potential is null on the sphere[4] at infinity. In addition, the total charge on the whole coil (the sum of the loops charge) must be null[5] and, the potential of the reference conductor must be computed to satisfy this condition. Our implementation allows us to introduce a conducting shield around the casing. Such a shield is floating with respect to the coil turns. The corresponding potential may also be computed by imposing that the total charge on the shield must be null. Practically, in our implementation, we have defined 'conductor groups' with a reference conductor in each group. The potential of each reference conductor is computed to ensure that the total charge on the corresponding conductor group is null. The potential difference between the reference conductor and the other conductors of a group must be provided as input. Hence, groups are physically connected conductors. For our problem, two groups are used. One group for the coil loops and another group for the shield.

The MAS geometry is illustrated in Fig. 2.5 for the TX coil of the Schiebel. The wires (circles) are conductors and the medium between the coils, inside the casing is supposed to be a homogeneous dielectric (with dielectric constant ϵ_c). The medium outside the casing is air and there is thus a dielectric discontinuity at the boundary of the casing (rounded square).

To compute the potential outside the casing, the whole space is filled with air (ϵ_0) and the potential is then computed using the free space Green's function (Equ. 2.6, with $\epsilon = \epsilon_0$) from fictious sources located inside the casing (blue points in Fig. 2.5 (c)). Similarly, to compute the potential inside the casing (but outside the wires), a full-space Green's function (Equ. 2.6, with $\epsilon = \epsilon_c$) is used and fictious sources are placed outside the casing (green points in Fig. 2.5 (c)) and inside the wires (blue points in Fig. 2.5 (b)). The potential inside the wires is constant and needs no to be computed. The boundary conditions are expressed at a number of 'field' points located at the interfaces between regions

[4]More precisely the cylinder, because with the 2D approximation, conductors extend to infinity.

[5]The coil may carry a net total charge (for example if it has been touched by a charged body during maintenance) but this is then a constant (DC) charge. Here, we are interested in the low frequency regime and the total charge may not have such a low frequency component because there is no connection between the coil and the infinite sphere (or more practically the soil) and no current can flow on and off the coil.

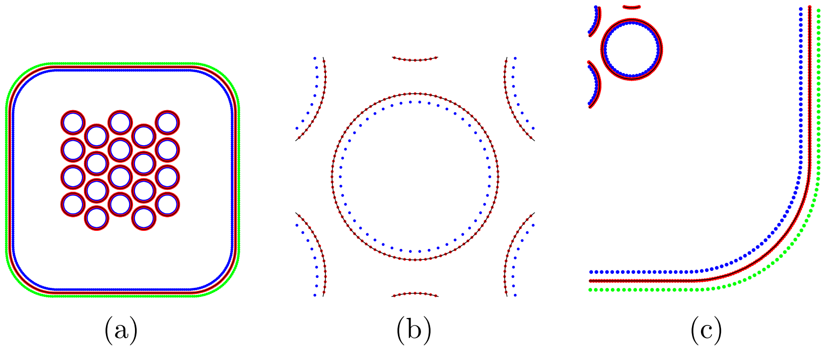

Figure 2.5: *MAS geometry for the TX coil. Inner sources are shown in blue, outer sources in green, test points in red, and region contour in black. (a) Global view, (b) zoom on central wire and (c) zoom on lower right corner of casing. Turn layout has been modified and is for illustration only.*

(red points in Fig. 2.5).

This yields a linear system of equations:

$$\underline{V} = \underline{\underline{Z}}\,\underline{Q} \tag{2.8}$$

With $\underline{V}$ a known column vector containing the potential difference with the reference conductor and a number of zeros for the lines expressing the continuity of ϕ and D_{n}, $\underline{Q}$ an unknown column vector containing the charge for each source as well as the reference potentials for each conductor group. $\underline{\underline{Z}}$ is a 2D matrix computed in such a way that (2.8) expresses the boundary conditions as well as the constraint that the total charge on each conductor group is null. Note that charges, displacement fields and potentials may have very different scales and this yields an ill-conditioned matrix. To avoid this pitfall, the lines of (2.8) are multiplied by a well chosen factor to have the same order of magnitude for the various terms.

To get a unique solution, one must use as many field points as source points for each region. In practice, we will use more field points (typically two times more) and use the Least Mean Square (LMS) solution of the overdetermined system (2.8). It is then possible to assess the residual error. If this error is small, the source points have been well chosen and the boundary conditions are expected to be well satisfied on the whole boundary; not only at the field points.

The dimensions of the various terms are:

$$\{n_\mathrm{s} + n_\mathrm{g}, 1\}$$

for $\underline{Q}$,

$$\{\alpha_\mathrm{o}(2n_\mathrm{fd} + n_\mathrm{fc}) + n_\mathrm{g}, 1\}$$

for $\underline{V}$ and

$$\{\alpha_\mathrm{o}(2n_\mathrm{fd} + n_\mathrm{fc}) + n_\mathrm{g}, n_\mathrm{s} + n_\mathrm{g}\}$$

for $\underline{\underline{Z}}$ with n_s the number of source points, n_g the number of conductor groups, n_fd the number of field points at the boundary between two dielectric regions, n_fc the number of field points at the boundary of conductors and α_o the over-determination factor.

The source distribution can then be obtained by inverting (2.8). As an illustration, we consider the solution at low frequency, far below the first resonant frequency and for a voltage of one volt applied to the coil: $V_\mathrm{coil} = 1$. In that regime, according to the model of Fig. 2.3 (b), the current in the capacitances remains small and the voltage is mainly fixed by the inductors. Hence, for equal induction for each turn and equal mutual coupling between turns, the potential evolves linearly along the coil. Hence, the potential difference between two consecutive turns is $V_\mathrm{t,t+1} = V_\mathrm{coil}/n_\mathrm{t}$ with V_coil the voltage applied on the coil and n_t the number of turns.

The resulting auxiliary sources are illustrated in Fig.2.6. The corresponding excitation vector $\underline{V}$ is shown in Fig. 2.7. The first 1600 elements are null because they correspond to equations that are expressing the continuity constraints on the casing boundary (800 points, 2 equations per point; one for the continuity of potential and the other for the continuity of D_n). The next 2000 elements (100 field points per turn, 20 turns) are the potential differences between the considered turn (t) and the reference turn (1): $V_\mathrm{t}^1 = (t-1)/n_\mathrm{t}$. The last element is null and corresponds to the constraint imposing that the total charge on the coil is zero. Together with the imposed value of $\underline{V}$ (red), the value obtained by plugging the solution for the auxiliary sources ($\underline{Q}$) in (2.8) is also shown in black. The difference between the imposed and the reconstructed value is the residue of the LMS inversion. One sees that this residue is small, which indicates that the boundary conditions are well satisfied, even with an over-determination factor of two, and this gives confidence that the auxiliary source distribution has been well chosen.

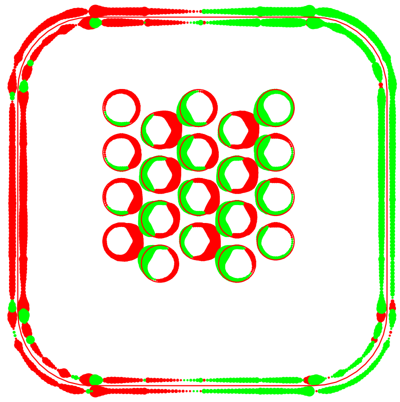

Figure 2.6: *MAS charge distribution for TX coil at low frequencies. Positive charges are indicated by green disks and negative charges are indicated by red disks. The size of the disk indicates the magnitude of the charge. Turn layout has been modified and is for illustration only.*

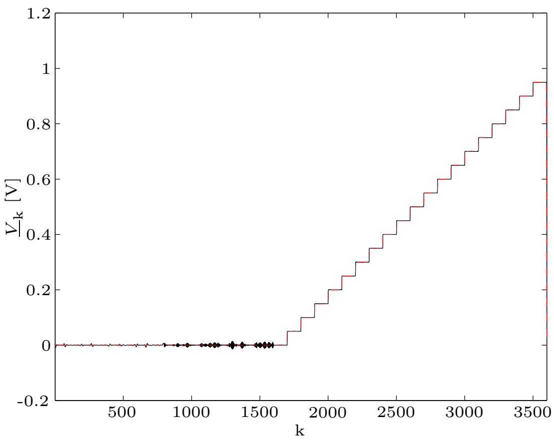

Figure 2.7: $\underline{V}$ *imposed (red) and reconstructed (black) for the MAS geometry of the TX coil shown in Fig. 2.5. The first 1600 equation are for the continuity on the casing boundary, the next are for the wire voltages and the last is for the total zero charge constraint.*

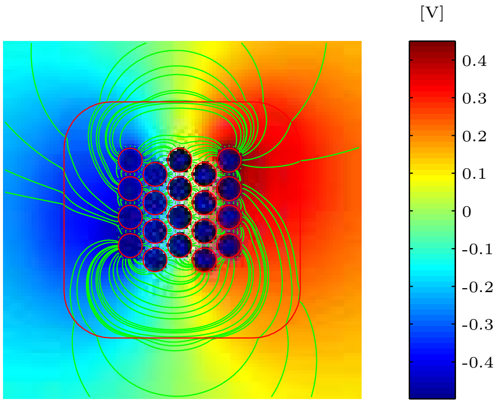

Figure 2.8: *Potential (in Volts) and E-field line for the Schiebel TX coil. The computation has been done with the MAS, assuming $V_{\text{coil}} = 1$ and a frequency much lower than the first coil resonance frequency. The resulting reference potential is $V_{\text{ref}} = -0.48\,V$. Turn layout has been modified and is for illustration only.*

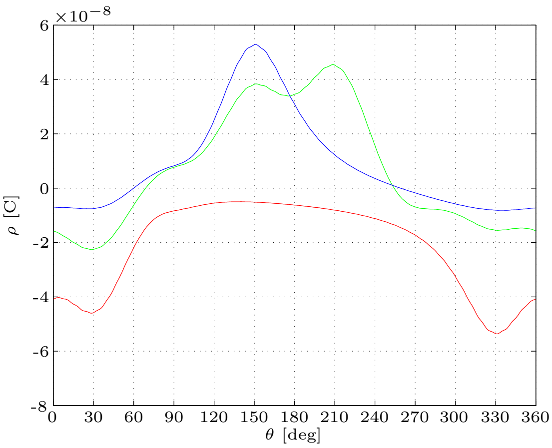

Figure 2.9: *Charge distribution on turns 1 (red), 7 (green) and 8 (blue) of the TX coil (see Fig. 2.2 (a) for turn numbering).*

Once the charge distribution has been calculated, one may compute the potential and the field everywhere. This is illustrated in Fig. 2.8 where the potential and the field lines are indicated. Recall that turn 1 is the reference one and that its potential is calculated to get a zero total charge on the coil. For the example considered, the voltage applied to the coil is $V_{\text{coil}} = 1$ and the reference potential is $V_{\text{ref}} = -0.48$, leading to an average coil potential which is approximatively zero as expected for an uncharged coil (zero total charge). Indeed, the charge induced on the infinite sphere by a given loop is proportional to the loop potential and to the capacitance between the loop considered and the infinite sphere. If the loop-to-infinite-sphere capacitances were all equal, the total charge on the infinite sphere (which is equal to the total coil charge) would be proportional to the average coil potential. In practice, the total coil charge is zero and the loop-to-infinite-sphere capacitances are nearly equal and, therefore, the average coil potential must be approximately zero.

Using $\rho = D_{\text{n}}^{+}$ at the boundary of a conductor, one can also compute the charge distribution on the wire. This is illustrated in Fig. 2.9. One sees that the (absolute) charge density is the largest on conductors 1 and 8 at their point of closest approach ($\theta = 330°$ for conductor 1 and $\theta = 150°$ for conductor 8[6]) because the voltage between those two conductors is the largest (the voltage is proportional to the difference between conductor indexes: here 7=8-1). One also notes a plateau of charge density at the closest approach between conductors 7 and 8 ($\theta = 270°$ for conductor 7 and $\theta = 90°$ for conductor 8). The effect is smaller because the voltage between conductors 7 and 8 is (7 times) smaller than between conductors 1 and 8.

Finally, imposing a one volt voltage between a chosen turn (i) and all the others (which are short- circuited together), one can compute one line of the capacitance matrix from the solution of (2.8):

$$C^{\text{t}}_{\text{i,j}} = Q_{\text{j}} \tag{2.9}$$

Repeating this for all the conductors yields the turn-to-turn capacitance matrix. This is illustrated in Fig. 2.10 where the turn-to-turn capacitance matrices of the Schiebel TX and RX coils are shown. One sees that the capacitances are the largest between two neighboring turns as expected. For example, the first line of the TX capacitance matrix shows

[6] The trigonometric convention as been used for θ. θ=0 is thus on the horizontal line through the conductor center, at the right of it.

the largest values (appearing in brown and orange) for columns 2, 7 and 8 which corresponds to the turns neighboring turn 1. One also sees that the value of the capacitances between two neighboring coils varies significantly due to proximity effects; confirming that the analytic solution for two isolated conductors is not appropriate and that a numerical method such as the MAS should be used to compute the capacitance matrices. Finally, (2.1) can be used to compute the node-to-node capacitance matrix needed for the circuit model.

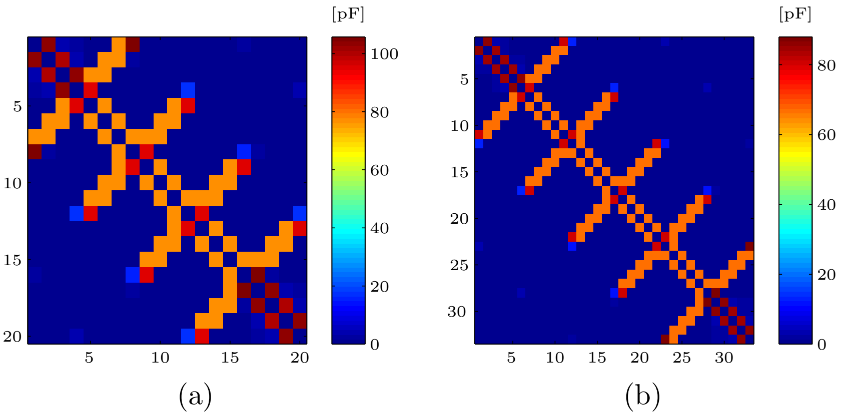

Figure 2.10: *Turn-to-turn capacitance matrix for (a) the TX coil and (b) the RX coil of the Schiebel detector.*

2.2.2 Simple circuit parameters

The parameters of the simple equivalent circuit of Fig. 2.3 (a) have been measured [27] as follows:

$$\begin{aligned} C_{\mathrm{TX}} &= 154pF \\ L_{\mathrm{TX}} &= 241\mu H \\ R^{\mathrm{L}}_{\mathrm{TX}} &= 0.69\Omega \\ C_{\mathrm{RX}} &= 161pF \\ L_{\mathrm{RX}} &= 461\mu H \\ R^{\mathrm{L}}_{\mathrm{RX}} &= 2.46\Omega \end{aligned} \tag{2.10}$$

Our objective is to compute the equivalent parameters ($R_{\mathrm{TX/RX,equ}}$, $L^{\mathrm{R}}_{\mathrm{TX/RX,equ}}$, $C_{\mathrm{TX/RX,equ}}$) of the simple circuit from those of the detailed circuit such that both circuits present a good matching. This will allow us to compare the measured and computed parameters for the simple circuit.

If the circuits match, the input current and voltage and hence the active and reactive power flowing in both circuits must be equal. According to the frequency domain Poynting theorem [35, Section 1.10][31, Section 2.20], there is conservation of both the active and reactive power. Hence, the active power dissipated in the resistors and the reactive power 'dissipated' in the inductors and 'generated' in the capacitors must be equal for both circuits. The complex power dissipated in an impedance Z is given by:

$$S_{\mathrm{Z}} = P_{\mathrm{Z}} + iQ_{\mathrm{Z}} = V_{\mathrm{Z}} I_{\mathrm{Z}}^{*} = Z|I_{\mathrm{Z}}|^2 = \frac{|V_{\mathrm{Z}}|^2}{Z^*} \tag{2.11}$$

with P_{Z} and Q_{Z} the corresponding active and reactive power, I_{Z} the current through the impedance, V_{Z} the corresponding voltage drop and '*' indicates the complex conjugate.

Obviously, the two circuits can only match below the first resonance frequency. In that frequency band, we can assume that the same current I_{coil} flows through all inductor branches. The active power dissipated in the resistor of the inductor branch is then:

$$P_{\mathrm{R^L}} = R^{\mathrm{L}}_{\mathrm{equ}} |I_{\mathrm{coil}}|^2 \tag{2.12}$$

for the simple circuit and:

$$P_{\mathrm{R^L}} = \sum R^{\mathrm{L}}_{\mathrm{i}} |I_{\mathrm{coil}}|^2 \tag{2.13}$$

for the detailed circuit.

As the current in the capacitive branches is much smaller than the current in the inductive branches and as the resistors in the capacitive branches are also much smaller than the resistors in the inductor branches, the power dissipated in the resistors of the capacitor branches is negligible when compared to that dissipated in the inductor branch resistors. Therefore, conservation of active power implies that (2.12) and (2.13) must be equal and therefore:

$$R^{\mathrm{L}}_{\mathrm{equ}} = \sum_{i} R^{\mathrm{L}}_{\mathrm{i}} \tag{2.14}$$

Similarly, for the simple circuit, the reactive power dissipated in the inductors is:

$$Q_{\mathrm{L}} = \omega L_{\mathrm{equ}} |I_{\mathrm{coil}}|^2 \tag{2.15}$$

For the detailed circuit, noting that the voltage drop across an inductor i is:

$$V_{\mathrm{L_i}} = \sum_k j\omega M_{\mathrm{i,k}} I_{\mathrm{coil}} \tag{2.16}$$

with $M_{\mathrm{i,k}}$ the mutual coupling matrix (to be consistent with Fig. 2.3 where the self induction terms were denoted L_{i}, we have $L_{\mathrm{i}} = M_{\mathrm{i,i}}$) , the reactive power dissipated in the inductors is:

$$Q_{\mathrm{L}} = \sum_{i,j} \omega M_{\mathrm{i,j}} |I_{\mathrm{coil}}|^2 \tag{2.17}$$

Finally, for the simple circuit, the reactive power dissipated in the capacitors is:

$$Q_{\mathrm{C}} = -\omega C_{\mathrm{equ}} |V_{\mathrm{C}}|^2 \tag{2.18}$$

with

$$V_{\mathrm{C}} = j\omega L_{\mathrm{equ}} I_{\mathrm{coil}} \tag{2.19}$$

where we have neglected the resistor R^{L} because in the frequency of interest for the MD, the voltage is mainly dictated by the inductor. For example, for the TX coil, $\omega L > R^{\mathrm{L}}$ for a frequency above about 500 Hz.

Similarly, for the detailed circuit, the reactive power dissipated in the capacitors is :

$$Q_{\mathrm{C}} = -\omega \sum_{i,j} C_{\mathrm{i,j}} |V_{\mathrm{i}} - V_{\mathrm{j}}|^2 \tag{2.20}$$

with V_{i} the node voltage. Again neglecting the resistors, the node voltages can be computed by cumulating the voltage drops across the inductors:

$$V_{\mathrm{i+1}} = V_{\mathrm{i}} + V_{\mathrm{L_i}} \tag{2.21}$$

where L_{i} can be computed according to (2.16).

From the above expressions, it is apparent that the frequency dependency of the reactive power dissipated in the inductors is different from that dissipated in the capacitors[7]. Therefore, to get the best matching, both Q_{L} and Q_{C} must be equal for the simple and the detailed circuits.

Matching the reactive power dissipated in the inductors then yields the following equivalent inductor:

$$L_{\mathrm{equ}} = \sum_{i,j} M_{\mathrm{i,j}} \tag{2.22}$$

[7]For a frequency independent coil current I_{coil}, the frequency dependences of Q_{L} and Q_{C} are ω and ω^3 respectively.

Similarly, matching the reactive power dissipated in the capacitors yields:

$$C_{\mathrm{equ}} = \frac{\sum_{i,j} C_{\mathrm{i,j}} |V_{\mathrm{i}} - V_{\mathrm{j}}|^2}{|V_{\mathrm{C}}|^2} \tag{2.23}$$

which is frequency independent as required because, according to (2.19) and (2.21), the frequency dependency of V_{C} and V_{i} are the same.

The parameters of the detailed circuit have been computed from the coil description, as explained in the previous sections. The corresponding equivalent parameters are:

$$\begin{aligned}
C_{\mathrm{TX,equ}} &= 154pF \\
L_{\mathrm{TX,equ}} &= 255\mu H \\
R^{\mathrm{L}}_{\mathrm{TX,equ}} &= 0.56\Omega \\
C_{\mathrm{RX,equ}} &= 161pF \\
L_{\mathrm{RX,equ}} &= 489\mu H \\
R^{\mathrm{L}}_{\mathrm{RX,equ}} &= 2.41\Omega
\end{aligned} \tag{2.24}$$

When compared to the measured parameters (2.10), one sees that the capacitors are identical and that the inductances and resistors are well estimated. For the resistors, the estimated values are slightly smaller than the measured ones. This difference may be explained by measurement errors and by the fact that we did not take into account the resistance of the wire connecting the coil to the electronics and the resistance of the connectors. The inductances are also slightly underestimated. This may be due to the fact that we have assumed a coil build of a single uniform wire whereas in reality, Litz wires are used. The use of Litz wire is indeed expected to increase the self-inductance of the loops.

The capacitances match perfectly but this is because there are unknown coil parameters that were optimized to match the computed capacitances with the measured ones. Namely, the dielectric permittivity of the casing, the dielectric permittivity of the cable insulators and possibly the location of air gaps between the casing and the wire insulators are unknown. Assuming the same permittivity for the insulator and the casing and assuming that there are no voids, the matching of C_{TX} was obtained for a relative permittivity of the casing: $\epsilon^{\mathrm{r}}_{\mathrm{c}} = 4.23$ which seems quite realistic. The same permittivity was used for the RX coil, but as the thickness of the insulator of the RX wires could not be determined accurately from the available drawings, it was also optimized to match

C_{RX}. The obtained value is 0.07mm which is compatible with the 0.1mm estimated from the drawing.

For the capacitance estimation also, the wire has been modeled as a single uniform wire and the potential has been assumed on its section. With Litz wire, strands are isolated and they could have different potentials. However, as the strands are twisted, we expect the potential to vary little on the wire section and this section differs little from the circle used for the capacitance computation. Hence, the computation should remain appropriate for Litz wire.

2.2.3 Corrected parameters

We saw that the equivalent parameters are close to the measured ones but there remains a small difference. The detailed model is thus in good agreement with the measurements but it may still be improved by correcting its parameters so that the equivalent parameters exactly match the measured one. This was already done for the capacitances because some parameters such as the permittivity of the casing were not known and they were estimated in order to match the equivalent capacitances with the measured ones. The estimated parameters were found to be quite realistic and this gave us good confidence in the model.

The detailed model was thus further improved by correcting the resistors $R_{\mathrm{i}}^{\mathrm{L}}$ and the inductance matrix $\underline{\underline{M}}$ in such a way that the equivalent parameter exactly matches the measured ones. More precisely, the correction used is:

$$R_{\mathrm{i,corr}}^{\mathrm{L}} = \alpha_{\mathrm{R}} R_{\mathrm{i}}^{\mathrm{L}} \tag{2.25}$$

and

$$M_{\mathrm{i,i,corr}} = \alpha_{\mathrm{L}} M_{\mathrm{i,i}}^{\mathrm{L}} \tag{2.26}$$

with α_{R} and α_{L}, two multiplicative factors independent of i. For the mutual coupling matrix, we have only corrected the diagonal elements which correspond to the self-induction terms because those terms are the most sensitive to small geometrical errors.

With this correction, any remaining discrepancy between the simple and the detailed model can only come from an inaccuracy of the expressions (2.14), (2.22) and (2.23) that were used to compute the equivalent parameters. We will show in the next section that the two models match very accurately and this will validate the expressions used to compute the equivalent parameters.

2.3 Coil dynamics

Our objective is to better understand the frequency limit for the validity of the simple model and to better understand the coil behavior at higher frequencies. For this, we have computed the state-space representations of the simple and detailed[8] coil model as explained in Appendix A and using as input the current injected in the coil I_{coil} and as output the voltage on the coil V_{coil}. The resulting transfer function is the impedance of the coil. This impedance can easily be computed for the simple model. Neglecting the resistance of the capacitance branch R^{C}, this yields:

$$Z_{\text{coil}} = R^{\text{L}}\omega_0^2 \frac{1 + sT_{\text{L}}}{s^2 + 2\zeta\omega_0 + \omega_0^2} \tag{2.27}$$

with s the Laplace variable, $\omega_0 = 1/\sqrt{LC}$ the undamped resonance angular frequency , $\zeta = 0.5R^{\text{L}}\sqrt{C/L}$ the damping factor and $T_{\text{L}} = L/R^{\text{L}}$ the time constant of the inductance branch[9]. The gain is R^{L} as expected, the poles are located at $s = \omega_0(-\zeta \pm i\sqrt{1-\zeta^2})$. For example, considering the measured parameters for the TX coil (2.10), this yields $\omega_0 = 5.19 \times 10^6$rad/s (the corresponding resonance frequency is 826kHz), $\zeta = 2.7 \times 10^{-4}$, $T_{\text{L}} = 349\mu s$ and the poles are located at $s = -1.43 \times 10^3 \pm 5.19 \times 10^6 i$

The poles and zeros of the state-space systems are shown in Fig. 2.11 for both the simple and the detailed model. One sees that the poles of the simple system correspond to the ones computed according to the analytic solution (2.27) and that the dominant poles and zeros of the detailed system are close to those of the simple system. The detailed system has additional pairs of complex conjugate resonant poles and zeros; 19 each. This yields, as expected, one pair of complex conjugate poles per turn. In addition, the detailed system has 122 extra real poles. Those poles are orders of magnitude faster than the resonant poles. They have no influence on the coil response and are therefore not shown in the figure. The precise location of those poles is a function of the capacitive branch resistors $R^{\text{C}}_{\text{i,j}}$ which were introduced to avoid loops of capacitors that would yield impossible circuits equations. Those resistors exist physically but they are small compared to R^{L}_{i}. We did not

[8]To keep a tractable size for the detailed state-space model, the negligible capacitances ($C < 0.1pF$) were suppressed from the circuit.

[9]This is the time constant for the current response when excited with a voltage source.

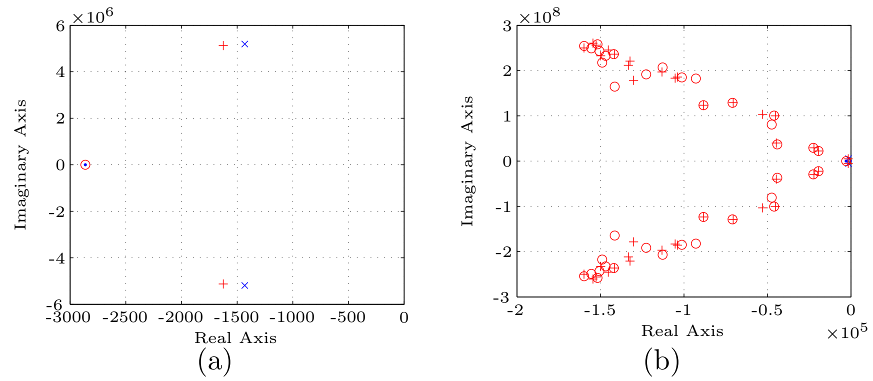

Figure 2.11: *Poles (+ and ×) and zeros (o) of the Schiebel TX coil impedance for the simple (blue) and the detailed (red) models. Dominant poles (a) and all poles except for the real ones far away from complex ones (b).*

estimate the capacitance branch resistances but fixed them arbitrarily to $R^{\mathrm{C}}_{\mathrm{i,j}} = R^{\mathrm{L}}_{\mathrm{i}}/100$. We see that this choice is appropriate because the corresponding poles have no influence and the precise value of $R^{\mathrm{C}}_{\mathrm{i,j}}$ is irrelevant as long as it is small enough.

To further compare the two models, the Bode curves of the impedances are shown in Fig. 2.12. One sees that the matching is very good up to the first resonance, confirming the validity of (2.14), (2.22) and (2.23). One also sees that, as expected, the detailed model shows additional resonance peaks.

Finally, to understand the current repartition across the coil, the eigenvectors[10] of the state-space matrix $\underline{\underline{A}}$ corresponding to the first three resonant frequencies are shown in Fig. (2.13). One sees that at the first resonance, the current evolves approximately parabolically across the coil and the maximum current occurs around the middle turn. One sees also as expected that higher order modes become more complex, with more maximums and minimums.

It is also interesting to visualize the same eigenvectors for the coil admittance. Indeed, the poles of the admittance are the zeros of the

[10]The eigenvectors are state vectors and, therefore, they include the currents in the inductance I_{L} as well as other states. Only the part corresponding to the inductance current is shown.

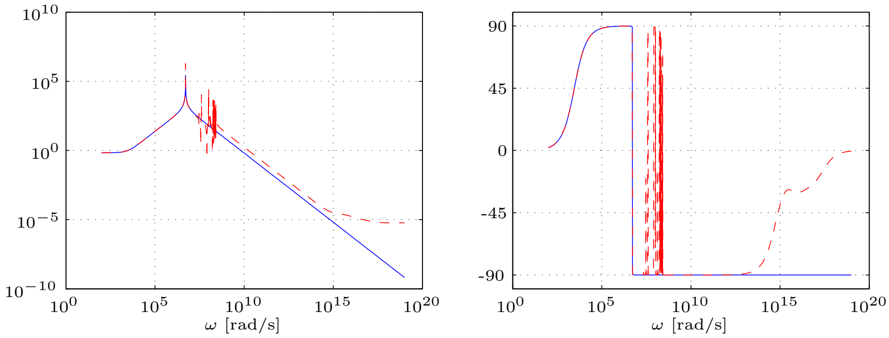

(a) (b)

Figure 2.12: *Bode curves of the Schiebel TX coil impedance for the simple (blue) and the detailed (red) models. Magnitude (a) and phase (in degrees) (b) of the impedance are shown as a function of* ω.

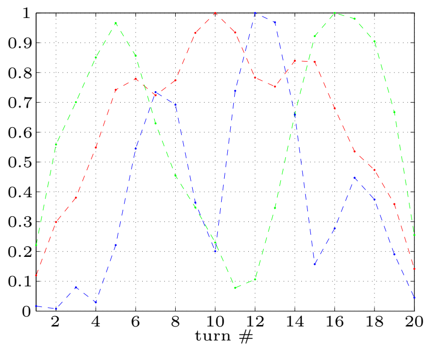

Figure 2.13: *Current repartition through the coil at the first (red), second (green) and third (blue) resonant frequencies of the impedance.*

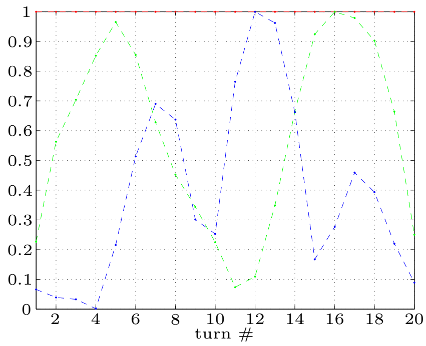

Figure 2.14: *Current repartition through the coil at the first mode (red — the current remains constant at 1. the curve is thus superimposed on the upper axis and may therefore be difficult to see), second (green) and third (blue) resonant frequencies of the admittance.*

impedance. Hence the dominant pole is real and corresponds to the time constant of the inductor T_L. This time constant characterizes the evolution of the current in the coil when excited with a voltage source. For such a slow-time variation (when compared to the first resonance frequency) the effect of the coil capacitors can be neglected. Therefore as confirmed in Fig. 2.14 for the first mode, corresponding to the dominant time constant T_L, the current remains constant along the coil.

2.4 Coil induced voltage

2.4.1 Introduction

Our objective is to compute the voltage induced in a coil by external fields. For the coil of a MD, the external sources to consider include eddy-currents induced in a metallic object[11], magnetic dipoles induced in ferrous objects or in magnetic soils and current flowing in power lines.

As illustrated in Fig. 2.15, the effect of external fields is often modeled by introducing a voltage source e_L representing the induced voltage

[11]The MD is an active device and therefore, the real source is obviously not in the metallic object but in the TX part of the detector. One may however split the computation in two parts by first computing the currents induced in the metallic object then, replacing the metallic object by equivalent sources and computing the voltage induced in the RX coil by those sources.

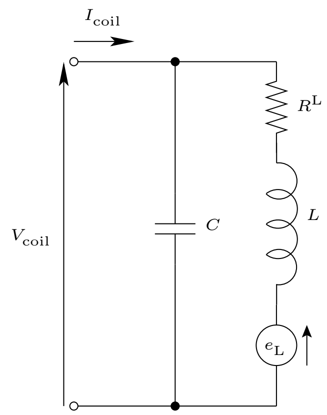

Figure 2.15: *Simple coil model with induced voltage.*

in the L branch and the induced voltage is assumed to be:

$$e_{\text{L}} = \frac{\mathrm{d}\psi}{\mathrm{d}t} \tag{2.28}$$

where ψ is the magnetic flux flowing through the coil and produced by external sources[12] Note that we use the induced voltage e_{L} and not the electromotive force ξ. Those are related concepts; only the sign changes: $e_{\text{L}} = -\xi$.

This simple model is not sufficient to explain some observed phenomena such as the effect of water on the head of a MD. We will resort to reciprocity to develop an enhanced model. According to that enhanced model, the induced voltage has two contributions. The first is a magnetic contribution, identical to that of the simple model. In addition, there is an electrical contribution that will be related to coil parasitic capacitances through the resulting charge distribution that may appear on the coil. As a result of the electrical contribution, and contrary to what is predicted by the simple model, EQS fields may induce a voltage in the coil. We will show that water droplets may produce such an EQS field and that the additional electrical contribution appearing in the enhanced model may explain some of the effects that water has on the head.

[12]The magnetic flux due to the current in the coil itself must not be included in ψ because its effect is modeled by the inductor in the equivalent circuit.

We first consider a detector with a single coil connected to a perfectly shielded electronic box by a perfectly shielded coaxial cable. The effect of a non-perfect shield or the use of other cables as well as the effect of the second coil used in some heads (such as the Schiebel) will then be discussed.

2.4.2 Problem formulation

The configuration considered is depicted in Fig. 2.16. The detector is composed of an electronic box linked to the coil by a coaxial cable. The electronic box is bounded by $\mathcal{S}_\mathrm{e}$. It is assumed perfectly shielded by a Perfect Electric Conductor (PEC) and therefore, the electric field is zero everywhere on $\mathcal{S}_\mathrm{e}$ except on the coaxial cable connection $\mathcal{S}_\mathrm{c}$. We define a surface $\mathcal{S}_\mathrm{d}$ which is closed, large enough to completely include the detector and small enough to avoid any external source or contrast. In other words, $\mathcal{S}_\mathrm{d}$ only includes air (which for our purpose is equivalent to free space) and the detector. Our objective is to compute the response induced in the coil by sources or contrasts located outside $\mathcal{S}_\mathrm{d}$. For the time being, we will consider contrasts as being a specific case of sources. This is always possible because any contrast can be replaced by equivalent (surface or volume) sources [35, Section 3.5]. Obviously those equivalent sources $\boldsymbol{J}_\mathrm{s}$ are induced in the contrast and must be computed as a function of the field emitted by the detector.

The coil[13] is assumed linear and it can therefore be represented by its Thevenin equivalent[14]:

$$V_\mathrm{coil} = Z_\mathrm{coil} I_\mathrm{coil} + e \tag{2.29}$$

where V_coil is the voltage between the coil terminals, I_coil is the current flowing into the coil, Z_coil is the coil impedance and e is the voltage induced by the external sources. The coil impedance can easily be measured. For this the coil should be put in free space (or air) and the effect of any background EM field should be minimized. It can also be estimated as discussed above but this requires a detailed knowledge of the coil geometry and of the EM properties of the material used. Note

[13]This assumption is not needed for the electronics for which it is in general not valid because the electronics may include nonlinear components.

[14]This assumes that there is no coupling between the currents and charges inside the electronics and the coil. This is rigorously valid for a perfectly shielded electronics and is also valid in good approximation for all (realistic) electronics. See Section 2.4.7 for more details.

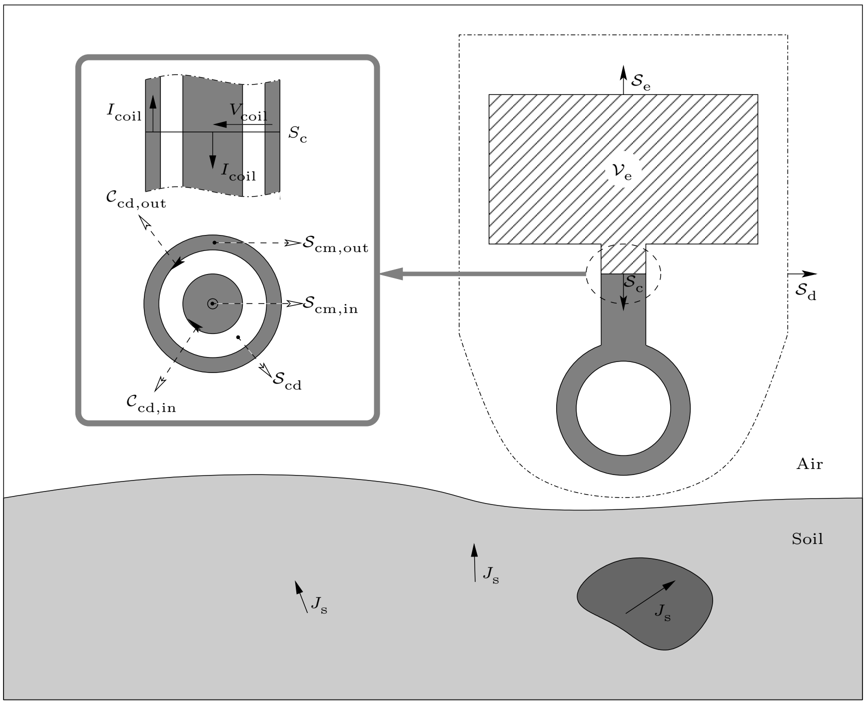

Figure 2.16: *Problem configuration to compute the voltage induced in the coil. The detector, composed of an electronic box (inside $\mathcal{V}_e$) and a coil, is located above a soil that may be inhomogeneous and contain metallic objects. The soil is replaced by equivalent currents J_s. $\mathcal{S}_c$ is the part of $\mathcal{S}_e$ inside the coaxial cable and it is divided into $\mathcal{S}_{\text{cd}}$ (the dielectric part), $\mathcal{S}_{\text{cm,in}}$ and $\mathcal{S}_{\text{cm,out}}$ (the inner and outer metallic part of the coaxial cable section). $\mathcal{C}_{\text{cd,in}}$ and $\mathcal{C}_{\text{cd,out}}$ are the inner and outer contour of $\mathcal{S}_{\text{cd}}$. $\mathcal{S}_d$ is a surface containing the electronics and the coil but not the soil. The positive normal and contours are indicated with solid and slanted arrows. Currents and voltages are shown with solid and straight arrows. Insert on the left: close-up on the coaxial cable with (top) a longitudinal cut and, (bottom) a transverse cut through $\mathcal{S}_c$. The transverse cut is seen looking from the coil to the electronics.*

that the induced voltage e appearing in (2.29) is slightly different from e_{L} that appears in Fig. 2.15. Indeed, the former is located in series with the coil seen as a whole whereas the latter is located in the inductive branch. This will be further discussed in Section 2.4.6.

2.4.3 Sign conventions

As various sign conventions may be found in the literature, we now clarify the sign convention used.

The convention for the coil current, the coil voltage and the induced voltage are those of Fig. 2.15. This is usually called the *motor convention.* Note that a positive induced voltage e yields a positive voltage at the coil terminals V_{coil}.

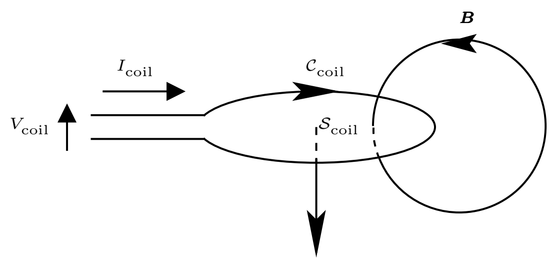

Figure 2.17: *Simple coil model with sign conventions for positive coil current I_{coil}, positive coil voltage V_{coil}, and corresponding positive coil contour $\mathcal{C}_{\mathrm{coil}}$ and coil surface $\mathcal{S}_{\mathrm{coil}}$ with its positive normal. The magnetic induction $\boldsymbol{B}$ corresponding to a positive current is also indicated.*

The sign of the flux is chosen such that a positive current produces a positive flux through the coil. If, as illustrated in Fig. 2.17, the coil is defined by a closed contour $\mathcal{C}_{\mathrm{coil}}$ oriented according to the positive current (a positive current flows along the positive direction of the contour), then the flux can be computed as:

$$\psi = \int_{\mathcal{S}_{\mathrm{coil}}} \boldsymbol{B} \cdot \mathrm{d}\boldsymbol{S} \tag{2.30}$$

with $\mathcal{S}_{\mathrm{coil}}$ any oriented surface bounded by the oriented contour $\mathcal{C}_{\mathrm{coil}}$ and oriented according to our general convention (the positive normal of $\mathcal{S}_{\mathrm{coil}}$ is chosen such that it is related to the positive tangent of $\mathcal{C}_{\mathrm{coil}}$ by the right-hand rule). One sees on Fig. 2.17 that with those conventions, a positive current indeed produces a positive flux.

Introducing (2.30) in (2.28), expressing $\boldsymbol{B}$ according to the Faraday law and applying the Stokes theorem, the induced voltage may be expressed as:

$$e_{\mathrm{L}} = -\int_{\mathcal{C}_{\mathrm{coil}}} \boldsymbol{E} \cdot \mathrm{d}\boldsymbol{\ell} \tag{2.31}$$

with $\boldsymbol{E}$ the electric field produced by the external sources. This shows that e_{L} is indeed an induced voltage and not the magnetomotive force.

The coherence of (2.28) with our sign convention can easily be checked on Fig. 2.17. Indeed, consider an external flux that increases ($\frac{\mathrm{d}\psi}{\mathrm{d}t} > 0$). According to the Lenz's law, a current will be induced in the coil to oppose the flux change. In other words, current will be induced in the coil to produce a negative flux that will oppose the increase of the external flux. By definition of the positive flux, this corresponds to a negative current and according to Fig. 2.15 this corresponds to a positive e. Hence, with our conventions, an increase of the flux produces a positive induced voltage. This is indeed coherent with (2.28).

2.4.4 Relation between induced voltage and fields on a surface $\mathcal{S}_{\mathrm{d}}$ surrounding the detector

To express the induced voltage e, we resort to reciprocity. Reciprocity expressions are usually expressed in the frequency domain and they allow us to relate the fields and sources pertaining to two configurations called 'states'. Several reciprocity expressions exist[31, 41, 35, 42, 43] and vary in their generality. For example [43] considers different media in the two states and therefore includes a contrast term whereas [41] assumes the same medium in both states. The general reciprocity expression is developed in Appendix C. It relates the fields and sources pertaining to states 'A' and 'B' in a volume $\mathcal{V}_{\mathrm{r}}$ which is bounded by a surface $\mathcal{S}_{\mathrm{r}}$. The underlying assumption is that the medium inside $\mathcal{V}_{\mathrm{r}}$ is linear in the two states. It does not need to be the same in the two states and does not need to be homogeneous. The medium outside $\mathcal{V}_{\mathrm{r}}$ is arbitrary (it may be nonlinear).

For our problem, we consider the two following states:

- $\Sigma_{\mathrm{s}}^{(\mathrm{d})}$ for which a source distribution $\boldsymbol{J}_{\mathrm{s}}$ radiates in presence of the detector (as indicated by the superscript '(d)' appearing in the state notation) and no current flows in the coil (RX electronics is an open circuit). This configuration is representative of the physical configuration and, as indicated by the subscript 's', it includes the source distribution $\boldsymbol{J}_{\mathrm{s}}$ for which one wants to compute the detector response.

- $\Sigma_{\mathrm{RX}}^{(\mathrm{fs})}$ for which the detector is in free space and the external sources are switched off ($\boldsymbol{J}_{\mathrm{s}} = 0$). A current $\boldsymbol{I}_{\mathrm{RX}}$ flows in the RX coil. This state is not physical but we will see with this choice, that reciprocity allows to express conveniently the voltage induced in the coil for the physical configuration of interest.

We then express the reciprocity relation between those two states in a volume $\mathcal{V}_{\mathrm{r}}$ which is bounded externally by $\mathcal{S}_{\mathrm{d}}$ and internally by $\mathcal{S}_{\mathrm{e}}$. There are no sources[15] in $\mathcal{V}_{\mathrm{r}}$ and the medium remains the same for the two states in that volume. Therefore, only the boundary term $B^{\mathrm{EH}}_{\mathcal{S}_{\mathrm{r}}}$ remains in (C.1.1). This yields:

$$\begin{aligned} &\oint_{\mathcal{S}_{\mathrm{d}}} \left(\boldsymbol{E}_{\mathrm{s}}^{(\mathrm{d})} \times \boldsymbol{H}_{\mathrm{RX}}^{(\mathrm{fs})} - \boldsymbol{E}_{\mathrm{RX}}^{(\mathrm{fs})} \times \boldsymbol{H}_{\mathrm{s}}^{(\mathrm{d})} \right) \cdot \mathrm{d}\boldsymbol{S} \\ &\qquad = \int_{\mathcal{S}_{\mathrm{c}}} \left(\boldsymbol{E}_{\mathrm{s}}^{(\mathrm{d})} \times \boldsymbol{H}_{\mathrm{RX}}^{(\mathrm{fs})} - \boldsymbol{E}_{\mathrm{RX}}^{(\mathrm{fs})} \times \boldsymbol{H}_{\mathrm{s}}^{(\mathrm{d})} \right) \cdot \mathrm{d}\boldsymbol{S} \end{aligned} \tag{2.32}$$

with $\left(\boldsymbol{E}_{\mathrm{s}}^{(\mathrm{d})}, \boldsymbol{H}_{\mathrm{s}}^{(\mathrm{d})}\right)$ and $\left(\boldsymbol{E}_{\mathrm{RX}}^{(\mathrm{fs})}, \boldsymbol{H}_{\mathrm{RX}}^{(\mathrm{fs})}\right)$ the fields in states $\Sigma_{\mathrm{s}}^{(\mathrm{d})}$ and $\Sigma_{\mathrm{RX}}^{(\mathrm{fs})}$ respectively. Note that the positive normal of $\mathcal{S}_{\mathrm{d}}$ points outside $\mathcal{V}_{\mathrm{r}}$ whereas the positive normal of $\mathcal{S}_{\mathrm{e}}$ points inside $\mathcal{V}_{\mathrm{r}}$. Therefore the boundary contribution on $\mathcal{S}_{\mathrm{e}}$ has a negative sign. It may thus be written with a positive sign on right hand side (r.h.s.) of (2.32). The electronics has further been assumed to be bounded by a PEC and therefore the boundary contribution of $\mathcal{S}_{\mathrm{e}}$ is reduced to the integral on the cable section $\mathcal{S}_{\mathrm{c}}$. Note that electronics may contain nonlinear material (diodes, transistors, ...) without affecting the validity of (2.32) because the electronics is outside $\mathcal{V}_{\mathrm{r}}$.

We can further develop the integral on the coaxial cable section by noting that at the frequencies of interest, only the Transverse Electromagnetic (TEM) mode propagates in a coaxial cable, the other modes

[15] We consider only the true current sources $\boldsymbol{J}_{\mathrm{s}}$, not the total current $\boldsymbol{J}$. As discussed in C.6 this is possible, as long as the conductivity is introduced in the permittivity. The use of ϵ_σ instead of ϵ does not introduce a contrast term because the medium is the same in the two states considered.

being attenuated exponentially with a characteristic length of the order of the radius of the coaxial cable. Therefore, assuming that $\mathcal{S}_\mathrm{c}$ is located at more than a cable radius from an end of the cable, only the TEM mode is present at $\mathcal{S}_\mathrm{c}$ and the transverse electric field derives from a scalar potential $\boldsymbol{E} = -\nabla\phi$ [44, Section 10]. Therefore:

$$\begin{aligned}\int_{\mathcal{S}_\mathrm{c}} \boldsymbol{E}_\mathrm{s}^{(\mathrm{d})} \times \boldsymbol{H}_\mathrm{RX}^{(\mathrm{fs})} \cdot \mathrm{d}\boldsymbol{S} &= \int_{\mathcal{S}_\mathrm{cd}} -\nabla\phi_\mathrm{s}^{(\mathrm{d})} \times \boldsymbol{H}_\mathrm{RX}^{(\mathrm{fs})} \cdot \mathrm{d}\boldsymbol{S} \\ &= -\int_{\mathcal{S}_\mathrm{cd}} \nabla \times \left(\phi_\mathrm{s}^{(\mathrm{d})} \boldsymbol{H}_\mathrm{RX}^{(\mathrm{fs})}\right) \cdot \mathrm{d}\boldsymbol{S} \end{aligned} \quad (2.33)$$

where the first equality has been obtained by noting that for an ideal coaxial cable (build with a PEC) the electric field is non-zero only on $\mathcal{S}_\mathrm{cd}$, the dielectric part of the cable section. The second equality has been obtained by using the vectorial identity (B.1.2) and by noting that $\nabla \times \boldsymbol{H}_\mathrm{RX}^{(\mathrm{fs})}$ does not contribute to the integral because no current flows in the dielectric and the displacement field has no component along the normal of $\mathcal{S}_\mathrm{cd}$.

Using the Stokes theorem, (2.33) then yields:

$$\int_{\mathcal{S}_\mathrm{c}} \boldsymbol{E}_\mathrm{s}^{(\mathrm{d})} \times \boldsymbol{H}_\mathrm{RX}^{(\mathrm{fs})} \cdot \mathrm{d}\boldsymbol{S} = \int_{\mathcal{C}_\mathrm{cd,in}} \phi_\mathrm{s}^{(\mathrm{d})} \boldsymbol{H}_\mathrm{RX}^{(\mathrm{fs})} \cdot \mathrm{d}\boldsymbol{\ell} - \int_{\mathcal{C}_\mathrm{cd,out}} \phi_\mathrm{s}^{(\mathrm{d})} \boldsymbol{H}_\mathrm{RX}^{(\mathrm{fs})} \cdot \mathrm{d}\boldsymbol{\ell} \quad (2.34)$$

where $\mathcal{C}_\mathrm{cd,in}$ and $\mathcal{C}_\mathrm{cd,out}$ are the inner and outer contours of $\mathcal{S}_\mathrm{cd}$. The positive tangent of those contours are defined from the positive normal of $\mathcal{S}_\mathrm{e}$ by the right hand rule and therefore, to be consistent with $\mathcal{S}_\mathrm{cd}$, the sign of the integral on the inner contour ($\mathcal{C}_\mathrm{cd,in}$) must be reversed.

For the ideal coaxial cable (build with PEC) considered, the potential is constant both on $\mathcal{C}_\mathrm{cd,in}$ and $\mathcal{C}_\mathrm{cd,out}$. We may thus define ϕ_in and ϕ_out as the potential respectively on $\mathcal{C}_\mathrm{cd,in}$ and $\mathcal{C}_\mathrm{cd,out}$. With our sign convention, the coil voltage is $V_\mathrm{coil} = \phi_\mathrm{in} - \phi_\mathrm{out}$. Furthermore, as both ϕ_in and ϕ_out correspond to state $\Sigma_\mathrm{s}^{(\mathrm{d})}$ in which the RX coil is open and the external sources are on, $V_\mathrm{coil} = e$, the unknown induced voltage. In addition, both the inner and the outer contours encircle I_RX and therefore, $\int_{\mathcal{C}_\mathrm{cd,out/in}} \boldsymbol{H}_\mathrm{RX}^{(\mathrm{fs})} \cdot \mathrm{d}\boldsymbol{\ell} = I_\mathrm{RX}$ where the current is positive according to our sign convention. Indeed, the coil current I_coil has been defined positive when it flows from the electronics to the coil (in the direction of the positive normal of $\mathcal{S}_\mathrm{c}$) in the inner conductor (it flows in the reverse direction in the outer conductor). Equation (2.34) then yields:

$$\int_{\mathcal{S}_c} \boldsymbol{E}_s^{(d)} \times \boldsymbol{H}_{RX}^{(fs)} \cdot d\boldsymbol{S} = eI_{RX} \tag{2.35}$$

Applying the same development to the r.h.s. second term of (2.32) yields zero because for state $\Sigma_s^{(d)}$ the current in the coaxial cable is zero. Therefore, (2.32) yields:

$$e = \oint_{\mathcal{S}_d} \left(\boldsymbol{E}_s^{(d)} \times \check{\boldsymbol{H}}_{RX}^{(fs)} - \check{\boldsymbol{E}}_{RX}^{(fs)} \times \boldsymbol{H}_s^{(d)} \right) \cdot d\boldsymbol{S} \tag{2.36}$$

where we have introduced $\check{\boldsymbol{E}}_{RX}^{(fs)} = \boldsymbol{E}_{RX}^{(fs)}/I_{RX}$ and $\check{\boldsymbol{H}}_{RX}^{(fs)} = \boldsymbol{H}_{RX}^{(fs)}/I_{RX}$, the normalized fields[16] produced by a unit current I_{RX}.

Equation (2.36) makes it possible to compute the induced voltage as a function of the fields on $\mathcal{S}_d$. However, this expression makes use of the fields produced by the external sources *in presence* of the detector. We will now show that the fields produced by those sources in free space may be used instead. This is advantageous because the latter fields are usually much simpler to compute than the former. For this, we note that the fields in presence of the detector may be expressed as:

$$\begin{aligned} \boldsymbol{E}_s^{(d)} &= \boldsymbol{E}_s^{(fs)} + \boldsymbol{E}_{scat}^{(fs)} \\ \boldsymbol{H}_s^{(d)} &= \boldsymbol{H}_s^{(fs)} + \boldsymbol{H}_{scat}^{(fs)} \end{aligned} \tag{2.37}$$

where $\boldsymbol{E}_s^{(fs)}$ and $\boldsymbol{H}_s^{(fs)}$ are the electric and magnetic fields produced by the external sources in absence of the detector and $\boldsymbol{E}_{scat}^{(fs)}$ and $\boldsymbol{H}_{scat}^{(fs)}$ are the fields scattered by the detector which can be computed from equivalent sources located on the detector boundary and scattering in free space. Those sources are located inside $\mathcal{S}_d$ and the sources appearing in state $\Sigma_{RX}^{(fs)}$ are also located inside $\mathcal{S}_d$. Therefore, expressing the reciprocity between the states $\Sigma_{scat}^{(fs)}$ and $\Sigma_{RX}^{(fs)}$ in the volume outside $\mathcal{S}_d$ and considering that the integral on the infinite sphere $\mathcal{S}_\infty$ vanishes according to the far field behavior of fields, only the boundary term $B_{\mathcal{S}_r}^{EH}$ of (C.1.1) remains. This yields:

$$\oint_{\mathcal{S}_d} \left(\boldsymbol{E}_{scat}^{(fs)} \times \boldsymbol{H}_{RX}^{(fs)} - \boldsymbol{E}_{RX}^{(fs)} \times \boldsymbol{H}_{scat}^{(fs)} \right) \cdot d\boldsymbol{S} = 0 \tag{2.38}$$

[16] The unit of the normalized quantities are different from those of the corresponding fields. The units of $\boldsymbol{E}$ and $\check{\boldsymbol{E}}$ are respectively [V/m] and [V/Am]. The units of $\boldsymbol{H}$ and $\check{\boldsymbol{H}}$ are respectively [A/m] and [1/m].

and (2.36) can therefore be rewritten as follows:

$$e = \oint_{\mathcal{S}_\mathrm{d}} \left(\boldsymbol{E}_\mathrm{s}^{(\mathrm{fs})} \times \check{\boldsymbol{H}}_\mathrm{RX}^{(\mathrm{fs})} - \check{\boldsymbol{E}}_\mathrm{RX}^{(\mathrm{fs})} \times \boldsymbol{H}_\mathrm{s}^{(\mathrm{fs})} \right) \cdot \mathrm{d}\boldsymbol{S} \tag{2.39}$$

which is more convenient than (2.36) because it only makes use of the free space fields.

2.4.5 Equivalent sources on the coil

Our objective is to replace the coil by equivalent currents and charges and to relate the induced voltage to those distributions. According to (2.39) the coil may be replaced by any source distribution that produces the same fields on $\mathcal{S}_\mathrm{d}$ as the real coil. This allows a significant simplification of the coil modeling. Indeed, fine coil details have little effect on the field at some distance from the coil. Therefore, the coil model may be chosen simpler when $\mathcal{S}_\mathrm{d}$ can be chosen further away from the coil, which is possible if all contrasts and external sources are far enough from the coil. Typically, for a target at some distance from the coil, it is not necessary to model all the turns of the coil winding; a single turn coil carrying a stronger current then becomes sufficient.

We now assume that we can find a coil equivalent current distribution $\boldsymbol{J}_\mathrm{RX,equ}$, located inside $\mathcal{S}_\mathrm{d}$ and radiating in absence of the detector (i.e. in free space), that produces the same fields on $\mathcal{S}_\mathrm{d}$ as the detector in state $\Sigma_\mathrm{RX}^{(\mathrm{fs})}$. This allows us to define $\Sigma_\mathrm{RX,equ}^{(\mathrm{fs})}$, a state equivalent to $\Sigma_\mathrm{RX}^{(\mathrm{fs})}$ where the detector is replaced by an equivalent source distribution $\boldsymbol{J}_\mathrm{RX,equ}$. Applying reciprocity between $\Sigma_\mathrm{RX,equ}^{(\mathrm{fs})}$ and $\Sigma_\mathrm{s}^{(\mathrm{d})}$ in the volume $\mathcal{V}_\mathrm{d}$ then yields:

$$\oint_{\mathcal{S}_\mathrm{d}} \left(\boldsymbol{E}_\mathrm{s}^{(\mathrm{fs})} \times \boldsymbol{H}_\mathrm{RX}^{(\mathrm{fs})} - \boldsymbol{E}_\mathrm{RX}^{(\mathrm{fs})} \times \boldsymbol{H}_\mathrm{s}^{(\mathrm{fs})} \right) \cdot \mathrm{d}\boldsymbol{S} = - \int_{\mathcal{V}_\mathrm{d}} \boldsymbol{E}_\mathrm{s}^{(\mathrm{fs})} \cdot \boldsymbol{J}_\mathrm{RX,equ} \mathrm{d}V \tag{2.40}$$

where the left hand side (l.h.s.)and the r.h.s. are respectively the boundary (C.1.2) and the source (C.1.3) contribution. We have dropped the subscript 'equiv' for the fields because by definition the fields produced by equivalent and original sources are equal on $\mathcal{S}_\mathrm{d}$. To simplify the notations, we will also drop from now the subscript 'equiv' for the current $\boldsymbol{J}_\mathrm{RX,equ}$ as this brings no confusion.

Introducing (2.40) in (2.39) yields another expression for the induced voltage:

$$e = - \int_{\mathcal{V}_\mathrm{d}} \boldsymbol{E}_\mathrm{s}^{(\mathrm{fs})} \cdot \check{\boldsymbol{J}}_\mathrm{RX} \mathrm{d}V \tag{2.41}$$

with $\check{\boldsymbol{J}}_{\mathrm{RX}} = \frac{\boldsymbol{J}_{\mathrm{RX}}}{I_{\mathrm{RX}}}$, the coil equivalent current distribution for a *unit* current injected in the coil.

To make the effect of charge accumulation apparent, we split the coil equivalent current $\boldsymbol{J}_{\mathrm{RX}}$ in two components; one solenoidal $\boldsymbol{J}^0_{\mathrm{RX}}$ and the other irrotational $\boldsymbol{J}^1_{\mathrm{RX}}$. The first component does not yield any charge accumulation ($\nabla \cdot \boldsymbol{J}^0_{\mathrm{RX}} = 0$) while the second component yields a charge distribution ρ_{RX} :

$$\nabla \cdot \boldsymbol{J}^1_{\mathrm{RX}} = -j\omega\rho_{\mathrm{RX}} \tag{2.42}$$

The total current distribution is then:

$$\boldsymbol{J}_{\mathrm{RX}} = \boldsymbol{J}^0_{\mathrm{RX}} + \boldsymbol{J}^1_{\mathrm{RX}} \tag{2.43}$$

Such a decomposition and the corresponding charge distribution is directly available from our detailed coil model illustrated in Fig. 2.2. The current distribution $\boldsymbol{J}^0_{\mathrm{RX}}$ is then characterized by the currents in the inductors (it is a filamentary distribution with a constant current in each turn) and $\boldsymbol{J}^1_{\mathrm{RX}}$ is characterized by the currents in the capacitors. We will see that the current distribution $\boldsymbol{J}^1_{\mathrm{RX}}$ itself is not needed; only the corresponding charge distribution $\boldsymbol{\rho}_{\mathrm{RX}}$ is required. Further, this charge distribution is available from the computation of the capacitance matrix and is shown in Fig. 2.6.

According to (2.41) the induced voltage has two components:

$$e = e_{\mathrm{M}} + e_{\mathrm{E}} \tag{2.44}$$

where we define e_{M} as the contribution of $\boldsymbol{J}^0_{\mathrm{RX}}$ and e_{E} as the contribution of $\boldsymbol{J}^1_{\mathrm{RX}}$.

Using the QS approximation (as defined in Appendix B.3.3) of the source term of the reciprocity expression (C.4.18) and noting that $J_{\mathcal{S}_{\mathrm{d}}} = 0$ ($J_{\mathrm{RX}} = 0$ on $\mathcal{S}_{\mathrm{d}}$), the r.h.s. of (2.40) can be rewritten as $j\omega\left(S^{\mathrm{J}_0}_{\mathcal{V}_{\mathrm{d}}} + S^{\rho}_{\mathcal{V}_{\mathrm{d}}}\right)$. This yields:

$$e_{\mathrm{M}} = j\omega \int_{\mathcal{V}_{\mathrm{d}}} \boldsymbol{A}^{(\mathrm{fs})}_{\mathrm{s},0} \cdot \check{\boldsymbol{J}}^0_{\mathrm{RX}} \mathrm{d}V \tag{2.45}$$

and

$$e_{\mathrm{E}} = j\omega \int_{\mathcal{V}_{\mathrm{d}}} \phi^{(\mathrm{fs})}_{\mathrm{s}} \check{\rho}_{\mathrm{RX}} \mathrm{d}V \tag{2.46}$$

with $\check{\rho}_{\mathrm{RX}} = \frac{\rho_{\mathrm{RX}}}{I_{\mathrm{RX}}}$, the charge distribution for a *unit* current injected in the RX coil.

For completeness and to better understand the approximations made by using the QS reciprocity expression, we now compute the two contribution e_{M} and e_{E} without resorting to the QS reciprocity.

2.4.5.1 Magnetic contribution

According to (2.41) the magnetic contribution to the induced voltage e_{M} can be expressed as follows:

$$e_{\mathrm{M}} = -\int_{\mathcal{V}_{\mathrm{d}}} \boldsymbol{E}_{\mathrm{s}}^{(\mathrm{fs})} \cdot \check{\boldsymbol{J}}_{\mathrm{RX}}^{0} \mathrm{d}V \tag{2.47}$$

One notes that an EQS field (which derives from a scalar potential) does not contribute to e_{M}. Indeed, introducing such a field $\boldsymbol{E}_{\mathrm{s}}^{(\mathrm{fs})} = -\nabla\phi_{\mathrm{s}}^{(\mathrm{fs})}$ in (2.47), using the vector identity (B.1.3) and noting that $\check{\boldsymbol{J}}_{\mathrm{RX}}^{0}$ is null on $\mathcal{S}_{\mathrm{d}}$, one gets:

$$e_{\mathrm{M}}^{\phi_{\mathrm{s}}} = \int_{\mathcal{V}_{\mathrm{d}}} \nabla\phi_{\mathrm{s}}^{(\mathrm{fs})} \cdot \check{\boldsymbol{J}}_{\mathrm{RX}}^{0} \mathrm{d}V = -\int_{\mathcal{V}_{\mathrm{d}}} \phi_{\mathrm{s}}^{(\mathrm{fs})} \nabla \cdot \check{\boldsymbol{J}}_{\mathrm{RX}}^{0} \mathrm{d}V = 0 \tag{2.48}$$

which is null because the divergence of $\boldsymbol{J}_{\mathrm{RX}}^{0}$ is null by definition.

Therefore, only the vector potential contribution to the electric field must be kept in (2.47). This yields:

$$e_{\mathrm{M}} = j\omega \int_{\mathcal{V}_{\mathrm{d}}} \boldsymbol{A}_{\mathrm{s}}^{(\mathrm{fs})} \cdot \check{\boldsymbol{J}}_{\mathrm{RX}}^{0} \mathrm{d}V \tag{2.49}$$

Note that we could have made the same reasoning starting from (2.36) instead of (2.39) and $\boldsymbol{A}_{\mathrm{s}}^{(\mathrm{d})}$ would then appear in (2.49) instead of $\boldsymbol{A}_{\mathrm{s}}^{(\mathrm{fs})}$. This shows that the vector potential in the presence or in the absence of the detector may be used indifferently in (2.49) to compute the induced voltage. Both give the same result but the free space potentials are in general preferred because they are easier to compute.

Comparing (2.49) with (2.45) that was obtained using the QS reciprocity expression, one sees that under the QS approximation, $\boldsymbol{A}_{\mathrm{s},0}$, the first term in the magnetic potential power series expansion (B.3.30), is used instead of $\boldsymbol{A}_{\mathrm{s}}$.

We now show that for a filamentary coil, e_{M} is equal to the induced voltage computed with the classical expression (2.28). Indeed, with a filamentary coil, and neglecting charge accumulation, $\check{\boldsymbol{J}}_{\mathrm{RX}}^{0}$ is directed along the coil contour $\mathcal{C}_{\mathrm{RX}}$ and its modulus is one throughout the coil. Equation (2.47) then yields:

$$e_{\mathrm{M}} = -\oint_{\mathcal{C}_{\mathrm{RX}}} \boldsymbol{E}_{\mathrm{s}}^{(\mathrm{fs})} \cdot \mathrm{d}\boldsymbol{\ell} = \int_{\mathcal{S}_{\mathrm{RX}}} \frac{\mathrm{d}\boldsymbol{B}_{\mathrm{s}}^{(\mathrm{fs})}}{\mathrm{d}t} \cdot \mathrm{d}\boldsymbol{S} = \frac{\mathrm{d}\psi_{\mathrm{s}}^{(\mathrm{fs})}}{\mathrm{d}t} \tag{2.50}$$

with $\psi_{\mathrm{s}}^{(\mathrm{fs})}$ the flux linked by $\mathcal{C}_{\mathrm{RX}}$ in free space. Note that the Faraday law was used to obtain the second equality.

Recall that $\check{\boldsymbol{J}}_{\mathrm{RX}}^{0}$ does not need to be the real current distribution; any distribution that yields the same fields on $\mathcal{S}_{\mathrm{d}}$ can be used. This yields some insight on the validity of the filamentary assumption as a function of the target location. Indeed, $\mathcal{S}_{\mathrm{d}}$ may not include any target (external source) and it is thus the target that restricts the maximum distance from the coil at which $\mathcal{S}_{\mathrm{d}}$ can be chosen. If the targets are not too close to the coil, $\mathcal{S}_{\mathrm{d}}$ may be chosen at some distance from the coil and the current distribution in the wire section then becomes irrelevant to compute the fields on $\mathcal{S}_{\mathrm{d}}$. The filament approximation may then be used. Furthermore, at some distance from the coil, the details of the coil winding also become irrelevant to compute the fields and the coil model may be further simplified by considering a single turn carrying a filamentary current.

2.4.5.2 Electric contribution

We first consider an EQS external field and proceed as in (2.48) but with $\boldsymbol{J}_{\mathrm{RX}}^{1}$ instead of $\boldsymbol{J}_{\mathrm{RX}}^{0}$. This yields, using (2.42):

$$e_{\mathrm{E}} = j\omega \int_{\mathcal{V}_{\mathrm{d}}} \phi_{\mathrm{s}}^{(\mathrm{fs})} \check{\rho}_{\mathrm{RX}} \mathrm{d}V \tag{2.51}$$

with $\check{\rho}_{\mathrm{RX}} = \frac{\rho_{\mathrm{RX}}}{I_{\mathrm{RX}}}$, the charge distribution for a *unit* current injected in the RX coil.

Note that again we could have made the same reasoning starting from (2.36) instead of (2.39) and $\phi_{\mathrm{s}}^{(\mathrm{d})}$ would then appear in (2.51) instead of $\phi_{\mathrm{s}}^{(\mathrm{fs})}$. This shows that the scalar potential in the presence or in the absence of the detector may be used indifferently in (2.51) to compute the induced voltage. Both give the same result but the free space potentials are in general preferred because they are easier to compute.

For a general external field:

$$\boldsymbol{E}_{\mathrm{s}}^{(\mathrm{fs})} = -\nabla \phi_{\mathrm{s}}^{(\mathrm{fs})} - j\omega \boldsymbol{A}_{\mathrm{s}}^{(\mathrm{fs})} \tag{2.52}$$

the vector potential also contributes to e_{E} and yields a contribution similar to (2.49) but with $\boldsymbol{J}_{\mathrm{RX}}^{0}$ replaced by $\check{\boldsymbol{J}}_{\mathrm{RX}}^{1}$. However, in the frequency band of interest, this contribution can in general be neglected. For a coil, in the frequency band of interest (which is below the first resonance frequency) $\boldsymbol{J}^1_{\mathrm{RX}} \ll \boldsymbol{J}^0_{\mathrm{RX}}$ and therefore, the contribution of the vector potential to e_{E} may indeed be neglected compared to its contribution to e_{M}.

2.4.6 Equivalent circuit

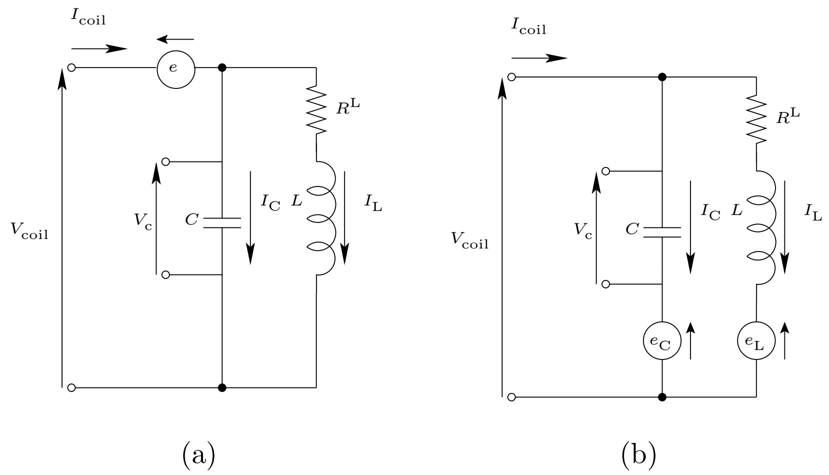

Figure 2.18: *Simple coil model. Induced voltage may be represented (a) with a global and single voltage source e or (b) with two voltage sources (e_{L}) and (e_{C}) respectively for the inductor and capacitive branch contribution. Positive currents and voltages are indicated by the arrows.*

Our objective is to introduce the induced voltage computed by (2.49) and (2.51) into the (simple or detailed) coil circuit model illustrated in Fig. 2.2. This can be done by introducing a voltage source $e = e_{\mathrm{M}} + e_{\mathrm{E}}$ at the input port of the coil circuit as illustrated in Fig. 2.18. The induced voltage can then be computed as a function of the external sources and the currents and charge distribution appearing when a *unitary* current is injected in the coil: $\check{\boldsymbol{J}}^0_{\mathrm{RX}}$ and $\check{\rho}_{\mathrm{RX}}$.

The detailed circuit of Fig. 2.3 (b) assumes a number of closed loop (one per turn) for which the current remains constant in any cross-section. As explained above, if the external sources are at some distance from the coil, the details of the current distribution inside the wire become irrelevant and we may use a filamentary current. The current distribution is thus fully characterized by the currents $I^{\mathrm{k}}_{\mathrm{L}}$ appearing in the circuit when a unit current is injected in the coil. The charge distribution can be obtained from the elementary charge distribution resulting from a 1V potential difference between two turns. This elementary charge distribution has been computed in Section 2.2.1 by using the MAS. The global charge distribution is then obtained by multiplying the elementary charge distribution by the turn-to-turn voltage appearing when a unit current is injected in the coil and summing all turn-to-turn contributions.

To summarize, the induced voltage can be computed from the external sources *and* the solution of the circuit (branch currents and node voltages) when it is connected to a unit current source. The problem is that this circuit solution is frequency dependent. To compute the induced voltage in the time-domain, one must thus convolve the impulse response of the circuit with the external sources and this is not very practical.

A more convenient circuit is obtained by introducing, as illustrated in Fig. 2.18, voltage sources e_{L} and e_{C} respectively in the inductor and capacitor branches. We will indeed show that e_{L} can then be computed using an expression similar to (2.49) which was developed for e_{M}. This new expression (2.57) is however more convenient because it does not include the frequency dependent source term $\check{\boldsymbol{J}}^0_{\mathrm{RX}}$. Similarly, the new expression for e_{C} (2.58) is more convenient than (2.51) that was obtained for e_{E} because it does not include the frequency dependent source term $\check{\rho}_{\mathrm{RX}}$. Those frequency dependent source terms introduce a convolution in the time domain and are difficult to introduce in a state-space representation of the coil. Furthermore, the commonly used circuit model of coil shown in Fig. 2.15 is then recovered when e_{C} can be neglected.

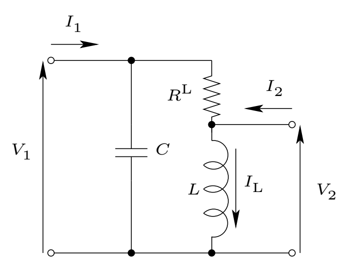

Figure 2.19: *Two-port network used for reciprocity.*

To show that e_{L} and e_{C} are equivalent to e, we apply circuit reciprocity (C.5.27) to the two-port network shown in Fig. 2.19. This yields:

$$V_1^{\mathrm{A}} I_1^{\mathrm{B}} + V_2^{\mathrm{A}} I_2^{\mathrm{B}} = V_1^{\mathrm{B}} I_1^{\mathrm{A}} + V_2^{\mathrm{B}} I_2^{\mathrm{A}} \tag{2.53}$$

We now consider the following two states:

1. state A: $I_1^{\mathrm{A}} = 1$ and $I_2^{\mathrm{A}} = 0$. In that state, a unit current is injected in the coil and, therefore, the current in the inductor is $\check{I}_{\mathrm{L}}$. Hence, $V_2^{\mathrm{A}} = j\omega L \check{I}_{\mathrm{L}}$.

2. state B: $I_1^{\mathrm{B}} = 0$ and $I_2^{\mathrm{B}} = 1/(j\omega L)$. In that state, a current source $I_{\mathrm{s}} = 1/(j\omega L)$ is thus in parallel with the inductor. This current source may be replaced by its Thevenin equivalent which is a voltage source $V_{\mathrm{s}} = j\omega L I_{\mathrm{s}} = 1$ in series with the inductor. This configuration corresponds to $e_{\mathrm{L}} = 1$ in Fig. 2.18(b) and the voltage appearing at the left terminals of the two-port is by definition V_1^{B}. The same terminal voltage can be obtained by introducing a voltage source $e = V_1^{\mathrm{B}}$ in Fig. 2.18(a). As this terminal voltage source is equivalent to a unit voltage source in the inductance branch source ($e_{\mathrm{L}} = 1$ in Fig. 2.18(b)), we denote this terminal source $\check{e}$ and $V_1^{\mathrm{B}} = \check{e}$.

In summary, with the states considered, we have $I_1^{\mathrm{A}} = 1$, $I_2^{\mathrm{A}} = 0$, $I_1^{\mathrm{B}} = 0$, $I_2^{\mathrm{B}} = 1/(j\omega L)$, $V_2^{\mathrm{A}} = j\omega L \check{I}_{\mathrm{L}}$ and $V_1^{\mathrm{B}} = \check{e}$. Introducing those values in (2.53) yields:

$$\check{e} = \check{I}_{\mathrm{L}} \tag{2.54}$$

which shows that a unit voltage source in the L-branch is equivalent to a terminal voltage source $\check{I}_{\mathrm{L}}$. Hence, a terminal voltage source e_{M} is equivalent to a L-branch voltage source $e_{\mathrm{L}} = e_{\mathrm{M}}/\check{I}_{\mathrm{L}}$.

The circuits presented in Figs. 2.18 and 2.19 only include a single inductor and a single capacitor branch. However, the reasoning leading to (2.54) is based on the general reciprocity expression (2.53) and, therefore, the result (2.54) remains valid for circuits with more branches, such as the detailed coil model.

Further, assuming that the current remains constant along each loop and considering an infinitely thin wire[17], (2.49) can be rewritten as:

$$e_{\mathrm{M}} = \sum_{k=1:n_{\mathrm{turn}}} e_{\mathrm{M}}^{\mathrm{k}} \tag{2.55}$$

[17] This last assumption allows a simpler development but can easily be relaxed.

with n_{turn} the number of turns and:

$$e_{\text{M}}^{\text{k}} = j\omega \sum_{k=1:n_{\text{turn}}} \int_{\mathcal{C}_{\text{turn}}^{\text{k}}} \boldsymbol{A}_{\text{s}}^{(\text{fs})} \check{I}_{\text{L}}^{\text{k}} \cdot \mathrm{d}\boldsymbol{\ell} \tag{2.56}$$

with $\mathcal{C}_{\text{turn}}^{\text{k}}$ the contour describing turn k and $\check{I}_{\text{L}}^{\text{k}}$ the current in the corresponding inductance of the equivalent schema for a unit current in the coil.

The contribution e_{M}^{k} to the terminal voltage source e can then be moved in the corresponding L-branch according to the equivalence (2.54). The source to consider is then $e_{\text{L}}^{\text{k}} = e_{\text{M}}^{\text{k}}/\check{I}_{\text{L}}$. This yields:

$$e_{\text{L}}^{\text{k}} = j\omega \int_{\mathcal{C}_{\text{turn}}^{\text{k}}} \boldsymbol{A}_{\text{s}}^{(\text{fs})} \cdot \mathrm{d}\boldsymbol{\ell} \tag{2.57}$$

Proceeding with the electric contribution (2.51) as we did with the magnetic contribution, it appears that the terminal voltage e_{E} is equivalent to a voltage source in each capacitor branch:

$$e_{\text{C}}^{\text{k}} = \int_{\mathcal{V}_{\text{turn}}^{\text{k}}} \phi_{\text{s}}^{(\text{fs})} \check{\rho}_{\text{C,Q}}^{\text{k}} \mathrm{d}V \tag{2.58}$$

with $\check{\rho}_{\text{C,Q}}^{\text{k}}$, the charge distribution on capacitor k for a *unit total charge* on that capacitor (the subscript 'Q' together with the normalization symbol '$\check{\ }$' indicates that the charge distribution is normalized to yield a unit total charge). The charge distribution has been computed in Section 2.2.1 with the MAS for a unit voltage across the capacitor. This charge distribution has to be normalized by the total capacitor charge Q_{c}^{k} to yield the required distribution $\check{\rho}_{\text{C,Q}}^{\text{k}}$. With the sign convention of Fig. 2.18 for the capacitor voltage V_{c}, a unit voltage yields a positive charge $Q_{\text{c}}^{\text{k}} = C_{\text{k}}$. Note that it is actually the turn-to-turn capacitance and the corresponding charge distribution that is computed with the MAS whereas the capacitors considered in the circuit are the node-to-node capacitance. They are obtained, according to (2.1), as the sum of two half turn-to-turn capacitors. Those capacitors are in parallel and therefore, half of the charge distribution for a turn-to-turn voltage of one volt must be used for each contribution.

Note that auxiliary sources computed with the MAS may be used in (2.58) instead of the real charge distribution because both distributions yield the same field. The volume integral then becomes a sum on the (line) auxiliary sources and this can easily be computed.

2.4.7 Imperfect shield and a non-coaxial cable

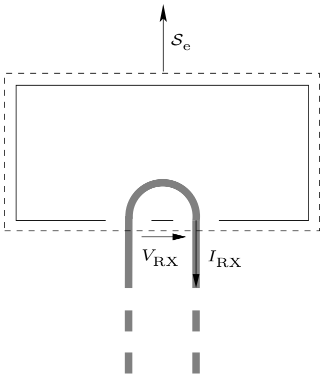

Figure 2.20: *Imperfectly shielded electronics with fictious current path.*

To assess the effect of an imperfect shield and a non-coaxial cable, we consider the configuration of Fig. 2.20. Without a perfect shield, the fields are not null on $\mathcal{S}_e$ and the surface integral appearing on the r.h.s. of (2.32) must now be performed on the whole surface $\mathcal{S}_e$. We define e^{PS} as the induced voltage that would be obtained under the perfect shield assumption and for which we have established a number of expressions (2.39), (2.41) and (2.44). For a perfectly shielded electronics and a coaxial cable connection, we have shown that the l.h.s. of (2.32) is equal to $e^{PS}I_{RX}$

Using the QS approximation of the boundary term (C.4.16) to express the r.h.s. of (2.32) and noting that $J_{\mathcal{S}_e} = eI_{RX}$ then immediately yields:

$$e^{PS} = e + j\omega \int_{\mathcal{S}_e} \left\{ \phi_s^{(d)} \check{\boldsymbol{D}}_{RX,0}^{(fs)} - \boldsymbol{A}_{s,0}^{(d)} \times \check{\boldsymbol{H}}_{RX,0}^{(fs)} - \check{\phi}_{RX}^{(fs)} \boldsymbol{D}_{s,0}^{(d)} + \check{\boldsymbol{A}}_{RX,0}^{(fs)} \times \boldsymbol{H}_{s,0}^{(d)} \right\} \cdot \mathrm{d}\boldsymbol{S} \tag{2.59}$$

with $\boldsymbol{D}_{s,0}^{(d)}$, $\boldsymbol{A}_{s,0}^{(d)}$, $\boldsymbol{H}_{s,0}^{(d)}$ and $\phi_s^{(d)}$ respectively the displacement fields, the magnetic vector potential, the magnetic field and the electric scalar potential pertaining to the state $\Sigma_s^{(d)}$ defined in Section 2.4.4. The subscript '0' indicates that it is the zero order fields and potential that are considered (those corresponding to the solenoidal current distribution contribution $\boldsymbol{J}_{\mathrm{s},0}$ to the source $\boldsymbol{J}_{\mathrm{s}}$ producing the external field). Similarly $\check{\boldsymbol{D}}^{(\mathrm{fs})}_{\mathrm{RX},0}$, $\check{\boldsymbol{A}}^{(\mathrm{fs})}_{\mathrm{RX},0}$, $\check{\boldsymbol{H}}^{(\mathrm{fs})}_{\mathrm{RX},0}$ and $\check{\phi}^{(\mathrm{fs})}_{\mathrm{RX}}$ are zero order fields and potential pertaining to state $\Sigma^{(\mathrm{fs})}_{\mathrm{RX}}$ defined in Section 2.4.4 and normalized by I_{RX} (as indicated by the ˇ symbol).

To further develop the integral, recall that we have applied reciprocity in the volume $\mathcal{V}_{\mathrm{r}}$ comprised between $\mathcal{S}_{\mathrm{d}}$ and $\mathcal{S}_{\mathrm{e}}$ and that the state $\Sigma^{(\mathrm{fs})}_{\mathrm{RX}}$ is a fictious one. The only requirements for that state are that:

- the medium inside $\mathcal{V}_{\mathrm{r}}$ is identical to that of the physical configuration in order to avoid extra terms in the reciprocity relation (2.32).
- a current $I_{\mathrm{RX}} \neq 0$ flows through the cable at its connection with the electronics to avoid that e is undetermined in (2.35).
- no sources are present in $\mathcal{V}_{\mathrm{r}}$ in order to avoid extra terms in the reciprocity relation (2.32).

We can thus choose the content of $\mathcal{V}_{\mathrm{e}}$ arbitrarily as long as it produces a current I_{RX} in the cable connector. In other words, we may replace the real electronics by a more convenient one. As illustrated in Fig. 2.20 we use a simple filamentary current source inside the electronics.

We now apply[18] QS reciprocity between the states $\Sigma^{(\mathrm{d})}_{\mathrm{s}}$ and $\Sigma^{(\mathrm{fs})}_{\mathrm{RX}}$ in $\mathcal{V}_{\mathrm{e}}$. The boundary term is nothing else but the r.h.s. of (2.59). It may thus be replaced by the source term (C.4.18). This yields:

$$e = e^{\mathrm{PS}} - j\omega \int_{\mathcal{V}_{\mathrm{e}}} \left\{ \boldsymbol{A}^{(\mathrm{d})}_{\mathrm{s},0} \cdot \check{\boldsymbol{J}}^{0}_{\mathrm{RX}} + \phi^{(\mathrm{d})}_{\mathrm{s}} \check{\rho}_{\mathrm{RX}} \right\} \mathrm{d}V \tag{2.60}$$

which makes apparent the effect of a non perfect shield. Indeed, according to (2.49) and (2.51)[19], the correction term is the voltage induced

[18] We said above that reciprocity can in general not be used inside the electronics, because it may include nonlinear components. This is not true for the fictious circuit inside the electronics that we are now considering because that fictious circuit is linear.

[19] Those equations use the free space potentials whereas (2.60) uses the potentials in the presence of the detector. We have however shown that (2.49) and (2.51) may be expressed using the free space potentials or, indifferently, those in presence of the detector . This is not true for (2.60) which can only be computed with the potentials in the presence of the detector. Indeed, the scattered field introduced in (2.37) now has sources on both sides of $\mathcal{S}_{\mathrm{e}}$, and (2.38) is not valid anymore.

in the (fictious) circuit inside the electronics. The correction term is difficult to compute because it includes the potentials generated by the external source *in presence* of the detector. We can however make it small by an appropriate choice of the fictious electronics. Indeed, the scalar potential contribution can be set to zero by choosing a solenoidal current (such that $\check{\rho}_{\mathrm{RX}} = 0$) inside $\mathcal{V}_{\mathrm{e}}$. Furthermore by choosing[20] the connection inside the fictious electronics as small as possible, the contribution of the vector potential can be made small[21] .

Finally, recall that the starting point of the reasoning was (2.29) which assumes that there is no coupling between the currents and charges inside the electronics and the coil. This is rigorously valid for a perfectly shielded electronics but for a non perfectly shielded electronics, a correction term must be introduced to yield:

$$V_{\mathrm{coil}} = Z_{\mathrm{coil}} I_{\mathrm{coil}} + e + j\omega M_{\mathrm{M}}^{\mathrm{e,c}} I_{\mathrm{coil}} + j\omega M_{\mathrm{E}}^{\mathrm{e,c}} V_{\mathrm{coil}} \tag{2.61}$$

with $M_{\mathrm{M}}^{\mathrm{e,c}}$ and $M_{\mathrm{E}}^{\mathrm{e,c}}$ respectively the magnetic and electric coupling between the electronics and the coil.

In normal use, the electronics is at some distance from the coil and the currents flowing in the RX coil and induced by the target are quite small (the coil is closed on a damping resistor) and the correction term should be negligible.

In conclusion, (2.39) is rigorous for a perfectly shielded electronics and valid in very good approximation for a non perfectly shielded electronics. The expressions for the induced voltage developed in Sections 2.4.4 and 2.4.5 may thus be used in general whether the electronics is either perfectly shielded or not and whether the coil is connected to the electronics either with a coaxial cable or with another type of cable.

[20] It may look strange that the correction term is a function of the chosen electronics. This is however logical because the term e^{PS} is also a function of the chosen fictious electronics and the resulting e, which is the only term that has a physical meaning, is independent of the chosen fictious electronics.

[21] $\boldsymbol{A}_{\mathrm{s},0}^{(\mathrm{d})}$ is the vector potential in state $\Sigma_{\mathrm{s}}^{(\mathrm{d})}$ for which no current flows in the RX terminal. There is thus no current close to the electronics and there is no reason for the vector potential to take extremely high values that would yield a large contribution for a small connection inside the electronics. This is not true for the scalar potential $\phi_{\mathrm{s}}^{(\mathrm{d})}$ that may take large values inside the electronics because charges are induced on the cable entering the electronics. The contribution of the scalar potential could however be set to zero by choosing a solenoidal current inside the electronics for the RX state.

2.4.8 Heads with two coils

Some detectors such as the Schiebel use a head with two coils; one for transmission and one for reception. The coupling between the TX and RX coils must then obviously be taken into account.

The schema of Fig. 2.16 must be extended to take into account the TX coil. This yields a second coaxial connection to the electronics. The surface integral on $\mathcal{S}_{\mathrm{e}}$ then includes an additional contribution $V_{\mathrm{s}}^{\mathrm{TX}} I_{\mathrm{RX}}^{\mathrm{TX}}$ with $V_{\mathrm{s}}^{\mathrm{TX}}$ the voltage at the terminals of the TX coil in state $\Sigma_{\mathrm{s}}^{(\mathrm{d})}$ and $I_{\mathrm{RX}}^{\mathrm{TX}}$ the current in the TX coil in the RX state. In addition, (2.29) must be extended as follows to take into account the coupling between the coils:

$$V_{\mathrm{coil}}^{\mathrm{RX}} = Z_{\mathrm{coil}}^{\mathrm{RX}} I_{\mathrm{coil}}^{\mathrm{RX}} + M_{\mathrm{TX,RX}} I_{\mathrm{coil}}^{\mathrm{TX}} + e \tag{2.62}$$

with $V_{\mathrm{coil}}^{\mathrm{RX}}$ the voltage at the terminals of the RX coil, $Z_{\mathrm{coil}}^{\mathrm{RX}}$ the impedance of the RX coil, $I_{\mathrm{coil}}^{\mathrm{RX}}$, the current in the RX coil, $M_{\mathrm{TX,RX}}$ the coupling between the coils and $I_{\mathrm{coil}}^{\mathrm{TX}}$ the current flowing into the TX coil.

One still has to define the state of the TX coil in the two states considered for reciprocity: $\Sigma_{\mathrm{s}}^{(\mathrm{d})}$ and $\Sigma_{\mathrm{RX}}^{(\mathrm{fs})}$. If we choose a null current in the TX coil for both states, the above mentioned additional $V_{\mathrm{s}}^{\mathrm{TX}} I_{\mathrm{RX}}^{\mathrm{TX}}$ and $M_{\mathrm{TX,RX}} I_{\mathrm{coil}}^{\mathrm{TX}}$ contributions are both zero. Therefore, the induced voltage e can still be computed as for a single coil using (2.41).

Even if the expression developed for a single coil detector is used, the two coils still have an influence on the induced voltage. Indeed:

- To compute the equivalent current representing the target scattering J_{s}, the total field emitted by the detector must be taken into account. This includes the current in the TX coil as well as any current induced in the RX coil.

- To compute the induced voltage, the current $\check{\boldsymbol{J}}_{\mathrm{RX}}$ must be used in (2.41). We recall that $\check{\boldsymbol{J}}_{\mathrm{RX}}$ is the true current distribution, or any equivalent current that produces the same fields as the detector, for a unit current in the RX coil and with the detector in state $\Sigma_{\mathrm{RX}}^{(\mathrm{fs})}$. In that state, the TX coil is open, but the RX current will still induce some current in the TX coil. This current will flow inside the coil through the capacitors.

- To compute the voltages and currents in the physical configuration, the true circuits connected to the TX and the RX coils must be taken into account. Contrary to the fictious states considered to apply reciprocity, a current flows in both coils and the cross-coupling $M_{\mathrm{TX,RX}} I_{\mathrm{coil}}^{\mathrm{TX}}$ must be taken into account.

The first two effects are usually small but the last one is very large; the cross-coupling being the dominant source of induced voltage in the RX coil. All effects are automatically taken into account with the equivalent circuit developed in Section 2.4.6. Indeed, with that circuit, the currents in the TX and RX coils are available and they can be used to compute the fields on the target, which in turn can be used to compute the target equivalent scattered currents. Furthermore, the contribution of the currents induced in the TX coil by a unit current in the RX coil to the voltage induced in the RX coil (second effect) is included in the sources e_{L} located in the inductor branches of the TX coil. This can be shown as we did in Section 2.4.6 by resorting to circuit reciprocity because this reciprocity expression remains valid for coupled coil circuits. The voltage sources e_{L} in the TX coil indeed yield an induced voltage in the RX coil because they induce currents in the TX coil which in turn, through the cross-coupling, will induce a voltage in the RX coil.

2.5 Coil shielding

The Schiebel coils are not shielded. However, most modern detectors use shielded coils. The shielding is performed by putting a thin conducting foil around the coil. One usually claims that the shield is there to prevent changes in the coil capacitance. We will see in Chapter 6 that the change of the coil capacitance is usually too small to affect the response but the electrical contribution to the induced voltage discussed in Section 2.4.5.2 can nevertheless produce a measurable response. The effect is more complex than a simple change in capacitance and is related to the charge distribution that would appear on the RX coil if a unit current was injected in it. More precisely, any charge distribution that produces the same EQS field at some distance from the coil as the real charge distribution can be used. The shield is an equipotential and it therefore confines the EQS field inside the shield. For a shielded coil, a null equivalent charge distribution can therefore be used and the resulting electrical contribution to the induced voltage is then null. Perturbations, such as the effect of water on the head then disappear.

The foil used for shielding must be insulated at its extremities to avoid the creation of conducting closed loop. If a closed loop was created, large eddy currents would be induced in the shield and this would yield a response that would be difficult to separate from that of a target. In extreme situations (thick, highly conducting closed shield), it could even significantly reduce the magnetic field generated by the coil because the eddy current induced in the shield could oppose the magnetic field produced by the coil.

With a well designed shield, the magnetic field is not significantly modified. The eddy currents will remain quite limited and will decay fast enough to have any influence on the response in the integration window.

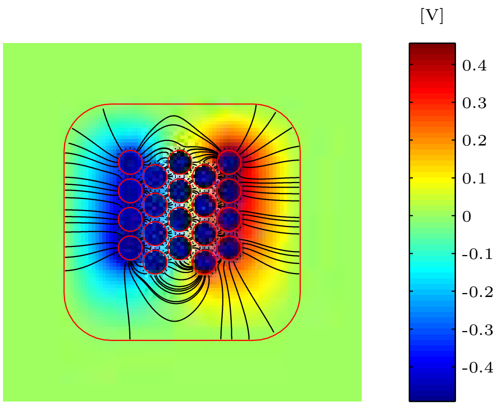

Figure 2.21: *Potential and E-field lines that would be obtained for the Schiebel TX coil if a shield was added. The computation has been done with the MAS, assuming $V_{\text{coil}} = 1$ and a frequency much lower than the first coil resonance frequency. Turn layout has been modified and is for illustration only.*

The MAS presented in Section 2.2.1 to compute the coil capacitance matrix can also be used to assess the effect of the shield on the turn-to-turn capacitance matrix. This only requires adding a floating conductor around the casing. This is illustrated in Fig. 2.21 where the potential and E-field lines are computed for the Schiebel TX coil to which a shield has been added. One sees that the potential is null on and outside the shield, as expected.

The resulting equivalent capacitance is then 175pF, to be compared with 154pF without shield. One sees that the shield increases the capacitance by 13 percent and this may have an impact on the impulse response of the coil.

As already mentioned, some delay is needed between the TX pulse and the beginning of the evaluation window to allow for the voltage induced in the RXcoil by the TX pulse (through direct coupling) to decay sufficiently in order to avoid saturation of the RX amplifier. This delay must be made as small as possible to detect small (fast) targets. Indeed, if the delay is too large, the target response becomes unmeasurable before the beginning of the evaluation window. We will see that, for the Schiebel detector, it is mainly the amplifier that imposes a minimum usable delay and that the increase of capacitance that a shield would produce has no measurable effect on the fast time response. For faster amplifiers however, the shield may have a measurable effect on the fast-time response and the coil capacitance may influence the minimum usable delay. The capacitance may then become the limiting factor to increase detector sensitivity and optimizing the shield may become necessary to develop even more sensitive detectors. Hence understanding of the various contributions to the induced voltage may help in developing better detectors. The in-depth analysis of the various contribution to the induced voltage that we have presented in the previous section may be quite useful to support the design of an optimal shield in that context.

2.6 Fast-time electronics

2.6.1 TX electronics

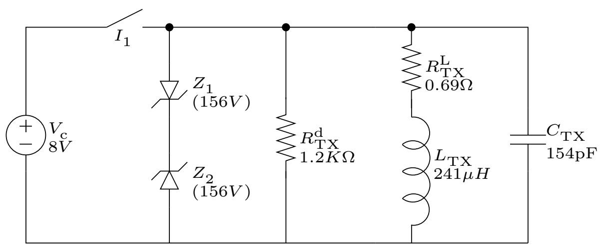

Figure 2.22: *Schiebel TX electronics and coil*

The Schiebel TX electronics is illustrated in Fig. 2.22. It only shows essential parts needed to develop our model. It does not include parts such as the detailed circuit for the switch (which is actually a power amplifier) or the timing electronics. The TX electronics works as follows. The coil is first 'charged' by connecting it to the voltage source V_c through the switch I_1. The current increases in the coil and, after $138\mu s$, the switch is opened. The coil current must then pass through the damping resistor R_{TX}^{d} but the initial discharge voltage is larger than the Zener breakdown voltage and part of the current flows through the back-to-back Zener diodes Z_1 and Z_2 to limit the coil voltage. The coil voltage then becomes lower than the Zener breakdown voltage which gets blocked and the coil discharge continues through the discharge resistor alone.

The timing electronics (not shown) controls the pulse timing. For the Schiebel, a bipolar pulse is sent every 15,2ms, yielding a PRF of 66 Hz. The motivation for using such a double pulse is to prevent the triggering of magnetic mines. The second pulse of the bipolar pulse is sent just after the first. Therefore, there is only one integration window for each bipolar pulse. This window is located after the second pulse and the response of the first pulse is thus not used. For newer metal detectors, the tendency seems to be towards an increase of the PRF, the PRF may also be tuned according to the prevailing EM background and the polarity of the whole bipolar pulses may be alternated to allow for better immunity against perturbing external fields (see Section 7.6.2 for more details).

Finally, some detectors also use two pulse durations. This allows to implement soil compensation with less sensitivity loss for the target (see Section 2.7 for more details).

2.6.2 RX electronics

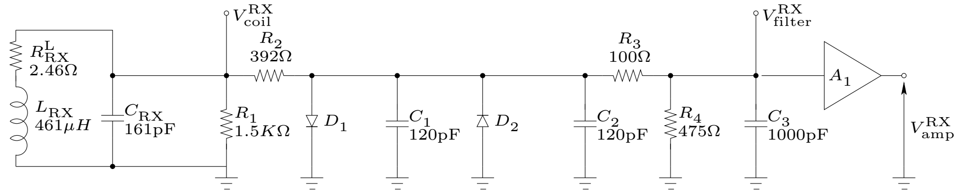

Figure 2.23: *Schiebel RX electronics and coil*

The Schiebel RX electronics is illustrated in Fig. 2.23. Its role is to condition, filter and amplify the RX coil voltage. It works as follows. The clamping diodes limit the voltage to $\pm 0.6V$ and avoid overdriving the amplifier A_1. When a clamping diode is conducting, the filtering circuit is equivalent to a damping resistor equal to R_1 and R_2 in parallel. When the clamping diodes are not conducting, the network is a second order low pass filter. The signal is then amplified. The amplifier has a large static gain (for the Schiebel detector $K_{\text{amp}} = 548$) because the responses of the targets of interest are quite small. The amplifier also behaves as a low pass filter and exhibits some complex behavior when getting out of saturation. We found out from measurements that the amplifier dynamics could be modeled with a good accuracy by considering a first order system with a time constant of $5\mu s$ and considering that the amplifiers ideally recovers from saturation after a delay of $10\mu s$. The filter dynamics can easily be computed from the circuit schematic. It is a second order low pass filter with a gain[22] $K_{\text{filt}} = 0.49$ and time constants of $0.3\mu s$ and $0.02\mu s$. From the value of the time constants, it is apparent the filter will not significantly affect the response in the listening window (which starts when the amplifier goes out of saturation) but it will significantly attenuate the high frequency EM background. The time constant of the amplifier itself is dominant compared to the time constants of the filter. It will affect the response in the evaluation

[22]This gain is often called the filter insertion loss.

window and also provide some additional low pass filtering for the EM background.

2.7 Evaluation window

The slow-time signal is obtained by processing the fast-time signal in the evaluation window, which is located a few tens of μs after the pulse. For highest sensitivity to small targets[23], this window should be placed as close as possible to the pulse. Some delay is however needed to allow that the direct coupling transient vanishes and that the amplifier recovers from saturation. For the Schiebel detector, a single window, located after the second pulse is used for each bipolar pulse. This window starts when $V_{\mathrm{amp}}^{\mathrm{RX}}$ goes below 1V and lasts for $T_{\mathrm{av}} = 10\mu s$. Note that the location of the integration window can thus vary with the response of the target or the soil. This may have important implications. For example, a conducting soil may produce a significant response during the pulse, but its response decays too fast to be measurable in the evaluation window, at least directly. The effect is then the same as if a pulse with a smaller amplitude was used. The complete RX transient is then scaled accordingly and if the window remained at the same place, the slow-time signal would also decrease, yielding a change of the background signal (in this case, a reduction that will induce a loss of sensitivity). A similar effect occurs due to the presence of the RX measurement resistor as illustrated in Fig. 3.4. When the location window is adapted as a function of the response, the effect disappears and a conducting soil should not affect the background signal. It might affect the target response if the displacement of the evaluation window is significant. Obviously, a conducting soil may also affect the field propagation and the target impulse response but this will not be further discussed here.

The slow-time signal is obtained by an analogue integration of the output of the amplifier in the evaluation window. More complex processing may be used to perform some target discrimination based on the target response or to allow for soil compensation. Detectors allowing for target discrimination are appearing on the market. Note that identifying the type of metal composing the target from its response is quite difficult [45] because the response is not only a function of the target conductivity but also (and dominantly) [46, Section 8.3.5] of its shape. Fitting the detector with some learning capabilities to discriminate be-

[23] Which have typically fast responses that vanish fast after the pulse.

tween targets of interest and clutter is also difficult because there are many factors that may influence the response of a given mine such as its age (through oxidation of the metal), its orientation (the modal responses are independent of the orientation but the contribution of the various modes is a function of the target orientation and relative position with respect to the detector head). Furthermore, different batches of the same mine type may have been built with different metals. The discrimination power of the new detector with those functionalities should thus be carefully evaluated.

Detectors with soil compensation have been on the market for a long time. Soil compensation may be performed at the slow-time level. One then speaks in general of a dynamic mode. This will be further discussed in Section 2.8. Soil compensation may also be performed at the fast-time level by using the fact that soil and target responses are in general different. Typically a magnetic soil exhibits a continuous distribution of time constants [26] whereas a metallic target exhibits a number of well separated poles. The impulse response is then a sum of exponentials for the target and a $1/t$ decay for a magnetic soil. Introducing a well chosen weight function $W(t)$, the slow-time signal then becomes:

$$V_{\mathrm{slow}} = \int_{t_{\mathrm{e}}}^{t_{\mathrm{e}}+T_{\mathrm{av}}} W(t) V_{\mathrm{amp}}^{\mathrm{RX}}(t) \mathrm{d}t \tag{2.63}$$

it is then possible to cancel the slow-time soil response without significantly attenuating the target response. A simple window is $W = 1$ for $t_{\mathrm{e}} < t < t_{\mathrm{w}}$ and $W = -1$ for $t_{\mathrm{w}} < t < t_{\mathrm{e}} + T_{\mathrm{av}}$. It is then possible to find t_{w} such that the soil response cancels. The value of t_{w} may then be tuned manually by the operator by adjusting a soil compensation knob until the soil response disappears. It may also be adjusted automatically. The adjustment is then typically triggered by the operator and the procedure requires the operator to move the sensor head up and down above the soil.

Obviously, for any t_{w}, it is also possible to find an exponential decay for which the slow-time response is zero. Some targets will thus be hardly detectable because they will generate a small or even null slow-time response. If the attenuation is not too large for the targets of interest, the procedure is efficient for soil compensation. The detector may be further improved by sending TX pulses of different duration (typically two durations are used). The underlying idea is that the shape of the soil response will vary with the duration of the TX pulse because the slower poles in the soil pole distribution will be more excited with longer pulses. On the contrary, the shape of the response of a first order target is independent of the pulse duration. The shape of the response for higher order targets may vary with the pulse width, but normally the effect will remain different for the soil and for the target. As the soil response is a function of the pulse duration, the weight function parameter t_{w} will be different for the various pulse lengths used and if the target response is strongly attenuated for a given pulse length, it should be much less attenuated for the other pulse lengths. The use of pulses with various duration has been patented [47] and is used in the Minelab detectors.

An additional integration window located much later after the TX pulse may also be used. The underlying idea is that long after the pulse, the target response has gone and the remaining signal is due to an asynchronous induced voltage that may be due to the low frequency EM background, such as generated by a power line (see Section 7.6.2 for more details) or by the movement of the head above a magnetic soil. The output of this late window may then be subtracted from the output of the main evaluation window to cancel those low frequency perturbations.

2.8 Slow-time electronics

The slow-time electronics includes the circuit generating the audio signal. It may also include a slow-time filter to perform background compensation. The idea behind background compensation is that a target is a small object and that its response will vary significantly when the detector is swept over the target. It will be maximum in the neighborhood of the target and vanish rapidly at some distance from it. In contrast, the response of the soil will vary more slowly. Hence, a high-pass filter can be used to significantly reduce the soil response without changing too much the target response. When such a high-pass filter is used, one generally speaks about a dynamic mode because the alarm will vanish if the detector remains fixed over the target. With such a detector, the scanning must always be performed at a minimum speed and an optimal scanning speed is often recommended in the manuals.

The slow-time signal, after background compensation, if implemented, is then used as input to generate an audio signal. This process is also called the alarm generation. The audio signal is typically modulated in amplitude and frequency as a function of the slow-time signal. In some cases, the audio signal changes progressively (increase of amplitude or change of frequency or both) with the amplitude of the slow-time signal. In other cases, the alarm is more binary. There are in general two settings to control the alarm generation. One to control the sound volume and the other to control the detector sensitivity. The sensitivity setting typically controls a threshold to which the slow-time signal is compared. No alarm is generated until the signal reaches that threshold. There are many variations in the audio generation from one detector to another. Furthermore, the design criteria are more at the ergonomics level and must include the functioning of the human earing. This falls outside the scope of this thesis and will therefore not be investigated further.

Finally, the slow-time electronics may control a number of additional settings, such as:

- A filter for the magnetic field generated by the electricity distribution network. A choice between 50Hz and 60Hz for the network frequency may then be available. Such a filter may be implemented by adapting the pulse repetition frequency. See Section 7.6.2 for more details.

- A selection between various modes or soil programs. This may control the slow-time filtering or the shape of the integration weight. It may also control the width of the TX pulse.

CHAPTER 3

Detector fast-time state-space model

This chapter develops a complete state-space of the detector fast-time signals, including the coil and the fast-time electronics. This model allows to compute the detector internal signals up to the output of the fast-time amplifier. The electronics includes non-linear elements but by defining a number of phases, linear state-space models can still be used: one per phase.

The model is validated by comparing the computed signals with the measured ones, showing a very good match. The state-space model is then extended to include a dipole target. Several target types (electric, magnetic and conducting) are considered. We show that the response may then be characterized by a geometric and a dynamic factor. The geometric factor is called the head *geometrical sensitivity* and includes the effect of head geometry and target location with respect to the head. The dynamic factor is called the detector *dynamic sensitivity* and includes the effect of the shape of the TX pulse and the RX electronics dynamics (filter and amplifier, integration in the evaluation window) and the target dynamics.

Finally, the response polarity is compared for the various target types, as this feature might be used to discriminate between the different target types.

Contents

3.1 Model development

The coil state-space model has been discussed in Section 2.3. The electronics includes non-linear elements and can thus not directly be modeled using a linear state-space system. However defining a new phase each time a diode changes state (blocking/conducting) or when the amplifier gets out of saturation and assuming ideal diodes and an ideal amplifier, a state-space model may be defined for each phase using the approach described in Appendix A and valid for linear circuits. Indeed, an ideal diode may be modeled as a voltage source in series with a resistor when it is conducting and as an open circuit when it is blocked. An ideal operational amplifier may be modeled as a first order linear system. The Schiebel amplifier is significantly saturated and the time needed to get out of saturation can not be neglected and we have taken this into account by introducing a delay to get out of saturation. This delay starts when the input gets below $V_{\text{sat}}/K_{\text{amp}}$ with V_{sat} the saturation voltage and K_{amp} the static gain of the amplifier. After this delay, the amplifier state is initialized to yield V_{sat} as output and a linear behavior is then considered from that point on.

Recall that the Schiebel detector sends a bipolar pulse. The second pulse is sent directly after the first one and there is only one evaluation window after the second pulse. As the transient related to the first pulse has gone[1] when the second voltage pulse is sent, modeling considering a single pulse detector is sufficient.

The detector may then be modeled by considering the following phases (phase numbers below correspond to those indicated in Fig. 3.1):

- On the TX side (see Fig. 2.22):

  1. Charge: the switch I_1 is closed and the TX coil charges (charging might be a misnomer as it is mainly the current that is increased, though to a lesser extent, charges appear on the parasitic capacitors. One also says that the coil is energized) on 8V.
  2. Discharge Zener: the switch I_1 is opened and the Zener diodes become conducting. The TX coil is discharged on the Zener voltage (138V).

[1]We consider the detector in absence of targets. With a very slow target, the transient of the first pulse might interact with the one of the second pulse. It may then be necessary to model the two pulses. This generalization is straightforward.

3. Discharge damping: the reverse Zener diode is getting blocked and the coil continues its discharge on the damping resistor alone $R^{\mathrm{d}}_{\mathrm{TX}}$.

- On the RX side (see Fig. 2.23):

4. Discharge filtered: the clamping diodes (D_1 and D_2) are both non-conducting and the RX coil voltage is propagated to the input of the amplifier amplifier.
5. Listen: the RX amplifier A_1 goes out of saturation. The amplifier output signal can the be used to detect a target.

Each phase is modeled by a linear state-space system obtained by combining the models of the coils and of the electronics. When switching from one phase to the other, the end values of the state variables are used as initial condition for the next phase.

3.2 Model evaluation

The TX and RX coil currents and voltages computed with the detector state-space model are shown in Fig. 3.1 where they are compared with the corresponding measured signals. The time limits for the various phases and the evaluation window are also indicated. One sees that the computed current and voltages match accurately the measured ones.

Similarly, the computed and measured outputs of the amplifier $V^{\mathrm{RX}}_{\mathrm{amp}}$ are shown in Fig. 3.2. To better understand the effect of the filter network and the amplifier, we have shown on the same figure the coil voltage $V^{\mathrm{RX}}_{\mathrm{coil}}$ and the output of the filter network $V^{\mathrm{RX}}_{\mathrm{filt}}$. To better visualize the effect of the filter and amplifier dynamics, we have multiplied $V^{\mathrm{RX}}_{\mathrm{coil}}$ and $V^{\mathrm{RX}}_{\mathrm{filt}}$ by the static gain of the transfer functions which relate them to $V^{\mathrm{RX}}_{\mathrm{amp}}$; : $K_{\mathrm{amp}}K_{\mathrm{filt}}$ and K_{amp} respectively. For an ideal amplifier and a filter, which do not distort the signal, the curves corresponding to $V^{\mathrm{RX}}_{\mathrm{coil}}$, $V^{\mathrm{RX}}_{\mathrm{filt}}$ and $V^{\mathrm{RX}}_{\mathrm{amp}}$ would then be identical. On the top figure, one sees clearly the effect of the clamping diodes, which limit $V^{\mathrm{RX}}_{\mathrm{filt}}$. As the gain of the amplifier is very large, the voltage scale used to show this effect is much too large to visualize the signals in the evaluation window. Therefore, the lower plot shows the same curves with a smaller voltage scale. One then clearly sees that the filter has little effect on the signal (except for the existence of a static gain) but that the amplifier significantly changes the response. This is compatible with the above

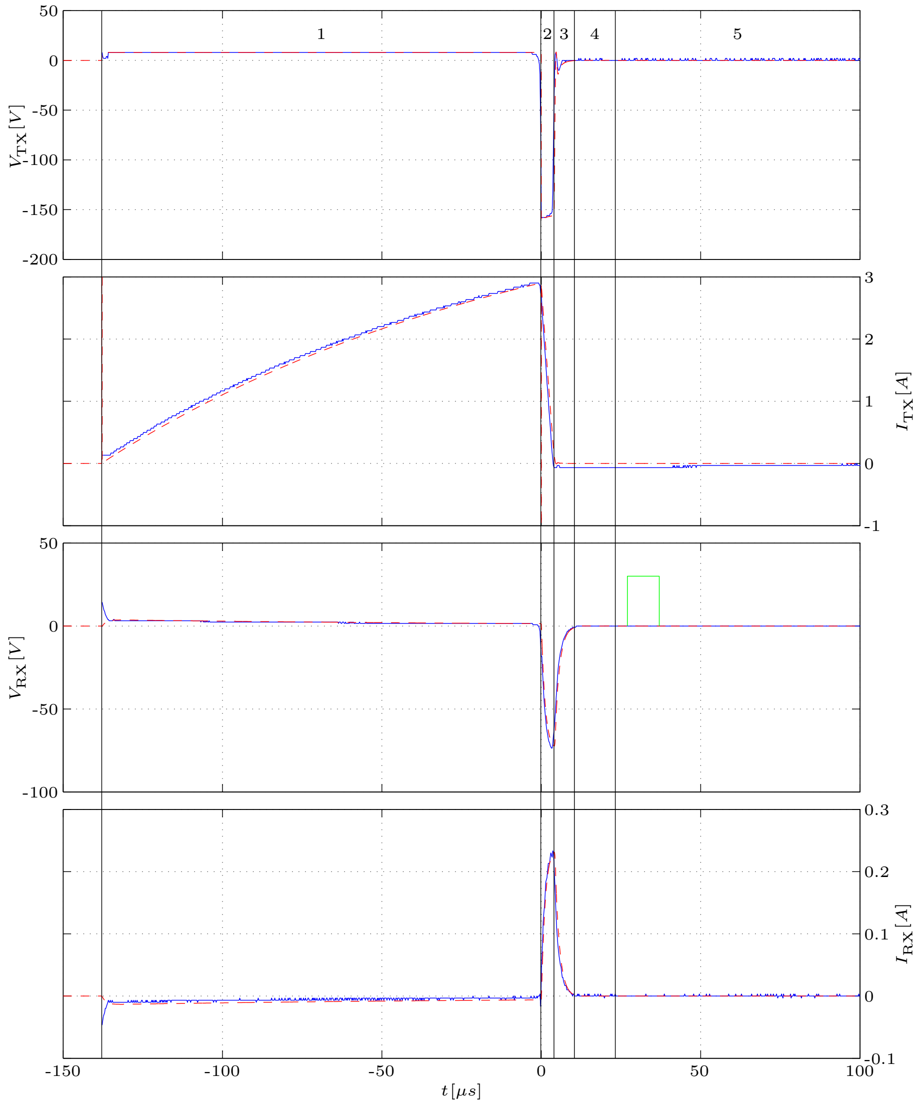

Figure 3.1: *Measured (blue) and computed (red) coils current and voltage using the simple coil model. Phase limits are indicated by vertical black lines. Phase number and evaluation window (green) are also indicated.*

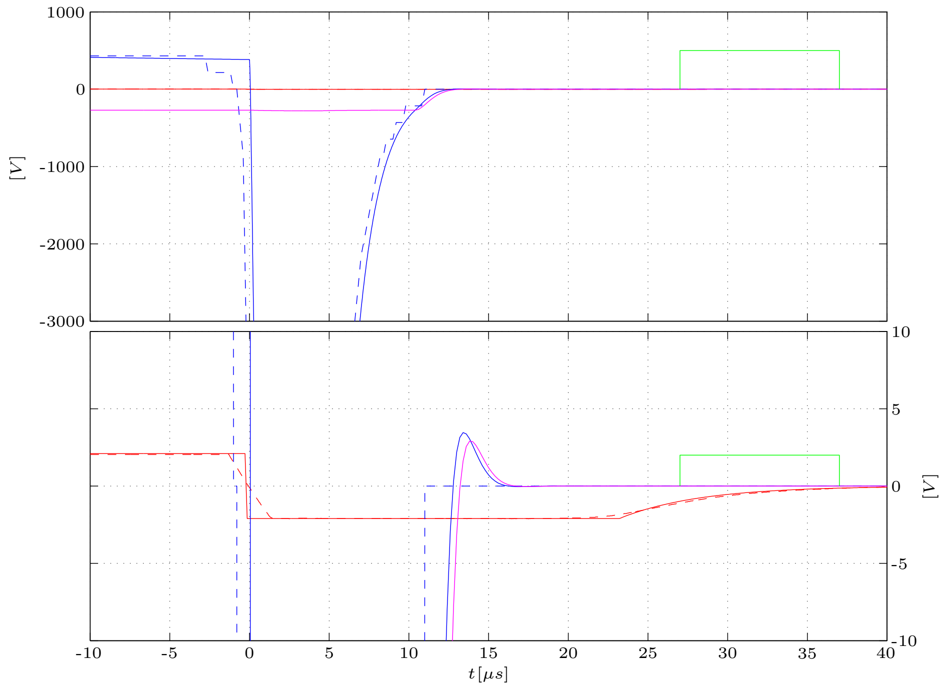

Figure 3.2: *Schiebel RX measured (– –) and computed (—), using the simple coil model, scaled coil voltage ($K_{\mathrm{amp}} K_{\mathrm{filt}} V_{\mathrm{coil}}^{\mathrm{RX}}$ in blue), scaled filtered voltage ($K_{\mathrm{amp}} V_{\mathrm{filt}}^{\mathrm{RX}}$ in magenta) and output of RX amplifier ($V_{\mathrm{amp}}^{\mathrm{RX}}$) in red) at two voltage scales. Evaluation window is also shown in green.*

discussion which attributes this behavior to the (rather fast) time constants of the filter, to the (rather slow) time constants of the amplifier and to the delay required for the amplifier to get out of saturation. On the figures, one also sees that the evaluation window indeed starts when the amplifier output reaches 1V as explained above.

Recall that 1Ω resistors were introduced both in the TX and RX circuits to measure the current. As mentioned above, the resistors modify the current pulse. This is illustrated in Figs. 3.3 and 3.4. in which the voltages and currents have been computed with and without the measurement resistors. One sees that, as a result of the extra resistors, the exponential shape of the first order charge current becomes apparent. The current reached is smaller, the duration of the discharge pulse is smaller and the listening window occurs somewhat earlier. The curves without the resistors are relevant for the detector in normal use. One sees that the charge time is smaller than the time constant of the coil and that the exponential behavior is barely visible. A linear triangular shape is thus a good approximation for the TX current.

Figures 3.1 to 3.4 were computed using the simple coil model. One sees that the resulting model (including the model for the electronics) is quite accurate and that all the computed and measured curves are in good agreement. We have also performed the same computations with the detailed coil model. This is illustrated in Figs. 3.5 and 3.6. The difference between the simple and detailed coil model is the presence of additional oscillation modes for the detailed model which are mainly visible in phases 2 and 5. Those oscillations are mainly generated at the fast variation of the TX voltage (in phase 2) and they are well visible in phase 5 because the dominant modes response became very small in comparison. Those oscillations are not visible in the measured signals and it is thus apparent that the simple model better predicts the detector signals. We attribute those spurious oscillations to the skin effects that were neglected. More specifically, the frequency of the spurious oscillations is around 10MHz. At this frequency, according to (2.5), the skin depth is $10\mu m$, which is much smaller than the RX wire strand diameter of $100\mu m$. Hence, the skin effect becomes significant, the loop resistance increases and the oscillations are getting much more damped. Introducing skin effect in a state-space system is not an easy task. This was however not necessary because the models are accurate enough for our purpose.

Recall that the main motivations for the development of the detailed

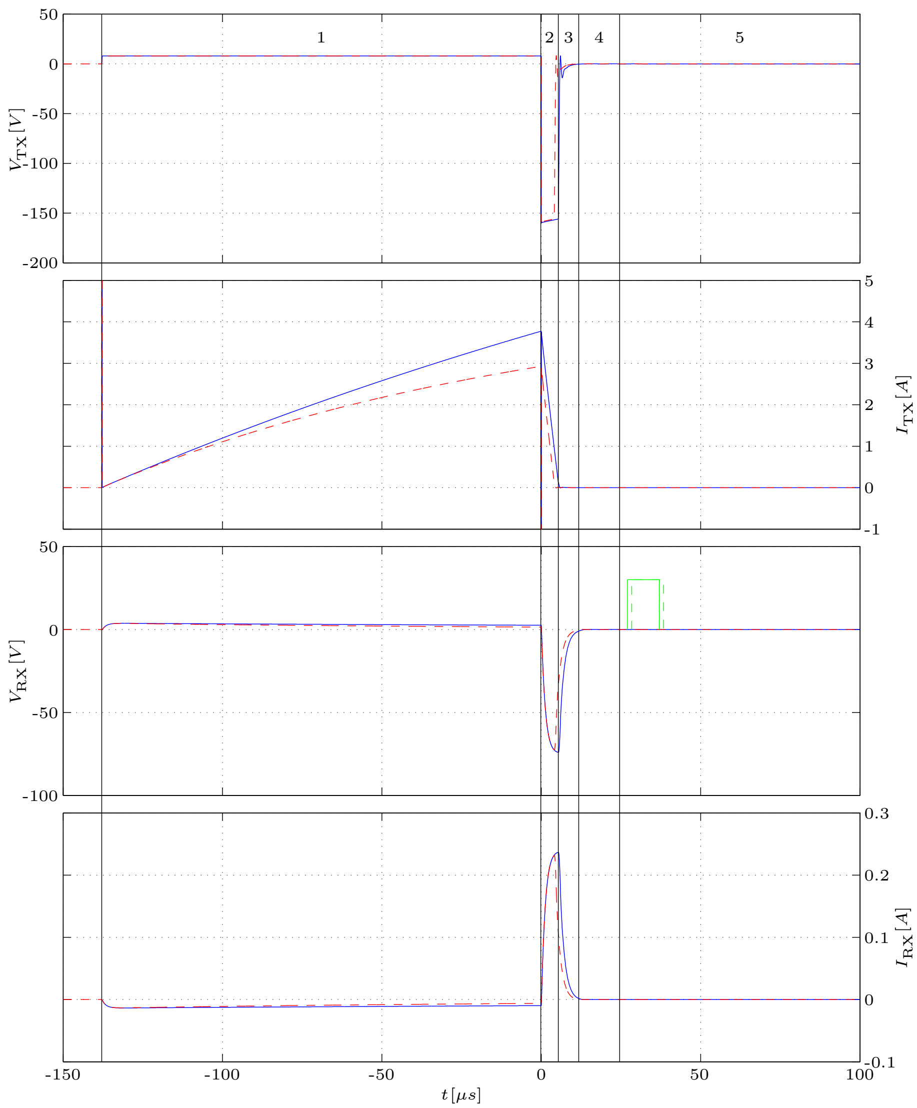

Figure 3.3: *Computed coils current and voltage with (red) and without (blue) measurement resistors. Phase limits are indicated for the response without measurement resistor by vertical black lines. Phase number and evaluation window (green) are also indicated. The simple coil model was used.*

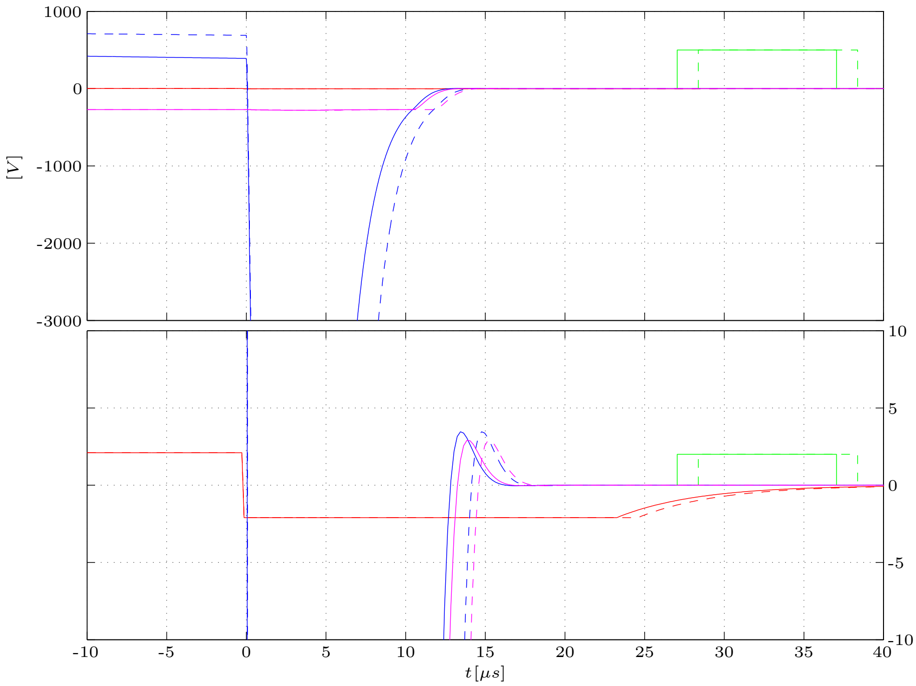

Figure 3.4: *Schiebel RX scaled coil voltage ($K_{\text{amp}} K_{\text{filt}} V_{\text{coil}}^{\text{RX}}$ in blue), scaled filtered voltage ($K_{\text{amp}} V_{\text{filt}}^{\text{RX}}$ in magenta) and output of RX amplifier ($V_{\text{amp}}^{\text{RX}}$) in red) at two voltage scales. Curves are computed with (—) and without (– –) the measurement resistor RX. The evaluation window is shown in green. The simple coil model was used.*

model were the estimation of the equivalent parameters of the simple model and the prediction of the charge distribution along the coils as it will be needed in Chapter 6 to understand the effect of water on the detector head. To explain the water effect, we will use the low frequency charge distribution and as it appears from Figs. 3.5 and 3.6, the detailed model is accurate below the first resonance (and even above, apart for some spurious oscillations). This is further confirmed by noting that the simple detector model is very accurate and that according to the Bode curves shown in Fig. 2.12, the detailed and the simple coil model are nearly identical below the first resonance.

Finally, note that the spurious oscillations are filtered by the amplifier and that therefore the detailed model also accurately predicts the detector response. There is however little justification to use the detailed model for that purpose because it is much more complicated than the simple one.

3.3 Extension of the state-space model to include a dipole target

The state-space model of the detector can easily be extended to take into account the presence of a target or of the soil by adding the target state-space representation and an appropriate feedback from the target to the coil induced voltages. Specific targets will be considered in the next part. Here, our objective is to consider simple target models and to compute the response of the detector as a function of the target dynamics.

3.3.1 Target type

Let us consider small isotropic targets that can be modeled by a dipole. Two main cases will be considered: an electric target that scatters as an electric dipole and a magnetic target that scatters as a magnetic dipole. In the frequency band of interest, the coupling between electric and magnetic phenomena are weak and we therefore assume that, for an electric target, the induced electric dipole can be computed from the incident electric field alone and that, for a magnetic target, the induced magnetic dipole can be computed from the incident magnetic field alone. Further assuming a linear target, the induced dipole can be computed using the polarizability tensor.

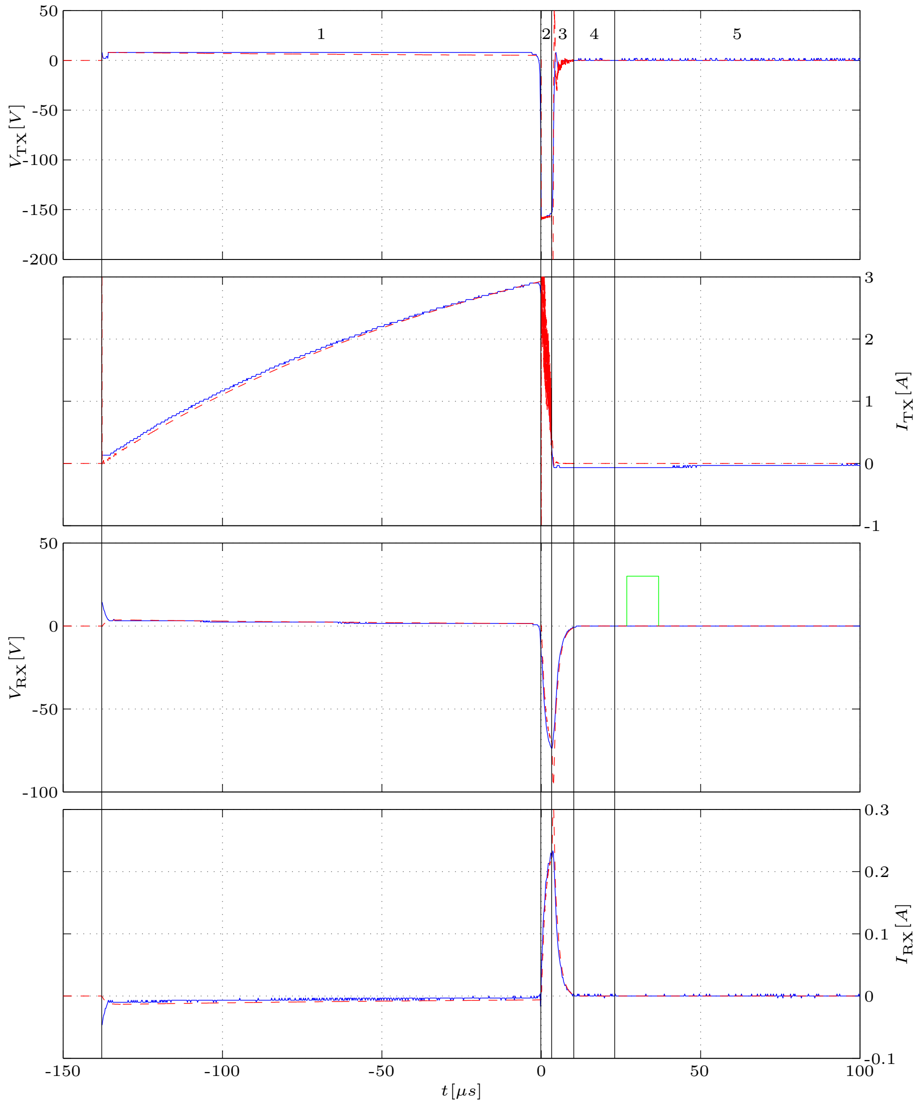

Figure 3.5: *Measured (blue) and computed (red) coils current and voltage. Phase limits are indicated by vertical black lines. Phase number and evaluation window (green) are also indicated. The detailed coil model was used.*

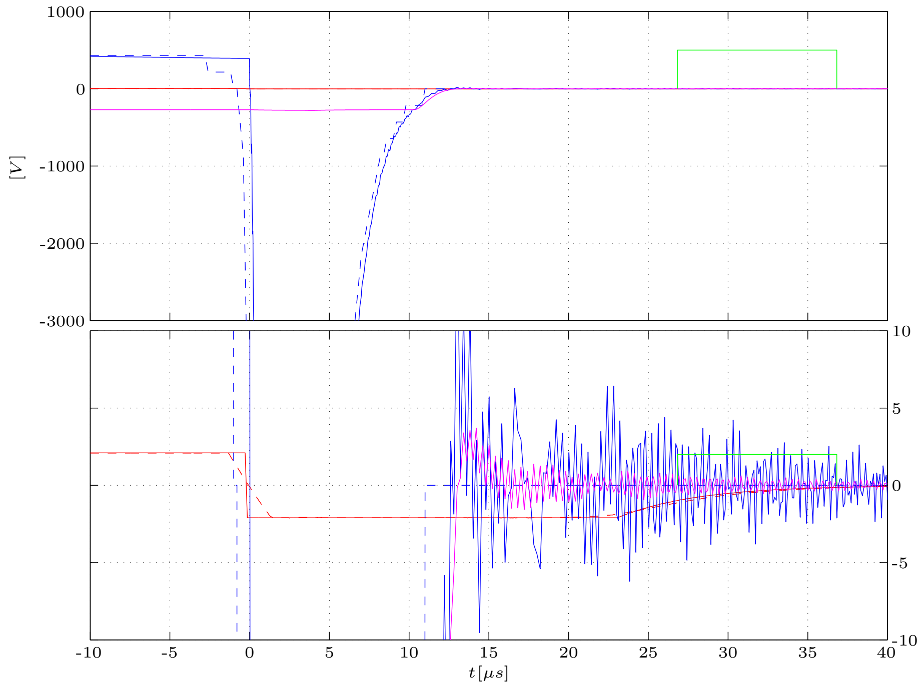

Figure 3.6: *Schiebel RX measured (– –) and computed (—) scaled coil voltage ($K_{\mathrm{amp}}K_{\mathrm{filt}}V_{\mathrm{coil}}^{\mathrm{RX}}$ in blue), scaled filtered voltage ($K_{\mathrm{amp}}V_{\mathrm{filt}}^{\mathrm{RX}}$ in magenta) and output of RX amplifier ($V_{\mathrm{amp}}^{\mathrm{RX}}$ in red) at two voltage scales. Evaluation window is also shown in green. The detailed coil model was used.*

For an electric target, we have:

$$\boldsymbol{p}_\mathrm{t} = \overline{\boldsymbol{P}}_\mathrm{t}\boldsymbol{E}_\mathrm{TX} \tag{3.1}$$

with $\boldsymbol{p}_\mathrm{t}$, the induced electric dipole, $\overline{\boldsymbol{P}}_\mathrm{t}$ the electric polarizability tensor and $\boldsymbol{E}_\mathrm{TX}$ the electric field incident on the target and produced by the detector. For an isotropic target, $\overline{\boldsymbol{P}}_\mathrm{t} = P_\mathrm{t}\overline{\boldsymbol{I}}$ with $\overline{\boldsymbol{I}}$ the identity tensor.

Similarly, for a magnetic target, the induced dipole can be expressed as:

$$\boldsymbol{m}_\mathrm{t} = \overline{\boldsymbol{M}}_\mathrm{t}\boldsymbol{H}_\mathrm{TX} \tag{3.2}$$

with $\boldsymbol{m}_\mathrm{t}$, the induced magnetic dipole, $\overline{\boldsymbol{M}}_\mathrm{t}$ the magnetic polarizability tensor and $\boldsymbol{H}_\mathrm{TX}$ the magnetic field incident on the target and produced by the detector. For an isotropic target, $\overline{\boldsymbol{M}}_\mathrm{t} = M_\mathrm{t}\overline{\boldsymbol{I}}$.

A typical electric target is a small dielectric object. However, for the pulsed detectors considered, a target can only be detected if its response remains measurable in the evaluation window, some time after the TX pulse. This requires a frequency dependent polarizability $\overline{\boldsymbol{P}}_\mathrm{t}(\omega)$. We have not found an example of such a target producing a measurable response. A more relevant example of an electric target for a pulsed detector is a small conducting object for which the conductivity is too small to produce a significant magnetic dipole (small eddy currents) but yet large enough to produce a significant electric dipole by means of charge separation. This will occur for a small water droplet as discussed in Chapter 6. We further consider the simplest possible frequency dependency for the polarizability:

$$P_\mathrm{t} = \frac{K_\mathrm{t}}{1 + j\omega T_\mathrm{t}} \tag{3.3}$$

which as will be shown in Chapter 6 (see Equ. 6.41) is the exact solution (up to an irrelevant direct feedthrough) for a water ellipsoid. Note that $K_\mathrm{t} > 0$ because for an (isotropic) conducting object, the polarization is in the direction of the incident field. This is also true for most dielectric objects because in general, $\epsilon_\mathrm{r} > 1$.

A typical magnetic target is a small magnetic object. Here also, to yield a measurable response, the polarizability should be frequency dependent. Some naturally occurring soils exhibit a frequency varying susceptibility (also known as viscous remnant magnetization, magnetic viscosity, magnetic relaxation or magnetic after-effect) [48, 49, 26, 25].

Hence, a sample of soil can be considered as a small magnetic target. An extended magnetic soil is obviously too large to be modeled by a dipole. Nevertheless the conclusions that we will draw on the time domain signature of a dipole magnetic target are still expected to be valid for a magnetic soil. Indeed, for a magnetic soil, the time domain response is independent of the spacial repartition of the magnetic material (see 4.3.2). To simplify the developments, we will further consider a first order frequency dependent magnetic polarizability:

$$M_{\mathrm{t}}^{\mathrm{mag}} = \frac{K_{\mathrm{t}}}{1 + j\omega T_{\mathrm{t}}} \tag{3.4}$$

For a magnetic soil (as for all paramagnetic and ferromagnetic materials) the permeability $\mu_{\mathrm{r}} > 1$. The induced dipole is then induced in the direction of the incident field and therefore, $K_{\mathrm{t}} > 0$.

Another common example of a magnetic target is a small highly conducting object, such as a small metallic piece. We will however see that the magnetic polarizability of a conducting object significantly differs from that of a magnetic object (3.4). To clearly distinguish the two cases, we will use the term 'magnetic target' only for magnetic objects. Conducting objects that produce magnetic dipoles will then be called 'conducting targets'. They should however not be confused with the weakly conducting objects discussed above and that produce an electric dipole (3.3). The latter being called 'electric targets'

For a first order conducting target (such as an RL loop), the currents and voltages induced in the target are related by a first order transfer function. Furthermore, the induced magnetic dipole moment is proportional to the induced currents and the voltage induced in the target is proportional to $j\omega \boldsymbol{B}_{\mathrm{TX}}$. The magnetic polarizability is therefore given by:

$$M_{\mathrm{t}}^{\mathrm{cond}} = -\frac{j\omega K_{\mathrm{t}} T_{\mathrm{t}}}{1 + j\omega T_{\mathrm{t}}} \tag{3.5}$$

with $K_{\mathrm{t}} > 0$ and T_{t} respectively the gain and time constant of the target. The minus sign is required to have a scattered dipole that generate magnetic fields opposing the incident magnetic field, as required by Lenz's law. This can easily be checked considering the limit for the frequency tending towards infinity. Indeed, the target may then be considered PEC and the magnetic polarizability must then be negative, as is the case in (3.5) for $\omega \to \infty$.

Most conducting objects have a polarizability that present a more complex frequency variation than the first order model considered in

(3.5). They can then be modeled using a a number of discrete poles [46, Chapter 6] and the first order model can then be seen as a first order approximation in which the higher orders are neglected.

3.3.2 Voltage induced by the target

Our objective is to compute the voltage induced by the target in the RX coil. We start with the electric contribution. Proceeding as in Section 2.4.5 but considering the volume outside instead of the volume inside $\mathcal{S}_\mathrm{d}$, one gets the following expression instead of (2.51):

$$e_\mathrm{E} = -j\omega \int_{\mathcal{V}_\mathrm{t}} \check{\phi}^{(\mathrm{fs})}_\mathrm{RX} \rho_\mathrm{t} \mathrm{d}V \tag{3.6}$$

with $\mathcal{V}_\mathrm{t}$ a volume containing the target, ρ_t an equivalent charge distribution inside the target that produces the same scattering as the target and $\check{\phi}_\mathrm{RX}$ the scalar potential produced by the RX coil when a unit current flows into it. The sign difference between (3.6) and (2.51) stems from the fact that the direction of positive normal is opposite for the volumes internal and external to $\mathcal{S}_\mathrm{d}$.

Instead of using an equivalent charge distribution ρ_t, an equivalent dipole distribution $\boldsymbol{\tau}_\mathrm{t}$ may also be considered. The two distributions are equivalent if $\rho_\mathrm{t} = -\nabla \cdot \boldsymbol{\tau}_\mathrm{t}$ [50, Section 6.1, Equ. 6]. Introducing this charge distribution in (3.6), assuming a continuous dipole distribution fully included inside $\mathcal{V}_\mathrm{t}$ and using the vector identity (B.1.3) then yields:

$$e_\mathrm{E} = -j\omega \int_{\mathcal{V}_\mathrm{t}} \check{\boldsymbol{E}}^{(\mathrm{fs})}_\mathrm{RX0} \cdot \boldsymbol{\tau}_\mathrm{t} \mathrm{d}V \tag{3.7}$$

with $\check{\boldsymbol{E}}^{(\mathrm{fs})}_\mathrm{RX0} = -\nabla \check{\phi}^{(\mathrm{fs})}_\mathrm{RX}$, the order zero electric field produced by the RX coil for a unit RX coil current.

If the incident electric field, is constant on the target volume, the induced voltage can further be expressed as:

$$e_\mathrm{E} = -j\omega \check{\boldsymbol{E}}^{(\mathrm{fs})}_\mathrm{RX0} \cdot \boldsymbol{p}_\mathrm{t} \tag{3.8}$$

with $\boldsymbol{p}_\mathrm{t} = \int_{\mathcal{V}_\mathrm{t}} \boldsymbol{\tau}_\mathrm{t} \mathrm{d}V$, the target equivalent dipole. This further shows that an electric target can be represented by an electric dipole if the incident electric field is constant on the target volume.

Using (3.1) to express the target polarizability with $\boldsymbol{E}_\mathrm{TX} \simeq \check{\boldsymbol{E}}^{(\mathrm{fs})}_\mathrm{TX0} I_\mathrm{TX}$ then yields:

$$e_\mathrm{E} = -j\omega S^\mathrm{E}_\mathrm{head} P_\mathrm{t} I_\mathrm{TX} \tag{3.9}$$

with I_{TX} the TX current and

$$S^{\mathrm{E}}_{\mathrm{head}} = \check{\boldsymbol{E}}^{(\mathrm{fs})}_{\mathrm{RX0}} \cdot \check{\boldsymbol{E}}^{(\mathrm{fs})}_{\mathrm{TX0}} \tag{3.10}$$

the head electric sensitivity with $\boldsymbol{E}^{(\mathrm{fs})}_{\mathrm{TX0}}$ the order zero electric field produced by the detector for a unit TX current. Rigorously speaking, $\boldsymbol{E}^{(\mathrm{fs})}_{\mathrm{TX}}$ should be used instead of $\boldsymbol{E}^{(\mathrm{fs})}_{\mathrm{TX0}}$ in (3.10). In other words, the polarization induced by $\boldsymbol{E}^{(\mathrm{fs})}_{\mathrm{TX1}}$ in the target has been neglected. This neglected electric field is induced by $\boldsymbol{B}^{(\mathrm{fs})}_{\mathrm{TX0}}$ which itself is produced by the solenoid current $\boldsymbol{J}_0$. Hence, the neglected electric dipole originates from a coupling between electric and magnetic phenomenas. This coupling is usually weak in the frequency band of interest. For the problem at hand, the assumption was checked numerically. Just below the casing of the Schiebel TX coil, $\boldsymbol{E}^{(\mathrm{fs})}_{\mathrm{TX0}}$ was found to be more than thousand times larger than $\boldsymbol{E}^{(\mathrm{fs})}_{\mathrm{TX1}}$. This ratio decreases with the distance to the coil and at large distances, $\boldsymbol{E}^{(\mathrm{fs})}_{\mathrm{TX1}}$ becomes dominant (but it will always be smaller than just below the coil). However, we will show in Chapter 6, that an electric target just below the coil can produce a measurable signal but a signal thousand times smaller would clearly be unmeasurable. Hence, the contribution of $\boldsymbol{E}^{(\mathrm{fs})}_{\mathrm{TX1}}$ will everywhere be too small to be measurable. It can thus always be neglected in practice. In some cases, as for a shielded coil for which $\boldsymbol{E}^{(\mathrm{fs})}_{\mathrm{TX0}} = 0$. $\boldsymbol{E}^{(\mathrm{fs})}_{\mathrm{TX1}}$ may be dominant but it will yield a response too small to be measurable.

Further, neglecting $\boldsymbol{E}^{(\mathrm{fs})}_{\mathrm{TX1}}$ has a number of practical advantages. First, the magnetic and electric responses are completely decoupled which will allow for an easier inclusion of e_{E} in the circuit model. Second, according to (3.10), the target response remains unchanged if the he TX and RX coils are exchanged as required for the exact solution (according to the full-wave reciprocity). Hence, the approximation used in (3.10) is consistent with that used to establish the QS reciprocity expression (C.4.13) at the origin of (3.6).

The response of a magnetic dipole can be derived similarly, by considering the generalized Maxwell equations which include magnetic currents ($\boldsymbol{M}$) and charges (ρ_{m}). The result can be obtained without any new development by making use of the duality which exists between magnetic and electric quantities [35, Section 3.2].

The solution for magnetic sources can then be obtained from that for electric sources by the following substitution:

$$\boldsymbol{E} \leftarrow \boldsymbol{H} \quad \boldsymbol{H} \leftarrow -\boldsymbol{E} \quad \boldsymbol{J} \leftarrow \boldsymbol{M} \quad \rho \leftarrow \rho_{\mathrm{m}} \quad \boldsymbol{p} \leftarrow \mu \boldsymbol{m} \tag{3.11}$$

where $x \leftarrow y$ means 'replace x by y' and $\boldsymbol{m}$ is a magnetic dipole. The factor μ appearing in the dipole substitution stems from the fact that the classical definition of the magnetic dipole is not dual to the definition of the electric dipole. The first definition is based on a small current loop whereas the latter is based on a pair of electric charges. The dual of the electric dipole would thus be defined from two magnetic charges. Both definitions are equivalent up to a factor μ.

Making the substitution then yields:

$$e_{\mathrm{M}} = j\omega\mu \check{\boldsymbol{H}}^{(\mathrm{fs})}_{\mathrm{RX0}} \cdot \boldsymbol{m}_{\mathrm{t}} \tag{3.12}$$

with $\boldsymbol{m}_{\mathrm{t}}$ the target magnetic dipole and $\check{\boldsymbol{H}}^{(\mathrm{fs})}_{\mathrm{RX0}}$ the order zero magnetic field produced by the RX coil for a unit RX coil current. The sign change between (3.8) and (3.12) stems from the fact that the induced voltage is related to the fields through (2.31) and this expression changes sign when performing the duality replacement (3.11).

Introducing the target polarizability then yields:

$$e_{\mathrm{M}} = j\omega\mu S^{\mathrm{M}}_{\mathrm{head}} M_{\mathrm{t}} I_{\mathrm{TX}} \tag{3.13}$$

with I_{TX} the TX current and

$$S^{\mathrm{M}}_{\mathrm{head}} = \check{\boldsymbol{H}}^{(\mathrm{fs})}_{\mathrm{RX0}} \cdot \check{\boldsymbol{H}}^{(\mathrm{fs})}_{\mathrm{TX0}} \tag{3.14}$$

the head magnetic sensitivity with $\boldsymbol{H}^{(\mathrm{fs})}_{\mathrm{TX0}}$ the order zero magnetic field produced by the detector for a unit TX current. As for the electric case, and for the same reasons, we have used $\boldsymbol{H}^{(\mathrm{fs})}_{\mathrm{TX0}}$ instead of $\boldsymbol{H}^{(\mathrm{fs})}_{\mathrm{TX1}}$. This approximation is obviously a good one because for a coil the solenoidal current is clearly dominant $\boldsymbol{J}_{\mathrm{TX0}} \gg \boldsymbol{J}_{\mathrm{TX1}}$. Further, with an appropriate choice of current decomposition (see B.3.35), $\boldsymbol{H}^{(\mathrm{fs})}_{\mathrm{TX1}}$ can be made null.

3.3.3 Interconnection between the target and the general coil model

Expression (3.9) and (3.13) for e_{E} and e_{M} are not convenient to use in the state-space representation because they involve the head sensitivities $S^{\mathrm{E}}_{\mathrm{head}}$ and $S^{\mathrm{M}}_{\mathrm{head}}$ which exhibit a complex frequency dependence. This problem has already been discussed in Section 2.4.6 where we have shown that the global induced voltage e_{E} can be replaced by a contribution e_{E} in each capacitive branch and e_{M} can be replaced by a contribution e_{L} in each inductive branch and that those contributions are easier to compute because they only involve the field produced by a unit current in the inductor or a unit charge on the capacitor and not the global circuit solution.

3.3.3.1 Electric target

An electric target will induce voltages $e_{\mathrm{C_j}}$ in each capacitor branch. Proceeding as in Section 2.4.6 to compute $e_{\mathrm{C_j}}$ from e_{E} but starting from (3.8) yields:

$$e_{\mathrm{C_j}} = -\check{\boldsymbol{E}}^{(\mathrm{fs})}_{\mathrm{C_j,Q}} \cdot \boldsymbol{p}_{\mathrm{t}} \tag{3.15}$$

with $\check{\boldsymbol{E}}^{(\mathrm{fs})}_{\mathrm{C_i,Q}}$ the electric field produced by a unit charge on the capacitor i.

The incident field on the target $\boldsymbol{E}^{(\mathrm{fs})}_{\mathrm{TX0}}$ can also be expressed as a sum of capacitor contributions:

$$\boldsymbol{E}^{(\mathrm{fs})}_{\mathrm{TX0}} = \sum_i \check{\boldsymbol{E}}^{(\mathrm{fs})}_{\mathrm{C_i,Q}} Q_{\mathrm{C_i}} \tag{3.16}$$

with $Q_{\mathrm{C_i}}$ the total charge on capacitor i. Note that the TX and RX coils are coupled. Therefore, when the transmit pulse is emitted, charges appear on the capacitors of the RX equivalent circuits and those capacitors must be considered in the sum (3.16). The contributions of the RX coil to the transmit electric field is not negligible because the Schiebel head can be seen as a transformer with a voltage step down of about[2] 0.5, the secondary being connected on the damping resistor. As this resistor is large, the current in the RX coil is rather small but the RX voltage has the same order of magnitude as the TX voltage.

Each capacitor C_{j} yields the following contribution to $e_{\mathrm{C_i}}$:

$$e_{\mathrm{C_i,C_j}} = -\check{\boldsymbol{E}}^{(\mathrm{fs})}_{\mathrm{C_i,Q}} \cdot \check{\boldsymbol{E}}^{(\mathrm{fs})}_{\mathrm{C_j,Q}} P_{\mathrm{t}} Q_{\mathrm{C_i}} \tag{3.17}$$

This contribution can easily be introduced in the state-space model because the electric fields appearing in (3.17) are frequency independent

[2] There are about two times more turns in the secondary than in the primary. This should yield a voltage step up of 2 for an ideal coupling but the leakage flux is high, leading to a voltage step down of about 0.5.

and those fields can be computed from the charge distribution $\check{\boldsymbol{\rho}}^{(\mathrm{fs})}_{\mathrm{C_i},\mathrm{Q}}$ appearing on a single capacitor for a unit charge on that capacitor. This charge distribution is available from the MAS solution as discussed in Section 2.4.6. Furthermore, $Q_{\mathrm{C_i}}$ is related to the node voltages and is thus available in the state-space representation of the coil.

More precisely, the first order electric target can be introduced in the state-space representation by adding the following state equation:

$$\frac{\mathrm{d}x_{\mathrm{t}}^{\mathrm{j}}}{\mathrm{d}t} = -\frac{x_{\mathrm{t}}^{\mathrm{j}}}{T_{\mathrm{t}}} + \frac{K_{\mathrm{t}}}{T_{\mathrm{t}}} u_{\mathrm{j}} \tag{3.18}$$

with the input u_{j} connected to the coil state variables $V_{\mathrm{C_i}}$ to yield:

$$u_{\mathrm{j}} = -\sum_i \check{\boldsymbol{E}}^{(\mathrm{fs})}_{\mathrm{C_i},\mathrm{Q}} \cdot \check{\boldsymbol{E}}^{(\mathrm{fs})}_{\mathrm{C_j},\mathrm{Q}} Q_{\mathrm{C_i}} \tag{3.19}$$

and the state x_{j} is connected to the input $e_{\mathrm{C_j}}$ of the coil state-space model, which is a voltage source located in the j^{th} capacitor branch.

An index j had to be used for the target state-space variable $x_{\mathrm{t}}^{\mathrm{j}}$ because the excitation u_{j} is different for the voltage source $e_{\mathrm{C_j}}$ in each capacitor branch. This is not efficient when many capacitors exist in the model. Indeed, although a first order target is considered, the target is modeled by a large state vector with one state variable $x_{\mathrm{t}}^{\mathrm{j}}$ for each capacitor branch.

For a large number of capacitors, it is more efficient to use one state variable for each component of the target dipole components p_{t}^{α} with $\alpha = \{x, y, z\}$. This only requires three state variables for the target:

$$\frac{\mathrm{d}p_{\mathrm{t}}^{\alpha}}{\mathrm{d}t} = -\frac{p_{\mathrm{t}}^{\alpha}}{T_{\mathrm{t}}} + \frac{K_{\mathrm{t}}}{T_{\mathrm{t}}} u_{\alpha} \tag{3.20}$$

the input u_α is connected to the coil state variables to yield $u_\alpha = E^{(\mathrm{fs}),\alpha}_{\mathrm{TX0}} = \sum_i \check{E}^{(\mathrm{fs}),\alpha}_{\mathrm{C_i},\mathrm{Q}} Q_{\mathrm{C_i}}$ where the superscript α again indicates one of the coordinates : x, y and z. The various inputs of the coil state-space model $e_{\mathrm{C_j}}$ are then connected to the states p_{t}^{α} through:

$$e_{\mathrm{C_j}} = -\boldsymbol{p}_{\mathrm{t}} \cdot \check{\boldsymbol{E}}^{(\mathrm{fs})}_{\mathrm{C_j},\mathrm{Q}} \tag{3.21}$$

3.3.3.2 Magnetic target

Proceeding as for the electric target immediately yields the following induced voltage in each inductor branch for a magnetic target:

$$e_{\mathrm{L_j}} = j\omega\mu \check{\boldsymbol{H}}^{(\mathrm{fs})}_{\mathrm{L_j}} \cdot \boldsymbol{m}_{\mathrm{t}} \tag{3.22}$$

with $\check{\boldsymbol{H}}^{(\mathrm{fs})}_{\mathrm{L_i}}$ the magnetic field produced by a unit current in the inductor i, or equivalently, in the corresponding coil turn.

The incident field on the target $\boldsymbol{H}^{(\mathrm{fs})}_{\mathrm{TX0}}$ can be expressed as a sum of inductor contributions:

$$\boldsymbol{H}^{(\mathrm{fs})}_{\mathrm{TX0}} = \sum_i \check{\boldsymbol{H}}^{(\mathrm{fs})}_{\mathrm{L_i}} I_{\mathrm{L_i}} \tag{3.23}$$

with $I_{\mathrm{L_i}}$ the current in the inductor i. Here also, the TX and RX coils are coupled. The transmit pulse induces current in the RX coil and the current in inductors of the RX coil equivalent circuit must be taken into account to compute the total incident field. The contribution of the RX coil is however less important than in the electric case because, as already mentioned, the RX damping resistor is large and the current induced in the RX coil is much smaller than the TX current.

Each inductor L_{j} yields the following contribution to $e_{\mathrm{L_i}}$:

$$e_{\mathrm{L_i,L_j}} = j\omega \check{\boldsymbol{H}}^{(\mathrm{fs})}_{\mathrm{L_i}} \cdot \check{\boldsymbol{H}}^{(\mathrm{fs})}_{\mathrm{L_j}} M^{\mathrm{mag}}_{\mathrm{t}} I_{\mathrm{L_i}} \tag{3.24}$$

Introducing (3.24) in the state-space representation of the coil is somewhat more complex than for an electric target because, comparing (3.17) with (3.24) shows that the latter includes an additional time derivative operator $j\omega$. Apart from that, the problem is similar. Indeed, the magnetic fields appearing in (3.24) are frequency independent and those fields can be computed from the turn shape. Furthermore, the currents $I_{\mathrm{L_i}}$ are state-space variables of the coil model and the state-space representation of the first order polarizability $M^{\mathrm{mag}}_{\mathrm{t}}$ can easily be computed.

The extra time-derivative operator appearing in (3.24) can be taken into account by using $\frac{\mathrm{d}\underline{I}_{\mathrm{L}}}{\mathrm{d}t}$ instead of $I_{\mathrm{L_i}}$ as input of the target state-space model and $\frac{\mathrm{d}\underline{I}_{\mathrm{L}}}{\mathrm{d}t}$ can be computed from the state and input variables of the coil state-space model. Indeed, the state-space equation for the inductor current can be written:

$$\frac{\mathrm{d}\underline{I}_{\mathrm{L}}}{\mathrm{d}t} = \underline{\underline{A}}_{\mathrm{I_L}} \underline{X} + \underline{\underline{B}}_{\mathrm{I_L}} \underline{U} \tag{3.25}$$

with $\underline{\underline{A}}_{\mathrm{I_L}}$ built by concatenating the lines of coil state-space matrix $\underline{\underline{A}}$ corresponding to $\underline{I}_{\mathrm{L}}$. Similarly, $\underline{\underline{B}}_{\mathrm{I_L}}$ is built by concatenating the lines of coil state-space matrix $\underline{\underline{B}}$ corresponding to $\underline{I}_{\mathrm{L}}$. Thus one can add $\frac{\mathrm{d}\underline{I}_{\mathrm{L}}}{\mathrm{d}t}$ to the output vector $\underline{Y}$ by adding the following output equations:

$$\underline{Y}_{\mathrm{dI_L}} = \underline{\underline{A}}_{\mathrm{I_L}} \underline{X} + \underline{\underline{B}}_{\mathrm{I_L}} \underline{U} \tag{3.26}$$

The first order magnetic target can then be introduced in the coil state-space representation by adding the following state equation:

$$\frac{\mathrm{d}x_{\mathrm{t}}^{\mathrm{j}}}{\mathrm{d}t} = -\frac{x_{\mathrm{t}}^{\mathrm{j}}}{T_{\mathrm{t}}} + \frac{K_{\mathrm{t}}}{T_{\mathrm{t}}} u_{\mathrm{j}} \tag{3.27}$$

with the input u_{j} connected to the coil state variables to yield $u_{\mathrm{j}} = \sum_i \check{\boldsymbol{H}}_{\mathrm{L_i}}^{(\mathrm{fs})} \cdot \check{\boldsymbol{H}}_{\mathrm{L_j}}^{(\mathrm{fs})} Y_{\mathrm{dI_L}}$ and the target state x_{j} is connected to the input $e_{\mathrm{L_j}}$ of the coil state-space model, which is a voltage source located in the j^{th} inductor branch.

As for the electric target, an index j had to be used for the target state-space variable $x_{\mathrm{t}}^{\mathrm{j}}$ because the excitation u_{j} is different for the voltage source e_{j} in each inductor branch. For a large number of inductors, it may be more efficient to use the target magnetic dipole components m_{t}^{α} with $\alpha = \{x, y, z\}$ as state variables. This only requires three state variables for the target. The development is identical to the electric target case and expressions similar to (3.20) and (3.21) are obtained.

3.3.3.3 Conducting target

The conducting target is similar to the magnetic target, except for a sign change and the presence of an additional time-derivative in the magnetic polarizability (3.5). The state-space equations (3.27) can easily be extended, to take into account this additional time-derivative, by adding an output $y_{\mathrm{t}}^{\mathrm{j}}$, which is equal the time-derivative of $x_{\mathrm{t}}^{\mathrm{j}}$, to the target state-space model:

$$\frac{\mathrm{d}x_{\mathrm{t}}^{\mathrm{j}}}{\mathrm{d}t} = -\frac{x_{\mathrm{t}}^{\mathrm{j}}}{T_{\mathrm{t}}} + \frac{K_{\mathrm{t}}}{T_{\mathrm{t}}} u_{\mathrm{j}} \tag{3.28a}$$

$$y_{\mathrm{t}}^{\mathrm{j}} = -\frac{x_{\mathrm{t}}^{\mathrm{j}}}{T_{\mathrm{t}}} + \frac{K_{\mathrm{t}}}{T_{\mathrm{t}}} u_{\mathrm{j}} \tag{3.28b}$$

Comparing (3.28a) with (3.28b) one can easily check that $y_{\mathrm{t}}^{\mathrm{j}}$ indeed is equal to the time-derivative of $x_{\mathrm{t}}^{\mathrm{j}}$.

The conducting target can then be taken into account by connecting $y_{\mathrm{t}}^{\mathrm{j}}$ to the input $e_{\mathrm{L_j}}$ of the coil state-space model.

3.3.4 Interconnection between the target and the simple coil model

We now consider the simple coil model and we neglect the voltage induced in the TX coil because for targets of interest, this voltage is always very small compared to the excitation voltage.

3.3.4.1 Electric target

Let us consider an electric target located just under the RX coil. Then we may neglect the electric incident field produced by the TX coil, compared to the one produced by the RX coil which is much closer to the target. (This configuration is representative of a water layer on the head that will be considered in Chapter 6). There is then only one contribution (3.17) and the induced voltage in the RX capacitor branch is thus:

$$e_{\mathrm{C_{RX}}} = -S_{\mathrm{head}}^{\mathrm{C_{RX}}} P_{\mathrm{t}} Q_{\mathrm{C_{RX}}} \tag{3.29}$$

where

$$S_{\mathrm{head}}^{\mathrm{C_{RX}}} = \check{\boldsymbol{E}}_{\mathrm{C_{RX}},\mathrm{Q}}^{(\mathrm{fs})} \cdot \check{\boldsymbol{E}}_{\mathrm{C_{RX}},\mathrm{Q}}^{(\mathrm{fs})} \tag{3.30}$$

which can also be interpreted as a head sensitivity. It should however not be confused with $S_{\mathrm{head}}^{\mathrm{E}}$ defined by (3.10). $S_{\mathrm{head}}^{\mathrm{C_{RX}}}$ is frequency independent and $S_{\mathrm{head}}^{\mathrm{E}}$ is frequency dependent and varying in first approximation as ω^2. Furthermore, the former is used to compute e_{C} while the latter is used to compute e_{E}.

3.3.4.2 Magnetic and conducting targets

For the magnetic and conducting targets, we assume that the incident magnetic field produced by the RX coil can be neglected, compared to the one produced by the TX coil. This assumption is in general valid because the current induced in the RX coil is about twenty times smaller than the current in the TX coil as seen in Fig. 3.3. Furthermore, as there are about twice as many turns in the RX coil as in the TX coil and as the two coils have approximatively the same dimension, at some distance from the coils, the TX magnetic field is about ten times larger than the RX magnetic field. At some distance from the coils, the TX and RX magnetic fields are getting parallel and the relative contribution of the TX and RX incident fields may then be assessed by comparing the modulus of the fields. However, close to the RX coil, the direction of the fields significantly differs and to assess the relative contributions, one must compare $\boldsymbol{H}_{\mathrm{TX0}} \cdot \check{\boldsymbol{H}}_{\mathrm{RX0}}$ with $\boldsymbol{H}_{\mathrm{RX0}} \cdot \check{\boldsymbol{H}}_{\mathrm{RX0}}$. Just below the RX coil, the contribution of the incident field $\boldsymbol{H}_{\mathrm{RX0}}$ is dominant. However, 1cm below the coil, which is the closest distance a target will get to in a normal usage, the contribution of the incident field $\boldsymbol{H}_{\mathrm{RX0}}$ is four times smaller than the contribution of the incident field $\boldsymbol{H}_{\mathrm{TX0}}$. We have just discussed the relative peak values of the TX and RX incident magnetic field. The temporal shapes of the field pulses are also important and they are significantly different, as can be seen in Fig. 3.3. For example, for a conducting target, the transfer function includes a derivative. The derivative of the TX current is in first approximation a monopole pulse and the derivative of the RX current is in first approximation a bipolar pulse. The former will obviously induce a much stronger dipole in the target than the latter. Hence, neglecting the incident field generated by the RX coil is a good approximation for realistic configurations. In case of doubt, this incident field can always be taken into account in the computation; this only requires to include the corresponding contribution in the state-space model according to the general expression (3.24).

Neglecting the incident field generated by the RX coil, one gets:

$$e_{\mathrm{L_{RX}}} = j\omega\mu S_{\mathrm{head}}^{\mathrm{L_{RX}}} M_{\mathrm{t}} I_{\mathrm{L_{TX}}} \tag{3.31}$$

where

$$S_{\mathrm{head}}^{\mathrm{L_{RX}}} = \check{\boldsymbol{H}}_{\mathrm{L_{TX}}}^{(\mathrm{fs})} \cdot \check{\boldsymbol{H}}_{\mathrm{L_{RX}}}^{(\mathrm{fs})} \tag{3.32}$$

which can also be interpreted as a head sensitivity. $S_{\mathrm{head}}^{\mathrm{L_{RX}}}$ is however not rigorously equal to $S_{\mathrm{head}}^{\mathrm{M}}$ defined by (3.14). The first makes use of $\check{\boldsymbol{H}}_{\mathrm{L_{TX/RX}}}^{(\mathrm{fs})}$, the field produced by the TX/RX coil for a unit current in the corresponding inductor of the equivalent circuit while the latter makes use $\check{\boldsymbol{H}}_{\mathrm{TX/RX}}^{(\mathrm{fs})}$, the field produced by the TX/RX coil for a unit current in the coil. The difference being related to the current flowing in the capacitor of the equivalent schema. The other difference between $S_{\mathrm{head}}^{\mathrm{L_{RX}}}$ and $S_{\mathrm{head}}^{\mathrm{M}}$ is that the first is used to compute a voltage source $e_{\mathrm{L_{RX}}}$ to be put in the L-branch of the coil equivalent circuit, whereas the second is used to compute the voltage source e_{M} to be put at the input terminal of the coil. Note however that putting a voltage source in the inductor branch or at the input terminal of the coil does not make much difference below the first resonance frequency. The two head sensitivities $S_{\text{head}}^{\text{L}_{\text{RX}}}$ and $S_{\text{head}}^{\text{M}}$ therefore have similar values below the coil first resonance frequency.

3.3.5 Dynamic sensitivity maps

Our objective is to understand the effect of the target dynamics on the target slow-time response. The target slow-time response is defined as the difference between the slow-time signal in presence of the target and that in absence of the target. We recall that the slow-time signal is the integration of the amplifier output in the evaluation window.

According to (3.31), for a conducting or magnetic target, the response is a function of:

- the head geometry and the target location through the term $S_{\text{head}}^{\text{L}_{\text{RX}}}$
- the target dynamics through the term M_{t}
- the time-domain wave form emitted through the term $I_{\text{L}_{\text{TX}}}$

Equation (3.29) yields similar conclusions for an electric target. As our objective here is to assess the effect of the target dynamics on the response, we will set the geometrical factors S_{head} to one. The target slow-time response is then computed as a function of the target gain and time constants by introducing the target models in the simple coil model as explained in Section 3.3.4. This yields the detector *dynamic sensitivity maps* of the Schiebel detector which are illustrated in Fig. 3.7 for simple conducting, magnetic and electric targets. For a better comparison, we have presented the absolute value of the slow-time response. The polarity of the response is however important and will be discussed in the next section. Various types of target should not be compared because the geometric factors have been set to one where in fact, they may have different orders of magnitudes. To get results representative of targets that would give a measurable response, we have chosen, for each target type a maximum gain such that the slow-time response is about 0.5V. We have then used the normalized gains: $\mathsf{K}_{\text{t}} = K_{\text{t}}/K_{\text{t}}^{\max}$ ($K_{\text{t}}^{\max}$ is the same for the conducting and magnetic targets but is different for the electric target).

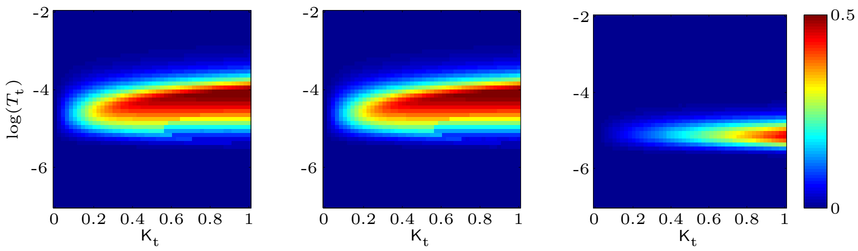

(a) (b) (c)

Figure 3.7: *Absolute value of the time-domain sensitivity maps for a magnetic (a), a conductive (b) and an electric (c) dipole first order target. Gains are normalized.*

One sees that only targets which are neither too slow nor too fast will yield a significant response. Too slow targets are not excited enough during the $4\mu s$ TX pulse and the response of too fast targets has vanished before the evaluation window starts. The peak of sensitivity being around $50\mu s$ for a conducting or magnetic target and around $10\mu s$ for an electric target. One also sees that the magnetic and conducting target have a very similar sensitivity map. This may look surprising because the conducting target has an additional derivative operator and an opposite polarity, compared to the magnetic target. However, both transfer functions are of first order and, therefore, for a given time constant they yield the same exponential decay up to a possible multiplicative factor. One can easily check that the two transfer functions (3.4) and (3.5) yield the same initial value for a step off and therefore the responses are identical for a current step-off. The TX current is in good approximation a step off function and therefore the responses are nearly identical.

The maximum of sensitivity occurs for faster targets for the electric case, compared to the conducting or magnetic cases. This is related to the fact that, in good approximation below the first coil resonance, the electric head sensitivity $S^{\mathrm{E}}_{\mathrm{head}}$ defined by (3.10) has an ω^2 frequency dependence whereas the magnetic sensitivity $S^{\mathrm{M}}_{\mathrm{head}}$ defined by (3.14) is frequency independent. Indeed, below the first resonance frequency of the coil, the electric field emitted by a coil can be approximated by:

$$\check{\boldsymbol{E}}^{(\mathrm{fs})}_{\mathrm{coil}} = j\omega L_{\mathrm{coil}} C_{\mathrm{coil}} \check{\boldsymbol{E}}^{(\mathrm{fs})}_{\mathrm{coil,Q}} \tag{3.33}$$

with $\check{\boldsymbol{E}}^{(\mathrm{fs})}_{\mathrm{coil,Q}}$, the electric field produced by the coil for a unit charge on the capacitor in the equivalent circuit. This last field is frequency independent and $S^{\mathrm{E}}_{\mathrm{head}}$ has thus indeed an ω^2 frequency dependence.

Displaying the sensitivity map as a mesh or looking at 2D cuts (not shown), it appears that the slow-time response increases linearly with the gain for small target gains K_{t}. For larger gains, the target response influences the position of the evaluation window. We will see in the next section that for the conducting and magnetic targets, the response is negative whereas for the electric target, the response is positive. We have seen that the evaluation window starts when the output of the amplifier reaches a given negative threshold. This threshold is reached later for a large negative target. The evaluation thus comes later for a large conducting or a large magnetic target, at a moment where the target response is smaller. Therefore, the slow-time response increases less than linearly with the gain for large conducting and magnetic targets. Similarly, for a large electric target, the evaluation window comes earlier and the slow-time response therefore increases more than linearly.

3.3.6 Polarity of the response

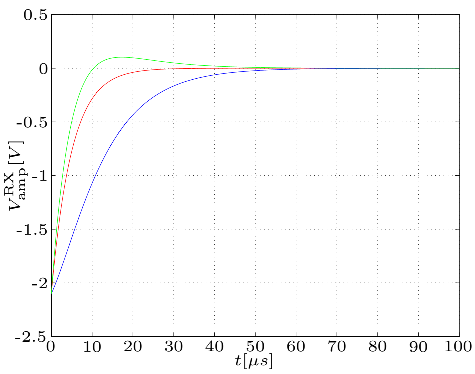

Figure 3.8: *Typical response for a conducting or magnetic (blue) and an electric target (green); both with $T_{\mathrm{t}} = 10\mu s$. Response in absence of target is also shown (red).*

The polarity of the response for different types of targets is an important feature. Indeed if different types of target show a response with opposite polarity, the response polarity might be used to determine the type of target. Typical target responses are shown in Fig. 3.8 for a conducting and an electric target. The response of the magnetic target can be made identical to the response of the conducting target by an appropriate choice of the target gains. It is thus impossible to use the shape of the response to discriminate between a conducting and a magnetic target (at least for the first order targets considered here).

One sees that the polarity of the response is negative for the conducting and the magnetic target and it is positive for the electric target. This is to be compared to the polarity of the voltage pulse in the TX and RX coils which are both negative. In other words, the response of the conductive or magnetic target has the same polarity as the background signal (due to the direct coupling) and the response of the electric target has an opposite polarity. The polarity of the response can thus not be used to distinguish between a conducting and a magnetic target. It might be used to distinguish an electric target but in most modern detectors the response of an electric target is canceled by shielding the coil. The potentiality of using the response polarity for target discrimination thus seems very limited. Discrimination might however be possible by analyzing the time-domain shape of the target response.

To compute the target response in Fig. 3.8, we have assumed that the geometrical factors S_{head} are positive. According to (3.30) this is always true for $S_{\mathrm{head}}^{\mathrm{C_{RX}}}$ because this expression was obtained by considering that both the transmitter and the receiver for the electric target were the RX coil. According to (3.32) this would also be true for $S_{\mathrm{head}}^{\mathrm{L_{RX}}}$ if a head with a single coil is used. Indeed, we then have $\check{\boldsymbol{H}}_{\mathrm{L_{RX}}}^{(\mathrm{fs})} = \check{\boldsymbol{H}}_{\mathrm{L_{TX}}}^{(\mathrm{fs})}$. For the Schiebel detector this is not true and $S_{\mathrm{head}}^{\mathrm{L_{RX}}}$ may be negative. However, at some distance from the detector head, the magnetic field generated by the TX and the RX coil becomes parallel and the $S_{\mathrm{head}}^{\mathrm{L_{RX}}}$ is therefore guaranteed positive[3]. Close to the head, $S_{\mathrm{head}}^{\mathrm{L_{RX}}}$ may be negative and the polarity of the magnetic and electric responses would then be reversed. In Section 4.4.1, the Schiebel head geometrical sensitivity is computed and this shows that there is indeed an area where this sensitivity is negative but this area is small and located very close to the head where targets are never present in practice because the head must always be swept at a certain height above the ground.

[3]With our definition of positive currents and voltages and assuming that the RX and TX coils are wound in the same direction. Should the winding be in opposite direction or the positive voltage convention changed, the polarity of $S_{\mathrm{head}}^{\mathrm{L_{RX}}}$ would change but this is irrelevant because the polarity of the direct coupling would change as well. The polarity of the target should indeed not be considered in absolute terms but as a relative comparison between various target responses and the direct coupling.

Part II

Model of the environment

CHAPTER 4

Soil response

In many applications, the soil can be considered as transparent for a MD. However, in the scope of humanitarian demining, the targets of interest may contain a very limited amount of metal. The soil response may then become significant when compared to the target response and this may affect the performances of a MD. To mitigate this problem high end detectors used in the scope of humanitarian demining include soil compensation functions.

Due to the reduced dimension of coils used in the scope of humanitarian demining, soil conductivity plays little role but the soil magnetic susceptibility may significantly affect the detector, especially if it exhibits a frequency variation. For most soils encountered in practice, even those considered highly magnetic, the magnetic susceptibility remains much smaller than unity. Therefore, the Born approximation can be used and this allows for significant simplifications. Indeed, the soil response can then be expressed as a simple integral on the soil volume of the magnetic susceptibility multiplied with the *head sensitivity*. As a result, realistic scenarios, taking into account the head geometry, the soil inhomogeneities and the soil relief can efficiently be simulated.

Finally, a number of head characteristics: the sensitivity maps, the zero equi-sensitivity surface and the HS response are computed for a number of typical head geometries. We show that those head characteristics can be used to better understand the head behavior and for example its ability to intrinsically compensate the soil response.

Contents

4.1 Introduction

The soil can significantly affect the performances of a MD. This is well-known by the manufacturers who therefore include soil compensation techniques in most high-end MDs. Unfortunately, due to competition among manufacturers, details of those compensation techniques are often proprietary, although some information is available in patents [23].

The effect of the soil has been studied for a long time in the scope of geophysical applications [21, 22]. In those applications, large coils and/or large separation between the TX and RX coils are used and they sense a large soil volume. As a result, the skin depth and the problem characteristic dimensions are of the same order of magnitude and the soil conductivity may play an important role. In contrast, in the scope of mine action, much smaller coils are used and soil conductivity has little effect on the response. This may explain why in most publications in the scope of mine action, the soil was considered transparent until recently. The soil can indeed be considered transparent in the sense that, in general, it does not significantly affect the target response [24, 51, 25, 52, 53]. The soil can however produce an additional response that is mainly due to its magnetic susceptibility. That response is relatively small and may be considered negligible for many applications. However, in the scope of mine action, the metallic content of some mines is getting very small. Low metal mines can still be detected because the detectors have become more and more sensitive. However, when compared to the response of some mines, the soil response can not be neglected anymore. Understanding the soil response then becomes of prime importance because it can be the source of false alarms or require the use of a lower detector sensitivity setting which in turn will reduce the target detectability.

The soil response is influenced by many factors such as the current waveform in the TX coil, the detector head geometry, the coil electrical characteristics, the detector electronics and the soil electromagnetic properties. Some of these factors have been studied [54, 25, 53, 22, 26, 21], but many open questions still remain. For example, in many cases analytical models have been used and, as a result, the analysis was restricted to simple coil arrangements such as concentric circular coils, and to homogeneous soils with a flat air-soil interface. However, the shape and relative position of the coils have a major impact on detector performance which is indicated by the amount of different coil arrangements used in practice [55]. The soil relief and soil inhomogeneities also have a major impact on detector performance.

We show that the soil response can be expressed for general head geometries and for general soil inhomogeneities and reliefs by resorting to a general form of reciprocity and we directly derive that reciprocity expression for the MQS regime relevant to MDs. The resulting expression for the soil response includes the magnetic field produced by the TX coil in the presence of soil. Computing that field for a general soil and for a general head geometry requires the use of computationally intensive numerical methods.

However, several publications [25, 26] suggest that for most soils of interest the response is mainly due to the soil magnetic susceptibility and therefore effects of soil conductivity may be neglected. Furthermore, the magnetic susceptibilities of most natural soils are quite low [56, 8, 57, 58, 48, 59, 49].

In this chapter we show that for such soils, with negligible electric conductivity and low magnetic susceptibility, major simplifications can be achieved by using the Born approximation. This also allows more realistic scenarios to be studied efficiently and the effects of head geometry, soil inhomogeneity and relief on MD performance to be taken into account.

In addition to this general model, a second model based on image theory is developed. That model is only valid for a homogeneous HS but it does not require the Born approximation. It is therefore also valid for soils with high magnetic susceptibilities. The responses predicted by both models are compared with each other and also with available analytical solutions. The comparison shows good agreement between the results and this provides a means of validation for the models and their implementations. Comparing the two models also allows us to establish an expression for the error incurred when using the Born approximation. In the light of susceptibility measurements of many soils found in the literature it appears that, for most soils of interest to mine clearance, the corresponding error is negligible.

The models are developed in the frequency domain. It is then shown that, under reasonable assumptions, the results can efficiently be extended to the time-domain.

The chapter is organized as follows. Section 4.2 describes the problem. Two models to compute the soil response in the frequency domain are presented in Section 4.3.1. The first is valid for arbitrary soil inhomogeneity and relief but relies on the Born approximation whereas the second is only valid for homogeneous HS configurations but does not require the Born approximation. Section 4.3.1.4 compares both models in order to assess the accuracy of the Born approximation. Section 4.3.2 extends the models to apply to the time-domain which is better suited to analyze pulse induction detectors.

Section 4.4 discusses some characteristics that can be derived from the proposed models and that are useful to compare various head geometries. Note that the comparison is based on the soil response alone. This yields useful information but a complete comparison should also take into account the target response. Indeed, a given head might better compensate the soil response than another one, but this is not necessarily beneficial if the target response is also reduced. In this respect, the performances of the electronic soil compensation should also be considered. If it is efficient enough, the head geometry should not be optimized to reduce the soil response but to increase the target sensitivity.

4.2 Problem description

The problem considered is sketched in Fig. 4.1 (a). A MD head is located at an arbitrary position and with an arbitrary orientation above the soil. The head is in general composed of a TX and a RX coil, but a single coil can also be used for both reception and transmission.

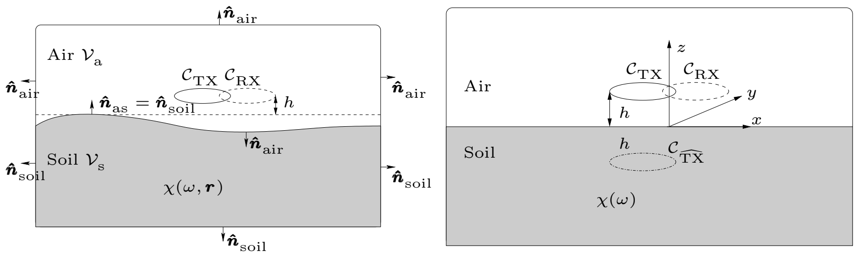

Figure 4.1: *MD composed of TX and RX coils ($\mathcal{C}_{\text{TX}}$ and $\mathcal{C}_{\text{RX}}$) of arbitrary shapes above magnetic soil. (a) general inhomogeneous soil exhibiting some relief and (b) homogeneous HS with $\mathcal{C}_{\widehat{\text{TX}}}$ the mirror image of the TX coil, used to compute the soil response, and h the height of the head above the soil.*

The soil is assumed to be non-conductive and has a magnetic susceptibility varying both with frequency and position. The magnetic susceptibility is denoted $\chi(\omega, \boldsymbol{r})$, with ω the angular frequency and $\boldsymbol{r}$ the position vector.

Consideration of magnetic susceptibility that varies spatially allows us to take into account soils with arbitrary inhomogeneity and relief. In addition, we consider a magnetic susceptibility that varies with frequency because some naturally occurring soils exhibit such behavior [48, 49] and it has been shown [26, 25] that this frequency variation (also known as viscous remnant magnetization, magnetic viscosity, magnetic relaxation or magnetic after-effect) has a significant effect on MDs.

The model can be used for an arbitrary head configuration and Fig. 4.2 presents commonly used [55] head configurations which will be considered in this chapter.

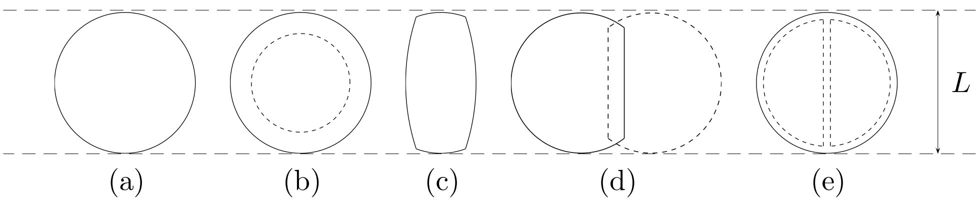

Figure 4.2: *Head configurations considered. TX — and RX - - coils for (a) circular, (b) concentric, (c) elliptic, (d) double-D and (e) quad heads. For circular and elliptic heads, a single coil is used for RX and TX. L is the head characteristic length.*

The coil overlap for the double-D head is chosen to obtain zero coupling between the coils in the absence of soil. The quad coil is composed of two RX half-circles connected in opposition (i.e., the current flows in opposite directions in the two circular segments and in the same direction in the two straight segments).

4.3 Development of soil response models

4.3.1 Soil response in the frequency domain

In this section, we describe the development of a general model valid for arbitrary soil relief and inhomogeneity. We then describe our development of a simpler model that is only applicable to HS homogeneous soils. Both models can be used for a HS configuration and comparing their results allows the accuracy of the Born approximation underlying the general model to be assessed (see Section 4.3.1.4).

4.3.1.1 Assumptions

Since we are considering the case of low conductivity soils and that frequencies used in EMI detectors are less than 100kHz the MQS approximation can be used as discussed in Appendix B.3.

Let us consider a head composed of ideal TX and RX coils. An ideal TX coil is comprised of a single closed-loop made of an infinitely thin wire where the current remains constant because no charge is accumulated due to parasitic capacitance. Under these conditions the current distribution $\boldsymbol{J}_{\mathrm{TX}}$ is fully defined by the closed curve $\mathcal{C}_{\mathrm{TX}}$ corresponding to the shape of the coil and by the current I_{TX} flowing through any cross-section.

Similarly, an ideal RX coil is defined by the closed curve $\mathcal{C}_{\mathrm{RX}}$ and the induced voltage[1] is equal to the derivative of the magnetic flux through a surface $\mathcal{S}_{\mathrm{RX}}$ bound by the contour $\mathcal{C}_{\mathrm{RX}}$:

$$e_{\mathrm{RX}} = j\omega \int_{\mathcal{S}_{\mathrm{RX}}} \boldsymbol{B}_{\mathrm{TX}}^{(\mathrm{as})} \cdot \mathrm{d}\boldsymbol{S} = j\omega \oint_{\mathcal{C}_{\mathrm{RX}}} \boldsymbol{A}_{\mathrm{TX}}^{(\mathrm{as})} \cdot \mathrm{d}\boldsymbol{\ell} \tag{4.1}$$

Where $\boldsymbol{B}_{\mathrm{TX}}^{(\mathrm{as})}$ and $\boldsymbol{A}_{\mathrm{TX}}^{(\mathrm{as})}$ are the magnetic induction and the magnetic vector potential produced by the source current distribution $\boldsymbol{J}_{\mathrm{TX}}$ in the TX coil and the term '(as)' indicates that the environment is composed of air and soil.

In the case of a two-coil head, current may be induced in the RX coil. This current should be considered as part of the TX current $\boldsymbol{J}_{\mathrm{TX}}$. As a result, $\boldsymbol{J}_{\mathrm{TX}}$ should be described by two currents, one flowing on $\mathcal{C}_{\mathrm{TX}}$ and the other on $\mathcal{C}_{\mathrm{RX}}$. This generalization is straightforward and will therefore not be discussed further.

In general, the TX current when the head is in the presence of soil may be different than when it is in free space. We use the TX current in the presence of soil in equation (4.1) and in the rest of this chapter unless explicitly stated. As this current varies with soil properties, sensor height and orientation it should be related to the free space TX current, which can be measured and considered as a detector characteristic. For

[1]the induced voltage is $e = -\oint_{\mathcal{C}_{\mathrm{RX}}} \boldsymbol{E}_{\mathrm{TX}}^{(\mathrm{as})} \cdot \mathrm{d}\boldsymbol{\ell}$. It is related to the electromotive force ξ by $e = -\xi$ and is equal to the voltage that would be measured at the coil open terminal, the voltage direction being such that going from the minus to the plus inside the voltmeter closes the circuit in the direction of the contour $\mathcal{C}_{\mathrm{RX}}$.

most cases this distinction is not critical because the soil response is small and will not significantly change the TX current. The TX current in the presence of soil is further discussed in Appendix D.1.

4.3.1.2 General model

The voltage induced in the RX coil (4.1) includes the following two contributions:

- $e_{\mathrm{RX}}^{\mathrm{TX}}$ resulting from the direct coupling between TX and RX coils
- $e_{\mathrm{RX}}^{\mathrm{soil}} \triangleq e_{\mathrm{RX}} - e_{\mathrm{RX}}^{\mathrm{TX}}$ resulting from the soil response

The direct coupling is often of little interest because it remains constant[2] and it is canceled by the detector electronics. If required, it can be calculated using an expression similar to (4.1):

$$e_{\mathrm{RX}}^{\mathrm{TX}} = j\omega \oint_{\mathcal{C}_{\mathrm{RX}}} \boldsymbol{A}_{\mathrm{TX}}^{(\mathrm{fs})} \cdot \mathrm{d}\boldsymbol{\ell} \tag{4.2}$$

where '(fs)' indicates the free space environment. It can also be expressed as $e_{\mathrm{RX}}^{\mathrm{TX}} = j\omega M_{\mathrm{TX,RX}} I_{\mathrm{TX}}$ where the mutual induction coefficient $M_{\mathrm{TX,RX}}$ between the TX and RX coils can be measured directly. For single coil detectors, the direct coupling becomes $e_{\mathrm{RX}}^{\mathrm{TX}} = j\omega L_{\mathrm{TX}} I_{\mathrm{TX}}$ where L_{TX} is the TX coil self-induction coefficient. For the single coil case, (4.2) can no longer be used because $A_{\mathrm{TX}}^{(\mathrm{fs})}$ becomes infinite on the coil. This singularity is due to the filament assumption and disappears if the current distribution across the coil conductor is taken into account. Nevertheless, measuring L_{TX} is straightforward.

We define the voltage $e_{\mathrm{RX}}^{\mathrm{soil}}$ induced in the RX coil by the soil as the *soil response*. To simplify the notation, it will be denoted V_{soil} given by:

$$V_{\mathrm{soil}} = j\omega \oint_{\mathcal{C}_{\mathrm{RX}}} \boldsymbol{A}_{\mathrm{soil}}^{(\mathrm{fs})} \cdot \mathrm{d}\boldsymbol{\ell} \tag{4.3}$$

with $\boldsymbol{A}_{\mathrm{soil}}^{(\mathrm{fs})} = \boldsymbol{A}_{\mathrm{TX}}^{(\mathrm{as})} - \boldsymbol{A}_{\mathrm{TX}}^{(\mathrm{fs})}$ which can be interpreted as the magnetic vector potential produced by equivalent currents[3] $\boldsymbol{J}_{\mathrm{soil}}$ in the soil volume. Indeed the soil, like any other medium, can be substituted by equivalent

[2] Assuming that the soil does not significantly change I_{TX} (see Appendix D.1)

[3] These currents do not exist physically because the soil was assumed non-conductive.

currents flowing in free space [41, 31]. It should be noted that $\boldsymbol{A}_{\text{soil}}^{(\text{fs})}$ is always finite, making (4.3) valid for single coil detectors.

Equation (4.3) is computationally inefficient because of the requirement to calculate the soil equivalent current distribution and the corresponding vector potential $\boldsymbol{A}_{\text{soil}}^{(\text{fs})}$ which requires an integration on the soil volume. Finally, a line integration on the RX coil must be performed.

A more practical expression can be obtained by the use of reciprocity to relate fields in two configurations (called states). Various reciprocity relations can be found in the literature [31, 41, 35] but the most generic expression, which takes into account different media in both states, is seldom used [42, 43]. As already mentioned, the MQS approximation is valid for the problem at hand and the MQS reciprocity expression C.3.10 developed in Appendix C.3 can then be used. Note that this expressions can also be obtained by introducing[4] the MQS approximations in [43, Equ. 3].

Applying reciprocity (Equ. C.3.10 over $\mathcal{V}_\infty$ (the whole space) with the two following states:

- $\Sigma_{\text{TX}}^{(\text{as})}$ which is the state for which the current I_{TX} flows in the TX coil in presence of soil
- $\Sigma_{\text{RX}}^{(\text{fs})}$ which is the state for which the current I_{RX} flows[5] in the RX coil in absence of soil

yields:

$$\int_{\mathcal{S}_\infty} \left(\boldsymbol{A}_{\text{TX}}^{(\text{as})} \times \boldsymbol{H}_{\text{RX}}^{(\text{fs})} - \boldsymbol{A}_{\text{RX}}^{(\text{fs})} \times \boldsymbol{H}_{\text{TX}}^{(\text{as})}\right) \cdot \mathrm{d}\boldsymbol{S} = \int_{\mathcal{V}_\infty} \Big\{(\mu_{\text{TX}} - \mu_{\text{RX}})\boldsymbol{H}_{\text{TX}}^{(\text{as})} \cdot \boldsymbol{H}_{\text{RX}}^{(\text{fs})} + \boldsymbol{J}_{\text{TX}} \cdot \boldsymbol{A}_{\text{RX}}^{(\text{fs})} - \boldsymbol{J}_{\text{RX}} \cdot \boldsymbol{A}_{\text{TX}}^{(\text{as})}\Big\}\,\mathrm{d}V \quad (4.4)$$

where μ_{TX} and μ_{RX} are the magnetic permeabilities for states $\Sigma_{\text{TX}}^{(\text{as})}$ and $\Sigma_{\text{RX}}^{(\text{fs})}$ respectively.

[4] Replace $\boldsymbol{E}$ by $-j\omega\boldsymbol{A}$, note that there is no electric charge and no magnetic current in this case and take the limit as $\omega \to 0$.

[5] As already mentioned, current may be induced in the RX coil by the TX current. This induced current should not be confused with I_{RX} which is a fictitious current used to apply reciprocity.

The contrast $\mu_{\mathrm{TX}} - \mu_{\mathrm{RX}}$ is zero except in the soil volume $\mathcal{V}_{\mathrm{s}}$ (see Fig. 4.1) where it is equal to $\mu_0\chi$ where χ is the magnetic susceptibility of the soil. The contribution of the sources to the volume integral reduces to the sum of two contour integrals, one on $\mathcal{C}_{\mathrm{TX}}$ and the other on $\mathcal{C}_{\mathrm{RX}}$ because the sources are concentrated on those contours. By considering that the integral on the infinite sphere $\mathcal{S}_\infty$ vanishes according to the far field behavior of fields and potentials, simplifying (4.4) to:

$$\mu_0 \int_{\mathcal{V}_{\mathrm{s}}} \chi \boldsymbol{H}_{\mathrm{TX}}^{(\mathrm{as})} \cdot \boldsymbol{H}_{\mathrm{RX}}^{(\mathrm{fs})} \mathrm{d}V = I_{\mathrm{RX}} \oint_{\mathcal{C}_{\mathrm{RX}}} \boldsymbol{A}_{\mathrm{soil}}^{(\mathrm{fs})} \cdot \mathrm{d}\boldsymbol{\ell} \tag{4.5}$$

where the contour integral on $\mathcal{C}_{\mathrm{TX}}$ was replaced according to:

$$I_{\mathrm{RX}} \oint_{\mathcal{C}_{\mathrm{RX}}} \boldsymbol{A}_{\mathrm{TX}}^{(\mathrm{fs})} \cdot \mathrm{d}\boldsymbol{\ell} = I_{\mathrm{TX}} \oint_{\mathcal{C}_{\mathrm{TX}}} \boldsymbol{A}_{\mathrm{RX}}^{(\mathrm{fs})} \cdot \mathrm{d}\boldsymbol{\ell} \tag{4.6}$$

which is obtained easily by applying reciprocity over the whole space, while considering the states $\Sigma_{\mathrm{TX}}^{(\mathrm{fs})}$ and $\Sigma_{\mathrm{RX}}^{(\mathrm{fs})}$ defined as above, but with the free space environment for both states. Indeed, replacing the air-soil (as) with the free space (fs) environment in (4.4), $\mu_{\mathrm{TX}} = \mu_{\mathrm{RX}}$ and all terms vanish except for the two last terms of the r.h.s.. This yields:

$$\int_{\mathcal{V}_\infty} \boldsymbol{J}_{\mathrm{TX}} \cdot \boldsymbol{A}_{\mathrm{RX}}^{(\mathrm{fs})} \mathrm{d}V = \int_{\mathcal{V}_\infty} \boldsymbol{J}_{\mathrm{RX}} \cdot \boldsymbol{A}_{\mathrm{TX}}^{(\mathrm{fs})} \mathrm{d}V \tag{4.7}$$

which for the infinitely thin coil considered indeed yields (4.6).

With (4.5), (4.3) becomes:

$$V_{\mathrm{soil}} = j\omega\mu_0 I_{\mathrm{TX}} \int_{\mathcal{V}_{\mathrm{s}}} \chi \check{\boldsymbol{H}}_{\mathrm{TX}}^{(\mathrm{as})} \cdot \check{\boldsymbol{H}}_{\mathrm{RX}}^{(\mathrm{fs})} \mathrm{d}V \tag{4.8}$$

with $\check{\boldsymbol{H}}_{\mathrm{coil}}^{(\mathrm{env})} = \boldsymbol{H}_{\mathrm{coil}}^{(\mathrm{env})}/I_{\mathrm{coil}}$ the magnetic field normalized with respect to the corresponding coil current[6]. Similar expressions have been obtained in the framework of nondestructive testing. For example, in [60, Equ. 16b] Auld *et al.* present an expression for the impedance variation $\triangle Z_{12}$ related to the soil response by $V_{\mathrm{soil}} = \triangle Z_{12} I_{\mathrm{TX}}$. This latter expression and (4.8) were obtained following different lines of reasoning and are identical under the MQS approximation, since the electric term appearing in [60, Equ. 16b] is then zero.

[6]The units of $\boldsymbol{H}$ and $\check{\boldsymbol{H}}$ are respectively [A/m] and [1/m].

Recalling that the voltage induced in the RX coil by a magnetic dipole $\boldsymbol{m}$ is [46, Equ. 2.21 p. 23]:

$$V_{\text{dip}} = j\omega\mu_0 \boldsymbol{m} \cdot \check{\boldsymbol{H}}_{\text{RX}}^{(\text{fs})} \tag{4.9}$$

equation (4.8) can be physically interpreted as the sum of contributions by elementary magnetic dipoles:

$$\mathbf{d}\boldsymbol{m} = \chi I_{\text{TX}} \check{\boldsymbol{H}}_{\text{TX}}^{(\text{as})} \text{d}V \tag{4.10}$$

The computation of $\boldsymbol{H}_{\text{TX}}^{(\text{as})}$ for a general soil usually requires numerical techniques which are computationally intensive. However, for low susceptibilities, $\boldsymbol{H}_{\text{TX}}^{(\text{as})}$ can be approximated accurately by $\boldsymbol{H}_{\text{TX}}^{(\text{fs})}$, which is easier to compute. This is the Born approximation[61, Equ. 8.10.1 p. 485] [60, Section 2.3.1.2]. In [62] the Born approximation is also used in the scope of landmine detection to compute the response of a dielectric mine. The accuracy of the Born approximation can be evaluated for simple configurations, such as a homogeneous HS, for which an analytical solution exist. This approximation is further discussed in Section 4.3.1.4 and it is shown to be quite accurate for most soils of interest.

Replacing $\check{\boldsymbol{H}}_{\text{TX}}^{(\text{as})}$ by $\check{\boldsymbol{H}}_{\text{TX}}^{(\text{fs})}$ in (4.8) yields for the soil response:

$$V_{\text{soil}} = j\omega\mu_0 I_{\text{TX}} \int_{\mathcal{V}_{\text{s}}} \chi S \text{d}V \tag{4.11}$$

where

$$S = \check{\boldsymbol{H}}_{\text{TX}}^{(\text{fs})} \cdot \check{\boldsymbol{H}}_{\text{RX}}^{(\text{fs})} \tag{4.12}$$

is defined as the sensitivity of the head. The concept of sensitivity map was first introduced in [63] to characterize the response of a MD to a small sphere. According to (4.11), it is also useful to compute the soil response. In [63], sensitivity maps were computed for rectangular coil arrangements. In Section 4.4.1 we present results for more complex heads.

Note that, the head sensitivity (4.12) is identical to that encountered in Section 3.3 to compute the response of a small conducting or magnetic target. Actually, two different expressions (3.14) and (3.32) were obtained. The first is used to compute a voltage source e_{M} to be put at the input terminal of the coil, whereas the second is used to compute the voltage source $e_{\text{L}_{\text{RX}}}$ to be put in the L-branch of the coil equivalent circuit. For the ideal coil considered in this Chapter, no coil parasitic capacitance is considered and the two expressions are then identical. A more accurate coil model can however be easily considered to compute the soil response as we did in Section 3.3 for the target response. $S_{\mathrm{head}}^{\mathrm{L_{RX}}}$ defined by (3.32) is then more convenient because it is frequency independent, while $S_{\mathrm{head}}^{\mathrm{M}}$ defined by (3.14) is not.

In (4.12), only free space magnetic fields appear; for an arbitrary coil geometry $\mathcal{C}_{\mathrm{coil}}$, they can be computed by means of the Biot-Savart law [31, Equ. 13 p. 230 and Equ. 11 p. 232]:

$$\check{\boldsymbol{H}}_{\mathrm{coil}}^{(\mathrm{fs})}(\boldsymbol{r}) = \frac{1}{4\pi}\int_{\mathcal{C}_{\mathrm{coil}}} \frac{\hat{\boldsymbol{\ell}}' \times \boldsymbol{R}}{R^3}\mathrm{d}\ell' \tag{4.13}$$

where $\mathcal{C}_{\mathrm{coil}}$ is the contour representing the coil, $\boldsymbol{r}$ a field point, $\boldsymbol{r}'$ a source point, $\boldsymbol{R} = \boldsymbol{r} - \boldsymbol{r}'$ is the vector joining a source point to a field point, $R = \|\boldsymbol{R}\|$ is the magnitude of $\boldsymbol{R}$ and $\hat{\boldsymbol{\ell}}'$ is the unit tangent to $\mathcal{C}_{\mathrm{coil}}$ at $\boldsymbol{r}'$. The coils considered in this chapter (see Fig. 4.2) and most coils used in practice are composed of circles, circular arcs and line segments. For such coils, the magnetic $\check{\boldsymbol{H}}_{\mathrm{coil}}^{(\mathrm{fs})}$ can be computed analytically [64]. This is quite a significant advantage because the magnetic fields must be computed for a large number of points to compute (4.11) accurately.

4.3.1.3 HS model

Analytical solutions for concentric circular coils above a homogeneous HS are well known [24]. In general, they require the computation of Sommerfeld integrals. Simpler solutions may be used under the MQS approximation. They can be obtained from the general solution as in [51]. In this section, we show that the same expression as in [51] can be obtained directly by using the image theory. Furthermore, this approach provides a better physical interpretation of the results and can be generalized to arbitrary head configurations.

The image theory is often presented [65, Section 2.14][35, Section 3.4] as a method to solve electro-static problems. Nevertheless, it is easily transposed to the MQS framework.

The configuration considered is sketched in Fig. 4.1 (b). The field in the upper HS is the sum of the field produced by the TX coil in absence of soil and the field scattered by the soil. According to image theory, the soil contribution is assumed equal to the field produced by a fictitious current $\alpha_{\mathrm{s}} I_{\mathrm{TX}}$ flowing through the image coil $\mathcal{C}_{\widehat{\mathrm{TX}}}$, this current being the mirror image of the TX coil through the air-soil interface and radiating in free space:

$$\boldsymbol{H}^{(\mathrm{as})}_{\mathrm{TX}}(\boldsymbol{r}_{\mathrm{air}}) = I_{\mathrm{TX}}\check{\boldsymbol{H}}^{(\mathrm{fs})}_{\mathrm{TX}} + \alpha_{\mathrm{s}} I_{\mathrm{TX}}\check{\boldsymbol{H}}^{(\mathrm{fs})}_{\widehat{\mathrm{TX}}} \tag{4.14}$$

where the argument $\boldsymbol{r}_{\mathrm{air}}$ has been introduced to emphasize the fact that the expression is only valid in the upper HS. Similarly, we assume that the field in the lower HS is equal to the one produced by a current $\alpha_{\mathrm{t}} I_{\mathrm{TX}}$ flowing in the TX coil $\mathcal{C}_{\mathrm{TX}}$ and radiating in infinite soil:

$$\boldsymbol{H}^{(\mathrm{as})}_{\mathrm{TX}}(\boldsymbol{r}_{\mathrm{soil}}) = \alpha_{\mathrm{t}} I_{\mathrm{TX}}\check{\boldsymbol{H}}^{(\mathrm{fs})}_{\mathrm{TX}} \tag{4.15}$$

where the argument $\boldsymbol{r}_{\mathrm{soil}}$ denotes that the expression is only valid in the lower HS. We replaced the normalized magnetic field $\check{\boldsymbol{H}}^{(\mathrm{soil})}_{\mathrm{TX}}$ produced by the TX current in an infinite space filled with soil by $\check{\boldsymbol{H}}^{(\mathrm{fs})}_{\mathrm{TX}}$, since both quantities are equal[7]. The fields appearing in (4.14) and (4.15) can be computed easily by means of the Biot-Savart law (4.13) because all equivalent currents are radiating in free space.

The coefficients are solved for by applying interface conditions (continuity of the tangential component of $\boldsymbol{H}$) and by resorting to the symmetry relations (D.2.6). This yields:

$$\alpha_{\mathrm{t}} = \frac{2\mu_0}{\mu_0 + \mu_{\mathrm{s}}} = \frac{2}{2+\chi} \tag{4.16a}$$

$$\alpha_{\mathrm{s}} = \frac{\mu_{\mathrm{s}} - \mu_0}{\mu_{\mathrm{s}} + \mu_0} = \frac{\chi}{2+\chi} \tag{4.16b}$$

with $\mu_{\mathrm{s}} = \mu_0(1+\chi)$ the soil magnetic permeability.

In Section 4.3.1.2, the soil response is defined as the additional voltage induced by the field scattered by the soil. Therefore, according to (4.14), it is equal to the voltage induced in the RX coil by a current $\alpha_{\mathrm{s}} I_{\mathrm{TX}}$ flowing through the mirrored TX coil, both coils being in free space. This voltage can be expressed as:

$$V_{\mathrm{HS}} = j\omega\alpha_{\mathrm{s}} I_{\mathrm{TX}} M_{\widehat{\mathrm{TX}},\mathrm{RX}} \tag{4.17}$$

where $M_{\widehat{\mathrm{TX}},\mathrm{RX}}$, the mutual induction coefficient between the RX coil and the mirrored TX coil, can be expressed as:

$$M_{\widehat{\mathrm{TX}},\mathrm{RX}} = \int_{\mathcal{C}_{\mathrm{RX}}} \check{\boldsymbol{A}}^{(\mathrm{fs})}_{\widehat{\mathrm{TX}}} \cdot \mathrm{d}\boldsymbol{\ell} \tag{4.18}$$

[7] For a homogeneous full-space, the equations governing the magnetic field are $\nabla \times \boldsymbol{H} = 0$ and $\nabla \cdot \boldsymbol{H} = 0$ which are independent of the medium permeability.

where $\breve{\boldsymbol{A}}^{(\mathrm{fs})}_{\widehat{\mathrm{TX}}} = \boldsymbol{A}^{(\mathrm{fs})}_{\widehat{\mathrm{TX}}}/I_{\mathrm{TX}}$, the magnetic vector potential produced by the mirrored TX coil and normalized by the corresponding current, is related to its source [31, Equ. 8 p. 231] by the following expression:

$$\breve{\boldsymbol{A}}^{(\mathrm{fs})}_{\widehat{\mathrm{TX}}}(\boldsymbol{r}) = \frac{\mu_0}{4\pi} \int_{\mathcal{C}_{\widehat{\mathrm{TX}}}} \frac{1}{R} \mathrm{d}\boldsymbol{\ell}' \tag{4.19}$$

with $\mathrm{d}\boldsymbol{\ell}'$ the unit tangent to $\mathcal{C}_{\widehat{\mathrm{TX}}}$ at the source point and R the distance between source and field points. For coils composed of circles, circular arcs and line segments, the magnetic potential $\breve{\boldsymbol{A}}^{(\mathrm{fs})}_{\widehat{\mathrm{TX}}}$ can be computed analytically [64]. In addition, for coaxial circular coils, (2.3) can be used to directly compute the mutual induction coefficient. Substitution of (2.3) into (4.17) yields an expression for the soil response that is identical to [51, Equ. 10]. However, our approach is more general and can be applied to other head configurations.

4.3.1.4 Accuracy of the general model for HS soils

The expression for a general soil response (4.11) was obtained under the Born approximation, which assumes that the soil does not significantly change the TX field ($\boldsymbol{H}^{(\mathrm{as})}_{\mathrm{TX}} \simeq \boldsymbol{H}^{(\mathrm{fs})}_{\mathrm{TX}}$). Such an assumption was not required to develop the HS model expression (4.17). Since both expressions can be used for a HS soil, the comparison of the results allows us to quantify the accuracy of the general expression (4.11) for that specific configuration.

As shown in Appendix D.2, the mutual induction coefficient appearing in (4.17) can be expressed as a volume integral on the soil volume (D.2.9). Furthermore, for a homogeneous HS, the magnetic susceptibility may be moved outside the integral (4.11). As a consequence, both approaches yield a similar expression for a uniform HS soil:

$$V^{\mathrm{i}}_{\mathrm{HS}} = \beta_{\mathrm{i}} j\omega\mu_0 I_{\mathrm{TX}} \int_{\mathcal{V}_{\mathrm{LHS}}} S \mathrm{d}V \tag{4.20}$$

where $\mathcal{V}_{\mathrm{LHS}}$ is the lower HS volume $z < 0$, 'i = g' and 'i = HS' respectively for the general and HS model. According to (4.11) $\beta_{\mathrm{g}} = \chi$ while according to (4.17) and (D.2.9) $\beta_{\mathrm{HS}} = 2\chi/(2+\chi)$.

The relative error due to the Born approximation is thus:

$$\left|\frac{\beta_{\mathrm{HS}} - \beta_{\mathrm{g}}}{\beta_{\mathrm{HS}}}\right| = \frac{|\chi|}{2} \tag{4.21}$$

In [66], soils are classified according to their magnetic susceptibility as neutral, moderate, severe, and very severe depending on their effect on MDs used in the framework of mine clearance. Very severe soils have susceptibilities above 0.02. Many soils of interest indeed have susceptibilities below 0.02, as confirmed by many measurement campaigns [56, 8, 57, 58, 48, 59, 49]. A noticeable exception is Playa Gorgana in Panama, which is rich in pure magnetite and for which susceptibilities close to 1 have been measured [48]. For a very severe soil with a magnetic susceptibility of 0.02, the relative error is 0.01, which shows that the approximation is expected to be quite good for most soils of interest in the framework of mine clearance.

4.3.2 Soil response in the time-domain

The time-domain response can be obtained from the frequency domain response by Fourier transform. This requires one to compute the spectral representation $I^{\omega}_{\mathrm{TX}}(\omega) = \mathcal{F}\{I^{\mathrm{t}}_{\mathrm{TX}}(t)\}$ of the time-domain TX current $I^{\mathrm{t}}_{\mathrm{TX}}(t)$ and to repeat the computation of the soil response (4.11) for a number of frequencies within the detector bandwidth.

The soil magnetic susceptibility is mainly due to ferrite minerals—magnetite and maghaemite—and the susceptibility frequency variation is dictated by the size and shape distribution of the magnetic domains of those ferrite minerals at sub-microscopic level [26]. It is expected that for some soils, this distribution remains identical everywhere in the soil and that only the overall concentration of ferrite changes.

When this assumption is applicable, the frequency dependence of the soil magnetic susceptibility is independent of the position, and a simpler and more efficient approach is possible. The magnetic susceptibility can be separated into a position-dependent factor and a frequency-dependent factor: $\chi(\boldsymbol{r},\omega) = \chi^{\mathrm{r}}(\boldsymbol{r})\chi^{\omega}(\omega)$. Furthermore the frequency-dependent factor can be moved out of the integral (4.11) to yield:

$$V^{\mathrm{t}}_{\mathrm{soil}}(t) = v_0(t)\int_{\mathcal{V}_{\mathrm{s}}} \chi^{\mathrm{r}} S \,\mathrm{d}V \tag{4.22}$$

with $V^{\mathrm{t}}_{\mathrm{soil}}(t)$ the time-domain soil response,

$$v_0(t) = \mathcal{F}^{-1}\{j\omega\mu_0 I^{\omega}_{\mathrm{TX}}(\omega)\chi^{\omega}(\omega)\} = \mu_0 \frac{\mathrm{d}I^{\mathrm{t}}_{\mathrm{TX}}(t)}{\mathrm{d}t} \otimes \chi^{\mathrm{t}}(t)$$

where $\otimes$ denotes a convolution and $\chi^{\mathrm{t}}(t) = \mathcal{F}^{-1}\{\chi^{\omega}(\omega)\}$ is the normalized impulse response of the magnetic material present in the soil[8].

Expression (4.22) has a form similar to its frequency-domain counterpart (4.11). It shows that $v_0(t)$ completely defines the shape of the time-domain response $V^{\mathrm{t}}_{\mathrm{soil}}(t)$, only influenced by the shape of the TX current $I^{\mathrm{t}}_{\mathrm{TX}}(t)$ and by the signature of the magnetic material $\chi^{\omega}(\omega)$ present in the soil. Hence, if χ is a separable function of space and frequency, the shape of the time-domain response is independent of soil relief, concentration of magnetic material $\chi^{\mathrm{r}}(\boldsymbol{r})$, head position and orientation. Those parameters only affect the magnitude of the response.

With those numerical optimizations, the sensitivity mesh corresponding to a given head is computed in a few minutes on a standard desktop computer and the response of an arbitrary soil can then be computed in a few seconds.

4.3.3 Implementation validation

The HS response can be computed using the general expression (4.11) or the simpler expression (4.17) valid only for a HS configuration. According to (4.20), $V^{\mathrm{g}}_{\mathrm{HS}}/\chi$ and $V^{\mathrm{HS}}_{\mathrm{HS}}(2+\chi)/\chi$ are independent of χ and should be equal.

Both expressions are computed using two different numerical algorithms. Indeed, according to (4.11), the general expression requires a volume integral on the soil volume, whereas according to (4.17), the HS expression requires a line integral on the RX coil. Comparing both results yields a cross-check and an indication on the accuracy of the numerical algorithms.

Furthermore, the general expression involves the magnetic fields produced by the coils while the HS expression involves the magnetic vector potential produced by the coils. Both are computed using the analytical solution for straight and circular segments. Comparing both solutions also yields a validation of the analytical expressions used and of their implementations.

To quantify the difference between the two results, the relative error:

$$\epsilon = \left| \frac{\mathsf{V}^{\mathrm{HS}}_{\mathrm{HS}}(2+\chi) - \mathsf{V}^{\mathrm{g}}_{\mathrm{HS}}}{\mathsf{V}^{\mathrm{HS}}_{\mathrm{HS}}(2+\chi)} \right| \tag{4.23}$$

is used.

[8] The unit of $\chi^{\mathrm{t}}(t)$ and $v_0(t)$ are respectively $[\mathrm{s}^{-1}]$ and [V/m].

It is worth emphasizing that this error, independent of χ, is used to cross-check the numerical implementations and cannot be used to assess the accuracy of the Born approximation. For this, (4.21), which does not require any numerical computation, should be used instead.

The χ-normalized response computed with both models, together with the corresponding error (ϵ), is presented in Table 4.1 for various heads and for a normalized head height $\mathsf{h} = 0.05$.

	$\frac{\mathsf{V}_{\mathrm{HS}}^{\mathrm{HS}}(2+\chi)}{\chi}$	$\frac{\mathsf{V}_{\mathrm{HS}}^{\mathrm{g}}}{\chi}$	ϵ
Circular	0.4285	0.4285	0
Concentric	0.2113	0.2112	0.0005
Elliptic	0.2716	0.2717	0.0001
Double-D	-0.0007	-0.0007	0.0035
Quad	0	0	na

Table 4.1: *χ-normalized dimensionless HS response computed with general ($\mathsf{V}_{\mathrm{HS}}^{\mathrm{g}}$) and HS ($\mathsf{V}_{\mathrm{HS}}^{\mathrm{HS}}$) expressions together with corresponding relative error (ϵ) for normalized head height* $\mathsf{h} = 0.05$.

To avoid any dependence on the frequency, on the TX current or on the head dimension L, the dimensionless soil response:

$$\mathsf{V}_{\mathrm{HS}} = V_{\mathrm{HS}}/(j\omega\mu_0 L I_{\mathrm{TX}}) \tag{4.24}$$

is used. It is easy to check by appropriate changes of variables in the integrals (4.11) and (4.13) that V_{HS} is indeed independent of the head dimension L.

In the case of a quad detector, the error ϵ cannot be computed because the corresponding HS response is null. For other heads, the error is quite small, which yields a good check of the numerical implementations. However, the error is the biggest for the double-D detector because the HS response is small due to a significant compensation between the positive and negative contributions in the integral (4.11). Such a compensation between large positive and negative contributions requires both contributions to be computed with a high accuracy in order to reach a small relative error.

For the concentric head, an additional validation has been performed by comparing $\mathsf{V}_{\mathrm{HS}}^{\mathrm{HS}}$ based on a numerical integration (4.18) and on the analytical solution (2.3) to calculate the mutual induction coefficient.

The relative error was better than 10^{-15}, which provides a good validation of the implementation of (4.18).

4.4 Head characteristics

The general model (4.11) allows one to efficiently compute the response of magnetic soils with low susceptibility with arbitrary relief and inhomogeneity, for an arbitrary head shape in an arbitrary position and orientation above the soil. The soil response is obtained as a weighted sum of the soil susceptibility and the head sensitivity. Hence, visualizing the sensitivity map allows to better understand the head behavior. This will be discussed in Section 4.4.1.

The head sensitivity may change sign; it is in general positive far away from the head but it may be negative in a region close to the head. This sign change is at the origin of an intrinsic soil compensation for some heads and visualizing the zero sensitivity surface helps us to understand the compensation mechanism. This will be discussed in Section 4.4.2.

Another important characteristic that can be derived from the head sensitivity is the volume of influence. As this is a very important concept that requires a careful definition and a number of additional developments, we will devote Chapter 5 to this concept.

The intrinsic head compensation can also be assessed for a homogeneous and flat soil by computing the HS response. This will be discussed in Section 4.4.3 for a number of typical head geometries. Note that a real soil may significantly differ from an HS; showing significant relief and inhomogeneities. Conclusions obtained from HS should thus be used with care in practice. The model developed provides the right tool to compare the heads for more realistic soils. Such an analysis was not addressed in the scope of this thesis but we see this as a very promising path for further research. One could for example compare various heads for a sinusoidal soil relief or for a sinusoidal soil inhomogeneity. This would then highlight the kind of inhomogeneities or relief to which each head is the most sensitive.

4.4.1 Sensitivity maps

The sensitivity map of a head is obtained by using (4.12) to compute the sensitivity at various locations. This is illustrated in Figs. 4.3 and 4.4

were vertical and horizontal cuts of the sensitivity are shown for the head geometries presented in Fig. 4.2. For both cuts, the projections of the TX (—) and RX (– –) coils are drawn and the depths of the horizontal cuts are indicated in Fig. 4.3 by dot-dashed lines (– · –). For the vertical cuts, the absolute value of the sensitivity is represented in dB to capture the large dynamic range resulting from the very fast decrease of the sensitivity with depth. For the horizontal cuts, a linear scale is used and the sensitivity is first divided by a factor α to allow a common colormap to be used for all cuts. This factor is indicated above the cut and also represented graphically by the size of the horizontal bar appearing at the top of the images.

To obtain results that are valid for any head dimensions, normalized quantities are used. Horizontal (x,y) and vertical (z) dimensions as well as the head height (h) are normalized with respect to the head characteristic length L (see Fig. 4.2). The normalized quantities are denoted x, y, z and h respectively. In addition, the normalized sensitivity $\mathsf{S} = SL^2$ is presented. All those normalized quantities are dimensionless and one can easily check by appropriate change of variables in the integrals (4.12) and (4.13) that S is indeed independent of the head characteristic length L. The normalized head height used is $\mathsf{h} = 0.05$.

The sensitivity map allows us to better understand the head behavior. For example, for the double-D head it allows to visualize the soil response compensation mechanism. Indeed, the sensitivity is integrated over the soil volume and the negative and positive parts of the volume compensate each other to produce a smaller signal in the receiver. The sensitivity is negative in a volume, shaped as two connected washbowls, close to the head and positive elsewhere. The positive and negative volumes are directly apparent in Figs. 4.4 and 4.5. On the contrary, in Fig. 4.3, the sign of the sensitivity is not seen directly because, in order to capture the large dynamic, the absolute value of the sensitivity is represented using a logarithmic scale. However, the positive and negative volumes can be deduced from the sign reversal contour on which very strong negative values induced by the logarithmic scale appear. For clarity reasons, this contour has further been superimposed on the figures. The zero sensitivity surface is also represented in Fig. 4.6 (b).

According to (4.17), the compensation of a uniform HS response is perfect if the distance between the mirrored TX coil and the RX coil is equal to the distance between the TX and RX coils[9]. This only occurs at

[9]If, as we assumed, the coil overlap has been chosen to ensure a zero coupling

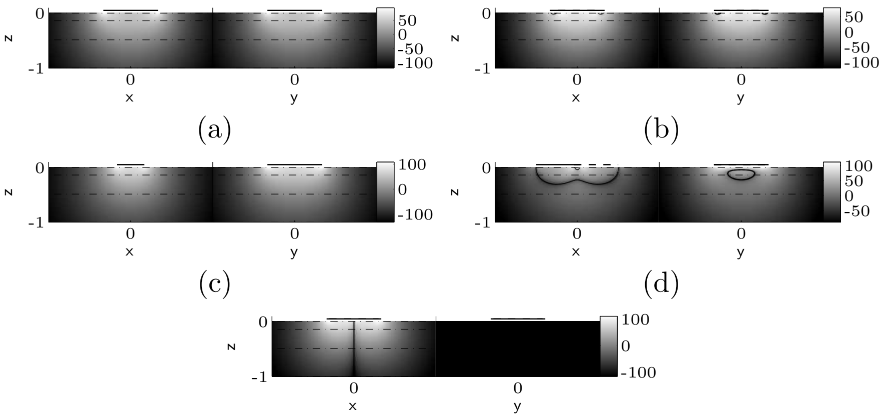

Figure 4.3: *Vertical XZ (left) and YZ (right) cuts of normalized absolute sensitivity ($|\mathsf{S}|$) in dB at* $\mathsf{h} = 0.05$ *for (a) circular, (b) concentric (c) elliptic, (d) quad (e) double-D heads. TX (—) and RX (– –) coils, depths of horizontal cuts ($- \cdot -$) as well as zero sensitivity contour (—) are also shown.*

a unique height. For other head heights, the soil response is still significantly attenuated but the compensation is not perfect. The sensitivity map also shows that the volume in which the sensitivity is negative is relatively small and exhibits high sensitivity values. Therefore, the soil properties in that volume have a strong impact on the soil response. The compensation is significantly reduced for a soil exhibiting a strong inhomogeneity or a large hole in the negative sensitivity volume.

4.4.2 Zero sensitivity surface

As already discussed, the sign of the sensitivity can change and the volume of negative sensitivity can cause a total or partial compensation of the soil response. Therefore, visualizing the zero sensitivity surface helps us to understand the compensation mechanism.

For single coil heads, according to (4.12), the sensitivity is always positive and there is no zero sensitivity surface. For the quad head, by symmetry, the zero sensitivity surface is the yz plane. The zero sensitivity for the other heads (concentric and double-D) are presented

between the coils in free space

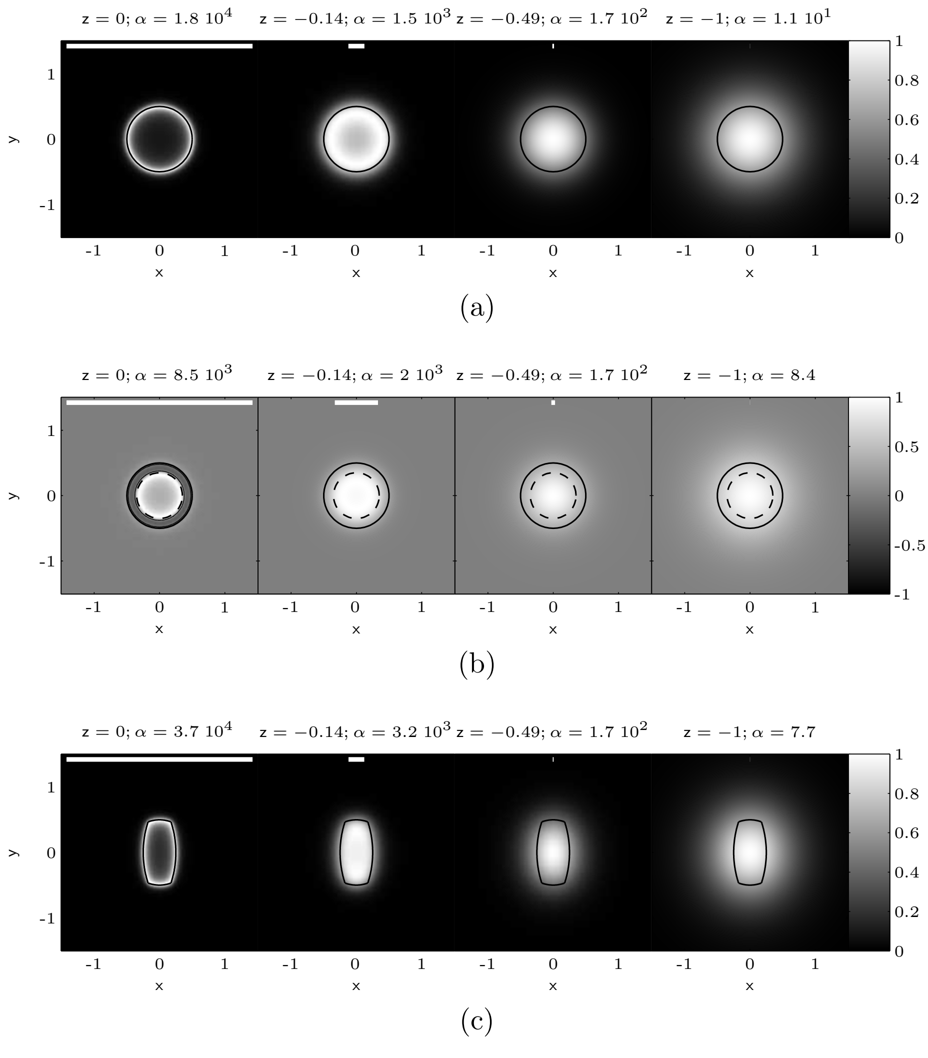

Figure 4.4: *Horizontal XY cuts of normalized sensitivity (S) at $\mathsf{h} = 0.05$ for (a) circular, (b) concentric (c) elliptic. Sensitivity scaling factor (α) and cut depth (z) are indicated above each cut. α is further represented by length of horizontal bar above in the image. TX (—) and RX (– –) coils as well as zero sensitivity contour (—) are shown.*

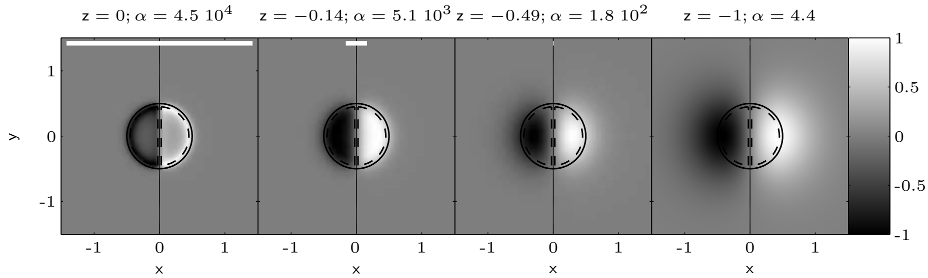

(d)

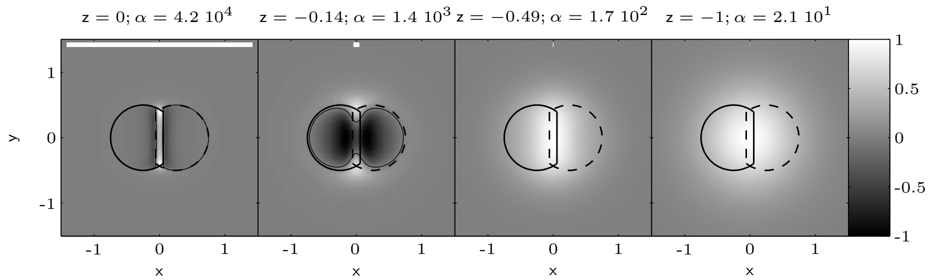

(e)

Figure 4.5: *Horizontal XY cuts of normalized sensitivity (S) at $\mathsf{h} = 0.05$ for (d) quad (e) double-D heads. Sensitivity scaling factor (α) and cut depth (z) are indicated above each cut. α is further represented by length of horizontal bar above in the image. TX (—) and RX (– –) coils as well as zero sensitivity contour (—) are shown.*

in Fig. 4.6.

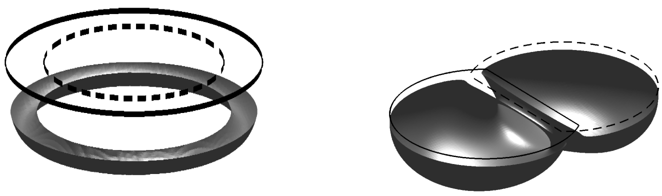

(a) (b)

Figure 4.6: *Zero sensitivity for (a) concentric and (b) double-D head. TX (—) and RX (- -) coils are shown.*

For the concentric head, the zero sensitivity surface looks like a circular gutter while, for the double-D head, it looks like two connected washbowls. For both heads, the negative sensitivity volume is rather small and, in that volume, the magnitude of the sensitivity is large. Therefore, holes or inhomogeneities in the negative sensitivity volume may significantly affect the soil compensation. This effect is most critical for the double-D head which exhibits a very good intrinsic compensation for homogeneous and flat soils.

4.4.3 HS response

The HS response has been computed for a number of typical head geometries and for a typical normalized head height $\mathsf{h} = 0.05$ in Section 4.3.3. The result are shown in Table 4.1.

One sees that the HS response is null for the quad head, as expected, due to the anti-symmetry of the head. Apart from the quad head, the double-D head has a much smaller response than the other heads. As discussed in Section 4.4.1, for the double-D head, the response is null only for a reference height different from the height used in Table 4.1.

Obviously, the height of the head has a strong impact on the HS response. This is illustrated in Fig. 4.7. The observations made above for $\mathsf{h} = 0.05$ remain valid for other heights. In addition, it is apparent that the response increases much more severely when the head approaches the soil for single coil heads than for double coil heads. This might be one of the reasons for which separate TX and RX coils are used in some PI detectors.

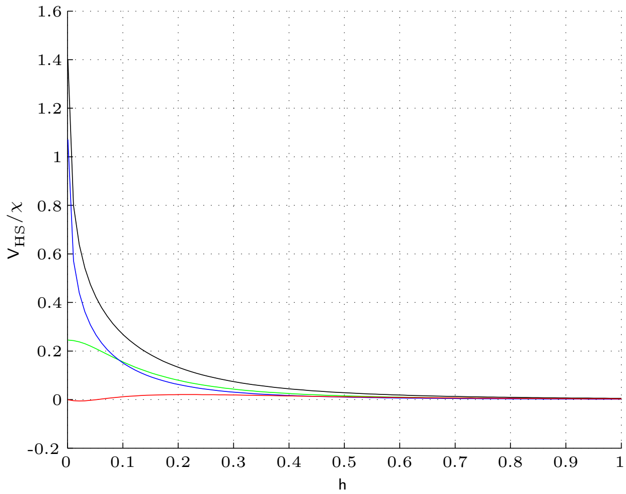

Figure 4.7: *χ-normalized dimensionless HS response $\mathsf{V}_{\mathrm{HS}}/\chi$ as a function of normalized height h for circular (black), concentric (green), elliptic (blue), double-D (red) heads. The response for the quad head is not shown as it is null for all heights.*

This behavior can easily be understood by resorting to (4.17) which indicates that the half space response is related to the coupling between the RX coil and the mirror of the TX coil. For a single coil and a small height, those coils become very close to each other and the coupling becomes quite large. At the limit, when the head touches the ground, the coupling becomes infinite. This singularity is due to the filamentary coil model used which is not appropriate for very small height for which the current distribution in the coil must be taken into account.

One sees that for the quad-head, the compensation is perfect for a uniform HS, whatever the height. This is not the case for the double-D head for which the compensation is perfect only for a single height. Here also the coil coupling interpretation (4.17) can be used to understand this behavior.

CHAPTER 5

Volume of influence

The concept of *volume of influence* allows to better understand the response of a magnetic soil to an electromagnetic induction sensor, as well as the effect of soil inhomogeneity on soil compensation. The concept sounds intuitive but we show that a simple definition has some drawback and we propose a rigorous and general definition.

The volume of influence is first defined as the volume producing a fraction α of the total response of a homogeneous HS. As this basic definition is not appropriate for sensor heads with intrinsic soil compensation, a generalized definition is then proposed. These definitions still do not yield a unique *volume of influence* and a constraint must be introduced to reach uniqueness. Two constraints are investigated: one yielding the *smallest volume of influence* and the other one the *layer of influence*. Those two specific *volumes of influence* have a number of practical applications which are discussed. The effect of soil inhomogeneity is also investigated, leading to the definition of a worst-case *volume of influence* for inhomogeneous soils.

The *smallest volume of influence* is illustrated for typical head geometries and we prove that, apart from differential heads such as the quad head, the shape of the *smallest volume of influence* is independent of the head geometry and can be computed from the far-field approximation. In addition, quantitative head characteristics are provided and show –among others– that double-D heads allow for a good soil compensation, assuming however approximate homogeneity over a larger volume of soil.

Contents

5.1 Introduction

Electromagnetic Induction (EMI) sensors are widely used in many applications such as mine clearance [1], treasure hunting [2] or geophysical and archaeological survey [3]. The soil can produce a significant response: either a signal of interest or clutter to be rejected. In all cases, it is useful to assess the VoI, i.e., the soil volume producing most of the soil response. If the soil response is the signal of interest, as in geophysical or archaeological surveys, the knowledge of the VoI allows the assessment of the soil volume that can be investigated by the sensor. In mine action, the soil response is considered as clutter and the VoI can be used to objectively define the soil volume to characterize in order to model the soil response. In the same context, some detector heads are designed to compensate the soil response. This design is usually optimized for a homogeneous and flat soil (also called a homogeneous HS) and the VoI enables the estimation of the soil volume that should be homogeneous for the compensation to be effective. In the same context again, when test lanes are built to evaluate EMI sensors for specific soils, the VoI allows the objective determination of the depth to which the original soil must be removed and replaced by the specific test soils.

The concept of VoI is not entirely new. It is for example discussed in [67] for capacitive probes. However, to the best knowledge of the author, it has never been rigorously defined and quantified for EMI detectors. As shown in Chapter 4, for such detectors, significant simplifications are possible to compute the soil response. As a result, the simple concept of VoI can be extended to take into account the effect of soil inhomogeneities. At first sight, the concept of VoI looks intuitive. However, to get an accurate and quantitative definition, what is called above 'most of the soil response' must be quantified. It seems natural to consider a homogeneous HS and to define the VoI as the volume producing a fraction of the total HS response. However this basic definition raises several issues. First, some heads are designed to compensate the soil response and the total HS response will then be close to zero. In that case, an arbitrary small volume fulfills the basic definition, which is clearly inappropriate. Indeed, even for such heads, the soil in an extended volume influences the response, which becomes apparent when soil inhomogeneity is present. We will therefore propose a generalized definition for the VoI which can be used even for heads with intrinsic soil compensation. For such heads, the new definition enables the determination of the soil volume that should be homogeneous for the compensation to be optimum. A second issue with the basic and intuitive definition of the VoI is that the corresponding volume is not unique. It is for example possible to find a soil layer (see Fig. 5.1 (b)) that fulfills the definition by increasing the depth of that layer until the required ratio of the HS response is reached. The resulting volume will be called the *Layer of Influence*. It is also possible to find a volume that fulfills the basic definition of the VoI by increasing the radius of a half-sphere (see Fig. 5.1 (a)) or by expanding any other shape of interest. Hence the shape of the VoI can be chosen arbitrarily and the size that yields a response equal to the chosen ratio of the total response can then be unequivocally computed. Imposing the shape of the VoI is a constraint that can be used to render the VoI unique. Other constraints can also be used. For example, imposing that the VoI be the *smallest possible*. This leads to the *smallest VoI*. As they are well suited for a number of practical applications, we will study in more detail two specific VoIs: the *smallest VoI* and the *Layer of Influence*.

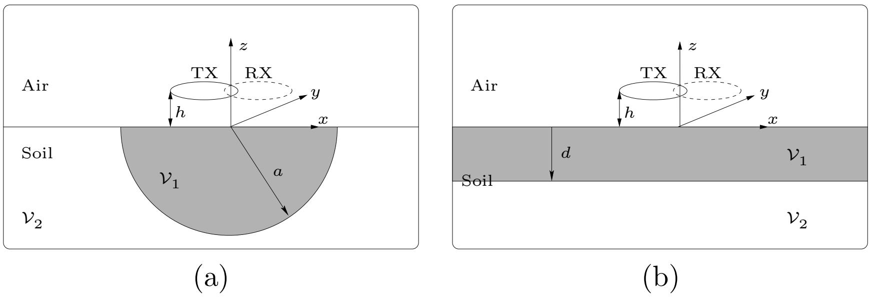

Figure 5.1: *Two shapes that may be used to define VoI (a) sphere of radius a and (b) layer of depth d leading respectively to the half-sphere of influence and to the* layer of influence. *TX (—) and RX (– –) coils are shown. h is the head height above the soil.*

The choice of the response ratio α is guided by the accuracy required for a given application. However, considering only homogeneous soils is a severe limitation for many applications. We will therefore consider a class of soil inhomogeneities and show that a worst-case VoI can be obtained by computing the VoI for a homogeneous soil, but considering an increased ratio α.

As explained above, to determine the VoI, the response of a soil volume with arbitrary shape needs to be computed, taking into account the geometry of the head (shape, size and relative position of the TX and RX coils). Analytic solutions are limited to elementary configurations such as a circular concentric head above a HS [54, 25, 22, 26, 21] and cannot be used to compute the VoI in the general case. Using generic numerical software would be computationally intensive because estimating the VoI requires computing the response of many volumes. Fortunately, the magnetic susceptibility dominates the response of most soils and their electric conductivity may be neglected[1] [25, 26]. Furthermore, the soil magnetic susceptibility is often quite small [56, 8, 57, 58, 48, 59, 49]. We will therefore restrict ourselves to those soils for which the solution presented in Chapter 4 can be used and it provides an efficient means to compute the response of an arbitrary soil volume, with arbitrary inhomogeneities, for an EMI sensor with arbitrary head geometry. This solution expresses the soil response as an integral on the soil volume of the product of head sensitivity and magnetic susceptibility. We will show that with this solution, the shape and extent of the VoI can be efficiently computed for the head geometries used in practice. This will be illustrated for the commonly used head geometries [55] presented in Fig. 4.2.

The remainder of this chapter is organized as follows. Section 5.2 defines the VoI: first the basic definition in Section 5.2.1 then the generalized definition in Section 5.2.2. Section 5.2.3 discusses the constraint that must be introduced in order to make the VoI unique and presents two examples: one yielding the *smallest VoI* and the other one the *layer of influence*. Section 5.2.4 describes how a worst-case VoI may be defined by taking the expected soil inhomogeneity into account and Section 5.2.5 discusses a number of practical applications for the *smallest VoI* and the *layer of influence*. Section 5.3 discusses the shape of the *smallest VoI* and Section 5.4 presents numerical results.

5.2 Definitions of the VoI

We first simply and intuitively define the VoI for a uniform HS. The definition is then extended and the effect of inhomogeneities is discussed. In addition, to obtain a unique VoI, a constraint must be introduced. Two constraints are discussed, yielding two specific volumes of influence:

[1] Conductivity may have a significant effect only for very conductive soils, such as beaches saturated with sea water, or for large coils, when the coil size is of the order of the skin depth.

the *smallest VoI* and the *layer of influence*.

5.2.1 Basic definition

At a given position of the sensor head, the VoI ($\mathcal{V}_{\text{inf}}^{\alpha}$) — where 'inf' stands for 'influence' — is defined as the volume producing a fraction α of the total soil response V_{HS} for an uniform HS. The fraction α is chosen according to the application and the expected inhomogeneities, as will be explained in Section 5.2.4.

For the soils with negligible conductivity and low magnetic susceptibility which are commonly encountered and considered in this chapter, the response of an arbitrary region $\mathcal{V}_{\text{reg}}$ of a homogeneous HS can be expressed using (4.11). This yields:

$$V_{\text{reg}} = j\omega\mu_0 I_{\text{TX}}\chi \int_{\mathcal{V}_{\text{reg}}} S \, \mathrm{d}V \tag{5.1}$$

The volume $\mathcal{V}_{\text{inf}}^{\alpha}$ can then be found by searching for a volume $\mathcal{V}_{\text{reg}}$ for which the response is:

$$V_{\text{reg}} = \alpha V_{\text{HS}} \tag{5.2}$$

where V_{HS}, the HS response, could be computed using (5.1), which unfortunately requires integration over a large volume. Alternatively, for a HS, it is more efficient to use (4.17). For the small susceptibilities of interest, this yields:

$$V_{\text{HS}} = j\omega\frac{\chi}{2} I_{\text{TX}} M_{\widehat{\text{TX}},\text{RX}} \tag{5.3}$$

where χ is the soil susceptibility, I_{TX} the current in the transmit coil and $M_{\widehat{\text{TX}},\text{RX}}$ the mutual induction coefficient between the RX coil and the mirrored TX coil ($\widehat{\text{TX}}$).

According to (5.1) and (5.3), the fraction $V_{\text{reg}}/V_{\text{HS}}$ is independent[2] of ω, χ and I_{TX}. Therefore, the VoI is only a function of the detector head geometry, position and orientation above the soil. In most cases, the head is kept horizontally above the ground during the scanning. Restricting ourselves to such a configuration, for a given head shape, the VoI is only a function of the head characteristic length L (see Fig. 4.2)

[2]At frequencies used by EMI sensors and in soils with negligible conductivity, the MQS approximation holds and the magnetic field (4.13) appearing in (4.12) is independent of the frequency.

and of the head height above the soil h (see Fig. 5.1). One easily checks that two configurations are in electromagnetic similitude if the dimensionless height $\mathsf{h} = h/L$ is kept constant. Therefore, the shape of the VoI and its dimensionless size (size normalized with characteristic length L) do not depend on the head dimension, they only depend on the shape and the dimensionless height h of the head above the ground.

5.2.2 Generalized definition

For single-coil heads, according to (4.12), the sensitivity is always positive and the basic definition of the VoI is appropriate. However, for two-coils heads, the sensitivity sign may change. This sign reversal leads to total or partial soil compensation inherent to some head geometries. For a differential head, such as the quad head presented in Fig. 4.2 (e), the soil compensation is perfect for a homogeneous HS and the corresponding soil response is zero. Therefore, an arbitrary small volume obeys the basic definition of the VoI, which is obviously not acceptable.

To avoid this pitfall, we note that the total soil response is

$$V = |V_+| - |V_-| \tag{5.4}$$

where V_+ (V_-) is the contribution of the soil volume $\mathcal{V}_+$ ($\mathcal{V}_-$) for which the sensitivity (4.12) is positive (negative). If V_- is not negligible compared to V_+, both soil volumes $\mathcal{V}_-$ and $\mathcal{V}_+$ significantly influence the total response. To isolate the two contributions, we consider a Half-Space with Holes (HSH) which is a specific kind of inhomogeneity. A HSH is defined as a soil of which the susceptibility only takes one of two values at each location: an arbitrary but constant value χ or zero. If the HSH is such that the susceptibility is χ inside $\mathcal{V}_+$ and zero outside, the total response is $V = V_+$. Similarly, the total response will be V_- for an HSH defined on $\mathcal{V}_-$. Applying the basic definitions on those two HSHs, one gets the positive and negative volumes of influence. The positive VoI ($V^{\alpha}_{\mathrm{inf},+}$) is defined as the part of $\mathcal{V}_+$ for which:

$$V^{\alpha}_{\mathrm{inf},+} = \alpha V_+ \tag{5.5}$$

and the negative VoI is similarly defined by replacing '+' by '-' in (5.5). As already mentioned, both $\mathcal{V}_+$ and $\mathcal{V}_-$ may significantly contribute to the total response. We therefore define the VoI as the union of the positive and negative volumes of influence:

$$\mathcal{V}^{\alpha}_{\mathrm{inf}} = \mathcal{V}^{\alpha}_{\mathrm{inf},+} \cup \mathcal{V}^{\alpha}_{\mathrm{inf},-} \tag{5.6}$$

For heads with intrinsic soil compensation, this generalized definition is also appropriate to assess the volume of soil that should be homogeneous for an efficient compensation. This is discussed in more details in Section 5.2.4. In addition, for single-coil heads, $\mathcal{V}_-$ is empty and the generalized definition is identical to the basic definition presented in Section 5.2.1.

As is apparent from Fig. 4.6 and as will be further discussed in Section 5.3, $\mathcal{V}_-$ is usually a small volume close to the head while $\mathcal{V}_+$ is a large volume extending towards infinity. Therefore, it is advantageous to calculate V_+ according to

$$V_+ = V_{\text{HS}} - V_- \tag{5.7}$$

where V_{HS} and V_- are computed according to (5.3) and (5.1) respectively.

In the above discussion, we assumed that the sensitivity is positive far away from the head. This is always possible for the co-planar coils considered in this chapter if the two coils have a non-vanishing dipolar moment. Indeed for such coils, the dipolar moments are parallel and (D.3.10) can then be applied to compute the far field sensitivity[3]. From this expression, it is apparent that the sensitivity does not change sign in the far field. It can therefore be made positive by an appropriate choice of the positive coil currents I_{TX} and I_{RX}, which is a question of convention. Indeed changing the positive direction for one of the coil currents changes the sign of the sensitivity everywhere. Apart from the RX coil of the quad head, all coils presented in Fig. 4.2 have non-vanishing dipolar moments and the positive coil current was chosen to ensure that the sensitivity is positive far away from the head. For the quad-head, the positive direction of the coil currents is not important as the head symmetry imposes positive and negative volumes with identical shape and size.

5.2.3 Introduction of constraints

There exists an infinity of volumes which satisfy the definition of the VoI. It is for example possible to generate a soil layer (see Fig. 5.1 (b))

[3]We define the far field as the region in which the field can be approximated by a dipole field (the first term of a multipole expansion). It should not be confused with the far-field approximation commonly used at higher frequencies and for which the field decreases as $1/R$ and can be characterized by a radiation pattern (see 5.3.2 for more details).

that fulfills the basic definition by increasing the depth of that layer until the required ratio of the HS response is reached. It is also possible to generate a volume that fulfills the basic definition by increasing the radius of a half-sphere (see Fig. 5.1 (a)) or by expanding any other shape of interest. As will be shown, for the general definition, a similar but slightly more complex procedure can be adopted to find the extent of the VoI for an arbitrary generating shape. Hence, to get a unique VoI, a constraint must be introduced. Imposing the shape of the VoI is a possible solution; imposing that the VoI should be the smallest possible is another one.

5.2.3.1 Shape defined VoIs

We now show how an arbitrary generating shape can be used to define a specific VoI satisfying the generalized definition given in Section 5.2.2. To indicate that the VoI considered is shape defined, it will be denoted $\mathcal{V}^{\alpha}_{\text{inf\_shape}}$. According to the definition, the VoI is the union of a positive and a negative VoI. The positive VoI must only include soil regions where the sensitivity is positive. Such a 'positive' volume can easily be obtained, keeping the idea of expanding a generating shape, by taking the intersection of the resulting volume with the soil volume in which the sensitivity is positive.

Formally speaking, starting from a shape-defined volume $\mathcal{V}^{\beta}_{\text{shape}}$, in which the subscript 'shape' is a placeholder for the chosen shape and the superscript β defines the size of the volume, the above mentioned 'positive' volume is defined by:

$$\mathcal{V}^{\beta}_{\text{shape},+} = \mathcal{V}^{\beta}_{\text{shape}} \cap \mathcal{V}_{+} \tag{5.8}$$

where $\mathcal{V}_{+}$ is the part of the lower HS in which the sensitivity is positive. The corresponding positive VoI ($\mathcal{V}^{\alpha}_{\text{inf\_shape},+}$) can then be computed for a given response ratio α, according to the general definition (5.5), by computing the response $V^{\beta}_{\text{shape},+}$ of the volume $\mathcal{V}^{\beta}_{\text{shape},+}$ as a function of the size β and finding the value of β for which $V^{\beta}_{\text{shape},+} = \alpha V_{+}$.

Note that for a given shape and response ratio α, β always exists and is unique. Indeed, by construction, the volume $\mathcal{V}^{\beta}_{\text{shape},+}$ grows from zero to $\mathcal{V}_{+}$ and the sensitivity is positive everywhere inside $\mathcal{V}^{\beta}_{\text{shape},+}$. Therefore, the response $V^{\beta}_{\text{shape},+}$ is a monotonic function increasing from zero to V_{+} as β varies from 0 to ∞, and the value of the parameter β for which $V^{\beta}_{\text{shape},+} = \alpha V_{+}$ always exists and is unique.

The negative VoI ($\mathcal{V}^{\alpha}_{\text{inf\_shape},-}$) can be found similarly and is also unique. Therefore, a unique shape defined VoI ($\mathcal{V}^{\alpha}_{\text{inf\_shape}}$) is obtained as the union of the positive and the negative VoIs:

$$\mathcal{V}^{\alpha}_{\text{inf\_shape}} = \mathcal{V}^{\beta}_{\text{shape},+} \cup \mathcal{V}^{\beta}_{\text{shape},-} \tag{5.9}$$

An example of shape-defined VoI is the *layer of influence* which is obtained by using as generating volume ($\mathcal{V}^{\beta}_{\text{shape}}$) a layer of soil extending from the surface to a given depth d. This is illustrated in Fig. 5.2 for a double-D head and for a response ratio $\alpha = 0.95$. The parameter β is then the depth d and the corresponding values for the positive and negative *layers of influence* are called the positive and negative *depth of influence* and they are denoted d_+ and d_-. Note that the *layer of influence*, which is the union of the positive and the negative layers of influence is not a full layer; some holes are apparent (in white on the figure). To understand the origin of those holes, note that the sensitivity is positive in the dark gray region and negative elsewhere in the lower HS. Hence, the sensitivity is negative in the region appearing in white which is therefore not part of the positive layer of influence. This white area is further below d_- and is therefore also not part of the negative *layer of influence*; it forms a hole in the layer of influence. This hole is however small (and will become smaller for larger values of α) and considering the hole as part of the VoI does not significantly enlarge the VoI. This is acceptable for most applications and the *layer of influence* can then efficiently be visualized as a full layer extending from the surface to a depth d_+. This parameter d_+ can then be used to fully characterize the VoI and will be called the *depth of influence*.

We have shown that holes may appear in a shape-defined VoI and that therefore, rigorously speaking, its shape differs from that of the generating volume $\mathcal{V}^{\beta}_{\text{shape}}$. However, we saw that for the previous example, those holes may be ignored for most applications. This is expected to remain the case for most heads and for most VoIs. Indeed, $\mathcal{V}_-$ (the volume where the sensitivity is negative) is in general a small volume located close to the head whereas $\mathcal{V}_+$ extends towards infinity. It is therefore $\mathcal{V}_+$ which contributes the most to the VoI, especially for a large response ratio α, and using $\mathcal{V}_-$ instead of the negative VoI only yields a small enlargement the VoI. When this is done, the holes disappear, the shape of the of VoI becomes identical to that of the generating volume and the VoI can efficiently be characterized by a single parameter β_+ obtained by searching for the positive VoI.

Figure 5.2: Layer of influence *for the double-D head and for a response ratio* $\alpha = 0.95$. *Vertical cut through the center of the head is illustrated and shows the projection of TX (—) and RX (– –) coils, the border of generating volume (– · –), the positive (dark gray) and negative (light gray) layer of influence with corresponding positive and negative* depths of influence d_+ *and* d_-. *The holes in the* layer of influence *appear in white.*

5.2.3.2 Smallest VoIs

As already mentioned, another constraint that can be used to get a unique VoI is to impose that the VoI be the smallest possible. This constraint can be translated into a constraint similar to that of the shape-defined VoIs discussed above because the *smallest VoI* can be shown to be bound by an equi-sensitivity surface. It can therefore be computed as described above using the volume bound by an equi-sensitivity surface $\mathcal{V}^{\beta}_{\text{equi}}$ (with β the corresponding sensitivity) for $\mathcal{V}^{\beta}_{\text{shape}}$. The only difference is that by changing the parameter β, it is not only the size, but also the shape of the volume, that changes.

To prove that the *smallest VoI* is bound by an an equi-sensitivity surface, we now show that any other volume of the same size has a smaller response. This other volume can be constructed from $\mathcal{V}^{\beta}_{\text{equi}}$ by removing a part of it and adding a volume (of the same size as the removed part) outside $\mathcal{V}^{\beta}_{\text{equi}}$. By construction, the sensitivity is everywhere smaller in the added volume than in the removed part and the resulting response is smaller, which concludes the proof.

5.2.4 Effect of soil inhomogeneity

5.2.4.1 Effect on the VoI

Once a shape is chosen, the procedure described in Section 5.2.3 can still be used to compute the VoI in presence of any soil inhomogeneity. The only difference with the case of a homogeneous soil is that the space-dependent susceptibility must be used in the integral (5.1) to compute the response of the parametric volume. We have shown in Section 5.2.3 that for a homogeneous soil, the *smallest VoI* is bound by an equi-sensitivity surface. The proof can be extended to an inhomogeneous soil by using the product $S\chi$ instead of S in the reasoning. Hence, for an inhomogeneous soil, the *smallest VoI* is bound by a surface for which the product of sensitivity with magnetic susceptibility ($S\chi$) is constant. This being said, except for very specific applications, the precise soil inhomogeneity is unknown and defining a representative inhomogeneity may be difficult. Using a worst-case approach is then a possible alternative.

For this, let us consider an inhomogeneous soil for which the susceptibility is unknown and varies arbitrarily over the volume but we assume that it remains in the range $[\chi_{\min}, \chi_{\max} = \rho\chi_{\min}]$ where ρ is defined as the inhomogeneity ratio and let us analyze the effect of this inhomogeneity on the positive VoI (the results are identical for the negative VoI). The positive VoI is then the volume $\mathcal{V}^{\beta}_{\text{shape},+}$ (defined by the parameter β) for which the response in presence of the worst inhomogeneity $V^{\beta,\text{i}}_{\text{shape},+}$ is related to the response of the (positive) HS V^{i}_{+} in presence of the same inhomogeneity by $V^{\beta,\text{i}}_{\text{shape},+} = \alpha^{\text{i}} V^{\text{i}}_{+}$. The superscript 'i' indicates that the worst inhomogeneity is considered. The worst inhomogeneity corresponds to the susceptibility distribution (in the range $[\chi_{\min}, \chi_{\max}]$) for which the (positive) VoI is the largest for a given α^{i}. Equivalently, the worst inhomogeneity can be defined for a given volume $\mathcal{V}^{\beta}_{\text{shape},+}$ defined by β as that yielding the smallest α^{i}. For a given β, the fraction α^{i} will be the smallest if the soil susceptibilities are $\chi_{\min}$ and $\chi_{\max}$, respectively inside and outside the volume $\mathcal{V}^{\beta}_{\text{shape},+}$. The corresponding fraction α^{i} is then given by

$$\alpha^{\text{i}} = \frac{V^{\beta,\text{i}}_{\text{shape},+}}{V^{\text{i}}_{+}} = \frac{V^{\beta}_{\text{shape},+}}{V^{\beta}_{\text{shape},+} + \rho V^{\beta}_{\text{out},+}} \tag{5.10}$$

where $V^{\beta}_{\text{shape},+}$ and $V^{\beta}_{\text{out},+}$ are the responses respectively of a soil volume $\mathcal{V}^{\beta}_{\text{shape},+}$ and of a soil volume $\mathcal{V}^{\beta}_{\text{out},+} = \mathcal{V}_{+} \setminus \mathcal{V}^{\beta}_{\text{shape},+}$ (points in $\mathcal{V}_{+}$ but not in $\mathcal{V}^{\beta}_{\text{shape},+}$)with a uniform susceptibility $\chi_{\min}$ (the term $\rho V^{\beta}_{\text{out},+}$ appearing in the denominator is then the response of a soil volume $\mathcal{V}^{\beta}_{\text{out},+} = \mathcal{V}_{+} \setminus \mathcal{V}^{\beta}_{\text{shape},+}$ with a uniform susceptibility $\chi_{\max}$ as required).

Equation (5.10) could be used directly to determine the (positive) VoI by computing α^{i} as a function of β in order to determine the value of β corresponding to the chosen response ratio α^{i}. A more convenient approach is to first cast the chosen response ratio α^{i} into a response ratio α that would be obtained with the searched for VoI in presence of a homogeneous HS. The routine developed for the homogeneous case can then be used to determine the VoI in presence of inhomogeneities but using the computed α. To find the relation between α and α^{i}, we note that for a volume $\mathcal{V}^{\beta}_{\mathrm{shape},+}$, the fraction α that would be obtained for a homogeneous HS can be computed by using[4] $\rho = 1$ in (5.10). It is then apparent that the searched for relation is:

$$\alpha = \frac{\alpha^{\mathrm{i}}\rho}{1 - \alpha^{\mathrm{i}} + \alpha^{\mathrm{i}}\rho} \tag{5.11}$$

The latter expression shows that, for a given inhomogeneity ratio ρ, the VoI can be computed as in the homogeneous case, but α must now be computed from the chosen response ratio α^{i}. For example, if the VoI is defined as the volume producing 99% of the total response ($\alpha^{\mathrm{i}} = 0.99$) and if the soil susceptibility is assumed to be, at most, ten times bigger outside the VoI than inside ($\rho = 10$), then the corrected fraction is $\alpha = 0.999$, yielding as expected a larger VoI in the presence of the worst inhomogeneity.

5.2.4.2 Effect on soil compensation

Soil inhomogeneities also have an effect on the intrinsic head compensation. A motivation for defining the VoI as the union of the positive and negative volumes of influence (5.6) is that, with that definition and if the real soil is homogeneous inside the VoI, the compensation should be nearly as good as for a homogeneous HS. This statement is rather intuitive and it is clear that strong inhomogeneities outside the VoI may strongly affect the soil compensation, even if the soil is homogeneous inside the VoI. To quantify the effect of inhomogeneities outside the VoI[5]

[4] the susceptibility of the homogeneous HS needs not to be specified because it factors out from the expression of α.

[5] Soil relief can be seen as a specific soil inhomogeneity, but as the air-soil interface is close to the head, the corresponding inhomogeneity will in general be located inside the VoI. Hence, the approach presented in this section can not be used to assess the effect of soil relief. Other methods should be developed for this purpose. See Section 8.2.

(computed assuming a uniform soil) on the compensation, we define the compensation ratio as:

$$\gamma^{\mathrm{i}} = \frac{|V_-^{\mathrm{i}}|}{V_+^{\mathrm{i}}} \tag{5.12}$$

where again the superscript 'i' denotes the worst inhomogeneity, i.e. in this case, yielding the worst compensation (γ^{i} minimum). We assume[6] and therefore $V_+^{\mathrm{i}} \geqslant |V_-^{\mathrm{i}}|$, the compensation ratio ranges from zero (no compensation) to 100% (perfect compensation). Let us start from a VoI defined for a homogeneous HS and yielding a response ratio α. We then consider inhomogeneities outside the VoI, keeping the soil susceptibility constant ($\chi = \chi_{\mathrm{in}}$) inside the VoI, and we assume that the susceptibility outside the VoI varies between $\chi_{\mathrm{min}} = \rho_{\mathrm{min}}\chi_{\mathrm{in}}$ and $\chi_{\mathrm{max}} = \rho_{\mathrm{max}}\chi_{\mathrm{in}}$. The worst inhomogeneity occurs then when $\chi = \chi_{\mathrm{min}}$ in $\mathcal{V}_- \setminus \mathcal{V}_{\mathrm{inf},-}^{\alpha}$ and $\chi = \chi_{\mathrm{max}}$ in $\mathcal{V}_+ \setminus \mathcal{V}_{\mathrm{inf},+}^{\alpha}$. Indeed, in this case V_-^{i} is minimum and V_+^{i} is maximum, yielding the minimum compensation ratio. The responses V_-^{i} and V_+^{i} occurring under the worst inhomogeneity are then related to their homogeneous counterparts by:

$$V_+^{\mathrm{i}} = \alpha V_+ + \rho_{\mathrm{max}}(1-\alpha)V_+ \tag{5.13a}$$

$$V_-^{\mathrm{i}} = \alpha V_- + \rho_{\mathrm{min}}(1-\alpha)V_- \tag{5.13b}$$

with V_+ and V_- the response of the volumes $\mathcal{V}_+$ and $\mathcal{V}_-$ for a homogeneous HS with susceptibility χ_{in}. The compensation ratio can then be expressed as:

$$\gamma^{\mathrm{i}} = \frac{(\alpha + \rho_{\mathrm{min}}(1-\alpha))}{(\alpha + \rho_{\mathrm{max}}(1-\alpha))} \frac{|V_-|}{V_+} \tag{5.14}$$

Defining the corresponding compensation ratio for a homogeneous soil as $\gamma = |V_-|/V_+$, the degradation of the compensation due to the worst-case inhomogeneity can be quantified by the degradation factor $\delta = \gamma^{\mathrm{i}}/\gamma$ which according to (5.14) can be expressed as:

$$\delta = \frac{\alpha + (1-\alpha)\rho_{\mathrm{min}}}{\alpha + (1-\alpha)\rho_{\mathrm{max}}} \tag{5.15}$$

Inverting this expression yields

$$\alpha = \frac{\rho_{\mathrm{min}} - \delta\rho_{\mathrm{max}}}{\rho_{\mathrm{min}} - 1 + \delta - \delta\rho_{\mathrm{max}}} \tag{5.16}$$

[6] The results can be transposed to the case $V_+^{\mathrm{i}} \leqslant |V_-^{\mathrm{i}}|$ by interchanging V_+^{i} and $|V_-^{\mathrm{i}}|$, with similar conclusions.

which can be used to translate a requirement on the efficiency of the soil compensation in the presence of soil inhomogeneities (δ) into a response ratio α from which the VoI can be determined. For example, if $\rho_{\text{min}} = 0.1$, $\rho_{\text{max}} = 10$ and if we require that $\delta = 0.99$, then one must use the VoI corresponding to $\alpha = 0.999$. In other words, if the soil is homogeneous in the VoI defined by $\alpha = 0.999$ and if outside that volume, the susceptibility ranges from one tenth to ten times the susceptibility inside the VoI, the compensation will be degraded by one percent in the worst case.

5.2.5 Smallest VoI and layer of influence

The *smallest VoI* and the *layer of influence* are two specific VoIs that were defined in Section 5.2.3. They are quite useful in a number of practical applications:

- the *smallest VoI* is useful to define the soil volume to be characterized in order to model the soil response *at a given location.* Indeed, by definition, measuring the magnetic susceptibility distribution inside any VoI allows the calculation of the response with an accuracy that depends on the response fraction α. This fraction may further be modified to take into account the expected soil inhomogeneity according to (5.11). By choosing the *smallest VoI*, this calculation requires the minimum number of soil samples. Sampling the *layer of influence* also allows the calculation of the soil response with the same accuracy but requires more soil sample measurements because the *layer of influence* is a much larger volume.

  The *smallest VoI* is also useful to visualize the volume that should be homogeneous to achieve a good compensation. The response ratio α should then be computed according to (5.16). Requiring that the *layer of influence* be homogeneous would yield the same result but this is a much more stringent requirement, since the *layer of influence* is a much larger volume than the *smallest VoI.*

- the *layer of influence* is useful to define the soil volume to be characterized in order to model the soil response *for all points of the scanning plane* with an accuracy that depends on the fraction α and on the expected soil inhomogeneity. Indeed, following the same reasoning as above for the *smallest VoI*, the required accuracy is reached for the head location used to calculate the *layer* *of influence*. In addition, by symmetry, the result is valid for all points of the scanning plane[7]. Note that it is also appropriate to sample the soil in the volume defined as the union of the smallest VoIs (or the union of any other VoIs), one for each point of the scanning plane, but the resulting volume is larger. As will be confirmed in Figs. 5.6 and 5.7, the depth of the *smallest VoI* (L_{z}, see Fig. 5.3) is indeed larger than the *depth of influence* (d).

The *layer of influence* is also useful to build a test lane. It can then be used to objectively define the *depth of influence* to which the native soil should be replaced by a soil of interest in order for the underlying native soil to have an influence negligible up to a given tolerance. The expected native and test soil susceptibilities should then be used in (5.11) to compute the *depth of influence*. Again, considering the union of other VoIs would also be appropriate but this would require to replace the native soil with the soil of interest to a depth L_{z} which is larger than the *depth of influence*, hence demanding more work than necessary.

5.3 Shape of the smallest volume of influence

Analyzing the shape of the *smallest VoI* may enable a better understanding of the head behavior. Therefore we present in this section the shape of representative volumes of influence for various heads and fractions α. It is interesting to note that for large values of α, the shape of most volumes of influence becomes similar. This is discussed in Section 5.3.2 in the light of the far-field approximation[8].

5.3.1 Exact shape

Fig. 5.3 presents the *smallest VoI* for a double-D head and a fraction α of 0.5, 0.90 and 0.99 together with the *smallest VoI* bounding box. The dimensions of the bounding box along the axes are denoted by L_{x}, L_{y} and L_{z}. In all cases, the dimensionless head height above the soil h amounts to 0.05 and the soil is assumed to be a homogeneous HS.

[7] For a general inhomogeneity, the *layer of influence* may depend on the location of the head. However, with the worst-case approach considered in Section 5.2.4, the *layer of influence* remains indeed the same for all point of the scanning plane.

[8] Recall that we define the far field as the region in which the field can be approximated by a dipole. It should not be confused with the far-field approximation commonly used at higher frequencies (see 5.3.2 for more details).

The positive VoI is plotted in gray and the negative one in white. The shape for $\alpha = 0.5$ is the most complex one and may appear difficult to visualize in 3D. The positive volume looks like a twin washbowl with a hole in the bottom and the negative volume looks like two thin plates partly covering the washbowl. Note that the negative VoI is close to the head and small compared to the positive VoI. For large values of α, the *smallest VoI* has a similar shape for all heads considered in this chapter, except for the quad head. This is illustrated in Fig. 5.4 and a theoretical justification is presented in Section 5.3.2. Note that for large values of α and except for some small holes which are irrelevant in practice, the *smallest VoI* is bounded by the air-soil interface and by an approximate ellipsoid denoted $\mathcal{S}^{\alpha}_{\text{inf,out}}$.

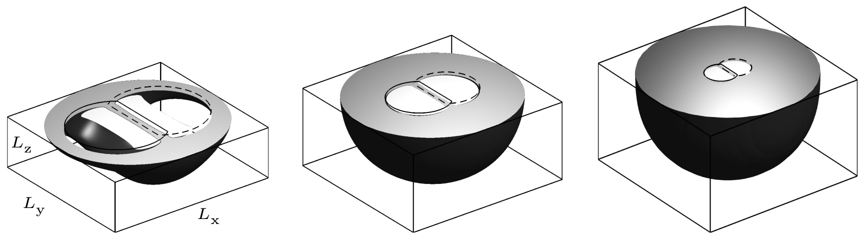

(a) (b) (c)

Figure 5.3: *Smallest VoI and corresponding bounding box for the double-D head with dimensionless height* $\mathsf{h} = 0.05$. *(a)* $\alpha = 0.5$, *(b)* $\alpha = 0.90$ *and (c)* $\alpha = 0.99$. L_x, L_y *and* L_z *are the dimensions of the bounding box along the corresponding axes.*

5.3.2 Approximate shape

The surface $\mathcal{S}^{\alpha}_{\text{inf,out}}$ is far away from the detector. Therefore, on that surface, the field can be approximated by the first term of a multipole expansion. We call this the far-field approximation, although it must not be confused with the far-field approximation commonly used at higher frequencies and for which the field decreases as $1/R$ and can be characterized by a radiation pattern. For horizontal coils with a dipolar term, Appendix D.3 develops the expression of the far-field sensitivity. According to (D.3.10), a far-field equi-sensitivity surface is given by:

$$R = K(1 + 3\cos^2\theta)^{\frac{1}{6}} \tag{5.17}$$

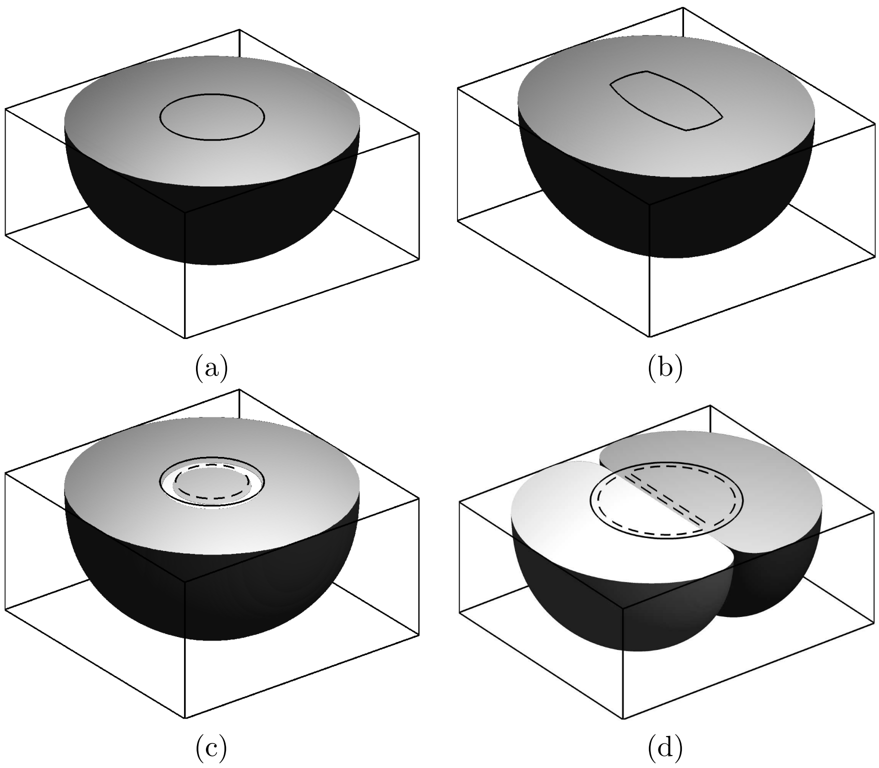

Figure 5.4: *Smallest VoI and corresponding bounding box for the circular (a), elliptic (b), concentric (c) and quad (d) heads with dimensionless height* $\mathsf{h} = 0.05$ *and* $\alpha = 0.99$.

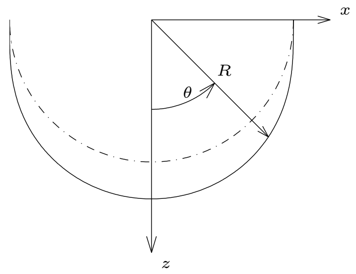

Figure 5.5: *Shape of the far-field equi-sensitivity (—), and half-circle (– · –) for comparison.*

where θ and R are the coordinates of a point on the equi-sensitivity surface in a spherical coordinate system with z oriented vertically and the origin taken in the middle of the head (see Fig. 5.5). K is a scaling factor related to the chosen sensitivity value. From (5.17), it appears that the equi-sensitivity surface exhibits a symmetry of revolution around the z axis and that its shape is invariant; only its size changes with K. This invariant shape is illustrated in Fig. 5.5 together with a half-circle for comparison; it is valid for most heads and for large response ratio α. A noticeable exception is the quad-head for which the dipolar moment of the RX coil is zero. The quadrupole term must then be taken into account, which yields a different shape (see Fig. 5.4 (d)).

To assess the accuracy of the approximated shape[9] of the *smallest VoI* obtained with the far-field approximation, we note that according to (5.17), the dimensions of the *smallest VoI* bounding box obey[10] $L_\mathrm{x} = L_\mathrm{y}$ and $2L_\mathrm{z} = 4^{\frac{1}{6}} L_\mathrm{x}$. Therefore, the xy error:

$$\epsilon_{\mathrm{xy}} = \frac{L_\mathrm{x}}{L_\mathrm{y}} - 1 \tag{5.18}$$

[9]only the shape of the *smallest VoI* can be estimated using the far-field approximation, not its size. Indeed, the size of the VoI depends on the sensitivity everywhere in the soil, hence also close to the head where the far-field approximation is very inaccurate. To compute the size of the VoI, the exact shape of the coils must still be used.

[10]L_x and L_y are obtained by computing R for $\theta = \pi/2$. L_z is obtained by computing R for $\theta = 0$. In addition, the bounding box along x and y is twice the radius while along z it is only once the radius.

and the z error:

$$\epsilon_{\mathrm{z}} = \frac{L_{\mathrm{z}}}{4^{\frac{1}{6}}(L_{\mathrm{x}} + L_{\mathrm{y}})} - 1 \tag{5.19}$$

will be small when the far-field shape approximation is accurate. This will be illustrated in Section 5.4.

5.4 Numerical results

In this section, numerical characteristics for the heads of Fig. 4.2 are provided. To avoid any dependence on the frequency, on the TX current or on the head dimension L, dimensionless quantities are used: the dimensionless response, $\mathsf{V} = V/(j\omega\mu_0 L I_{\mathrm{TX}})$, dimensionless lengths such as the dimensionless bounding box along x ($\mathsf{L}_{\mathrm{x}} = L_{\mathrm{x}}/L$) or the dimensionless head height ($\mathsf{h} = h/L$) and the dimensionless volumes $\mathsf{v} = v/L^3$. To assess the importance of the negative volume, Table 5.1 presents the response of the positive and negative volumes, V_+ and V_-, the corresponding compensation ratio $\gamma = |V_-|/V_+$ and the HS response $\mathsf{V}_{\mathrm{HS}} = \mathsf{V}_+ + \mathsf{V}_-$. Note that the negative volume response is significant for the double-D and quad heads and that it is the existence of that volume that allows for a significant compensation of the soil response. The dimensionless volume v_- of the negative volume is also indicated. Note that the latter is very small for the concentric head, relatively small for the double-D head and infinite for the quad head. The double-D head is quite specific in that respect, as the magnitude of the sensitivity is high in the small-negative volume and compensates the response of the infinite positive volume where the sensitivity is smaller on the average.

	V_+/χ	V_-/χ	γ	$\mathsf{V}_{\mathrm{HS}}/\chi$	v_-
Circular	0.4285	0	na	0.4285	0
Concentric	0.2124	-0.0011	0.0052	0.2113	0.0035
Elliptic	0.2716	0	na	0.2716	0
Double-D	0.0381	-0.0389	0.9807	-0.0007	0.2615
Quad	0.1486	-0.1486	1	0	∞

Table 5.1: *Dimensionless positive (V_+), negative (V_-) and HS (V_{HS}) response (normalized by χ) as well as dimensionless negative volume (v_-) and compensation ratio (γ) for various heads and dimensionless head height $\mathsf{h} = 0.05$. With the chosen normalization, results are independent of χ and of the frequency.*

Fig. 5.6 presents the size of the VoI as a function of α for the heads considered in this chapter. For the *smallest VoI*, the size of the dimensionless bounding box $\mathsf{L_x}$, $\mathsf{L_y}$ and $\mathsf{L_z}$ are shown. For the *layer of influence*, the dimensionless *depth of influence* $\mathsf{d} = d/L$ is shown. In all cases, the dimensionless head height is $\mathsf{h} = 0.05$. In addition Table 5.2 presents the same parameters together with the far-field approximation errors (ϵ_{xy} and ϵ_{z}) for α equal to 50, 90 and 99%. Note that the VoI is significantly bigger for the double-D head than for other heads. This indicates that for a double-D head, the soil compensation will be optimum only if the soil is homogeneous in a large volume as indicated by the size of the VoI. Note also that the *depth of influence* is always smaller than the depth of the VoI (L_{z}). This was already mentioned in Section 5.2.3 and confirms that choosing the right constraint to obtain the best VoI for the application may result in a significant gain. For example, if the objective is to build a test lane by replacing the native soil by a soil of interest, then the native soil should be replaced down to the *depth of influence* computed for a response ratio α chosen according to the needed test accuracy.

To assess the effect of the head height on the VoI, Fig. 5.7 presents the dimensionless size of the VoI as a function of the dimensionless head height h for $\alpha = 0.99$. Note that the size of the negative volume becomes zero for a sufficient height as the volume in which the sensitivity is negative, is small and close to the head, thus moving completely outside the soil volume. Note also that the positive volume becomes larger with increasing height. This may sound counter-intuitive but it can be understood by analyzing the spatial distribution of the head sensitivity. When lifting the head, the total response decreases but the spatial distribution of the sensitivity is such that a given volume close to the soil surface contributes less, proportionally to the total response, than when the head is closer to the soil.

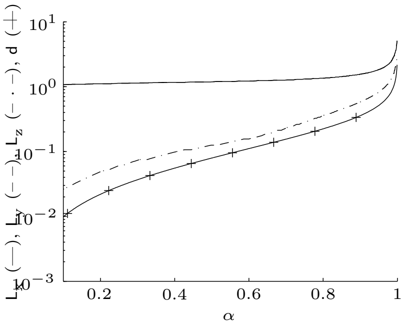

(a) circular

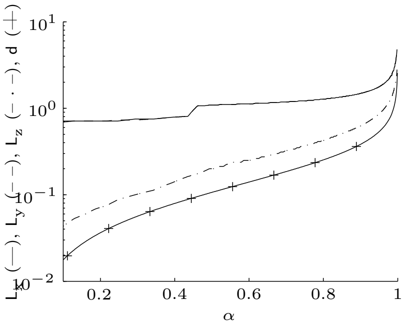

(b) concentric

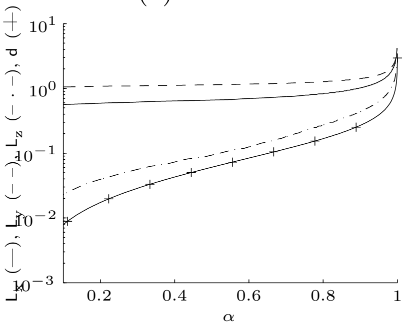

(c) elliptic

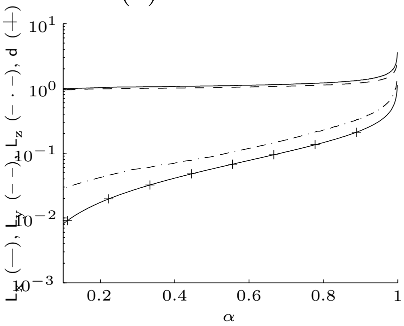

(d) quad

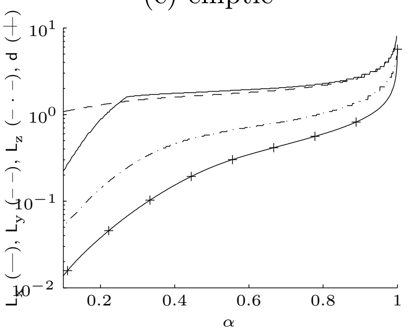

(e) double-D positive

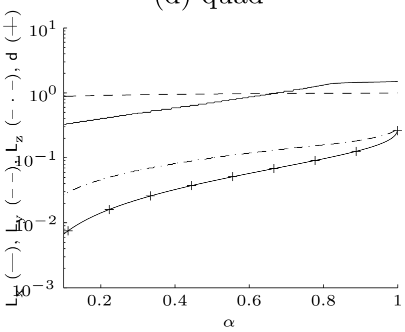

(f) double-D negative

Figure 5.6: *Size of positive (a-e) and negative (f) VoIs versus fraction α for circular (a), concentric (b), elliptic (c), quad (d) and double-D (e,f) heads. To characterize the* smallest VoI, *the size of the dimensionless bounding box $\mathsf{L_x}$ (—), $\mathsf{L_y}$ (– –) and $\mathsf{L_z}$ (– · –) are shown. To characterize* the layer of influence, *the dimensionless* depth of influence d *(+) is shown. In all cases, the dimensionless head height is* $\mathsf{h} = 0.05$.

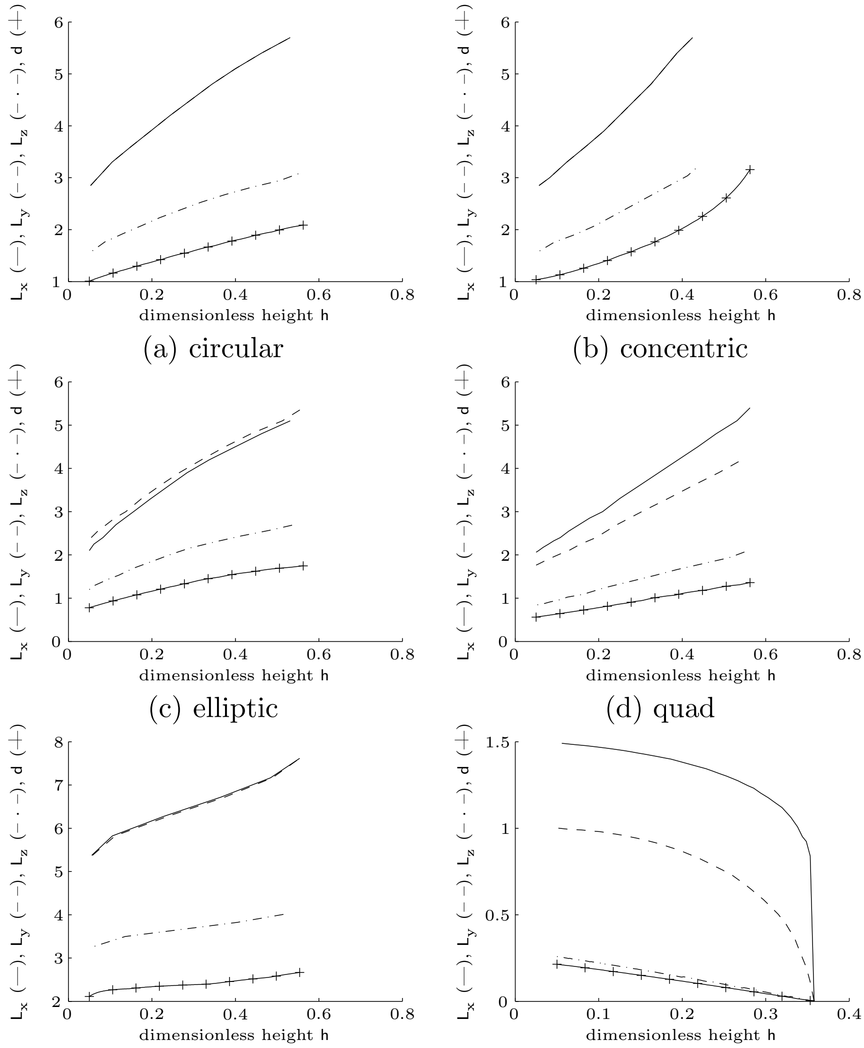

(a) circular

(b) concentric

(c) elliptic

(d) quad

(e) double-D positive

(f) double-D negative

Figure 5.7: *Size of positive (a–e) and negative (f) VoIs versus dimensionless height* h *for circular (a), concentric (b), elliptic (c), quad (d) and double-D (e,f) heads. To characterize the* smallest VoI, *the size of the dimensionless bounding box* $\mathsf{L_x}$ *(—),* $\mathsf{L_y}$ *(– –) and* $\mathsf{L_z}$ *(– · –) are shown. To characterize the* layer of influence, *the* depth of influence *(+) is shown. In all cases,* $\alpha = 0.99$.

	α	$\mathsf{v}^{\alpha}_{\mathrm{inf},+}$	$\mathsf{v}^{\alpha}_{\mathrm{inf},-}$	L_{x}	L_{y}	L_{z}
	50	0.0976	na	1.191	1.191	0.1232
Circular	90	0.7338	na	1.554	1.554	0.5814
	99	7.105	na	2.846	2.846	1.584
	50	0.0922	0.0009	1.089	1.089	0.201
Concentric	90	0.7068	0.0023	1.485	1.485	0.6271
	99	7.286	0.0031	2.841	2.841	1.627
	50	0.044	na	0.6623	1.137	0.0932
Elliptic	90	0.3409	na	1.018	1.419	0.4387
	99	3.456	na	2.146	2.378	1.237
	50	0.4054	0.0297	1.844	1.691	0.5952
Double-D	90	5.257	0.1253	2.767	2.678	1.416
	99	53.49	0.2076	5.427	5.386	
	50	0.027	0.027	1.093	1.033	0.0893
Quad	90	0.1519	0.1519	1.343	1.218	0.345
	99	0.8926	0.8926	2.079	1.768	

	α	d_{+}	d_{-}	ϵ_{xy}	ϵ_{z}
	50	0.0794	na	0	-0.8357
Circular	90	0.3572	na	0	-0.4059
	99	1.009	na	0	-0.1164
	50	0.1067	0.0042	0	-0.7069
Concentric	90	0.383	0.0108	0	-0.3297
	99	1.036	0.0155	0	-0.0907
	50	0.0607	na	-0.4176	-0.8355
Elliptic	90	0.2687	na	-0.2826	-0.4283
	99	0.7798	na	-0.0976	-0.1317
	50	0.2468	0.0439	0.0904	-0.4653
Double-D	90	0.8617	0.1314	0.0333	-0.1744
	99	2.111	0.2143	0.0076	-0.046
	50	0.0571	0.0571	na	na
Quad	90	0.2228	0.2228	na	na
	99	0.5628	0.5628	na	na

Table 5.2: *Dimensionless volume of positive* ($\mathsf{v}^{\alpha}_{\mathrm{inf},+}$) *and negative* ($\mathsf{v}^{\alpha}_{\mathrm{inf},-}$) *VoI, dimensionless bounding box of* smallest VoI (L_{x}, L_{y} *and* L_{z})*, dimensionless positive* (d_{+}) *and negative* (d_{-}) depth of influence *and far-field approximation errors* (ϵ_{xy} *and* ϵ_{z}) *for various heads and dimensionless head height* $\mathsf{h} = 0.05$

CHAPTER 6

Water effect

Several sources such as the Belgian MOD, the Canadian forces and others, have reported loss of sensitivity with the Schiebel AN-19/2 in the presence of moisture. The effect is more complex than a simple capacitive coupling as illustrated by the variety of phenomena observed. If the head is fully immersed in the water, no effect is observed. When the head is lifted out of the water, a large response, similar to that of a metallic object, is observed while large quantities of water are dripping from the head. Finally, when enough water has dripped and only a thin water layer remains on the head, a response with opposite polarity is observed. The latter case is the most important from a practical point of view as it is at the origin of the reduction of sensitivity observed on the field.

The problem was investigated in the nineties by the Defence Research and Development Canada (DRDC) Suffield. The phenomenon could be reproduced and the conditions under which the loss of sensitivity occurs were well understood but the underlying physics could not be explained. We performed additional measurements, to assess the effect of water conductivity. This shows that water conductivity has a significant effect and this yields additional insight in the underlying physics.

For the three observed phenomena, a circuit model is proposed and for the most critical phenomenon (the reduction of sensitivity) a more detailed field-level model is also proposed. We show that the response is due to the EQS fields backscattered. The accurate expression for the induced voltage that was developed in the first part of this thesis is therefore required to predict the observed response.

Contents

6.1 Introduction

Several sources such as the Belgian MOD, the Canadian forces and others, have reported problems with the Schiebel AN-19/2 in the presence of moisture. The problem was investigated in the nineties by DRDC Suffield. The problem could be reproduced and the conditions under which it occurs were well understood but the underlying physics could not be explained. The findings were reported to us in a private communication with Yogadhish Das[1] and can be summarized as follows:

- The Schiebel AN-19/2 suffers a serious degradation in sensitivity in some moisture conditions. Schiebel proposed to cover the detector head with a plastic bag as an ad-hoc temporary measure, but the effectiveness of this procedure was unknown. Similar ad-hoc procedures were reported by the Belgian MOD[2] which mentioned the use of vaseline to mitigate the problem.
- The problem could be reproduced in laboratory conditions. The output of the RX amplifier was measured and it was noted that:
  - There is no effect when the head is completely immersed in water. Schiebel suspected that the problem came from moisture penetrating or affecting the plastic of the head. The head was therefore left for a long time in water (a month) and no change in the detector response was observed. The idea of moisture penetrating or affecting the head plastic was thus rejected.
  - When the head is lifted out of the water, a large change of the response is observed when the head breaks the surface and a large quantity of water slides of the head. The measured signal is similar to that in the presence of a large metallic target. With our convention of Section 3.3.6, the polarity of the response is negative.
  - When enough water has dripped from the head, the signal reverses polarity. This is at the origin of the observed loss of sensitivity. Indeed, due to the positive contribution of the water, a larger target, producing a larger negative response, is required to get a slow-time signal reaching the sensitivity

[1] Yogadhish Das is with Defence R&D Canada – Suffield, Alberta, Canada
[2] Eric Van Meldert, private communication.

threshold in order to generate an alarm. A similar effect was observed when lightly misting the head from a bottle sprayer.

– When the head is in the water, touching the water with a finger also produces a positive signal, as in the previous case but the signal is larger. Sweeping the finger seems to increase the response.

– Tests were first performed with distilled water to discard the effect of water mineralization. Test were also performed with tap water and the same results were obtained.

- The physics was not understood. No model explaining the observed phenomena was developed. It was however speculated that the effect was likely due to coupling of the electric field which is usually ignored in the analysis of metal detectors and it was suggested that shielding the coils should reduce the effect.

Further moisture sensitivity tests have been performed on a number of detectors at DRDC in the scope of the International Pilot Project for Technology Co-operation (IPPTC) [68] but we are not aware of any new theoretical investigation on this topic. On modern detectors, the problem is solved by shielding the head. However, the use of a shield also has some drawbacks as discussed in Section 2.5 and understanding the underlying physics may help optimizing the shield.

To further investigate the problem, we made our own measurements with the detector and we were able to reproduce the phenomenon described above, apart from the test with the bottle sprayer. With respect to that last test, we sprayed the head with water but we could not observe any change in the fast time signal. Maybe a loss of sensitivity occurs but the effect is too small to be visible on the fast-time response (we didn't acquire the slow-time response and we didn't make any detection test).

We have further studied the effect of water conductivity. For this, we used distilled water to which we have added an increasing quantity of salt. The resulting conductivity was monitored and the measurements were repeated for a number of conductivities. This showed clearly that the water conductivity has an effect. Surprisingly, the response disappears if the conductivity is too high. The measurements are presented in Section 6.2.

We have also found incidentally that the response, observed when touching the water while the head is fully immersed, disappears when standing on a wooden chair before touching the water. This led us to the idea that the effect is due to a connection between the water and the ground through the body of the operator. This idea was formalized in a circuit model presented in Section 6.3.2. The response predicted by this model closely matches the measured one. According to our model, touching the water introduces an RC coupling between the coil and the electronics. This coupling is actually made through the oscilloscope ground lid, its mains plug, the soil, the operator body, its finger and finally the water which is coupled capacitively to the coils. Obviously, this path does not exist in normal use and the effect is an artifact related to the use of an oscilloscope. Understanding this effect was nevertheless important because it paved the way for the development of models explaining the other observed phenomena.

Indeed, similar circuit models including different RC connections were developed to explain the other observed phenomena. As discussed in Section 6.3.3, the response observed when lifting the head out of the water can be explained by an RC connection between the TX and the RX coils. Similarly, as discussed in Section 6.3.4, the response observed when enough water has dripped from the head can be explained by an RC connection between coils and the water which is modeled as a fictive shield.

The circuit model used to explain the latter effect however shows some limitations. Furthermore, this effect is the most important from a practical point of view. Indeed, the head may become humid in normal use, for example in presence of dew or when scanning over moist grass. In contrast scanning with large quantities of water dripping from the head is rather unrealistic. Furthermore, the response observed in presence of thin layer of water on the head results in a loss of sensitivity without any notification to the operator and this is a critical situation that must be analyzed in details. We have therefore developed, an alternative field-level model in which the response is derived from the electric field scattered by the water layer according to the expressions established in Section 2.4.5.2. To compute the scattered field, we have assumed that the layer of water can be modeled as an ellipsoid and we have then used the corresponding analytic solution. The field-level model is presented in Section 6.3.5.

6.2 Measurements

6.2.1 Procedure

The fast-time response ($V_{\mathrm{amp}}^{\mathrm{RX}}$) was measured using an oscilloscope in different configurations. First, a reference response was measured with a dry head. The head was then immersed in a large container filled with water and the measurement was repeated. Thereafter , the head was pulled out of the water and the oscilloscope was stopped manually[3] when the largest negative deviations was observed and the corresponding response was saved. The same procedure was repeated to obtain the response with the largest positive deviation. Finally, while the head was totally immersed, the water was touched with a finger and the oscilloscope was stopped manually when a typical response was observed. This was repeated standing on the ground and standing on a wooden chair.

All the measurements were repeated for a number of water conductivities. The conductivity was varied by starting with distilled water and progressively adding salt. Conductivity was measured using a conductivity meter (the Consort C535).

6.2.2 Pulling the head out of water

The response with the largest positive (blue) and negative (green) deviation are shown together with the reference response (red) in Fig. 6.1 for various water conductivities. The figure only shows three curves but the response actually evolves continuously from the reference response to the response with the largest negative deviation, then to the curve with the largest positive deviation and finally back to the reference response. Typically, the largest negative deviation is reached less than a second after the head has been lifted; while large quantities of water is still dripping from the head. Typically again, the largest positive deviation is reached after about 10 seconds; when enough water has dripped from the head and only a thin layer of water[4] remains on the head and the response goes back to its reference position after about

[3]Automatic triggering is obviously used for each fast-time response. Manual triggering is used to stop the oscilloscope when the response with the largest deviation is observed.

[4]This layer is not necessarily continuous, it may break in smaller parts. It is however difficult to assess the exact state of the water layer when the largest response is observed.

20 seconds. Those figures were estimated manually and are therefore of limited accuracy. The slow-time dynamics is further highly dependent on the water conductivity and the mentioned values are only valid for average conductivities. For example, in the case of large conductivities, the negative deviation only starts after several seconds.

A more complex instrumentation could be used to accurately characterize the slow-time dynamics. This was however not deemed necessary because a detailed understanding of the slow-time dynamics would anyway require an hydraulic model to describe the water flow around the head and this falls outside the scope of this thesis. The simple measurements made will however be used to check if the proposed models are realistic with respect to the observed slow-time dynamics.

The raw measurements, as presented in Fig. 6.1, do not yield a general view of the effect of the conductivity on the responses. We have therefore computed, for each acquired fast-time response, the largest deviation from the reference response:

$$\Delta V_{\mathrm{amp}}^{\mathrm{RX}} = \max_t \left\{ V_{\mathrm{amp}}^{\mathrm{RX}}(t) - V_{\mathrm{amp}}^{\mathrm{RX,ref}}(t) \right\} \tag{6.1}$$

for a positive deviation and

$$\Delta V_{\mathrm{amp}}^{\mathrm{RX}} = \min_t \left\{ V_{\mathrm{amp}}^{\mathrm{RX}}(t) - V_{\mathrm{amp}}^{\mathrm{RX,ref}}(t) \right\} \tag{6.2}$$

for a negative deviation.

Those largest deviation are illustrated in Fig 6.2 as a function of the conductivity. The relatively high noise observed is related to the fact that the acquisition is manually triggered. Note that, as already mentioned, a faster variation of the slow-time response is observed at early times, when the water distribution is such that the response shows the largest negative deviation than later, when the water distribution is such that the response shows the largest positive deviation. Hence accurate manual triggering is easier in the latter case and, as observed on the figure, the measurement noise (mainly resulting from inaccurate triggering) is smaller for the largest positive deviation than for the largest negative deviation. The triggering noise could have been reduced by resorting to a more complex instrumentation, allowing an automatic triggering. This was however not deemed necessary for our purpose.

The following observations regarding the measurements can be made:

1. The largest deviations are clearly a function of the water conductivity.

2. For large conductivities (larger than about 7000 μS), no deviation is observed. The response remains identical to the reference response at all times.

3. For the lowest conductivities, no negative deviation is observed when the head is lifted out of the water. A positive deviation is still observed a few seconds after the head has been lifted out of the water.

4. The negative deviation starts to be observed for a conductivity of about $100\mu S$. It then increases to reach a maximum for a conductivity of about 1000 μS. It then decreases again and no deviation is observed anymore for conductivities larger than about 7000 μS.

5. For large conductivities, a negative deviation is observed only after a few seconds, i.e. when water does not drip from the head anymore. It is thus clearly not the movement of the water droplets that causes the response.

6. The positive deviation is the largest for the lowest conductivities. It decreases monotonically with the conductivity and disappears for a conductivity of about 3000 μS.

6.2.3 Touching the water with a finger

A large positive deviation was observed when touching the water with a finger. The response may vary significantly as a function of the precise position of the finger in the water. Moving the finger also seems to increase the response. It seems however that the water conductivity (at least in the range of the conductivities considered) has no effect on the response. Two typical responses are illustrated in Fig. 6.3.

The response disappears if the operator stands on a wooden chair. As already mentioned in the introduction, this led us to the idea that the response is due to an RC coupling between the electronic ground and the coil through the oscilloscope ground lid and plug, the soil, the operator body and finger and finally the water which is coupled capacitively to the coils. To confirm that the response is due to a connection between the water and the ground, we have directly connected an electric wire to the ground connector of an electric outlet on one side and put the other side of the wire in the water. This had no effect on the response. Several resistors were then connected in series with the wire; again without any

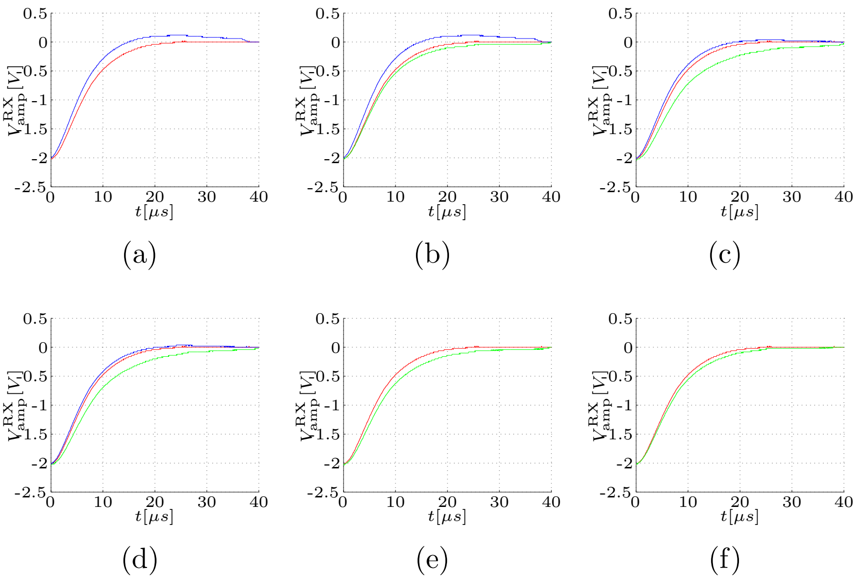

Figure 6.1: *Fast-time response for water dripping (green) and thin layer of water (blue) together with reference response for a dry head (red). From (a) to (f), the water conductivity increases. Conductivities considered are 27, 167, 1210, 1870, 3130, and 4680 μS. Note that for low conductivities (case (a)) no negative deviation is observed and for high conductivities no positive deviations is observed (cases (e) and (f)).*

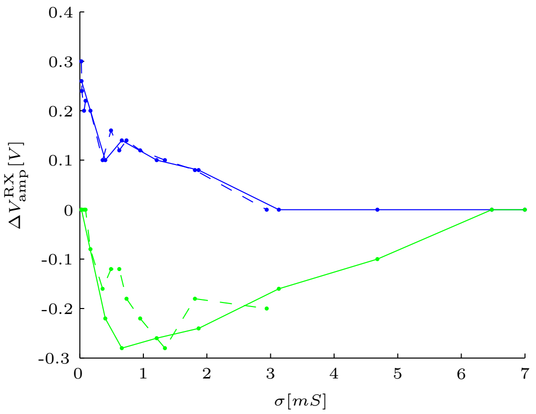

Figure 6.2: *Largest positive (blue) and negative (green) deviation of the fast-time response as a function of the conductivity. Two series of measurements have been performed. Full lines are used for the first series and dashed lines are used for the second series of measurements.*

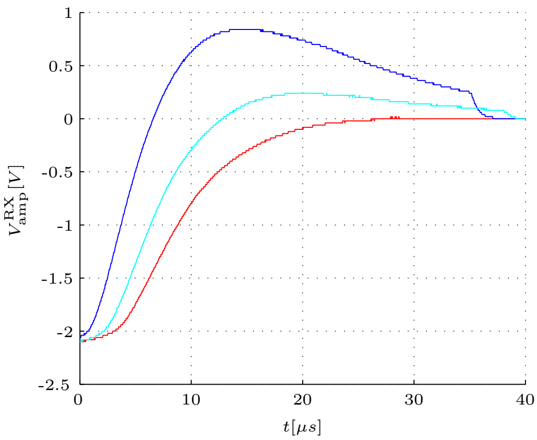

Figure 6.3: *Two typical response observed when touching the water surface with a finger (cyan and blue) together with the reference response (red). The head is completely immersed in the water.*

effect on the response. However, standing on the wooden chair, taking the extremity of the wire in one hand and touching the water with the other hand, the response was again observed. This led us to the conclusion that the contact resistance at the water interface is critical and that, with a thin wire, this contact resistor is too large. We have therefore tried other contact interfaces. A large response was observed by connecting the extremity of the wire to the inner side of a cartridge case and putting the cartridge in the water. The shape of the response is similar to that observed when touching the water with a finger but the deviation is larger. This confirms that the effect is due to a connection between the water and the ground and that the contact resistance at the water interface is a critical parameter.

6.3 Model development and evaluation

6.3.1 Head in water

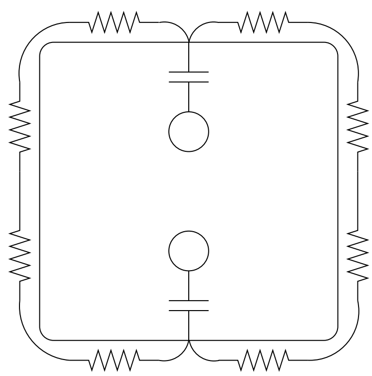

Figure 6.4: *Simplified model of coil in water. The casing, two turns and the corresponding turn-to-shield capacitances are shown. The resistors model the water.*

To model the head immersed in water, we assume that the water around the coil plays the role of a PEC shield for the EQS problem[5] at

[5] Water can clearly not be considered PEC for the magnetic field because for typical water conductivity, the skin depth is much larger than the dimensions of interest. Therefore, only small eddy currents are induced and the water is essentially transparent to the magnetic field. The phenomenon considered here is EQS in nature and

hand. It may look strange to consider that water is perfectly conducting. This can however be justified by referring to Fig. 6.4 where a simple model for a coil in water is presented (only two coil turns are illustrated). Assuming, for example, that the upper conductor is charged positively and the lower conductor is charged negatively, negative charges will appear on the casing close to the upper conductor and positive charges will appear close to the lower conductor. This requires charges to move in water from the lower to the upper part of the casing. Due to the limited conductivity of water, this path is modeled by a resistor. The two turns considered are thus connected via an RC circuit and the water may be considered as a PEC if the resistance, compared to the impedance of the capacitor, can be neglected. This will be the case if time constant $T = RC$, compared to the characteristic time of the detector, is small. The fastest dynamic occur during the TX current turn-off which lasts for a few micro-seconds. Hence the water can be considered as a PEC for the EQS field at hand if $T \ll 1\mu s$,

As an estimation of the capacitance, we use the turn-to-shield capacitance computed in Section 2.5 for a PEC shield. This estimation might become inaccurate for low water conductivity but it can be used for our purpose because we want to determine the conditions under which the water can be modeled as a PEC shield. Estimating the resistor is more complex because the path followed by the current is unknown. A conservative value can be obtained by assuming that the current flows in a thin water layer from the upper part to the lower part of the casing. The real resistance should indeed be smaller as the current is expected to spread out in a much larger water volume. Furthermore, the two turns considered in Fig. 6.4 are those yielding the largest resistance because the distance along which the charges must travel (on half of the casing perimeter) is the largest possible. The turn-to-shield capacitance is in the order of 10pF. As the two capacitors are in series, the capacitance to consider is about 5pF. For the considered uniform current layer, the resistance is $2w/(2\pi R_{\text{coil}} h\sigma)$ with w the width of the casing section, h the thickness of the water layer, R_{coil} the radius of the coil and σ the conductivity of the water. Noting that the left and right resistors are in parallel, the resistance to consider is about $25k\Omega$ for a water layer thickness of $1mm$ and for a conductivity $\sigma = 650\mu S$, which is typical for tap

only small currents are required to produce a significant charge distribution around the casing. It is for those divergent currents, that the water can be considered as perfectly conducting, not for the solenoidal eddy-currents.

water. The resulting time constant is $T = 0.1\mu s$ which is much smaller than the duration of the current turn-off and the water can indeed be considered as a PEC. For the distilled water used, the conductivity is $25\mu S$ and the corresponding time constant is about $5\mu s$. It is thus not clear whether distilled water can be considered as perfectly conducting. However, assuming that the current spreads out in a water layer of 1cm still seems realistic and the resulting time constant is then $0.5\mu s$ which allows to accept the PEC assumption.

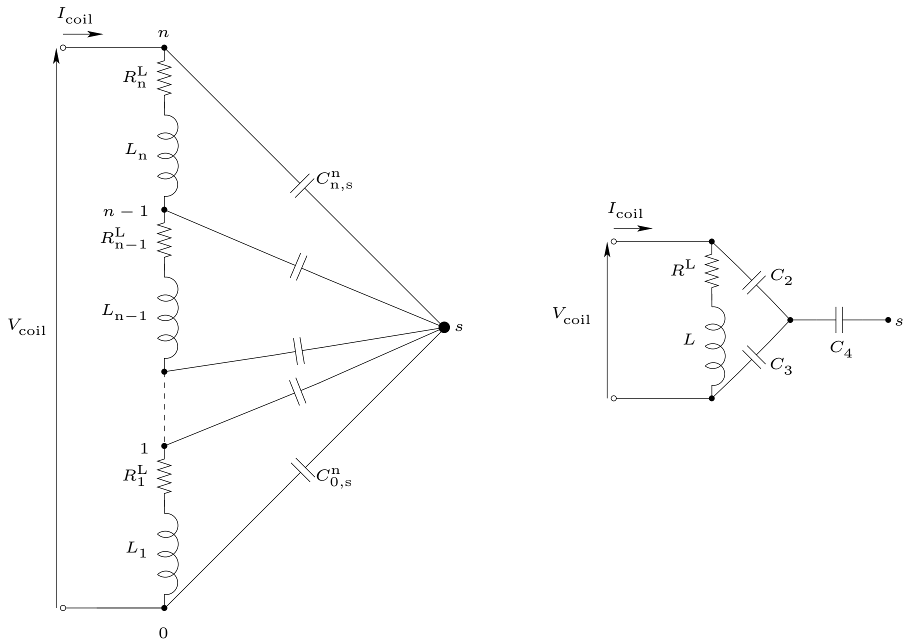

(a) (b)

Figure 6.5: *Additional capacitances due to the presence of the shield. Detailed model (a) and corresponding simple model (b). The turn-to-turn capacitance and turn-to-turn magnetic coupling are not shown.*

Assuming that water can be modeled as a PEC shield, immersing the detector results in the appearance of an additional capacitor between each turn and the shield. The detailed coil model of Fig. 2.3 (b) is then extended as illustrated in Fig. 6.5 (a). The turn-to-shield capacitors appearing in the circuit are computed by resorting to the MAS, as discussed in Section 2.5.

We have shown in Chapter 2 that the simple circuit presented in

Fig. 2.3 (b) can advantageously be used to model an unshielded coil. We now extend this simple model to take into account the shield. As explained in Section 2.2.2 the parameters of the simple circuit can be computed from those of the detailed one by imposing that the energy stored in the capacitors of the two circuits are equal.

The simplest way to introduce a shield in the simple coil model is to introduce two coil-to-shield capacitors. Referring to Fig. 6.5 (b), the shield would then be modeled by the capacitors C_2 and C_3. With those two capacitors alone, it is however not possible to match the energy stored in the capacitors *for all values* of the terminals voltages. Indeed, the energy stored in the capacitors of the simple and detailed circuit models are equal if:

$$\sum_{k=0:n_{\mathrm{turn}}} C^{\mathrm{n}}_{\mathrm{ks}} \left(\frac{kV_{\mathrm{coil}}}{n_{\mathrm{turn}}} - V_{\mathrm{s}} \right)^2 = C_3 V_{\mathrm{s}}^2 + C_2 \left(V_{\mathrm{coil}} - V_{\mathrm{s}} \right)^2 \tag{6.3}$$

with V_{s} the potential of the shield. We have assumed that, in the frequency band of interest, the current in the capacitor branches can be neglected to compute the turn voltages and that the inductance and mutual coupling coefficients are identical for all turns. The voltage then evolves linearly along the coil: $V_{\mathrm{k}} = kV_{\mathrm{coil}}/n_{\mathrm{turn}}$ with V_{k} the voltage at node k in the circuit of Fig. 6.5 (a).

Developing (6.3) yields three terms on both sides. One in V_{coil}^2, another in V_{s}^2 and the last one in $V_{\mathrm{coil}}V_{\mathrm{s}}$. Matching the corresponding three coefficient is impossible with only two capacitors and it is mandatory to add a third capacitor. One can easily check that adding the capacitor C_4 as in Fig. 6.5 (b) solves the problem.

To compute the equivalent capacitors, we first consider a floating shield. In that case, the capacitors in the simple circuit can be replaced by a single capacitor:

$$C_{23} = \frac{C_2 C_3}{(C_2 + C_3)} \tag{6.4}$$

Indeed, for a floating shield, C_4 plays no role and C_2 and C_3 are connected in series. The energy stored in the capacitors of the simple circuit is thus:

$$E_{\mathrm{C}}^{\mathrm{simple}} = 0.5 C_{23} V_{\mathrm{coil}}^2 \tag{6.5}$$

To calculate the energy stored in the capacitors of the detailed circuit, we first determine the shield voltage by noting that for a floating shield, the total charge must be zero:

$$\sum_{k=0:n_{\mathrm{turn}}} C_{\mathrm{ks}}^{\mathrm{n}} \left(\frac{kV_{\mathrm{coil}}}{n_{\mathrm{turn}}} - V_{\mathrm{s}} \right) = 0 \tag{6.6}$$

This relation is fulfilled for any coil voltage if:

$$V_{\mathrm{s}} = \alpha V_{\mathrm{coil}} \tag{6.7}$$

with:

$$\alpha = \frac{\sum_{k=0:n_{\mathrm{turn}}} kC_{\mathrm{ks}}^{\mathrm{n}}}{n_{\mathrm{turn}} \sum_{k=0:n_{\mathrm{turn}}} C_{\mathrm{ks}}^{\mathrm{n}}} \tag{6.8}$$

Once α is known, the energy stored in the capacitors of the detailed circuit can be computed:

$$E_{\mathrm{C}}^{\mathrm{detailed}} = 0.5V_{\mathrm{coil}}^2 \sum_{k=0:n_{\mathrm{turn}}} C_{\mathrm{ks}}^{\mathrm{n}} \left(\frac{k}{n_{\mathrm{turn}}} - \alpha \right)^2 \tag{6.9}$$

Matching the energies (6.5) and (6.9) then yields:

$$C_{23} = \sum_{k=0:n_{\mathrm{turn}}} C_{\mathrm{ks}}^{\mathrm{n}} \left(\frac{k}{n_{\mathrm{turn}}} - \alpha \right)^2 \tag{6.10}$$

The capacitor C_{23} can then be decomposed in its components C_2 and C_3 by imposing that the shield voltage is equal for the simple and detailed circuits. Hence (6.7) must be fulfilled and this yields $C_2 = C_{23}/(1-\alpha)$ and $C_3 = C_{23}/\alpha$.

Finally C_4 can be computed by imposing that the energy stored in the capacitors of the two circuits are still equal for another shield voltage. For example, choosing $V_{\mathrm{s}} = 0$, one can easily check that the energy stored in the in the turn-to-shield capacitors of the detailed circuit is equal to the energy that would be stored in a capacitor $C_{\mathrm{s0}}^{\mathrm{detailed}}$ located in parallel with the coil with:

$$C_{\mathrm{s0}}^{\mathrm{detailed}} = \sum_{k=0:n_{\mathrm{turn}}} C_{\mathrm{ks}}^{\mathrm{n}} \left(\frac{k}{n_{\mathrm{turn}}} \right)^2 \tag{6.11}$$

Considering now $V_{\mathrm{s}} = 0$ in the simple circuit, C_3 and C_4 appear in parallel and both are in series with C_2. The capacitors of the simple circuit can thus be replaced by a capacitor C_{s0}^{simple} located in parallel with the coil with:

$$C_{s0}^{\text{simple}} = \frac{C_2(C_3 + C_4)}{C_2 + C_3 + C_4} \tag{6.12}$$

Matching C_{s0}^{simple} and C_{s0}^{detail} then yields:

$$C_4 = \frac{C_2 C_{s0}}{C_2 - C_{s0}} - C_3 \tag{6.13}$$

For the Schiebel detector $\alpha \simeq 0.5$ and $C_2 \simeq C_3$ as could be expected from the coil (approximate) symmetry. Surprisingly, C_4 is negative and this capacitor is thus difficult to interpret physically. It nevertheless yields a simple circuit that is equivalent to the detailed circuit model at low frequencies as required and was confirmed by numerical comparisons[6].

6.3.1.1 Model evaluation

The immersed coil simple circuit model of Fig. 6.5 (b) has been introduced in the detector state-space model. The resulting response was then compared to the reference response obtained from the dry-head simple circuit model of Fig. 2.3. The maximum deviation between the two responses is about $1\mu V$. Such a small deviation is compatible with our measurements which did not show any measurable effect on the response when immersing the head in the water.

6.3.2 Touching the water with a finger

To confirm that the origin of the response observed when touching the water with a finger is the introduction of an additional RC path, such a path is now introduced in the detector model and the resulting response compared with the measurements. The model used is presented in Fig. 6.6. Water is again modeled as a PEC shield around each coil and the two shields (TX and RX) are short-circuited. In addition, a resistor R_{gs} is introduced between the shields and the ground to model the operator resistance. To assess if such a ground connection could yield a measurable effect, we have computed the maximum deviation between the response and the reference response, as a function of R_{gs}. This is

[6] Other equivalent circuit topologies might lead to positive capacitances. This was not further investigated because the negative capacitances did not yield any problem in the detector simulations.

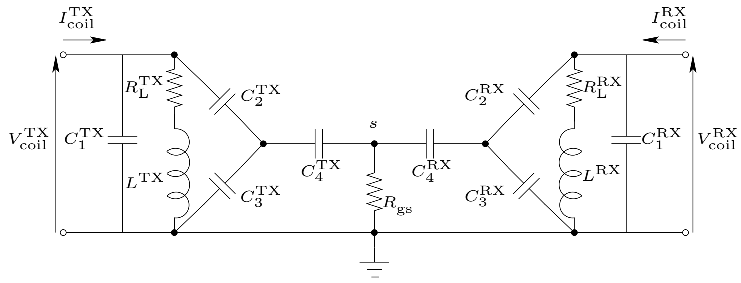

Figure 6.6: *Model of head in water. Ground connection appears when touching the water with a finger.*

illustrated in Fig. 6.7 which shows that the maximum deviation occurs for $R_{\mathrm{gs}} \simeq 15k\Omega$ and that the corresponding deviation is close to half a volt.

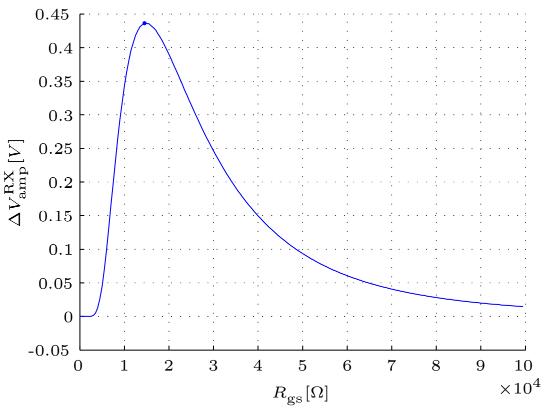

Figure 6.7: *Maximum deviation of the slow-time response as a function of ground connection resistor R_{gs}.*

The corresponding computed response is shown in Fig. 6.8 together with measurements obtained while touching the water with a finger. Two measurements are presented to highlight the fact that the response observed shows a high variability. It depends on the exact location and speed of the finger. The polarity and the order of magnitude of the response is compatible with the measurements. The computed response further matches quite well one of the two measurements. However, for

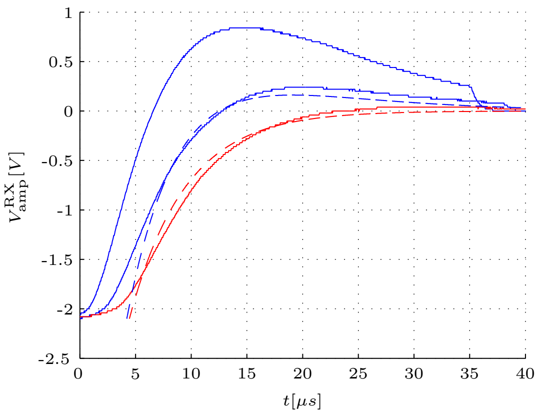

Figure 6.8: *Response (blue) acquired when touching the water with the head in the water together with reference response (red). Two measured responses (—) and response computed (– –) with the ground connection resistor R_{gs} yielding the largest deviation (about $15k\Omega$).*

the second measurement presented, which corresponds to one of the largest deviations observed, the effect is a few times larger than the computed one. The model is thus appropriate but it underestimates the deviation. This underestimation might be due to small errors in the coil geometry. Indeed, the drawing we have used to compute the coil parameters shows an ideal winding pattern. In practice, the turns might be closer to the casing and this may yield larger turn-to-shield capacitors which may result in larger deviations.

One still has to check if a resistor $R_{\text{gs}} = 15k\Omega$ is realistic. The body resistance may vary significantly from one person to another and from time to time. A value of $1.5k\Omega$ is commonly used as the resistance between major extremities of an average human body: hand to hand, or hand to foot. According to our model, such a small resistance would yield a much smaller response. The resistor to consider in the model may however be larger because the contact surface is small, especially for the hand holding the ground wire[7].

Finally, recall that an increase of the response was observed when moving the finger in the water. This effect can be understood in the

[7]Similar responses were observed when the operator was standing on the floor, without touching any ground wire. In that case, however, the resistance (and maybe the capacitance) of the shoes must be considered.

framework of our model by noting that moving the finger may change the contact resistance.

6.3.3 Lifting the head out of water

Figure 6.9: *Typical water film appearing when lifting the head out of the water.*

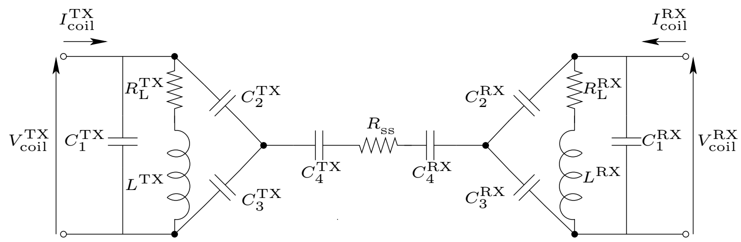

Figure 6.10: *Model of head valid when lifting the head out of the water.*

When lifting the head out of the water, a large quantity of water remains around the coils and a water path exists between the TX and the RX coils as illustrated in Fig. 6.9. The picture shows that the connection is through two vertical water films that connects the coils to the main water volume.

The exact shape of the water layer remaining around the coils is difficult to assess but we assume that it is thick enough to form a PEC shield (see Section 6.3.1). Furthermore, the water connection between the two coils is modeled by a resistor R_{ss} between the two shields. This yields the head circuit-model presented in Fig. 6.10. To assess if such

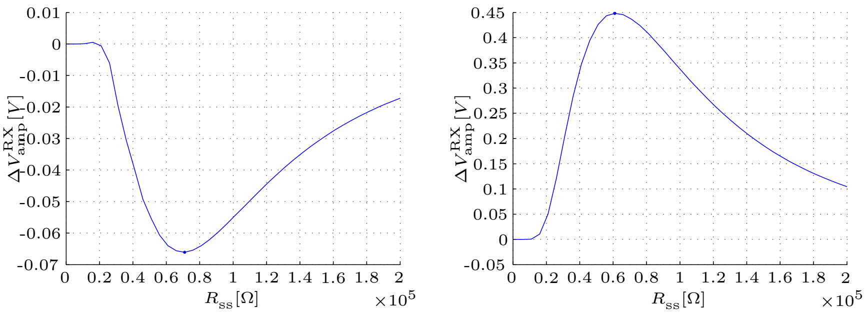

(a) (b)

Figure 6.11: *Maximum deviation of the fast-time response as a function of shield connection resistor R_{ss} for a positive (a) and a negative (b) mutual coupling between the coils.*

a shield connection could yield a measurable effect on the response, we have computed the maximum deviation of the fast-time response as a function of R_{ss}. This is illustrated in Fig. 6.11 (a) which shows that the maximum deviation occurs for $R_{ss} \simeq 70k\Omega$ and that the corresponding deviation is about $0.07V$. This deviation is large enough to be measurable.

The corresponding computed response is shown in Fig. 6.12 (a) together with a measurement acquired while lifting the head out of the water. The dynamics, the polarity and the order of magnitude of the response is compatible with the measurements. The computed deviation is however about ten times smaller than the measured one. It is worth noting that with a negative mutual coupling between the TX and the RX coil, the deviation changes polarity, but it also becomes larger as illustrated in Figs. 6.11 and 6.12 (b). This shows that the sign of the coupling has a major impact on the effect of the water.

Measurements have shown (Section 6.2) that the water response is influenced by its conductivity. The response disappears for small as well as for large conductivities and it is maximum for medium conductivities typical of tap water. This effect can be explained with the proposed model by noting that for tap water, a resistor $R_{ss} = 70k\Omega$ corresponds to a water film having a height of $1cm$ and a thickness of $0.5mm$. The

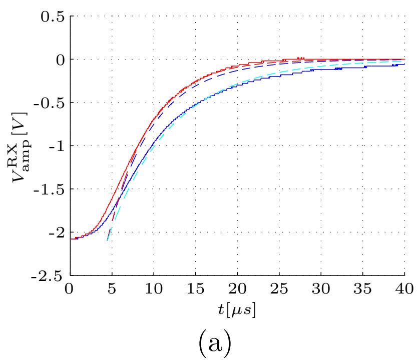

Figure 6.12: *Response (blue) acquired when lifting the head out of the water together with the reference response (red). Measured (—) response and response computed (– –) with the shield connection resistor $R_{\rm ss}$ yielding the largest deviation (about $70k\Omega$). Positive (a) and negative (b) mutual coupling between the coils are considered. For a better visualization of the response dynamics, water response in (a) is amplified by a factor 10 (cyan).*

formation of such a water film seems realistic. For lower conductivities, 'optimal' thickness of the water film increases. For distilled water, by considering again a height of $1cm$, the 'optimal' thickness of the water film is about $1.5cm$. Such a thick water film is clearly unrealistic and the 'optimal' resistor will not be reached in practice, which results in a much smaller response. Similarly, for high conductivities, the 'optimal' film thickness becomes thinner (or longer films must be considered). The water film will probably break before such film geometries are reached and the 'optimal' resistor will not be reached in practice, which again results in a much smaller response. We have further observed that for high water conductivities, the maximum deviation is observed later, when the water is no longer dripping from the head. This may be explained by noting that there is a plastic connection between the two coils (see Fig. 2.1). For large conductivities the largest deviation may occur after that the water film is broken and the coil connection occurs through a water layer on the plastic linking the two coils. For large water conductivities, this water layer may have the 'optimal' thickness at a later time.

6.3.4 Thin layer of water — Simple circuit model

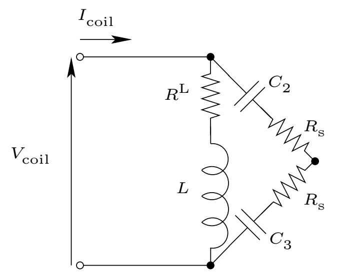

Figure 6.13: *Coil circuit model for thin water layer response.*

After that enough water has dripped and only a thin water layer remains on the head, the water may no longer be modeled as a PEC shield. However, in first approximation, the model of Fig. 6.4 can still be used. We further assume that the shield-to-turn capacitor computed for a PEC shield can still be used[8].

The effect of the water resistance can be taken into account in the simple coil model by introducing two resistors R_{s} as indicated in Fig. 6.13. The two resistors are in series and can therefore be chosen equal without loss of generality. Obviously, the additional resistors should be introduced in both the TX and the RX circuits. Rigorously speaking, their value may be different for the TX and RX coils but to simplify the model, we have considered equal resistors for the two coils.

To assess if the shield resistors R_{s} can yield a measurable effect on the response, we have computed the maximum deviation as a function of R_{s}. This is illustrated in Fig. 6.14 (e) which shows that the maximum deviation occurs for $R_{\text{s}} \simeq 120k\Omega$ and that the corresponding deviation is about 0.16V.

The response computed for the resistor yielding the largest deviation is shown in Fig. 6.14 (f) together with the measurement obtained for a conductivity of $650\mu S$ representative of tap water. The dynamics, the polarity and the order of magnitude of the response is compatible with the measurements. The computed response is slightly larger than the

[8]This may be justified by noting that the dominant capacitors correspond to the outer turns, close to the casing, and that for those turns, the charges are located on a small area of the casing, in the vicinity of the turn. For that small area, the PEC assumption should still be valid.

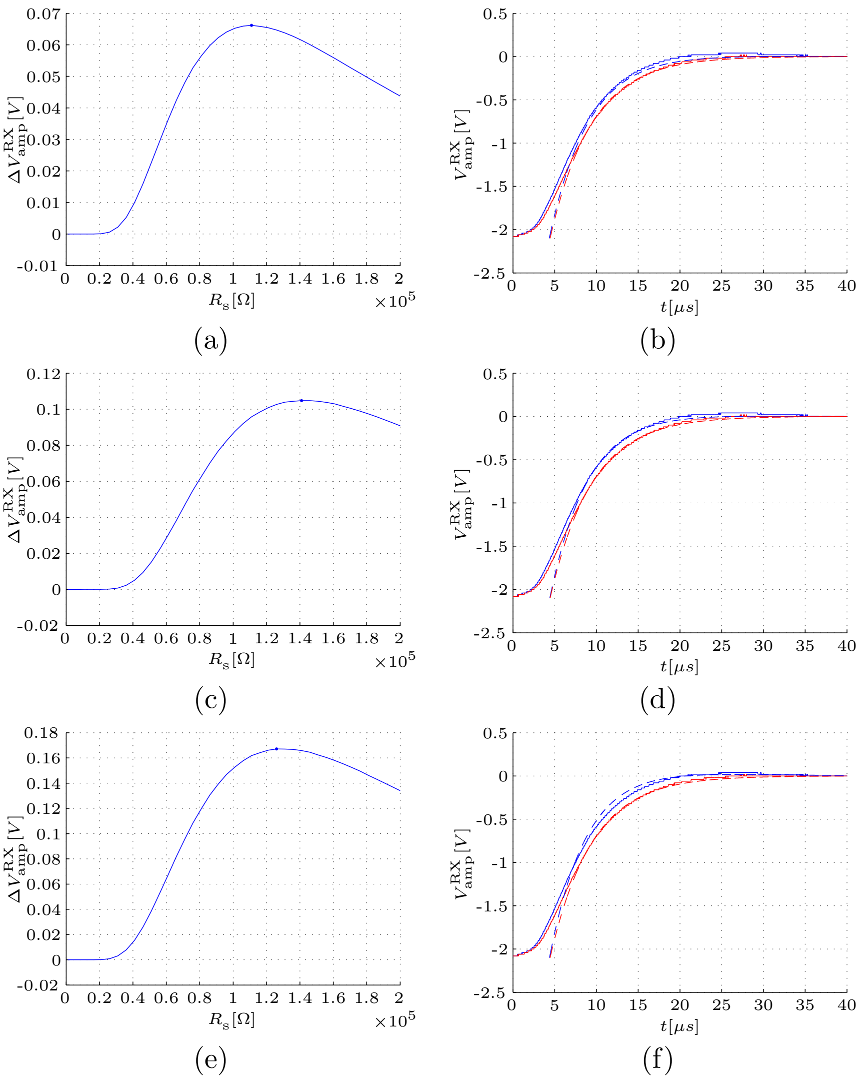

Figure 6.14: *Left: maximum deviation of the fast-time response as a function of the shield connection resistor R_{s}. Right: fast-time responses (blue) measured (—) for $\sigma = 650\mu S$ and computed (– –) with the resistor R_{s} yielding the largest deviation are shown together with the computed (– –) and measured (—) reference (red) responses. The resistor R_{s} is introduced in the TX coil alone (a) and (b), in the RX coil alone (c) and (d) and in both the TX and RX coils (e) and (f).*

measured one. However, according to Fig. 6.2, the largest response was measured for distilled water for which the response was about twice as large as in the case of tap water. The model thus underestimates the largest responses by a factor of about two.

Measurements have shown (Section 6.2) that the water response is influenced by its conductivity. The response disappears for large conductivities. This effect can be explained with the proposed model by noting that the thickness of the water layer yielding the 'optimal' resistance $R_s = 120k\Omega$ decreases when the water conductivity increases. For large conductivities, the required water layer may become unrealistically thin. In practice, the water layer will break before reaching the 'optimal' thickness, yielding a smaller response.

Similarly, the 'optimal' resistance will probably not be reached for small conductivities because the required water layer becomes unrealistically thick. We therefore expect that the water response decreases for small conductivities. This decrease was not observed in Fig. 6.2 but it may still occur for conductivities smaller than that of the distilled water used.

To assess the contribution of the TX and the RX coil to the total response, we have also introduced a shield resistor in the TX coil (Fig. 6.14) (a)-(b)) and in the RX coil (Fig. 6.14) (c)-(d)) alone. The contribution of the two coils have the same order of magnitude; the contribution of the RX coil being slightly larger. It may look surprising that introducing shield resistors in the TX coil may significantly affect the voltage on the RX side. This may however be understood by noting that a shield resistor on the TX side will yield an additional current mode. This current will in turn yield an induced voltage on the RX side through the magnetic coupling existing between the two coils.

6.3.5 Thin layer of water — Field-level model

The circuit model proposed in the previous section to explain the response of a thin water layer has some limitations. Indeed we have assumed that the turn-to-shield capacitors can still be computed as for the PEC case and this may have a limited validity. Furthermore, the water layer thickness could vary around the casing. Indeed, most of the water is expected to accumulate above and below the coil and only little water is expected to remain on the vertical sides.

We have therefore considered an alternative approach, in which the field scattered by the water layer and the corresponding induced voltage are explicitly computed. Water is weakly conducting and the eddy currents may be neglected but, even a weakly conducting water layer, may be polarized by separation of electric charges. This yields a scattered EQS field that may produce a response through the electric contribution to the induced voltage (e_{E}, see Section 2.4.5.2).

To keep a tractable model and to allow for a better physical interpretation our objective was to model the water layer using a simple geometry, for which an analytic solution exists, and that is still reasonably close to the actual geometry. Note that for the EQS problem at hand, the full-wave vectorial solution is not required; the scalar potential solution is sufficient. Amongst the shapes for which a scalar analytic solution exists, the ellipsoid was deemed the most appropriate to model a water layer. Note that, for an ellipsoid, the general solution is rather complex as it involves ellipsoidal harmonics but, for the problem at hand, considering a parallel field excitation is sufficient. Simpler expressions [69, Section 30][31, Section 3.26–3.27] can then be used.

A key factor that influences the dynamics of the ellipsoid response is the so-called depolarization factor (N_{i}) where i indicates the corresponding ellipsoid principal direction. A sphere is a specific case of ellipsoid and the corresponding depolarization factor is 1/3. With such a large depolarization factor, the response is much too fast to be measurable. In first approximation the response of a water sphere has a time constant $T = \epsilon/\sigma$. Considering typical parameters of tap water ($\epsilon = 80\epsilon_0$, $\sigma = 650\mu S$) yields $T = 13ns$ which is much too small to yield a measurable response in the evaluation window. For elongated ellipsoids, the depolarization factor along the long axis is much smaller. As a result, the time constant becomes much larger and this is the key to yield a measurable response.

In the next sections, we will first review the depolarization factors and the static solution for a conducting and for a dielectric ellipsoid. We will then show how those static solutions can be used to express the dynamic solution for the problem at hand. Next, we will show how this dynamic solution can be integrated in the state-space model of the detector to compute the water response. Finally, the computed responses will be compared with the measurements.

6.3.5.1 Ellipsoid depolarization factor

The depolarization factor is defined as [70] ‘The ratio of the internal electric field, induced by the charges on the surface of a dielectric when an external (incident) field is applied, to the polarization of the dielectric.'. This definition is ambiguous because the kind of incident field and the point at which the ratio must be computed is not specified. It can be made unambiguous by specifying that the scatterer is an ellipsoid and that the incident field is uniform and along one of its principal axes. Indeed, for such an incident field, the total field inside an ellipsoid and the internal electric field induced by the charges on the surface of a dielectric are also uniform and parallel to the incident field. The polarization inside the dielectric being proportional to the total field, it is also parallel to the incident field. [31, Sections 3.25—3.27][69, Section 30]

Mathematically, the depolarization factor is defined by:

$$N_{\mathrm{i}} = -\frac{\epsilon_0 E_{\rho,\mathrm{i}}^{\mathrm{diel,in}}}{P_{\mathrm{i}}^{\mathrm{diel}}} \tag{6.14}$$

where $i = 1, 3$ indicates the ellipsoid principal axis considered, $P_{\mathrm{i}}^{\mathrm{diel}}$ is the electric polarization inside the ellipsoid and $E_{\rho,\mathrm{i}}^{\mathrm{diel,in}}$ is the electric field produced inside the ellipsoid as a result of the dielectric polarization. The name $E_{\rho,\mathrm{i}}^{\mathrm{diel,in}}$ is chosen to make the link with above definition and because the (uniform) volume dipole distribution is indeed equivalent to a (bound) charge distribution ρ on the ellipsoid boundary. In other words, the field $E_{\rho,\mathrm{i}}^{\mathrm{diel,in}}$ can be computed considering a surface charge distribution ρ in free space[9]. The minus sign is introduced in (6.14) to get a positive depolarization factor. Indeed, $E_{\rho,\mathrm{i}}^{\mathrm{diel,in}}$ and $P_{\mathrm{i}}^{\mathrm{diel}}$ are anti-parallel ($E_{\rho,\mathrm{i}}^{\mathrm{diel,in}}$ partly opposes the incident field—hence the name depolarization).

The depolarization factor can be computed from the ellipsoid geometrical parameters according to [71]:

$$N_{\mathrm{i}} = \frac{abc}{2} \int_0^{\infty} \frac{ds}{(s + a_{\mathrm{i}}^2)\sqrt{(s + a_{\mathrm{j}}^2)(s + a_{\mathrm{k}}^2)(s + a_{\mathrm{i}}^2)}} \tag{6.15}$$

with i, j, k a cyclic permutation of $1, 2, 3$ and a_{i} the ellipsoid semi-axis along x, y and z for $i = 1, 2, 3$ respectively.

[9]Our general convention would require to use a superscript (fs) to indicate the environment. This superscript is not required in this Section because all sources considered are radiating in free space. It is therefore omitted to simplify notations.

6.3.5.2 Ellipsoid static scattering

We first consider the scattering of the ellipsoid for a uniform static electric field along one of its principal directions. Two cases have to be considered, the dielectric and the conducting ellipsoid. Note that as soon as the ellipsoid is conducting, whatever the conductivity, the field inside the ellipsoid is null[10] and the boundary of the ellipsoid is equipotential. In other words, as soon as the conductivity is not null, the static solution is identical to that of a PEC and the medium inside the ellipsoid plays no role. For the dielectric case, the field also becomes null inside the ellipsoid when the permittivity tends toward infinity. By uniqueness of the solution, the solution for the conducting case can thus be obtained from the dielectric case by taking the limit of an infinite permittivity.

Dielectric ellipsoid inner solution Knowing the depolarization factor, it is easy to compute the total field inside a dielectric ellipsoid (E^{in}) for a given incident field (E_{inc}). Indeed, the total field inside the ellipsoid is the sum of the incident field and the field $E_{\rho,\mathrm{i}}^{\mathrm{diel,in}}$ produced by the surface equivalent charge distribution:

$$E_{\mathrm{tot,i}}^{\mathrm{diel,in}} = E_{\rho,\mathrm{i}}^{\mathrm{diel,in}} + E_{\mathrm{inc,i}} \tag{6.16}$$

Introducing the definition of the depolarization factor (6.14) in (6.16) then yields:

$$E_{\mathrm{tot,i}}^{\mathrm{diel,in}} = -\frac{N_{\mathrm{i}} P_{\mathrm{i}}^{\mathrm{diel}}}{\epsilon_0} + E_{\mathrm{inc,i}} \tag{6.17}$$

By definition, the polarization is:

$$P_{\mathrm{i}}^{\mathrm{diel}} = \epsilon_0(\epsilon_{\mathrm{r}} - 1) E_{\mathrm{tot,i}}^{\mathrm{diel,in}} \tag{6.18}$$

Introducing this expression in (6.17) then yields:

$$E_{\mathrm{tot,i}}^{\mathrm{diel,in}} = \frac{E_{\mathrm{inc,i}}}{1 + N_{\mathrm{i}}(\epsilon_{\mathrm{r}} - 1)} \tag{6.19}$$

and:

$$P_{\mathrm{i}}^{\mathrm{diel}} = \frac{\epsilon_0(\epsilon_{\mathrm{r}} - 1)}{1 + N_{\mathrm{i}}(\epsilon_{\mathrm{r}} - 1)} E_{\mathrm{inc,i}} \tag{6.20}$$

[10]Otherwise, the current would not be null and charge would accumulate on the boundary, yielding a non-static solution.

Conducting ellipsoid inner solution As explained above, the conducting solution can be obtained by taking the limit of an infinite permittivity. According to (6.19), this yields a null inner field as required and according to (6.20) the polarization becomes:

$$P_{\mathrm{i}}^{\mathrm{cond}} = \frac{\epsilon_0}{N_{\mathrm{i}}} E_{\mathrm{inc,i}} \tag{6.21}$$

Obviously, the polarization has no physical meaning for a conducting ellipsoid. The scattered field is produced by a free charge distribution on the ellipsoid surface but mathematically, it can be computed from the fictive polarization (6.21) instead.

Equivalent source Physically, the scattered field is due to a free charge distribution on the boundary of the ellipsoid for the conducting case and it is due to a uniform distribution of dipoles (polarization) inside the ellipsoid for the dielectric case.

We have seen that mathematically, the scattering of a conducting ellipsoid can be computed from the fictive dipole distribution (6.21) instead of the real free charge distribution. According to (6.20) and (6.21) the dipole distribution for the electric and dielectric cases are related by:

$$P_{\mathrm{i}}^{\mathrm{diel}} = \alpha_{\mathrm{i}} P_{\mathrm{i}}^{\mathrm{cond}} \tag{6.22}$$

with

$$\alpha_{\mathrm{i}} = \frac{N_{\mathrm{i}}(\epsilon_{\mathrm{r}} - 1)}{1 + N_{\mathrm{i}}(\epsilon_{\mathrm{r}} - 1)} \tag{6.23}$$

According to (6.23), $\alpha_{\mathrm{i}} < 1$ as expected because a dielectric ellipsoid scatters less than a conducting one.

We have seen that the scattered field may be computed from a (real or fictive) dipole distribution both for the conducting and dielectric case. A surface distribution can also be used instead. Indeed, a dipole distribution is mathematically equivalent to a charge distribution [72, Equ. 418][31, Equ. 3 p183] $\rho = -\nabla \cdot \boldsymbol{P}$. Hence, the uniform volume dipole distribution is equivalent to a surface charge distribution:

$$\rho = \boldsymbol{P} \cdot \hat{\boldsymbol{n}} \tag{6.24}$$

According to (6.21), for the conducting case, the charge distribution can be expressed as

$$\rho_{\mathrm{i}}^{\mathrm{cond}} = \frac{\epsilon_0}{N_{\mathrm{i}}} E_{\mathrm{inc,i}} \cos\theta \tag{6.25}$$

with θ, the angle between the principal axis i and the ellipsoid normal $\hat{\boldsymbol{n}}$. According to (6.22), the charge distribution for the dielectric case is related to the conducting case by:

$$\rho_{\mathrm{i}}^{\mathrm{diel}} = \alpha_{\mathrm{i}} \rho_{\mathrm{i}}^{\mathrm{cond}} \tag{6.26}$$

Outer solution The field inside the ellipsoid is uniform but the solution is more complex outside the ellipsoid. As outside, the fields are not uniform, it is more convenient to express the solution in terms of the scalar potential. As for the inner solution (6.16), the total outer solution can be expressed as the sum of an incident contribution and a contribution due to a surface charge distribution. We first consider the conducting ellipsoid case:

$$\phi_{\mathrm{tot,i}}^{\mathrm{cond,out}} = \phi_{\rho,\mathrm{i}}^{\mathrm{cond,out}} + \phi_{\mathrm{inc,i}} \tag{6.27}$$

were the superscripts 'out' and 'cond' indicate that it is the *outer* solution for a *conducting* ellipsoid.

For an excitation $E_{\mathrm{inc,i}} \hat{\boldsymbol{x}}_{\mathrm{i}}$ along the principal axis i, the incident potential is $\phi_{\mathrm{inc,i}} = -E_{\mathrm{inc,i}} x_{\mathrm{i}}$ and the scattered potential $E_{\mathrm{inc,i}}$ can be expressed using ellipsoid coordinates as [69, Section 30][31, Section 3.26]:

$$\phi_{\rho,\mathrm{i}}^{\mathrm{cond,out}}(\xi) = -\phi_{\mathrm{inc,i}}^{\mathrm{inc}} \frac{\int_{\xi}^{\infty} \frac{ds}{(s+a_{\mathrm{i}}^2)\sqrt{(s+a_{\mathrm{i}}^2)(s+a_{\mathrm{j}}^2)(s+a_{\mathrm{k}}^2)}}}{\int_{0}^{\infty} \frac{ds}{(s+a_{\mathrm{i}}^2)\sqrt{(s+a_{\mathrm{i}}^2)(s+a_{\mathrm{j}}^2)(s+a_{\mathrm{k}}^2)}}} \tag{6.28}$$

with ξ the first ellipsoidal coordinate (surfaces of constant ξ are confocal ellipsoids and $\xi = 0$ on the boundary of the ellipsoid). One sees that on the boundary of the ellipsoid ($\xi = 0$), $\phi_{\rho,\mathrm{i}}^{\mathrm{cond,out}}(\xi) = -\phi_{\mathrm{inc,i}}$ and therefore, the total potential $\phi_{\mathrm{tot,i}}^{\mathrm{cond,out}} = 0$ as required for a conducting ellipsoid (the potential is constant on a conducting body and this constant is zero for a zero total charge.) We have seen that the scattered field can be computed from a dipole or a charge distribution, both for conducting and dielectric ellipsoids and that the source distributions is the same up to the factor α_{i} for the two cases. Hence the scattered fields are related by:

$$\phi_{\rho,\mathrm{i}}^{\mathrm{diel,out}} = \alpha_{\mathrm{i}} \phi_{\rho,\mathrm{i}}^{\mathrm{cond,out}} \tag{6.29}$$

which shows that the response of an elongated dielectric ellipsoid is much smaller than that of the corresponding conducting ellipsoid, even for large ϵ_{r} (as long as $N_{\mathrm{i}} \epsilon_{\mathrm{r}} \ll 1$).

The potential scattered by a dielectric ellipsoid is derived independently in [31, Section 3.27]. One can easily check that it is indeed related to the conducting case through (6.29).

6.3.5.3 Ellipsoid step-off response

We still consider an ellipsoid excited by a uniform electric field along one of its principal axis but we now want to assess the dynamics of the response for a step-off of the excitation field. To simplify the notations, from now on, we will drop the subscript i that was used to indicate the principal axis under consideration.

In the static case, we did not consider an ellipsoid that is both conducting and dielectric because the static field inside an (even imperfectly) conducting body is zero and the dielectric permittivity plays no role in the scattering. This is not true in the dynamic case and we now consider an ellipsoid that is both conducting and dielectric. In that case, the charge to consider on the ellipsoid boundary is $\rho = \rho^{\text{cond}} + \rho^{\text{diel}}$ with ρ^{cond} the free charge distribution appearing due to the conductivity and ρ^{diel} the bound charge distribution which is equivalent to the polarization P appearing inside a dielectric.

We consider a step-off at $t = 0$. Before the step-off, the excitation field was constant from an infinite long time: $E_{\text{inc}}(t < 0) = E_{\text{inc}}|_{0-}$. Therefore, the static solution for a conducting ellipsoid prevails and the ellipsoid electric permittivity plays no role. A free charge distribution $\rho^{\text{cond}}\big|_{0-}$ exists on the surface of the ellipsoid before the step-off. The total field inside the ellipsoid is null and, therefore, this surface charge distribution creates a field equal and opposite to the excitation field: $E_\rho^{\text{cond}}\big|_{0-} = -\,E_{\text{inc}}|_{0-}$.

Just after the step-off, the incident field becomes null but the free surface charge distribution remains unchanged $\rho^{\text{cond}}\big|_{0-} = \rho^{\text{cond}}\big|_{0+} = \rho^{\text{cond}}\big|_{0}$. Indeed, a current distribution appears instantaneously inside the ellipsoid, but as it is the derivative of the charge distribution that is related to the current, the charge distribution itself can not change instantaneously. Hence, the field produced by the surface free charge distribution is the same just before and just after the step-off: $E_\rho^{\text{cond,in}}\Big|_{0-} = E_\rho^{\text{cond,in}}\Big|_{0+} = -\,E_{\text{inc}}|_{0-}$.

After the step-off, the dielectric inside the ellipsoid will however be polarized very fast. Rigorously speaking, this polarization is not instantaneous and the full-wave solution should be used to compute the transient. We will however not consider this transient because it is much faster than the dynamics of interest[11]. After the step-off, the incident field is zero, but for the dielectric inside the ellipsoid, the field $\left.E_\rho^{\text{cond,in}}\right|_{0+}$ produced by the surface free charge distribution $\left.\rho^{\text{cond,in}}\right|_{0+}$ (which can be considered to be located just outside the ellipsoid), acts as an incident field. As discussed above, this field is further homogeneous. Hence, neglecting the transient, the polarization, or the equivalent surface charge distribution can be computed using the static solution for a dielectric ellipsoid derived in Section 6.3.5.2, considering an excitation $\left.E_\rho^{\text{cond,in}}\right|_{0+}$

According to (6.23), the dielectric solution is related to the conducting solution by a factor α. For a conducting ellipsoid and for an excitation $\left.E_\rho^{\text{cond,in}}\right|_{0+}$ produced by a charge distribution $\left.\rho^{\text{cond,in}}\right|_{0+}$ located just outside the ellipsoid, the charge distribution appearing on the surface is $-\left.\rho^{\text{cond,in}}\right|_{0+}$ (the charge distribution on the boundary then compensates the charge distribution just outside the ellipsoid and the resulting field inside the conducting ellipsoid is then zero as required). Hence, the bound charge distribution appearing just after the step-off is:

$$\left.\rho^{\text{diel}}\right|_{0+} = -\alpha \left.\rho^{\text{cond}}\right|_{0} \tag{6.30}$$

The field produced by the bound charges partly cancels the field produced by the free charges and the resulting total field inside the ellipsoid just after the step-off is:

$$\left.E_{\text{tot}}^{\text{in}}\right|_{0-} = -(1-\alpha)\left.E_{\text{inc}}\right|_{0-} \tag{6.31}$$

This field allows to compute the current just after the step-off: $\left.\boldsymbol{J}_{\text{in}}\right|_{0+} = \sigma \left.E_{\text{tot}}^{\text{in}}\right|_{0-} \hat{\boldsymbol{x}}_{\text{i}}$ which in turn allows to compute the variation of the surface free charge according to $\dfrac{\partial \rho^{\text{cond}}}{\partial t} = -\nabla \cdot \boldsymbol{J}$. This yields the following expression for the time derivative of the free charge distribution just

[11] To get an idea of the wave propagation duration, we consider an ellipsoid with a large semi-axis of 1cm and a relative permittivity of 80. In a homogeneous space with the same permittivity, a plane wave would travel across the ellipsoid dimension in about 0.6ns. This is much faster than any dynamics of interest with time constants in the order of several μs. Obviously wave propagation is different in the ellipsoid than in a homogeneous space. The wave propagation might be slower but, due to the large margin, the transient should still be fast enough to be neglected.

after the step-off:

$$\left.\frac{\partial \rho^{\mathrm{cond}}}{\partial t}\right|_{0+} = -\sigma \cos\theta (1-\alpha)\ E_{\mathrm{inc}}|_{0-} \tag{6.32}$$

With θ the angle between the ellipsoid normal and the incident field direction. Using (6.25) to express $E_{\mathrm{inc}}|_{0-}$ as a function of $\left.\rho^{\mathrm{cond}}\right|_0$ then yields

$$\left.\frac{\partial \rho^{\mathrm{cond}}}{\partial t}\right|_{0+} = -\frac{\sigma(1-\alpha)N}{\epsilon_0}\ \left.\rho^{\mathrm{cond}}\right|_0 \tag{6.33}$$

This expression is valid for any point on the surface (the term $\cos\theta$ has been canceled out) and therefore, a small time after the step-off, the shape of the charge distribution will remain unchanged and the field will remain uniform inside the ellipsoid. Therefore, the reasoning leading to (6.33) may be repeated from time step to time step and (6.33) is therefore valid at all time after the step-off[12]:

$$\frac{\partial \rho^{\mathrm{cond}}}{\partial t} = -\frac{\sigma(1-\alpha)N}{\epsilon_0}\rho^{\mathrm{cond}} \tag{6.34}$$

Equ. (6.33) describes a first order system. The free charge distribution decreases at each point as $\rho^{\mathrm{cond}}(t) = \left.\rho^{\mathrm{cond}}\right|_0 e^{-\frac{t}{T}}$ with:

$$T = \frac{\epsilon_0}{\sigma}\frac{1+N_{\mathrm{i}}(\epsilon_{\mathrm{r}}-1)}{N_{\mathrm{i}}} \tag{6.35}$$

the time constant of the response. A similar expression can be found in [71, Equ. 5.28 p. 119] where the process is called a Maxwell-Wagner relaxation.

To compute the scattered field, the total charge $\rho = \rho^{\mathrm{cond}} + \rho^{\mathrm{diel}}$ needs to be computed. We have seen that the bound charge distribution is null before the turn-off and it jumps instantaneously to $\left.\rho^{\mathrm{diel}}\right|_{0+} = -\alpha\ \left.\rho^{\mathrm{cond}}\right|_0$ after the step-off. Hence, the total charges is $\rho|_{0-} = \left.\rho^{\mathrm{cond}}\right|_0$ before the step-off and it then jumps instantaneously to:

$$\rho|_{0+} = (1-\alpha)\ \left.\rho^{\mathrm{cond}}\right|_0 \tag{6.36}$$

[12]This is an intuitive reasoning but the result may be demonstrated by first assuming that (6.33) is valid at all time. As shown below, all quantities then exhibit an exponential decay. Therefore, the inner field remains homogeneous for all time $t > 0$ and for such a homogeneous field, (6.33) is indeed valid for all time $t > 0$, thus as first assumed.

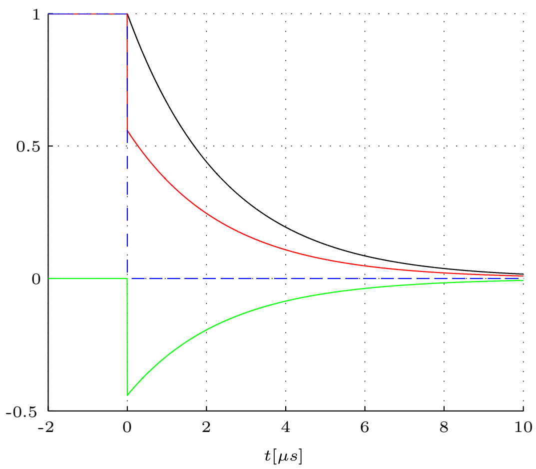

Figure 6.15: *Normalized bound charge* $\rho^{\text{diel}}/\left.\rho^{\text{cond}}\right|_0$ *(green), free charge* $\rho^{\text{cond}}/\left.\rho^{\text{cond}}\right|_0$ *(black) and total charge* $\rho/\left.\rho^{\text{cond}}\right|_0$ *(red) for a step-off excitation (blue) on an ellipsoid with relative permittivity* $\epsilon_{\text{r}} = 80$*, conductivity* $\sigma = 650\mu S$ *and depolarization factor* $N = 0.01$*. The corresponding* α *is about* 0.44*.*

The total charge then decreases exponentially with a time constant T. This is illustrated in Fig. 6.15 for typical tap water parameters ($\sigma = 650\mu S$ and $\epsilon_{\text{r}} = 80$) and for a depolarization factor $N = 0.01$.

6.3.5.4 Ellipsoid general excitation

We now consider a general time variation for the excitation and we also consider incident fields that are not rigorously uniform on the ellipsoid. The analytic solution developed in the previous sections is only valid for uniform fields but we assume that a reasonable approximation[13] can be

[13]This can be justified for a sphere in the light of modal expansion [31, Sections 9.22 – 9.24]. The uniform contribution is then the first order in the field expansion and this yield the dominant pole to the response. The other field components will yield higher order poles that may be irrelevant if they are out of the bandwidth of the detector. The same analysis may be performed for an ellipsoid but this is relatively complex to implement because ellipsoidal harmonics are involved. Furthermore, in ellipsoidal coordinates, only the scalar solution (that can be used for the electric potential) exists. The wave equation, to be used for the fields, is not separable. We did not investigate this modal expansion further but the analogy with the sphere gives us additional confidence in the approximation used.

obtained by considering the spatial average of the excitation, computed on the axes of the ellipsoid:

$$E_{\mathrm{inc,i}} = \langle \boldsymbol{E}^{\mathrm{inc}} \rangle_i = \frac{1}{2a_{\mathrm{i}}} \int_{\mathcal{A}_{\mathrm{i}}} \boldsymbol{E}_{\mathrm{inc}} \cdot \mathrm{d}\boldsymbol{\ell} \tag{6.37}$$

with $\mathcal{A}_{\mathrm{i}}$, the axis considered and a_{i}, half its length. The average excitation may be computed efficiently from the potential without the need for any integration:

$$\langle \boldsymbol{E}_{\mathrm{inc}} \rangle_i = \frac{\phi_{\mathrm{inc}}(\boldsymbol{a}_{\mathrm{i}}^{-}) - \phi_{\mathrm{inc}}(\boldsymbol{a}_{\mathrm{i}}^{+})}{2a_{\mathrm{i}}} \tag{6.38}$$

with $\phi_{\mathrm{inc}}(\boldsymbol{a}_{\mathrm{i}}^{-})$ and $\phi_{\mathrm{inc}}(\boldsymbol{a}_{\mathrm{i}}^{+})$ the incident potential at the two extremities of the axis i.

In practice, we will only consider the response for the excitation component along a single axis. The other contributions will be either null or yield responses that decay too fast to have a measurable effect in the integration window. We may therefore again drop the subscript i without any confusion.

A general time-domain excitation may then be characterized by:

$$u(t) = \langle \boldsymbol{E}^{\mathrm{inc}}(t) \rangle \tag{6.39}$$

To get general expressions, in the previous section, we have used x_{i} and a_{i} to denote the coordinate axes and the corresponding ellipsoid semi-axis length respectively. From now on, to get simpler expressions, we will denote those quantities x, y, z and a, b, c respectively. Referring to Fig. 6.17, the axes x and z are horizontal and vertical and y is perpendicular to the figure. The length of the horizontal and vertical semi-axes are thus a and c respectively and the length of the third semi-axis, which is not visible on the cut, is b.

We have seen that for a step-off excitation, the spatial distribution of the field is at all time proportional to the static solution for a conducting ellipsoid. This remains valid for a general time variation of the excitation because the general solution is related to the step-off solution through a time-domain convolution. Hence, for a general time-domain excitation characterized by $u(t)$, the field scattered by the ellipsoid at any point $\boldsymbol{r}$ is proportional to a scalar function $y(t)$:

$$\boldsymbol{E}_{\rho}^{\mathrm{out}}(t)(\boldsymbol{r}) = y(t)\check{\boldsymbol{E}}_{\rho}^{\mathrm{cond,out}}(\boldsymbol{r}) \tag{6.40}$$

with $\check{\boldsymbol{E}}^{\text{cond,out}}$ the static field scattered by a conducting ellipsoid for a unit excitation along the considered principal axis. $y(t)$ is further related to $u(t)$ through a transfer function that can easily be computed from the step-off response:

$$H(s) = \frac{Y(s)}{U(s)} = \alpha + \frac{(1-\alpha)}{1+sT} = \frac{1+\alpha T s}{1+sT} \tag{6.41}$$

with $H(s)$ the transfer function and $U(s)$ and $Y(s)$ the Laplace transform of $u(t)$ and $y(t)$. $H(s)$ has a unit gain, a pole in $s = -1/T$ and a zero in $s = -1/(\alpha T)$. As α is smaller than one, the zero is on the left of the pole. The relative position of the zero and the pole indicates the importance of the dielectric response. The further the zero is to the left, the less important is the dielectric response. At the limit, when the dielectric response gets very small ($\alpha \simeq 0$) and the zero moves towards minus infinity.

$y(t)$ was defined in (6.40) as the ratio between the electric field scattered for a general excitation and that scattered for a unit static excitation. Obviously, the same $y(t)$ also relates the scattered potential and the total surface charge distribution to their static solution counterpart. Hence $H(s)$ fully characterizes the dynamics of the ellipsoid along the direction considered. The response $y(t)$ is illustrated for a step excitation $u(t)$ in Fig. 6.16. Typical tap water parameters ($\sigma = 650\mu S$, $\epsilon_{\text{r}} = 80$) are considered together with various depolarization factors. One sees that decreasing the depolarization factor has two effects. It increases the time constant and it decreases the direct feedthrough. For comparison, we have also shown the same responses for free space permittivity $\epsilon_{\text{r}} = 1$. This clearly shows that increasing the dielectric permittivity increases the direct feedthrough and increases the time constant. The effect of the permittivity however decreases when the depolarization factor is decreased. For small depolarization factors, the permittivity has little effect.

As the slow-time response is obtained by integrating the fast-time response in the evaluation window, a few μs after the TX pulse, the direct feedthrough does not affect the slow-time response. It is only the exponential part of the response that can affect the response. For a tap water spherical droplet ($N = 1/3$, $\epsilon_{\text{r}} = 80$, the red dashed curve in Fig. 6.16), the amplitude of this exponential part is very small and the response is far too fast to yield a slow-time response. With smaller depolarization factor however, the amplitude of the exponential contri-

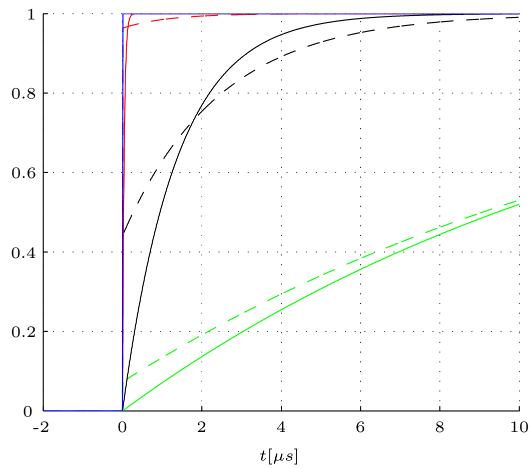

Figure 6.16: *Ellipsoid step response $y(t)$ for $\sigma = 650\mu S$ and depolarization factors of $1/3$ (red), $1/100$ (black) and $1/1000$ (green). Dielectric relative permittivity $\epsilon_{\mathrm{r}} = 1$ (—) and $\epsilon_{\mathrm{r}} = 80$ (- -) are considered. The excitation $u(t)$ is also shown in blue.*

bution is larger, the response is slower, and the droplet might produce a significant contribution to the slow-time response.

6.3.5.5 Ellipsoid state-space model

Our objective is to expand the state-space model of the detector developed in Chapter 3 to incorporate the effect of an ellipsoidal water layer. We consider the geometry presented in Fig. 6.17 which is representative of a thin layer of water below the RX coil[14] with a unit excitation along the x-axis. A vertical cut through the RX coil is shown. The problem is essentially 2D and the third dimension of the ellipsoid (y) is chosen large when compared to the other dimensions.

Only the response for an excitation along the x axis is of interest. Indeed, by symmetry, the component of the incident electric field (which is produced by the coils) along the y-axis (tangent to the coil) is zero. Furthermore, the depolarization factor is smaller than $1/3$ along x and larger than $1/3$ along z (the sum of the three depolarization factors is

[14]A water layer below the TX coil must also be considered because, as will be shown, both responses have the same order of magnitude. The development presented for the RX coil can be easily transposed to the TX case.

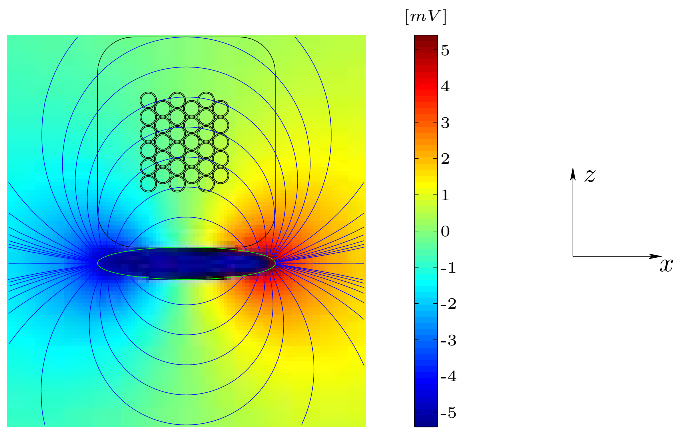

Figure 6.17: *Geometry considered to model a thin water layer. A vertical cut through the RX coil is shown together with an ellipsoid modeling the water layer. The potential scattered by the conducting ellipsoid for a static unit excitation along x and the corresponding electric field streamlines are also shown.*

one and the depolarization factor along y is very small because the corresponding ellipsoid axis is chosen much longer than the other axes.). The response will thus be faster than a sphere for an excitation along z and slower for an excitation along x and we have seen that the response for a sphere is too fast to yield a measurable effect. Hence, only the response for a horizontal excitation may be slow enough to yield a significant slow-time response.

We have seen that an ellipsoidal water layer can be modeled as a first order target and its transfer function (6.41) can be computed from the layer geometry and electrical properties. Its state-space model can easily be derived from this transfer function but we still have to establish the way the state-space model of the water layer must be connected to the state-space model of the detector. The result is shown in Fig. 6.18 where one sees that the input of the water layer model is connected to $V_{\mathrm{C}}^{\mathrm{RX}}$ (the voltage across the capacitance of the RX coil equivalent circuit) which is a state variable of the detector model and the output is connected to e_{C} which is an input of the detector model that was introduced to take into account the voltages induced in the coil by an electric field (see Fig. 2.18). The feedback in the model is used to take

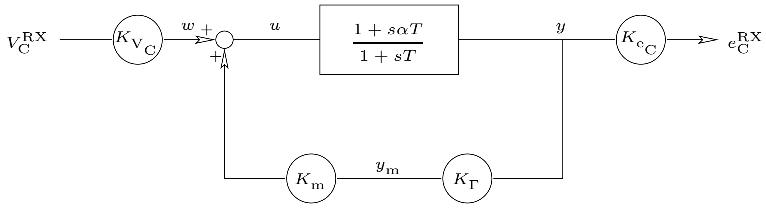

Figure 6.18: *State-space model of the water layer showing its connections to the detector state-pace model via $V_{\mathrm{C}}^{\mathrm{RX}}$, a coil state-variable and $e_{\mathrm{C}}^{\mathrm{RX}}$, a coil input variable. y characterizes the field scattered by the water layer and y_{m} characterizes the field scattered by the mirror layer.*

into account the multiple reflections[15] between the detector casing and the water layer. We will now justify the proposed model and establish the expression for the coupling gains ($K_{\mathrm{e_C}}$, $K_{\mathrm{V_C}}$, K_{Γ} and K_{m}).

Output connection The voltage $e_{\mathrm{C}}^{\mathrm{RX}}$ induced in the RX coil can be computed from the potential scattered by the water layer according to (2.58). This involves a discrete summation on the MAS equivalent sources for the casing outer region. The scattered potential is proportional to $y(t)$ and, according to (2.58), the induced voltage is therefore also proportional to $y(t)$. The proportionality factor is denoted $K_{\mathrm{e_C}}$ and it can be computed by using $\check{\phi}_{\rho}^{\mathrm{cond,out}}$ (the potential scattered by a conducting ellipsoid for a unit static excitation) in (2.58). Rigorously speaking, a voltage e_{C} is induced in both the TX and RX coils. However, for the configuration considered, in which the water layer is below the RX coil, the voltage induced in the RX coil is much larger than that induced in the TX coil and considering only the voltage induced in the RX coil yields a good approximation.

[15]The concept of multiple reflections is in general used in the context of wave propagation. It can nevertheless be used for the EQS problem at hand. Indeed, although it has been neglected to obtain the EQS approximation, wave propagation and hence multiple reflections do exist physically. Neglecting the propagation delays, the multiple reflections yield an algebraic series for the field incident on the ellipsoid: $E_{\mathrm{inc}} = (1 + R + R^2 + \cdots)E_{\mathrm{inc}}^0$ with E_{inc}^0, the incident field in absence of multiple reflections and $R^n E_{\mathrm{inc}}^0$ the additional incident field due to the n^{th} reflection. The series expansion can be rewritten to yield: $E_{\mathrm{inc}} = E_{\mathrm{inc}}^0/(1 - R)$ which shows that the multiple reflections can indeed be modeled by a feedback R.

Input connection The input of the water layer model must be connected to ensure that $u(t) = \langle \boldsymbol{E}_{\text{inc}}(t) \rangle$. The incident field to consider is that *in presence* of the water ellipsoid $\boldsymbol{E}_{\text{inc}}^{(\text{e})}$ and, due to the multiple reflections existing between the ellipsoid and the coil, this field may differ significantly from $E_{\text{inc}}^{(\text{fs})}$. The multiple reflections may be important because the water layer is very close to the coil. We first consider the case without multiple reflections. Then we will show that the multiple reflections can be taken into account by introducing a feedback in the model.

Without multiple reflections, the incident field is[16] $\boldsymbol{E}_{\rho_{\text{RX}}}^{(\text{fs})}$. This field can be computed from the charge distribution on the RX coil which was computed in Section 2.2.1 by resorting to the MAS as illustrated in Fig. 2.8 for the TX coil. The incident field is proportional to the RX capacitor voltage V_{C}^{RX} and the proportionality factor is denoted K_{V_C}. It can be computed by plugging the incident field (or potential) for a unit RX capacitor voltage ($V_{\text{C}}^{\text{RX}} = 1$) in (6.38).

Feedback connection Let us now introduce the multiple reflections. The field back-scattered by the detector head for a given charge distribution on the ellipsoid might be computed using the MAS but this would be computationally intensive as many ellipsoid geometries need to be considered and the MAS solution computed for all the considered geometries.

To avoid this pitfall, and to get a better understanding of the underlying physics, we use a simplified model in which the detector head is replaced by a homogeneous dielectric HS (with electric permittivity equal to that of the head casing). The back-scattered field may then be computed by resorting to the image theory [65, Section 2.14][35, Section 3.4]. Obviously, the half-space model is a crude approximation but we still expect to get a good order of magnitude for the back-scattered field. More research might be needed to check the accuracy of the approach.

[16]Rigorously speaking, the total free space electric field generated by the coil must be considered. It includes the contribution of the charges on the coil but also the contribution of the magnetic potential $j\omega\boldsymbol{A}$. Furthermore, both the contribution of the TX and the RX coils must be considered. The magnetic potential is however transverse and has thus no component along the principal direction considered and, the field generated by the TX coil charges is much smaller than that generated by the RX coil charges for the configuration considered in which the water layer is below the RX coil.

We thus consider a homogeneous upper dielectric HS with relative permittivity equal to that of the casing ($\epsilon_{\mathrm{r,c}}$) and a lower HS with free space permittivity. According to the image theory, the field back-scattered by the upper HS is then equal to that produced by a mirror charge distribution ρ_{mirror} located in the upper HS and related to the physical charge distribution $\rho_{\mathrm{ellipsoid}}$ (which is located in the lower HS on the boundary of the water ellipsoid) by:

$$\rho_{\mathrm{mirror}}(x, y, z) = K_\Gamma \rho_{\mathrm{ellipsoid}}(x, y, -z) \tag{6.42}$$

where K_Γ is given by [65, Equ. 2.150]:

$$K_\Gamma = -\frac{\epsilon_{\mathrm{r,c}} - 1}{\epsilon_{\mathrm{r,c}} + 1} \tag{6.43}$$

The mirror charge distribution is identical to the distribution that would appear on a mirror ellipsoid [17] located in free space and excited by an incident field $K_\Gamma E_{\mathrm{inc}}$ with E_{inc} the total incident field (including multiple reflections) on the physical ellipsoid. The field back-scattered by the casing is thus:

$$\boldsymbol{E}_{\mathrm{m}} = y_{\mathrm{m}}(t)\check{\boldsymbol{E}}_{\mathrm{m}} \tag{6.44}$$

with $\check{\boldsymbol{E}}_{\mathrm{m}}$ the field scattered by the mirror (conducting) ellipsoid for a static unit incident field and $y_{\mathrm{m}}(t) = K_\Gamma y(t)$. The potential $\check{\phi}_{\mathrm{m}}$, corresponding to $\check{\boldsymbol{E}}_{\mathrm{m}}$, can be computed by resorting to the analytic solution (6.28).

Finally, the contribution of the multiple reflections to the incident field on the water layer is proportional to $y_{\mathrm{m}}(t)$. The proportionality factor is denoted K_{m} and it can be computed by introducing $\check{\phi}_{\mathrm{m}}$ in (6.38).

In summary, the multiple reflections can be taken into account by introducing a feedback $K_{\mathrm{f}} = K_\Gamma K_{\mathrm{m}}$ as shown in Fig. 6.18. The effect of the feedback on the location of the poles and the zeros of the system as a function of the feedback gain is illustrated in Fig. 6.19. As expected, the zero remains unaffected and the pole moves to the right. The pole becomes unstable for a feedback $K_{\mathrm{f}} = 1$. An unstable system is only possible if power is introduced via active components. The casing is a passive system that back-scatters only part of the incident energy.

[17] The ellipsoid obtained by plane symmetry trough the HS interface and having the same EM properties as the physical droplet ellipsoid

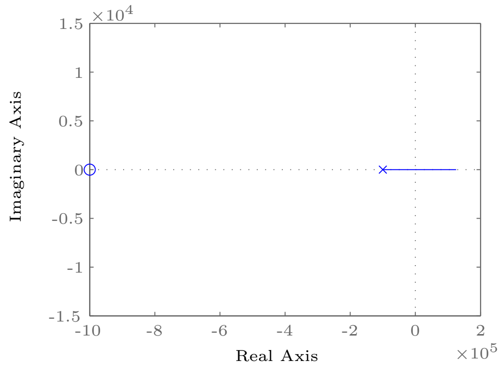

Figure 6.19: *Root locus for the water layer model as a function of the feedback gain $K_\mathrm{f} = K_\Gamma K_\mathrm{m}$. The open-loop transmittance parameters are $T = 1\mu s$ and $\alpha = 0.1$ and the gain K_f varies between 0 and 2. The zero (o) is not affected by the feedback. The pole locus is a line starting at the open-loop pole (x) and extending to the right. The closed-loop pole is at the origin (limit of stability) for $K_\mathrm{f} = 1$.*

Therefore, the feedback gain is always smaller than one and the closed-loop system remains stable. This was confirmed by our simulations.

The closed loop transfer function between w and y is:

$$H_\mathrm{cl} = K_\mathrm{cl} \frac{1 + s\alpha T}{1 + sT_\mathrm{cl}} \tag{6.45}$$

with $K_\mathrm{cl} = 1/(1 - K_\mathrm{f})$ and $T_\mathrm{cl} = T(1 - K_\mathrm{f}\alpha)/(1 - K_\mathrm{f})$, the closed-loop gain and time constant. This shows that the effect of the multiple reflections is thus to amplify and to slow down the response of the water layer.

6.3.5.6 Tap water response

The state-space model of the detector, extended in the previous section to include the water layer model, can be used to compute the fast-time response as a function of the layer thickness ($2c$) and the water EM properties. We have considered a conductivity $\sigma = 650\mu S$ and a relative permittivity $\epsilon_\mathrm{r} = 80$ typical for tap water. The maximum deviation of the response (when compared to the reference response obtained in absence of water) is shown in Fig. 6.20 as a function of the water layer

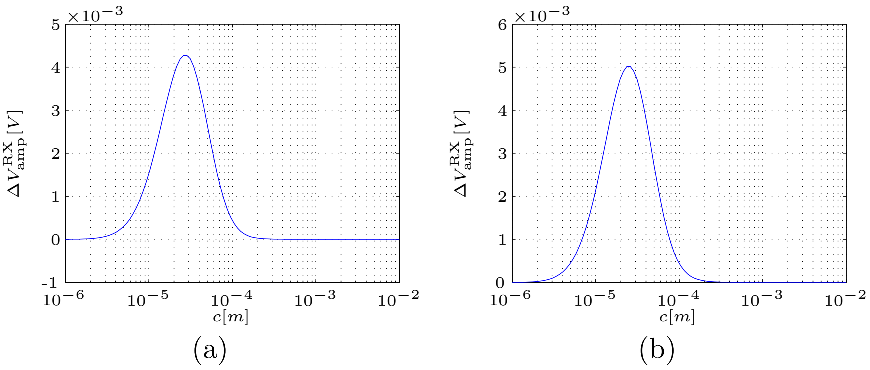

Figure 6.20: *Maximum deviation of the fast-time response for tap water ($\sigma = 650\mu S$, $\epsilon_{\mathrm{r}} = 80$) as a function of the ellipsoid semi-axis c (characterizing the water layer thickness). The other ellipsoid semi-axes are kept constant at $a = 5.5mm$ and $b = 10cm$. Water layers below the TX (a) and RX (b) coils are considered.*

thickness characterized by the ellipsoid semi-axis c and for a water layer below the TX and below the RX coil separately. One sees that the contributions of water layers below the TX and the RX coils have the same order of magnitude and that they both have a marked maximum for a layer semi-axis of about 20 to 30 microns. The corresponding response is about $5mV$. Similar responses are obtained for water layers above the coils. Hence, as in practice, we expect four layers to exist: one below and one above each coil, the total computed response is $20mV$.

The corresponding fast-time response is shown in Fig. 6.21 together with the response measured for a conductivity of $650\mu S$, representative of tap water. The magnitude of the computed water response is underestimated and we have therefore artificially multiplied that response by a factor of five for better visibility. One sees that apart from this factor of five, the computed response is very close to the measured one. The dynamics and the polarity of the response are well predicted.

To better understand the effect of the water layer thickness, we have shown in Fig. 6.22, a number of parameters influencing the response as a function of the ellipsoid semi-axis c. The curves are very similar for a water layer below the TX and the RX coil and we therefore only present the RX case.

The time constant of the water layer has a major impact on the slow-

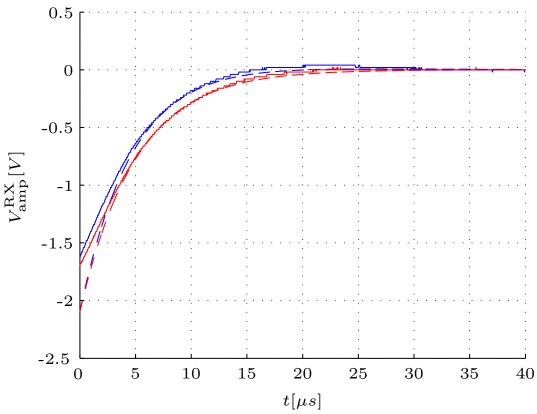

Figure 6.21: *Measured (—) and computed (– –) fast-time response with (blue) and without (red) a water layer. The water layer is characterized by $\sigma = 650\mu S$, $\epsilon_{\mathrm{r}} = 80$ and has the thickness that yields the largest response deviation. The water response is computed taking into account four water layers and, further, artificially multiplied by a factor 5.*

time response. As discussed in Section 3.3.5, the detector is sensitive to electric targets with time constants around $10\mu s$. The response of faster targets has decayed too much before the evaluation window starts and the TX pulse does not last long enough to significantly excite slower targets. Fig. 6.22 (d) shows that the (closed loop) time constant for a layer thickness yielding the largest response deviation (about 60 microns, $c = 30\mu m$) is indeed in the order of $10\mu s$. One also sees in Fig. 6.22 (a) that the depolarization factor increases with the water layer thickness and this explains the decrease of the time constant with c. Furthermore, the closed loop time constant is larger than the open-loop one and the difference is the largest for thin water layers. This difference is due to the multiple reflections which are indeed the strongest for thin water layers as confirmed by the feedback gain curve (K_{f}) shown in Fig. 6.22 (c).

Figure 6.20 shows that the deviation of the fast-time response decreases for thick water layers. As just discussed, this may be explained by the water layer time constant that becomes too large. A number of other factors also come into play. First, as already discussed, the multiple reflections become weaker and this reduces the magnitude of the fast-time response. Second, as seen in Fig. 6.22 (b), α increases

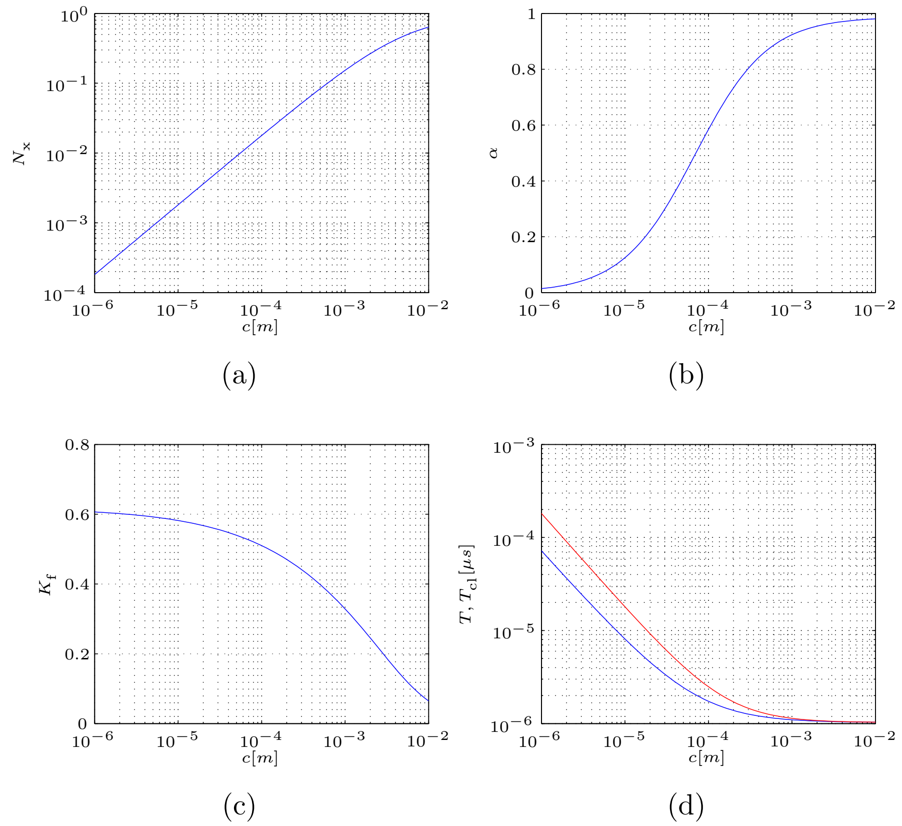

Figure 6.22: *Depolarization factor N_x, instantaneous response α, feedback gain K_f characterizing the multiple reflections together with the open (blue) and closed (red) loop time constants T and T_{cl} as a function of the water ellipsoid semi-axis c.*

and, as a result, the magnitude of the exponential part of the response $(1-\alpha)$ decreases. As only this exponential part (and not the direct feedthrough) contributes to the response in the listen phase, the largest deviation decreases when α increases. Note that the increase of α is related to the decrease of the depolarization factor. Finally, the water is on average further from the coil for thicker water layer and, therefore, the direct excitation decreases.

6.3.5.7 Effect of water conductivity

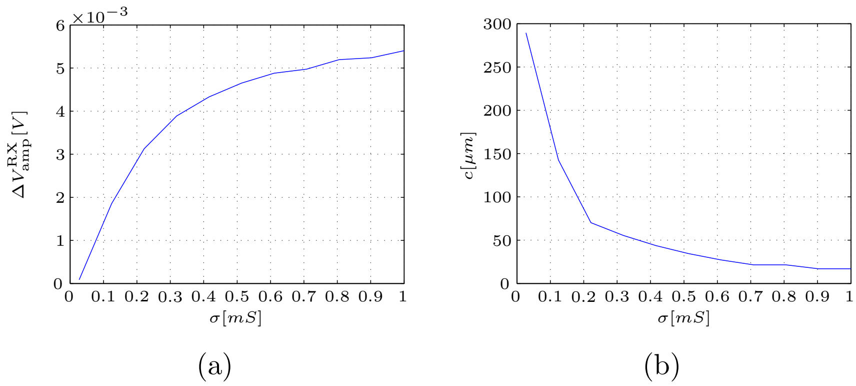

Figure 6.23: *Maximum deviation of the fast-time response as a function of the water conductivity for a single layer below the RX coil. The water layer thickness yielding the largest deviation is considered for each conductivity. The corresponding ellipsoid semi-axis c is also shown.*

Proceeding as in the previous Section for tap water but with other water conductivities, we have computed the maximum deviation of the fast-time response as a function of the water layer conductivity and thickness. For each conductivity, the thickness yielding the largest water response has been computed and is shown in Fig. 6.23 (b). The corresponding maximum deviation of the fast-time response is shown in Fig. 6.23 (a). Note that a single layer below the RX coil has been considered and the deviation should thus be multiplied by a factor of about four to take into account the water layers below and above the two coils.

The maximum response deviation was also measured for various conductivities (see blue curve Fig. 6.2). Unfortunately the computed curve is not compatible with the measured one. Indeed, the computed curve does not decrease for higher conductivities. Such a decrease can however be understood because, as shown in Fig. 6.23 (b), the thickness of the required water layer decreases with conductivity. For large conductivities, the required layer thickness may become unrealistically small. In practice, the water layer will break before reaching the required thickness, yielding water layers with smaller extent and non-'optimal' thickness and hence a smaller response.

The computed curve also shows a decrease of the response for small conductivities. Such a decrease is not shown by the measurements. As already discussed, in the scope of the simple circuit model presented in Section 6.3.4, such a decrease may nevertheless exist for conductivities smaller than that of the distilled water used and not available for the measurements. Even if this is the case, the model has a problem because it predicts a large decrease of the response for conductivities that were used for the measurements and this decrease was not observed. The reason for this discrepancy might be that, for lower conductivities, the higher order modes that were neglected in the model, start to dominate the response. For tap water, the higher modes (which are faster than the first order mode) are too fast to yield a significant response but for distilled water, the first order modes are getting too slow and the faster higher order modes may become important. Further investigation is needed to clarify those issues.

CHAPTER 7

Electromagnetic background influence

The EM background can significantly affect EMI detectors. This is confirmed by filtering techniques that are implemented on some metal detectors to mitigate the effect of power lines at 50 or 60 Hz. In addition, some of the newest metal detectors further minimize the effect of the background by automatically adjusting the PRF according to the dominant background.

This Chapter investigates the effect of the EM background. First the relation between an (harmonic) external field and the slow-time response is established as a function of the field frequency and amplitude. The result is more complex than might be expected at first sight because the external field influences the location of the evaluation window. As a result, two contribution to the response must be considered: a steady-state and a transient contribution.

The various effects that the EM background can have on the detector are discussed and related to possible counter-measures. The critical frequency band in which the EM background may significantly affect the detector is then defined according the maximum allowed fields. Finally, two important test-cases are investigated into more details: the effect a high voltage power line and the effect of fluorescent lamp with a high-frequency electronic ballast.

Contents

7.1 Introduction

A metal detector is a very sensitive device and the EM background may produce a significant response. The most common effect of the EM background is the generation of an erratic audio signal. The operator will in general set the sensitivity at the maximum value that does not yield any audio signal in absence of a target. The usable sensitivity is limited by the dominant noise source. This limitation may be due to the soil, but for neutral soils, the limitation will come from the EM background. It is thus important to understand the response of the detector to an EM background.

For large external fields, the effect on the detector may become quite complex because nonlinearities come into play. In extreme situations, the detector may completely stop working, and in the worst case, there may be no signal to warn the operator. Those nonlinear effects will be briefly discussed in Section 7.2. We will then focus on smaller fields, that are more representative of typical EM backgrounds encountered in practice, and for which the fast-time response remains linear. The model developed in Chapter 3 can then be used, without further adaptation, to compute the fast-time response.

This will be discussed in Section 7.3 where we will show that the problem is more complex than expected at first look because the detector behavior is characterized by a number of phases and several linear state-space model must be used; one for each phase. Rigorously speaking, for a given external field, a time-domain simulation must be performed through all the phases to get the fast-time response. This is not convenient because a large EM spectrum must be considered. Furthermore, various phases between the external field and the TX pulse must also be considered because the field is in general asynchronous with the TX pulses and this phase significantly affects the response. We will however show that the fast-time response to the external field can be decomposed in a transient and a steady state contribution and that those contributions can be computed from the listening-phase transfer function, without having to perform the complete time-domain simulation.

It is the slow-time response that is used to generate the audio signal, possibly after slow-time filtering. This slow-time signal will be computed in Section 7.4 where we will show that there also nonlinearities may come into play. Indeed, the slow-time response is obtained by integrating the fast-time signal in the evaluation window and this window starts when the fast-time signal reaches a given threshold. Hence, the external field may affect the time-domain location of the evaluation window and this yields nonlinear effects. When the displacement of the evaluation window can be neglected, regular sampling theory can be used to compute the slow-time response. We will then show that the slow-time response to a sinusoidal field is a discrete sinusoid with a frequency that is in general different from that of the external field due to the aliasing.

The conditions on the external field to meet the regular sampling assumption will be discussed in Section 7.5. Section 7.6.1 then discusses the practical effects of the external field on the detector and Section 7.6.2 presents a number of counter measures that can be implemented to mitigate those effects.

A metal detector works in the audio frequencies and we therefore expect a limited critical bandwidth, that is the frequency band to which the detector is sensitive, to be limited. This critical frequency band is discussed in Section 7.7 in the light of the existing legislation which limits the magnitude of the fields to which the public may be exposed.

Finally, two test cases will be discussed in Section 7.8. First, a high voltage line will be considered because it is well known that such lines may perturb metal detectors; as confirmed by the fact that some detectors are specifically designed to mitigate their effect. Second, a fluorescent lamp with a high frequency electronic ballast will be considered because this was the major noise source encountered while performing measurements on the detector.

7.2 Nonlinear effects

High external fields may introduce nonlinear effects that severely affect the detector functioning. In extreme cases, the external field may trigger the flyback diode during the coil charge phase. The coil would then be short-circuited and this will affect the TX pulse or even destroy the electronics.

Lower (but still large) fields may trigger the clamping diodes in the RX filtering and conditioning network. This may completely jeopardize the normal behavior of the amplifier even if the frequency is above the bandwidth of the amplifier. Indeed, in the presence of nonlinearities, the high frequency induced voltage affects the lower frequency components of the response (generation of sub-harmonics). This can easily be understood for large high-frequency induced voltages, when compared to the reference voltages observed in absence of external field. Indeed, the input of the amplifier will be clamped for most of the time and it will thus look like a clock signal oscillating between the upper and lower clamped voltages (typically $0.6V$) at the frequency of the external field. For the amplifier, this is equivalent to a zero input and no alarm will be generated, even in presence of a target.

Such a behavior was observed in presence of jammers. Other complex interactions with the jammer were also observed. We will however not discuss the effect of jammers further because the focus of this thesis is on humanitarian demining. Furthermore, our investigation on jammers only started recently; a lot of work remains to be done and the subject is rather sensitive. Going into more details may require classification of the work.

For even lower (but still high) fields, nonlinear effect will be observed at the output of the amplifier. Indeed, the external field may produce additional saturation phases of the amplifier. For fast variations, slew rating may also be observed. In presence of such nonlinearities, the response becomes much more complex and one may expect that most of the filtering techniques used to mitigate the effect of the EM-background (see Section 7.6.2) won't work anymore.

Apart from critical cases, as may occur in the presence of jammers and other fields that are large enough to generate nonlinearities, the audio output will become erratic. The operator is then aware that the detector is unusable in the prevailing environment.

We will not consider the effect of the above-mentioned nonlinearities further. Moderate fields may however introduce a nonlinearity on the slow-time response, even in absence of any saturation of the fast-time response. This is due to the fact that the slow-time response is obtained by averaging the fast-time signal in the evaluation window and this window starts when the fast-time response reaches a given threshold. As a consequence, the external field may affect the location of the evaluation window. As further discussed in Section 7.4, the displacement of the evaluation window renders the computation of the slow-time response more complex and, as discussed in Section 7.6.1, it may also affect the target response. The conditions under which the displacement of the evaluation window may be neglected will be discussed in Section 7.5.

7.3 Fast-time response

We consider external fields that are small enough to yield a linear fast-time response. The model developed in Chapter 3 can then be used to compute the fast-time response from the voltage e_{L} and e_{C} that are induced respectively by a magnetic or an electric field. Recall that the detector fast-time response is modeled by a number of linear state-space models; one for each phase. In each phase, the response is the sum of a transient and a steady state contribution. For a monochromatic sinusoidal external field, the steady state contribution can easily be computed from the frequency response of the corresponding phase, but the transient contribution is a weighted sum of the phase modes and the weights are a function of the initial conditions. Those initial conditions are obtained from the value of the state variables at the end of the previous phase and can thus in general not be computed from the phase transfer function alone.

Note however that at the beginning of the listening-phase, only the amplifier changes state. The state-space representation of the circuit in front of the amplifier remains unchanged[1]. The last state change of that front circuit was the blocking of the clamping diode (beginning of phase 4, when the filter starts to be active). This phase started more than $10\mu s$ before the amplifier goes out of saturation and the only excitation during those $10\mu s$ is due to the monochromatic external field. As all the modes of the circuit in front of the amplifier are much faster than $10\mu s$, the transient has vanished at the beginning of the listening-phase. Hence during the listening-phase, the input of the amplifier can be approximated by the steady state solution which can be computed from the listening-phase frequency response alone. No transient needs to be considered. However, for the output of the amplifier, the transient contribution is not negligible. Fortunately, if the amplifier is modeled as a first order system, the transient can be computed from the initial value of the amplifier output alone and, as the listening-phase begins when the amplifier gets out of saturation, this initial condition is simply the saturation voltage V_{sat}. The transient can thus be computed without having to run a time-domain simulation through all phases. This is a major advantage because many external field frequencies and phases will have to be considered and running a complete time-domain simulation

[1] It is not affected by the amplifier state because the amplifier has a high input impedance.

for each case would be computationally expensive. Note that a simple analysis would neglect the transient contribution but we will show that this is inaccurate because the transient contribution dominates the response for frequencies larger than about 50kHz.

Formally, we have:

$$V_{\mathrm{amp}}^{\mathrm{RX}}(t) = V_{\mathrm{fast}}^{\mathrm{r}}(t) + V_{\mathrm{fast}}^{\mathrm{t,tot}}(t) = V_{\mathrm{fast}}^{\mathrm{r}}(t) + V_{\mathrm{fast},\ell}^{\mathrm{t}}(t) + V_{\mathrm{fast},\ell}^{\mathrm{t0}}(t) \tag{7.1}$$

with $V_{\mathrm{fast}}^{\mathrm{r}}(t)$ and $V_{\mathrm{fast}}^{\mathrm{t,tot}}(t)$, respectively the steady state and transient contribution. The superscript 'tot' indicates that it is the total transient contribution which is the sum of the reference transient ($V_{\mathrm{fast},\ell}^{\mathrm{t0}}$), that exists in absence of any external field, and the transient contribution due to the external field $V_{\mathrm{fast},\ell}^{\mathrm{t}}$. The subscript ℓ is used to indicate that it is the listen phase transient contribution that is considered and to emphasize that the latter is a function of the phase considered and the corresponding threshold voltage (here the listen phase with a threshold voltage V_ℓ but, below, we will also consider the response defined with respect to the evaluation phase). The reference transient response ($V_{\mathrm{fast},\ell}^{\mathrm{t0}}(t)$) is indeed a function of the phase chosen (here, the listen phase) because, by definition, it is the response existing in absence of any external field *shifted* in a way that the beginning of the reference listen phase response matches the beginning of the listen phase response in presence of the external field. The shift is $t_\ell - t_{\ell 0}$ with t_ℓ and $t_{\ell 0}$ the beginning of the listen phase, respectively in presence and in absence of the external field. For the first order system considered, the reference transient can be written:

$$V_{\mathrm{fast},\ell}^{\mathrm{t0}}(t) = V_\ell e^{-(t-t_\ell)/T_{\mathrm{amp}}} \tag{7.2}$$

with T_{amp}, the amplifier time constant. Note that t_ℓ is a function of the amplitude and phase of the external field considered.

As the transient $V_{\mathrm{fast},\ell}^{\mathrm{t}}(t)$ is obtained by subtracting the reference response $V_{\mathrm{fast},\ell}^{\mathrm{t0}}(t)$ from the total transient response $V_{\mathrm{fast}}^{\mathrm{t,tot}}(t)$ it is obviously also a function of the phase considered, as emphasized by the subscript ℓ.

We also define the total response to the external magnetic field as the sum of the steady-state and transient responses:

$$V_{\mathrm{fast},\ell}(t) = V_{\mathrm{fast}}^{\mathrm{r}}(t) + V_{\mathrm{fast},\ell}^{\mathrm{t}}(t) \tag{7.3}$$

Note that we will use the same name to denote a phasor and the corresponding time-domain function. The function parameter '(t)' is then used to make the difference. For example, $V^{\mathrm{r}}_{\mathrm{fast}}$ is a phasor and $V^{\mathrm{r}}_{\mathrm{fast}}(t)$ the corresponding time-domain function. They are related by $V^{\mathrm{r}}_{\mathrm{fast}}(t) = \Re\{V^{\mathrm{r}}_{\mathrm{fast}} e^{j\omega t}\}$.

The steady state contribution can be computed from the listening-phase frequency response. For a magnetic field, an input voltage e_{L} must be introduced in the L branch of the coil equivalent circuit and the steady state contribution to the fast-time response is:

$$V^{\mathrm{r}}_{\mathrm{fast}} = H^{\mathrm{V_{amp}}}_{\mathrm{e_L}}(\omega) e_{\mathrm{L}} \tag{7.4}$$

with $H^{\mathrm{V_{amp}}}_{\mathrm{e_L}}$ the listening-phase transfer function between the induced voltage e_{L} and the amplifier output $V^{\mathrm{RX}}_{\mathrm{amp}}$ and ω the angular frequency of e_{L}.

Similarly, for an electric field, an input voltage e_{C} must be introduced in the C branch of the coil equivalent circuit and the steady state contribution to the fast-time response is:

$$V^{\mathrm{r}}_{\mathrm{fast}} = H^{\mathrm{V_{amp}}}_{\mathrm{e_C}}(\omega) e_{\mathrm{C}} \tag{7.5}$$

with $H^{\mathrm{V_{amp}}}_{\mathrm{e_C}}$ the listening-phase transfer function between the induced voltage e_{C} and the amplifier output $V^{\mathrm{RX}}_{\mathrm{amp}}$.

Generic expressions can be written for the two cases by defining a generic induced voltage e standing for e_{L} or e_{C} and the corresponding transfer function $H^{\mathrm{V_{amp}}}_{\mathrm{e}}$ standing for $H^{\mathrm{V_{amp}}}_{\mathrm{e_L}}$ or $H^{\mathrm{V_{amp}}}_{\mathrm{e_C}}$:

$$V^{\mathrm{r}}_{\mathrm{fast}} = H^{\mathrm{V_{amp}}}_{\mathrm{e}}(\omega) e \tag{7.6}$$

As the amplifier is modeled by a first order system, the total transient must be a simple exponential decay:

$$V^{\mathrm{t,tot}}_{\mathrm{fast}} = A^{\mathrm{t,tot}}_{\mathrm{fast},\ell} e^{-(t-t_\ell)/T_{\mathrm{amp}}} \tag{7.7}$$

where T_{amp} is the amplifier time constant and the amplitude $A^{\mathrm{t,tot}}_{\mathrm{fast}}$ is chosen in order to ensure that at at the beginning of the listen phase ($t = t_\ell$) the output of the amplifier is $V^{\mathrm{RX}}_{\mathrm{amp}}(t_\ell) = V_\ell = V_{\mathrm{sat}}$, with V_{sat} the amplifier saturation voltage. According to (7.1), the amplitude of the total transient is therefore: $A^{\mathrm{t,tot}}_{\mathrm{fast,l}} = V_{\mathrm{sat}} - V^{\mathrm{r}}_{\mathrm{fast}}(t_\ell)$. Subtracting the reference transient (7.2) from the total transient (7.7), one gets the following expression for the transient response:

$$V^{\mathrm{t}}_{\mathrm{fast},\ell}(t) = A^{\mathrm{t}}_{\mathrm{fast},\ell} e^{-(t-t_\ell)/T_{\mathrm{amp}}} \tag{7.8}$$

with

$$A^{\mathrm{t}}_{\mathrm{fast},\ell} = -V^{\mathrm{r}}_{\mathrm{fast}}(t_\ell) = -\Re\{V^{\mathrm{r}}_{\mathrm{fast}} e^{j\omega t_\ell}\} \tag{7.9}$$

the amplitude[2] of the transient.

Equ. (7.8) confirms that the transient contribution can be computed from the steady state solution alone and that no time-domain simulation through all phases is required. Note however that the detector is asynchronous with the external field and, therefore, the phase of the external field will in general vary from pulse to pulse. Depending on this phase, the amplitude of the transient will also take a different value for each pulse but this value must remain in the range $-A^{\mathrm{r}}_{\mathrm{fast}} < A^{\mathrm{t}}_{\mathrm{fast},\ell} < A^{\mathrm{r}}_{\mathrm{fast}}$ with $A^{\mathrm{r}}_{\mathrm{fast}} = |V^{\mathrm{r}}_{\mathrm{fast}}|$ the magnitude of the steady state response. The various contribution to the fast-time response are illustrated in Fig. 7.1 for various phases, yielding the largest positive and negative transient as well as an intermediate and null transient contribution.

7.4 Slow-time response

The slow-time response is obtained by averaging the fast-time response $V^{\mathrm{RX}}_{\mathrm{amp}}$ in the evaluation window. The evaluation window starts when the fast-time signal reaches a given threshold voltage V_{e} ($V_{\mathrm{e}} = 1V$ for the Schiebel detector). The response in the evaluation-phase can be expressed as a transient and a steady state contribution as we did in the previous section (see Equ. 7.3) for the listening-phase:

$$V_{\mathrm{fast,e}}(t) = V^{\mathrm{r}}_{\mathrm{fast}}(t) + V^{\mathrm{t}}_{\mathrm{fast,e}}(t) \tag{7.10}$$

where the subscript 'e' indicates that the threshold defining the initial condition is now V_{e} instead of V_ℓ that was used to define the fast-time response in (7.3). The threshold has no effect on the steady state contribution which is still defined by (7.4) or (7.5). The threshold however affects the transient contribution which now becomes:

$$V^{\mathrm{t}}_{\mathrm{fast,e}}(t) = A^{\mathrm{t}}_{\mathrm{fast,e}} e^{-(t-t_{\mathrm{e}})/T_{\mathrm{amp}}} \tag{7.11}$$

in which

$$A^{\mathrm{t}}_{\mathrm{fast,e}}(t) = -V^{\mathrm{r}}_{\mathrm{fast}}(t_{\mathrm{e}}) = -\Re\{V^{\mathrm{r}}_{\mathrm{fast}} e^{j\omega t_{\mathrm{e}}}\} \tag{7.12}$$

is the amplitude of the transient and t_{e} is the time at which the threshold V_{e} is first reached.

[2]we use the term amplitude although $A^{\mathrm{t}}_{\mathrm{fast},\ell}$ may be positive or negative.

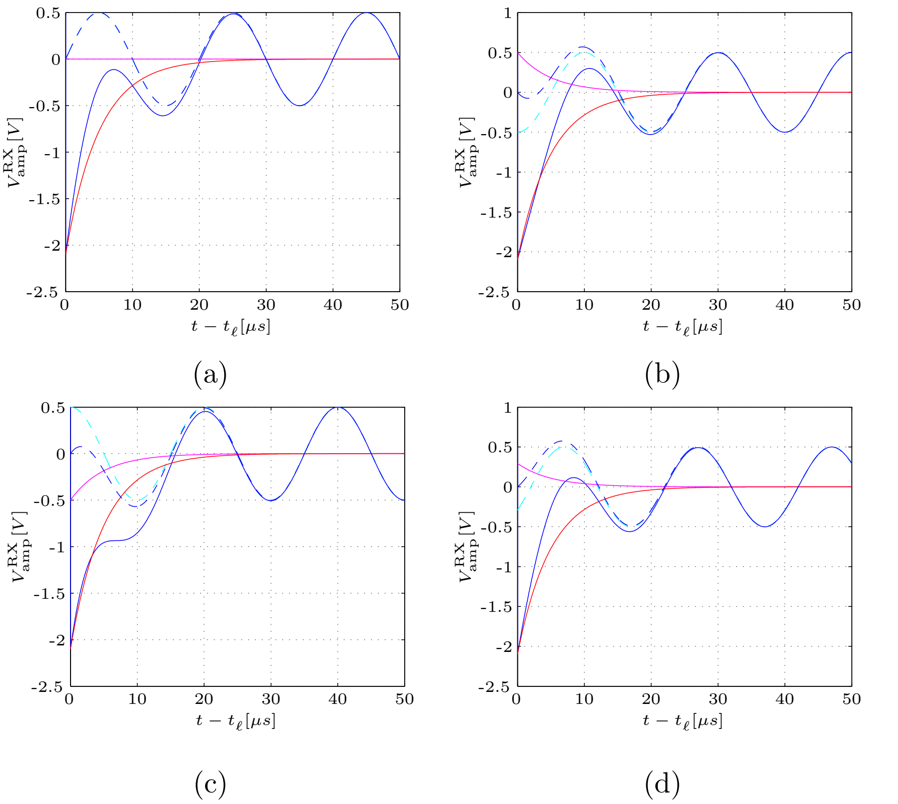

Figure 7.1: *Various contributions to the total (blue) fast-time response in presence of a monochromatic EM background at a frequency of 50kHz and with an amplitude yielding a steady-state sinusoidal response of 0.5V. The reference transient* $V^{\rm t0}_{\rm fast,\ell}(t)$ *(red), the transient* $V^{\rm t}_{\rm fast,\ell}(t)$ *(magenta) and the steady state* $V^{\rm r}_{\rm fast}(t)$ *(cyan) contributions to the external field fast-time response. Various phases of the external field are considered, yielding a null (a), the largest positive (b), the largest negative (c) and intermediate transient amplitude* $A^{\rm t}_{\rm fast,\ell}$.

According to (7.12), depending on the phase of the external field, the amplitude of the transient is in the range $-A^{\mathrm{r}}_{\mathrm{fast}} < A^{\mathrm{t}}_{\mathrm{fast,e}} < A^{\mathrm{r}}_{\mathrm{fast}}$ with $A^{\mathrm{r}}_{\mathrm{fast}} = |V^{\mathrm{r}}_{\mathrm{fast}}|$. The range is thus identical to that of the listening-phase transient. This may seem strange because the evaluation-phase starts after the listening-phase and one could thus expect a smaller evaluation-phase transient contribution. This is however not the case, because the response is defined as the difference between the response in presence and the response in absence of the external field; the latter being shifted to synchronize the two signals at the beginning of the phase considered before performing the subtraction (the shift is $t_\ell - t_{\ell 0}$ or $t_{\mathrm{e}} - t_{\mathrm{e}0}$ depending on the phase considered and in both cases, it depends on the magnitude and phase of the external field). In other words, the reference transient response is shifted by two different amounts before subtracting it from the total response and the evaluation-phase transient is therefore not simply the listening-phase transient considered in the evaluation window.

As just mentioned, the transient amplitude is in the range $-A^{\mathrm{r}}_{\mathrm{fast}} < A^{\mathrm{t}}_{\mathrm{fast,e}} < A^{\mathrm{r}}_{\mathrm{fast}}$. However, the whole range of transient amplitudes will be observed only for low frequencies. For higher frequencies, only amplitudes close to $A^{\mathrm{r}}_{\mathrm{fast}}$ will be observed and for intermediate frequencies an intermediate distribution, more and more biased towards $A^{\mathrm{r}}_{\mathrm{fast}}$ when the frequency increases, will be observed. This can be understood by considering the limit of an infinite frequency. The response will then take all values between $V^{\mathrm{t,tot}}_{\mathrm{fast,e}}(t) - A^{\mathrm{r}}_{\mathrm{fast}}$ and $V^{\mathrm{t,tot}}_{\mathrm{fast,e}}(t) + A^{\mathrm{r}}_{\mathrm{fast}}$ for all t. The threshold V_{e} will thus be reached for the first time[3] when the transient contribution is $V^{\mathrm{t,tot}}_{\mathrm{fast}}(t_{\mathrm{e}}) = V_{\mathrm{e}} - A^{\mathrm{r}}_{\mathrm{fast}}$ and the transient amplitude is $A^{\mathrm{t}}_{\mathrm{fast,e}} = -A^{\mathrm{r}}_{\mathrm{fast}}$. This is a good approximation as long as the variation of the transient during one period of the external field is small when compared to the amplitude of the steady state response.

Our objective is now to compute the evolution of the slow-time response as a function of the pulse index. This is a discrete signal that can be seen as a sampled version of the (integrated) fast-time signal. The displacement of the evaluation window however yields an irregular sampling and this is a major complication. To simplify the analysis, we assume that the displacement of the evaluation window is small when compared to the period of the external field, When this is the case, regular sampling can be assumed and the classical sampling theory can be

[3] We consider a negative threshold and a negative transient response as is the case for the Schiebel detector.

used.

The validity of the regular sampling assumption will be discussed in Section 7.5. We will show that for a given steady state contribution magnitude $A^{\mathrm{r}}_{\mathrm{fast}}$, the assumption is valid below a limit frequency and that this limit frequency is a decreasing function of $A^{\mathrm{r}}_{\mathrm{fast}}$. In other words, for any frequency, the regular sampling approximation is valid for a sufficiently small external field. Hence, the regular sampling solution may be termed 'Low frequency' or 'Small field' approximation.

7.4.1 Transient contribution

The contribution of the transient response to the slow-time response is obtained by integrating (7.11) form t_{e} to $t_{\mathrm{e}} + T_{\mathrm{av}}$ with T_{av} the duration of the evaluation window. This yields:

$$V^{\mathrm{t}}_{\mathrm{slow}} = -V^{\mathrm{r}}_{\mathrm{fast}}(t_{\mathrm{e}})K_{\mathrm{t}} \tag{7.13}$$

with

$$K_{\mathrm{t}} = \frac{T_{\mathrm{amp}}}{T_{\mathrm{av}}}\left(1 - e^{-T_{\mathrm{av}}/T_{\mathrm{amp}}}\right) \tag{7.14}$$

the gain for the transient contribution. For the Schiebel detector, as discussed in Sections 2.6.2 and 2.7, we use $T_{\mathrm{av}} = 10\mu s$ and $T_{\mathrm{amp}} = 5\mu s$ and this yield a gain $K_{\mathrm{t}} = 0.43$.

The pulses of the detector are sent at regular intervals, with a period T_{TX}. If the displacement of the evaluation window can be neglected, the evaluation window also starts at regular intervals with period T_{TX}. Assuming that the first evaluation window ($k = 0$) starts at $t = t_{\mathrm{e}}$, the amplitude of the transient for the k^{th} pulse is $A^{\mathrm{t}}_{\mathrm{fast,e}}(k) = -V^{\mathrm{r}}_{\mathrm{fast}}(kT_{\mathrm{TX}} + t_{\mathrm{e}})$ and the corresponding slow-time signal is $V^{\mathrm{t}}_{\mathrm{slow}}(k) = K_{\mathrm{t}}A^{\mathrm{t}}_{\mathrm{fast,e}}(k)$. As $V^{\mathrm{r}}_{\mathrm{fast}}$ is a sinusoid at frequency ν, the discrete slow-time signal is a discrete sinusoid:

$$V^{\mathrm{t}}_{\mathrm{slow}}(k) = \Re\left\{V^{\mathrm{t}}_{\mathrm{slow}} e^{j2\pi\tilde{\nu}k}\right\} \tag{7.15}$$

with

$$V^{\mathrm{t}}_{\mathrm{slow}} = -K_{\mathrm{t}}V^{\mathrm{r}}_{\mathrm{fast}} \tag{7.16}$$

the corresponding phasor and:

$$\tilde{\nu} = (\nu \mod \nu_{\mathrm{TX}})/\nu_{\mathrm{TX}} \tag{7.17}$$

the discrete normalized frequency and $\nu_{\mathrm{TX}} = 1/T_{\mathrm{TX}}$ is the transmit PRF.

One usually restricts the discrete normalized frequency to the interval $[0, 1/2]$. This can be done by using:

$$\tilde{\nu}' = 1 - \tilde{\nu} \tag{7.18a}$$

$$V^{\mathrm{t}'}_{\mathrm{slow}} = \left(V^{\mathrm{t}}_{\mathrm{slow}}\right)^* \tag{7.18b}$$

instead of $\tilde{\nu}$ and $V^{\mathrm{t}}_{\mathrm{slow}}$ if $\tilde{\nu} > 1/2$. One can easily check that this transformation leaves the discrete sinusoid unchanged and the discrete frequency is in the interval $[0, 1/2]$.

Equations (7.17) and (7.18) can be obtained directly from the sampling theory. Indeed, the effect of sampling on the spectrum is to repeat it periodically with a period ν_{TX}. A monochromatic continuous signal at frequency ν has a spectrum composed of two Dirac pulses at $\pm\nu$ and having complex conjugate amplitudes. The discrete sinusoid is then fully characterized by the aliased (copied) version of the original Dirac pulses at the lowest frequency. When this is a copy of the original Dirac pulse at ν, (7.17) is obtained directly. However, if this is a copy of the original Dirac pulse at $-\nu$, the transformation (7.18) should be used.

7.4.2 Steady state contribution

The steady state contribution to the slow-time response is obtained by integrating the steady state fast-time contribution in the evaluation window. Again assuming that the displacement of the evaluation window can be neglected, the discrete slow-time response contribution can be computed by passing the fast-time response through a moving average filter $V_{\mathrm{av}}(t) = \int_t^{t+T_{\mathrm{av}}} V^{\mathrm{r}}_{\mathrm{fast}} \mathrm{d}t$ and then sampling at regular times intervals $kT_{\mathrm{TX}} + t_{\mathrm{e}}$.

As for the transient contribution, the result will be a discrete sinusoid with a discrete frequency that can be computed according to (7.17) and (7.18). The corresponding phasor is[4]:

$$V^{\mathrm{r}}_{\mathrm{slow}} = V^{\mathrm{r}}_{\mathrm{fast}} H_{\mathrm{av}} \tag{7.19}$$

with

$$H_{\mathrm{av}} = \frac{1}{T_{\mathrm{av}} j\omega} \left(e^{j\omega T_{\mathrm{av}}} - 1\right) \tag{7.20}$$

the transfer function of the moving average filter.

[4]Obviously, if the frequency transformation (7.18a) is used, the phasor must be complex conjugated as in (7.18b).

7.4.3 Total response

The total response is the sum of the steady state and the transient contribution. This yields:

$$V_{\mathrm{slow}} = V_{\mathrm{slow}}^{\mathrm{r}} + V_{\mathrm{slow}}^{\mathrm{t}} = H_{\mathrm{e}}^{V_{\mathrm{amp}}} H_{\mathrm{rs}} e \tag{7.21}$$

with $H_{\mathrm{rs}} = H_{\mathrm{av}} - K_{\mathrm{t}}$ the transfer function from the fast-time steady state response to the slow-time total response, e the induced voltage (standing for e_{L} or e_{C} respectively for a magnetic and electric external field) and $H_{\mathrm{e}}^{V_{\mathrm{amp}}}$ the listening-phase transfer function between the corresponding induced voltage and the amplifier output (see (7.4) and (7.5)). The l.h.s. of (7.21) is a phasor representing a discrete sinusoid and its r.h.s. is a phasor representing a continuous sinusoid. The discrete and continuous frequencies are related through (7.17) and (7.18)

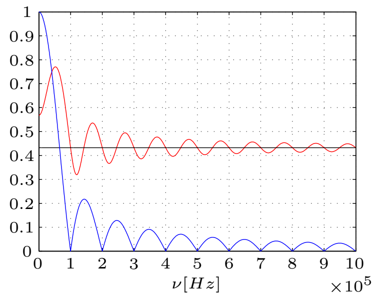

Figure 7.2: *Magnitude (red) of H_{rs}, the transfer function between the fast-time steady state response and the total slow-time response. Steady state ($|H_{\mathrm{av}}|$– blue) and transient (K_{t} – black) contributions to the slow-time response are also shown.*

Fig. 7.2 shows the magnitude of H_{rs} as a function of the frequency as well as the transient (K_{t}) and steady state ($|H_{\mathrm{av}}|$) contributions. As expected, the gain of the moving average filter H_{av} is equal to one for frequencies below $1/T_{\mathrm{av}} = 200kHz$. Furthermore, at low frequencies, both contributions are of the same order of magnitude, the transient contribution being the smallest and at higher frequencies the transient contribution becomes dominant. As a first approximation, the transient contribution alone can be used $H_{\mathrm{rs}} \simeq K_{\mathrm{t}}$ for the whole spectrum.

Equation (7.21) has been established for a monochromatic external field. In absence of saturation and with a regular sampling regime, the slow-time response is a linear function of the inputs and the result can be used for any external field. Equation (7.21) then relates the spectrum of the EM field to that of the slow-time signal. The effect of sampling is then still to shift any continuous frequency in the range $[-0.5, 0.5]$ of discrete frequencies. Obviously, several continuous frequencies will be shifted to the same discrete frequency. This is the well known aliasing phenomenon. The discrete spectrum is then the sum of shifted replications of the continuous spectrum.

7.5 Regular sampling regime

The displacement of the evaluation window is a major source of nonlinearity in the slow-time signal. Most practical expressions such as (7.21) and most of the counter-measures used to reduce the effect of the EM background are based on the regular sampling assumption and are thus only valid for small displacements of the evaluation window with respect to the TX pulse.

It is therefore important to determine the conditions under which the regular sampling assumption is valid; that is the conditions for which the displacement of the evaluation window is small when compared to the period of the external field. For this, we will first determine the maximal displacement of the evaluation window as a function of the frequency of the external field and of the amplitude of the steady state fast-time response $A^{\mathrm{r}}_{\mathrm{fast}}$. We will then define the region in the frequency amplitude plane for which the regular sampling assumption can be used.

7.5.1 Evaluation window displacement

The displacement of the evaluation window has two contributions; the displacement of the beginning of the listening-phase with respect to the TX pulse and the displacement of the evaluation window with respect to the beginning of the listening-phase. The transient at the input side of the amplifier is much faster than that at the output of the amplifier and therefore, the displacement of the listening-phase can in general be neglected.

The displacement of the evaluation window with respect to the beginning of the listening-phase can easily be computed numerically for a given amplitude $A^{\mathrm{r}}_{\mathrm{fast}}$ and phase $\phi^{\mathrm{r}}_{\mathrm{fast}}$ of the steady state fast-time response and for a given frequency (ν) of the external field. For this, (7.6) and (7.7) are introduced into (7.1) to compute $V_{\mathrm{amp}}^{\mathrm{RX}}(t)$. The first time $V_{\mathrm{amp}}^{\mathrm{RX}}(t)$ reaches the threshold V_{e} is then searched to determine the beginning of the evaluation window t_{e}. Performing the same computation in absence of external field yields the corresponding reference time t_{e}^{0} and the displacement of the evaluation $\Delta t_{\mathrm{e}} = t_{\mathrm{e}} - t_{\mathrm{e}}^{0}$ can then be calculated.

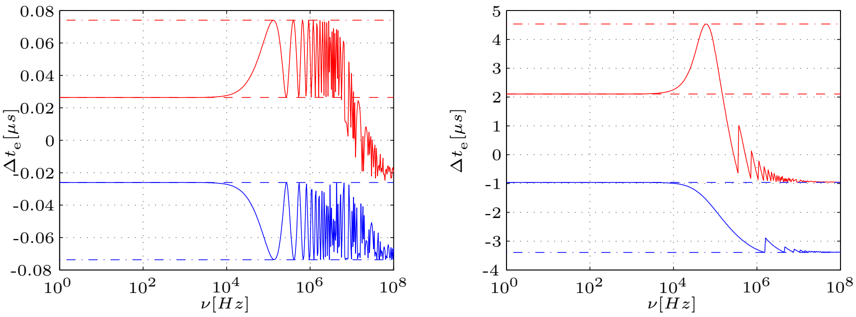

(a) (b)

Figure 7.3: *Upper (red) and lower (blue) bounds of the evaluation window displacement as a function of frequency for $A_{\mathrm{fast}}^{\mathrm{r}} = 0.01V$ (a) and $A_{\mathrm{fast}}^{\mathrm{r}} = 0.5V$ (b). Analytic low frequency bound (– –) computed according to (7.24) and (7.25) and overall bounds(—·—) computed according to (7.26) and (7.27) are also shown.*

For a given external field, ν and $A_{\mathrm{fast}}^{\mathrm{r}}$ are fixed but, as already mentioned, the field is in general asynchronous with the detector pulses and $\phi_{\mathrm{fast}}^{\mathrm{r}}$ varies from pulse to pulse. The largest positive and negative displacements can then be determined by computing Δt_{e} as a function of $\phi_{\mathrm{fast}}^{\mathrm{r}}$ for $0 < \phi_{\mathrm{fast}}^{\mathrm{r}} < 2\pi$ and by searching for the extrema. The result is shown in Fig. 7.3 for $A_{\mathrm{fast}}^{\mathrm{r}} = 0.01V$. The resulting curve is rather complex, but the low frequency as well as the overall upper and lower bounds of the evaluation window displacement can be computed analytically.

Indeed, according to (7.1) t_{e} is defined by:

$$[V_\ell - V_{\mathrm{fast}}^{\mathrm{r}}(t_\ell)]\, e^{-t_{\mathrm{e}}/T_{\mathrm{amp}}} + V_{\mathrm{fast}}^{\mathrm{r}}(t_{\mathrm{e}}) = V_{\mathrm{e}} \tag{7.22}$$

or

$$t_{\mathrm{e}} = T_{\mathrm{amp}} \ln \frac{V_\ell - V_{\mathrm{fast}}^{\mathrm{r}}(t_\ell)}{V_{\mathrm{e}} - V_{\mathrm{fast}}^{\mathrm{r}}(t_{\mathrm{e}})} \tag{7.23}$$

At low frequencies, $V_{\mathrm{fast}}^{\mathrm{r}}(t_{\mathrm{e}}) \simeq V_{\mathrm{fast}}^{\mathrm{r}}(t_\ell)$ and the maximal and minimal values of t_{e} are obtained by introducing $V_{\mathrm{fast}}^{\mathrm{r}}(t_{\mathrm{e}}) = V_{\mathrm{fast}}^{\mathrm{r}}(t_\ell) = \pm A_{\mathrm{fast}}^{\mathrm{r}}$ in

(7.23):

$$t_{\rm e}^{\rm min,LF} = T_{\rm amp} \ln \frac{V_\ell + A^{\rm r}_{\rm fast}}{V_{\rm e} + A^{\rm r}_{\rm fast}} \tag{7.24}$$

$$t_{\rm e}^{\rm max,LF} = T_{\rm amp} \ln \frac{V_\ell - A^{\rm r}_{\rm fast}}{V_{\rm e} - A^{\rm r}_{\rm fast}} \tag{7.25}$$

At high frequencies, $V^{\rm r}_{\rm fast}(t_{\rm e})$ and $V^{\rm r}_{\rm fast}(t_\ell)$ may become different and the extrema of $t_{\rm e}$ are obtained for $V^{\rm r}_{\rm fast}(t_{\rm e}) = \pm A^{\rm r}_{\rm fast}$ and $V^{\rm r}_{\rm fast}(t_\ell) = \mp A^{\rm r}_{\rm fast}$:

$$t_{\rm e}^{\rm min} = T_{\rm amp} \ln \frac{V_\ell - A^{\rm r}_{\rm fast}}{V_{\rm e} + A^{\rm r}_{\rm fast}} \tag{7.26}$$

$$t_{\rm e}^{\rm max} = T_{\rm amp} \ln \frac{V_\ell + A^{\rm r}_{\rm fast}}{V_{\rm e} - A^{\rm r}_{\rm fast}} \tag{7.27}$$

The largest (low frequency and overall) positive and negative displacement obtained from the analytic expressions (7.24)-(7.27) are shown Fig. 7.3 which confirms that those expressions are in agreement with the numerical solution.

It is further apparent that for $A^{\rm r}_{\rm fast} = 0.01V$, the low frequency largest displacements (7.25) are valid up to about $10kHz$. The upper (lower) bound for the displacement then varies between the positive (negative) low frequency limit and the overall largest positive (negative) displacement (7.27) for frequencies up to about $5MHz$. For even higher frequencies the overall largest positive displacement is not reached anymore. The upper bound then tends towards the low frequency largest negative displacement. This high frequency limit can be understood because, as explained in Section 7.4, for high frequencies, the evaluation window is always triggered for $V^{\rm r}_{\rm fast}(t_{\rm e}) = A^{\rm r}_{\rm fast}$. The upper bound is then reached for $V^{\rm r}_{\rm fast}(t_\ell) = A^{\rm r}_{\rm fast}$ and this yields the same expression as for the low frequency largest negative displacement (7.24).

Further comparing Fig. 7.3 (a) and (b), it appears that the limit of the low frequency regime is weakly dependent on $A^{\rm r}_{\rm fast}$. However, the high frequency regime starts at lower frequencies and the frequency band for the intermediate frequencies regime becomes smaller when $A^{\rm r}_{\rm fast}$ increases.

The overall and low frequency largest displacements of the evaluation window simply and efficiently characterize the displacement of the evaluation window. They are independent of the frequency and are thus convenient to quantify the displacement as a function of the amplitude of the steady state fast-time response $A^{\rm r}_{\rm fast}$. This is illustrated in Fig. 7.4.

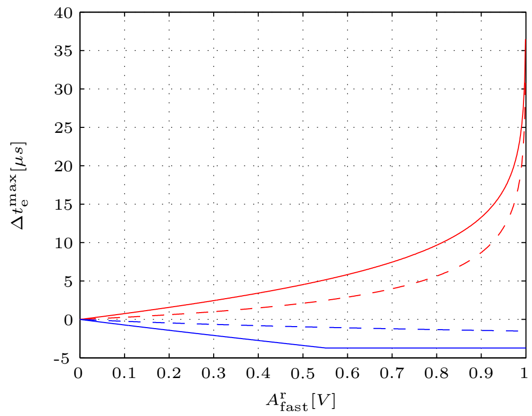

Figure 7.4: *Overall (—) and low frequency (– –) largest positive (red) and negative (blue) displacement of the evaluation window as a function of the amplitude of the steady state fast-time response* $A_{\mathrm{fast}}^{\mathrm{r}}$.

The angular point visible in the overall largest negative displacement stems for the fact that in addition to the bound (7.26), the beginning of the evaluation window must fulfill $t_{\mathrm{e}} > t_{\ell}$ and therefore, $\Delta t_{\mathrm{e}} > t_{\mathrm{l}}^{0} - t_{\mathrm{e}}^{0}$.

One sees that the overall largest positive displacement is an upper bound for the magnitude of the displacement. This single parameter can thus be used to characterize the largest displacement as a function of the $A_{\mathrm{fast}}^{\mathrm{r}}$. One sees that it remains below $5\mu s$ for $A_{\mathrm{fast}}^{\mathrm{r}} < 0.5V$. It is further increasing approximatively linearly with $A_{\mathrm{fast}}^{\mathrm{r}}$ in that region. It then increases quite fast for $A_{\mathrm{fast}}^{\mathrm{r}} > 0.5V$ and it gets undefined for $A_{\mathrm{fast}}^{\mathrm{r}} > 1V$. This stems from the fact that, for low frequencies and $A_{\mathrm{fast}}^{\mathrm{r}} > 1V$, the threshold will never be reached for some pulses. As will be discussed further in Section 7.6.1, large displacements may be critical because, in this case, the external field not only generates an additional slow-time signal but it also significantly changes the slow-time target response.

7.5.2 Frequency-amplitude limit

The overall largest positive displacement of the evaluation window can be used to define a conservative boundary for which the regular-sampling assumption is valid. Indeed, (7.27) yields the largest magnitude of the displacement as a function of $A_{\mathrm{fast}}^{\mathrm{r}}$ and independently of the frequency.

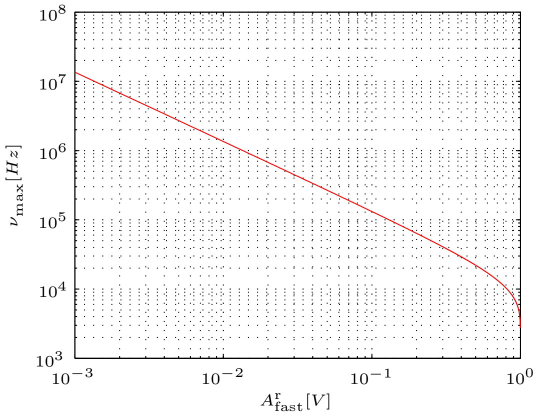

Figure 7.5: *Maximum frequency for the regular sampling assumption to be usable as a function of $A^{\rm r}_{\rm fast}$, the amplitude of the steady state fast-time response.*

The maximal frequency for which this displacement is negligible; that is for which the displacement is small when compared to the period of the external field, can then be computed. This is illustrated in Fig. 7.5 which shows the maximum frequency, for which the regular sampling assumption is valid, as a function of $A^{\rm r}_{\rm fast}$. The criterion used is $\Delta t_{\rm e}^{\rm max} < T/10$ with T the period of the external field.

The curve can also be used the other-way round. For a given frequency, it allows to determine the maximum $A^{\rm r}_{\rm fast}$ for which the regular sampling assumption is valid. As expected, the maximal steady state response amplitude is a decreasing function of the frequency. For example, at $1MHz$, the regular sampling assumption is valid for $A^{\rm r}_{\rm fast} < 10mV$.

7.6 Effect on the detector and counter measures

7.6.1 Effect on the detector

The most common and obvious effect of the EM background is the generation of an additional slow-time signal. If this signal is smaller than the electronic noise the EM background will have no noticeable effect. For larger fields, the additional signal may be translated into noise on the audio signal. The operator will then in general reduce the sensitivity of the detector to avoid this perturbing signal. This will obviously reduce the detection performance of the detector, but as long as the sensitivity can be kept high enough to detect the targets of interest to the required depth, the detector remains effective. In this context, it should be noted that the operational procedure does not necessarily require one to set the sensitivity at the maximum value compatible with the EM background. A lower sensitivity is sometimes intentionally used to reduce the number of false alarms. This is typically the case in the presence of a strong clutter and if the threat is composed of mines with a high metallic content.

The external field will also affect the location of the evaluation window. Hence, the external field not only produces an additional signal, but it also modifies the response of the target. For fields yielding a fast-time signal smaller than 0.5V, the displacement remains smaller than $5\mu s$ and this should have little effect for targets of interest[5] with time constants larger than $10\mu s$.

For fast-time responses between 0.5 and 1V the largest displacement of the evaluation window increases fast as shown in Fig. 7.4 and this may significantly affect the target response. Recall that the displacement of the evaluation window is a function of the phase of the external field with respect to the TX pulse. The displacement may be positive or negative and as apparent from the upper and lower bounds in Fig. 7.4, the largest displacements are positive. As the detector is asynchronous with the field, the phase will be different for each pulse and positive and negative displacements will occur. However, because of the asymmetry between the positive and negative displacements, a bias towards positive displacements will appear and will, on average, reduce the target response.

For fast-time signals larger than 1V, the threshold may not be reached for some pulses. As a result, the evaluation window is not triggered and this may jeopardize the normal functioning of the detector. The evaluation window is then not triggered and the corresponding target response is then completely missed.

As already mentioned, for even larger fields, non linear phenomenons may come into play and the detector may completely stop working. In most cases, the operator will be aware of the problem because the audio output will become very noisy but in some critical situations, the detector may stop working without any notification to the user; the

[5] The detector is getting inefficient for faster targets because they produce a very weak response.

audio remaining quiet.

7.6.2 Counter measures

A number of techniques can be used to reduce the effect of the EM background on the detector. The EM background is in general homogeneous on the RX head and its effect can therefore be significantly reduced by using a differential RX coil. This is however not necessarily the best solution because the distance at which a target can be detected is in general also reduced for a differential head.

For low frequency fields when compared to the time constants of the targets of interest (typically less than $100\mu s$), a second evaluation window can be used after the main one. The target response has become negligible in that second window and the voltage induced by the external field is approximately constant between the TX pulse and the end of the second evaluation window. The response in the second window can then be used to compensate the contribution of the external field to the slow-time response. This technique has been patented [47]. The main motivation for the introduction of this second evaluation window was to cancel the voltage induced when moving above an inhomogeneous static magnetic field, as when sweeping the detector over a magnetic stone, or more generally over an inhomogeneous magnetic soil. This window should however also be efficient to cancel the effect of low frequency EM background; for example close to a high voltage power line.

Another solution to mitigate the effect of low frequency fields is to alternate positive and negative useful pulses[6] as in the Vallon ML1620 or the newer Vallon VMH3. Typical low frequency fields are those generated by power lines but the technique should also be efficient for motional induced voltages, such as those generated when sweeping the detector over a magnetic stone, or more generally over an inhomogeneous magnetic soil. Indeed, both the motional induced voltage and the voltage induced by an external low frequency field do not vary significantly from pulse to pulse and their polarity is not correlated with that of the pulses. On the other hand, The target response polarity is correlated with that of the pulses emitted. The target response polarity is thus alternated and, as the processing further reverses one response out of two, the tar-

[6]The useful pulses are those followed by an evaluation window. Typically, for a bipolar pulse a single evaluation window is used after the second pulse. It is thus the whole bipolar pulse that must be alternated so that that the sign of the second pulse is reversed for each bipolar pulse.

get slow-time response remains constant while the slow-time response of the external field is reversed from pulse to pulse. Simple discrete filtering, such as a moving average can then significantly reduce the effect of the external field. If the PRF is chosen to be a multiple of the external field frequency $\nu_{\mathrm{TX}} = n\nu$, a moving average of $2n$ samples[7] will perfectly cancel the effect of the external field. With this respect, the Vallon ML1620 has a setting for canceling the effect of power lines. It can be set to cancel a frequency of 50 or 60 Hz. The solution consists in setting the PRF to 450Hz in the first case and to 420Hz in the second case. This corresponds respectively to nine and seven times the perturbing frequency.

Optimizing the slow-time filtering is obviously an efficient mean to reduce the effect of external fields. For this, the characteristics of the slow-time target response must be taken into account. The dynamics of the slow-time target response is related to the scanning speed and determines the frequency band that should not be filtered. Typically, a low pass filter is used and the cut-off frequency is determined from the maximum expected scanning speed. Some detectors include a dynamic mode which requires a minimal scanning speed to be used. A band-pass filter is then used and the lower cut-off frequency is chosen according to this minimal scanning speed.

Increasing the PRF may also help in reducing the effect of external fields. Indeed, as just mentioned a slow-time filter can be used to reduce the effect of the external field but a critical frequency band, in which the target response dominates, must be maintained. The PRF then determines the external field frequencies that will be aliased in that critical frequency band. Increasing the PRF reduces the aliasing phenomenon and, as a consequence, a smaller part of the spectrum is aliased in the critical frequency band. We have measured the PRF for the Schiebel AN-19/2, a more recent Vallon detector, the ML1620 and the newest Vallon detector, the VMH3. The result was 66Hz for the AN-19/2, 420 or 450Hz for the ML1620 and a selectable frequency between 1.5 and 2kHz for the VMH3. This confirms a tendency to use higher PRFs. The PRF may further be adapted to the prevailing EM background in a way that the dominant part of the background spectrum is not aliased in the critical frequency band. The Vallon VMH3 has this functionality. Several PRFs between 1.5 and 2kHz can be used. The selection of the optimal PRF can be performed automatically or manually.

[7] n samples would be sufficient if the pulse polarity is kept constant

Finally, we recall that complex nonlinear effects may occur for large external fields. Most of the above mentioned counter-measures then become inefficient and the detector may become unusable. This is in general not a critical issue because such high fields are not encountered in typical EM environments and in most cases, the operator will be alerted about the problem by a noisy audio signal. In extreme situations, as when jammers are used, the detector may stop working without any notification to the user. This is a critical issue and we are not aware of any counter-measures implemented on modern detectors. A simple solution might be to use a dedicated sensor that alerts the user in presence of a critical EM background.

7.7 Critical frequency band

Our objective is to define the part of the electromagnetic spectrum that may significantly affect the detector. Therefore, we use the state-space model of the detector to compute the needed transfer functions $H_{\mathrm{e_L}}^{\mathrm{V_{amp}}}$ and $H_{\mathrm{e_C}}^{\mathrm{V_{amp}}}$ between the induced voltage (e_{L} or e_{C}) and the amplifier output voltage in the listening-phase. We have used the simple coil state-space model. Similar results are obtained with the detailed coil model except for the presence of a number of resonance peaks above 10MHz. The induced voltages are related to the external fields through (2.57) and (2.58). To assess the sensitivity of the detector as a function of the frequency, we will first consider an external field with a reference magnitude independent of the frequency. We will then take into account realistic field strength which is dependent on the frequency.

7.7.1 Reference field

7.7.1.1 Magnetic field

To assess the sensitivity of the detector to an external magnetic field as a function of the frequency, we consider a reference field with amplitude $B_{\mathrm{ref}} = 1\mu T$ and oriented normal to the coil in order to yield the maximum response. Fig. 7.6 (b) shows the response to that field as a function of the frequency. The amplitude ($A_{\mathrm{fast}}^{\mathrm{r}}$) of the steady state contribution to the amplifier output ($V_{\mathrm{amp}}^{\mathrm{RX}}$) is shown together with the corresponding amplitude of the slow-time response A_{slow}. One sees that A_{slow} closely follows $A_{\mathrm{fast}}^{\mathrm{r}}$ as expected from Section 7.4.3 where we showed that, in

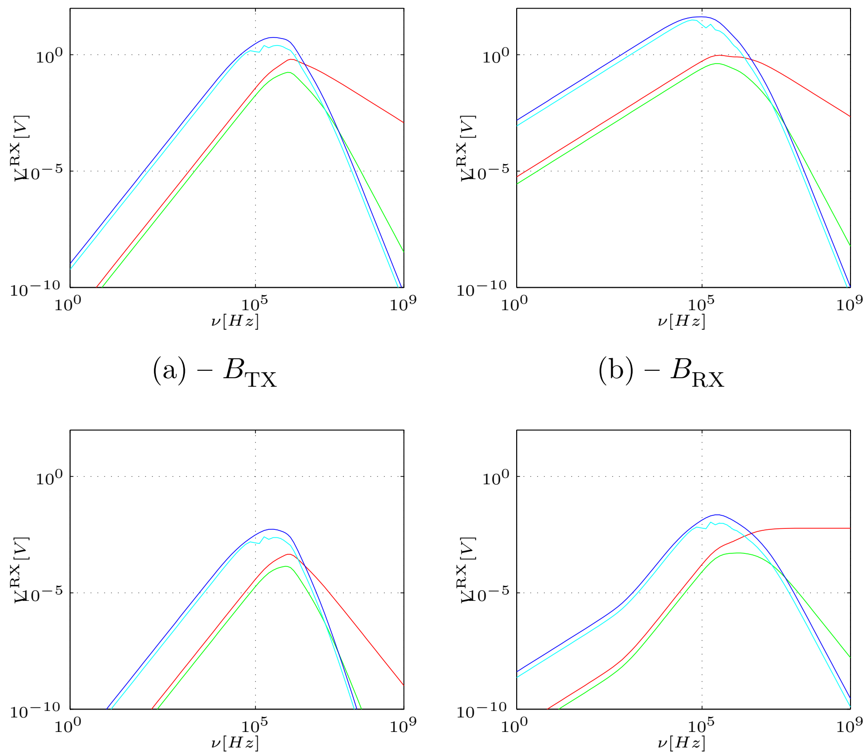

(a) – B_{TX} (b) – B_{RX}

(c) – E_{TX} (d) – E_{RX}

Figure 7.6: *(a) and (b) give the responses to a reference magnetic field $B_{\mathrm{ref}} = 1\mu T$. (c) and (d) give the responses to a reference electric field $E_{\mathrm{ref}} = 300V/m$ (c) and (d). The amplitude of the steady state contribution to $V^{\mathrm{RX}}_{\mathrm{coil}}$ (red), $V^{\mathrm{RX}}_{\mathrm{filt}}$ (green), $V^{\mathrm{RX}}_{\mathrm{amp}}$ (blue) and the corresponding amplitude of the slow-time signal A_{slow} (cyan) are shown. The contributions of the voltages induced in the TX ((a) and (c)) and in the RX ((b) and (d)) coils respectively are presented separately.*

first approximation, there exists a factor K_{t} between the two signals.

To assess the effect of the various components in the processing chain, the amplitudes of the steady state coil voltage $V_{\mathrm{coil}}^{\mathrm{RX}}$ and of the steady state filter output $V_{\mathrm{filt}}^{\mathrm{RX}}$ are also shown.

One sees that, below $100kHz$, $V_{\mathrm{coil}}^{\mathrm{RX}}$ increases with a slope of 20dB per decade as for an ideal coil ($V_{\mathrm{coil}} = j\omega\psi$). For higher frequencies, the parasitic capacitance shunts the inductor and as a result, the gain of the coil decreases. More precisely, as the coil is a second order system, it introduces a gain weakening of 40dB per decade, yielding a high frequency asymptote at -20dB/decade for $V_{\mathrm{coil}}^{\mathrm{RX}}$.

One also sees that up to about $100kHz$ the RX filter and amplifier (see Fig. 2.23) only introduce a multiplicative factor. For higher frequencies, they start to filter the signal. Recall that the amplifier and the filter are first and second order systems respectively. Hence, as expected, they introduce gain decreases of 20 and 40 dB per decade respectively. As a result, the effect of external fields decreases quite fast for frequencies above about $1MHz$.

7.7.1.2 Electric field

In most cases, the effect of an electric field on a coil is neglected. As illustrated in Chapter 6, the electric field may however play a significant role in some specific configurations. An electric field will generate an induced voltage e_{C} in the capacitive branch of the coil equivalent circuit. This voltage can be computed according to (2.51). By symmetry, no voltage will be induced by a field in the plane of the detector. We therefore consider a field along the coil axis with a reference magnitude $E_{\mathrm{ref}} = 300V/m$. The magnitude of the electric fields has been chosen to correspond to $B_{\mathrm{ref}} = 1\mu T$ in the far field ($E_{\mathrm{ref}} = B_{\mathrm{ref}} Z_0/\mu_0$ with Z_0 and μ_0 the impedance and the magnetic permeability of free space). The result is shown in Fig. 7.6 (d).

The comparison with the magnetic case, clearly shows that, in the far field, the dominant effect of an external source is through the magnetic field. In the near field however, the electric field may be much larger, when compared to the magnetic field, and the dominant effect may be through the electric field.

When compared to the magnetic case, the frequency dependency shows an additional derivative term above about $1kHz$. As a result, $V_{\mathrm{coil}}^{\mathrm{RX}}$ reaches a plateau for high frequencies and the decrease of the other signals (filtered $V_{\mathrm{filt}}^{\mathrm{RX}}$ and amplified $V_{\mathrm{amp}}^{\mathrm{RX}}$ RX voltage as well as slow-time response) is less pronounced (by a factor of 20dB per decade). The break point at $1kHz$ corresponds to the time constant of the RX coil $T_{\mathrm{L}}^{\mathrm{RX}} = L^{\mathrm{RX}}/R_{\mathrm{L}}^{\mathrm{RX}} = 187\mu s$. Indeed, the RL branch shunts the capacitive branch which includes the induced voltage (see Fig. 2.23). Below a frequency $\nu_{\mathrm{L}}^{\mathrm{RX}} = 1/(2\pi T_{\mathrm{L}}^{\mathrm{RX}}) = 850Hz$, the RL branch impedance is dominated by the resistor $R_{\mathrm{L}}^{\mathrm{RX}}$ and one can easily check that this yields a $j\omega$ frequency dependency. Similarly, above $\nu_{\mathrm{L}}^{\mathrm{RX}}$, the impedance is dominated by the inductor L^{RX} and this yields a $(j\omega)^2$ frequency dependency.

7.7.2 TX and RX contributions

In the previous sections, we have considered the voltage induced in the RX coil alone. Actually, an external field will also induce a voltage in the TX coil and, as the two coils are magnetically coupled, this will yield a response on the RX side. The TX contribution to the response is illustrated in Fig. 7.6 (a) and (c) for an external magnetic field and an electric field respectively. As expected, it is in general the RX coil that yields the dominant contribution. Note however that the frequency dependency is different for the TX and the RX cases and for some frequencies, both contributions are of the same order of magnitude.

7.7.3 Realistic field strength

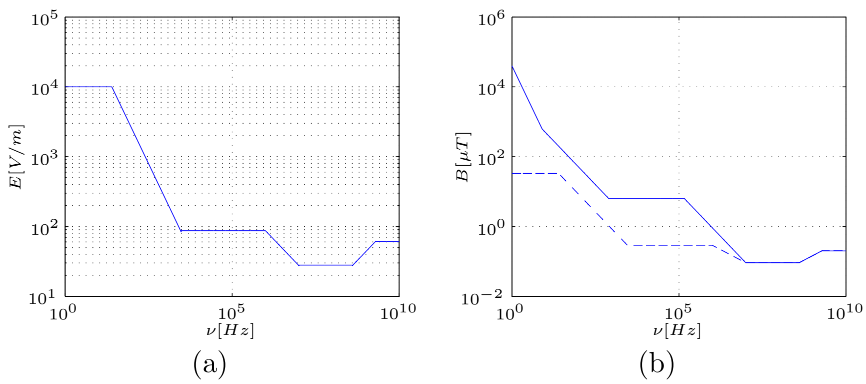

Figure 7.7: *Maximum electric (a) and magnetic (b) field for general public exposure according to ICNIRP. The far field maximum magnetic field is also shown (– –).*

The spectrum of the EM background is highly dependent on the location where the detector is used. It is influenced by the proximity of external sources such as power lines, radio or TV transmitters, radars etc. It may also vary with time.

There exits however a number of national and international legislations which limit the strength of the electric and magnetic fields. Most are based on the ICNIRP guidelines [73]. Those guidelines are based on the health risks of exposure to non-ionizing radiation. The interactions of the EM fields with the body are quite complex. They involve a number of coupling mechanism (induction of electric currents, polarization, heating, ...) and the resulting health risks are highly frequency dependent. The resulting maximum allowed fields for general public exposure are illustrated in Fig. 7.7.

Most sources are in the far-field. The electric field is then related to the magnetic field through the free space impedance. Both the electric and magnetic fields must then be below the allowed maximal value. The most stringent requirement is on the electric field and this yields an additional constraint on the magnetic field of a far-field source that is illustrated in Fig. 7.7 (b).

Taking into account the maximum allowed fields, the response of the detector is illustrated in Fig. 7.8. Comparing with Fig. 7.6, one sees that the peak of highest sensitivities is getting larger and that it is shifted towards the low frequencies because the allowed fields are much higher at those frequencies.

The external field will have a significant effect only if it is larger than the noise generated in the detector. This noise has several origins such as shot noise, thermal noise, flicker noise, burst noise and avalanche noise [74] and it may be generated in the various components of the electronics. For example, thermal noise will be generated in the resistors and shot noise in junctions. By assuming a good design, the main noise sources will be inside the operational amplifier. Noise characteristics of operational amplifier are provided in the data sheet. Typically, the equivalent input noise is provided as a function of the frequency. This equivalent noise is in general constant (white noise) above the corner noise frequency. Below this frequency, the noise typically evolves as $1/f$ (pink noise). For a large bandwidth, when compared to the corner frequency, the $1/f$ noise can be neglected and the equivalent input noise E_{in} can then be estimated by [74, Equ. 10-17]:

$$E_{\mathrm{in}} = E_{\mathrm{n}}\sqrt{f_{\mathrm{max}} - f_{\mathrm{min}}} \tag{7.28}$$

with E_{n}, the amplifier noise figure. The equivalent output noise is then

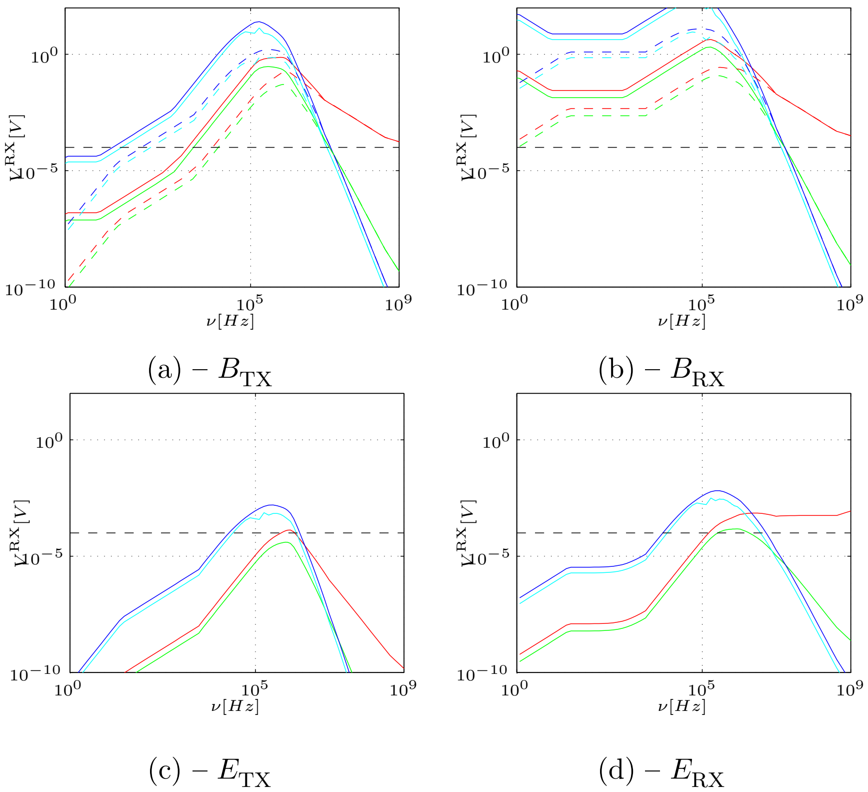

Figure 7.8: *Response to the maximum allowed magnetic ((a) and (b)) and electric ((c) and (d)) fields according to the ICNIRP guidelines. The dashed lines are obtained by taking into account the additional far-field constraint. The amplitude of the steady state contribution to V^{RX}_{coil} (red), V^{RX}_{filt} (green), V^{RX}_{amp} (blue) and corresponding amplitude of the slow-time signal A_{slow} (cyan) are shown. The contributions of the voltages induced in the TX ((a) and (c)) and in the RX ((b) and (d)) coils are presented separately. The dashed black line shows a reference noise level of 0.1mV.*

obtained by multiplying the input noise by the amplifier gain $E_{\text{out}} = K_{\text{amp}} E_{\text{in}}$.

For the Schiebel, $f_{\text{min}} = 0$, $f_{\text{max}} = 1/(2\pi T_{\text{amp}}) = 32kHz$ and $K_{\text{amp}} = 550$. Further considering a typical low-noise operational amplifier noise figure of $3nV/\sqrt{Hz}$, this yields an Root Mean Square (RMS) output noise of $0.3mV$. We will therefore use $100\mu V$ as a lower bound for which the external field may affect the detector. This bound is shown in Fig. 7.8 in which it is apparent that the bandwidth to consider for external fields is from below $1Hz$ to about $20MHz$. Indeed, outside that frequency band, the response to the external field, at the output of the RX amplifier $V_{\text{amp}}^{\text{RX}}$ will be hidden in the noise. There exists many sources of radiation in the critical frequency band such as high voltage lines, AM broadcasting antennas (short, medium and long waves), aircraft beacons, electronic fluorescent lamps, electrical drives and computer screens. The critical frequency band covers the following International Telecommunication Union (ITU) bands:

- Extremely Low Frequency (ELF), 3Hz to 30Hz
- Super Low Frequency (SLF), 30Hz to 300Hz
- Ultra Low Frequency (ULF), 300Hz to 3,000Hz
- Very Low Frequency (VLF), 3kHz to 30kHz
- Low Frequency (LF), 30kHz to 300kHz
- Medium Frequency (MF), 300kHz to 3,000kHz
- High Frequency (HF), 3MHz to 30MHz

Note that the precise value of the electronic noise level (chosen as $100\mu V$) is not critical because the fast-time signal decreases with a slope of about 80dB per decade at the upper frequency of interest. Hence, dividing or multiplying the electronic noise by ten will only affect the upper frequency by a quarter of a decade or in other words a factor smaller than two.

According to our model, the external field should have no effect above $20MHz$. Recall however that we have used the simple coil model that only takes into account the first coil resonance. Higher order coil resonances as well as resonances in the cable connection with the electronics actually exists above $20MHz$. Thanks to the fast decay of the fast-time response with the frequency, the linear model still predicts limited effect even at the resonance frequencies. The coil voltage however decreases much more slowly with the frequency (20 and 0dB per decade respectively for magnetic and electric external fields respectively) and non linear effects at the input of the filter (conduction of the clipping diodes) may become important at the resonance frequencies. This may explain some problems encountered with jammers. Note further that, above $20MHz$, the response to an electric field becomes of the same order of magnitude as the response to a magnetic field. It even becomes dominant for the highest frequencies. For such frequencies, the coil shield may thus also yield a useful filter against the external electric fields, especially at the coil or cable resonance frequencies.

In the frequency band up to $20MHz$, the fast-time response of the external fields may clearly dominate the electronic noise and this may significantly affect the detector. As can be seen in Fig. 7.8, the peak fast-time response is larger than 100V and occurs around $100kHz$ and values larger than $10V$ are observed up to $1MHz$. Important perturbations are thus expected close to a powerful AM broadcast facility emitting around 500kHz. The highest responses may however only be observed in the near field of the source. Nevertheless, even in the far-field, responses up to $10V$ are observed. Such high values will clearly saturate the amplifier output and the detector will most probably be unusable.

Fortunately, EM background fields are typically much lower than the allowed limits [75]. For example, a survey of the exposure to long, medium and shortwave radio services around Baden-Wurttemberg (Germany) has been presented in [76]. It shows a variation of the exposure between 0.0001 and 1% of the allowed limit with a median value of 0.01%.

With such fields, the detector should remain usable in most cases. The maximum usable sensitivity setting may however vary widely as a function of the operation location. In the quietest places, the response to the EM field is below the electronic noise and (in absence of other sources) the detector can be usable at its highest sensitivity. In contrast, for a field reaching 1% of the limit, fast-time responses up to $1V$ may arise and this will clearly require to decrease significantly the detector sensitivity. In all cases, the operator should determine if the maximum usable sensitivity is high enough to meet detection requirements in a particular situation.

7.8 Test cases

We have shown that, for the allowed strength of the EM fields, the EM background may significantly affect detector performance. In general, the field strength is significantly below the allowed limit and the effect on the detector is then limited. We now consider in more details two sources that may significantly affect the detector, a high voltage power line and a high-frequency fluorescent lamp.

Power lines (high-voltage or not) are known to disturb metal detectors. This is confirmed by the fact that some detectors are designed to mitigate the effect of high voltage lines. For example the Vallon ML1620 has a setting to filter 50Hz or 60Hz noise related to high-voltage lines (see Section 7.6.2).

We have also studied a fluorescent lamp with a high frequency electronic ballast, for our indoor measurements, this was found to be the dominant noise source. The analyses may seem academic in the scope of humanitarian demining because detectors are used outdoors. Nevertheless for other applications, such as airport security control gate, the detectors may however be used indoors.

7.8.1 High Voltage Line

Our objective is to determine the region in which a high voltage power line may interfere with the detector. According to Fig. 7.8 it is clear that, for frequencies as low as 50Hz, the effect of the electric field is always negligible and only the magnetic field must be considered.

There exists a large variety of high voltage power lines and the effect on the detector may vary significantly, depending on the line characteristics. As a test cases, we have considered a line studied in [77, p. 5, H Frame Structure] for the British Columbia Ministry of Transportation. It is a H frame structure with a horizontal conductor structure arrangement. The characteristics of the line are as follows:

- three phase conductors in a horizontal plane
- height of conductors: $H = 14.1m$
- distance between conductors: $D = 6.7m$
- phase-to-phase: voltage 287kV (RMS)
- phase current: $I_{\mathrm{L}} = 780A$ (RMS)

For the magnetic field, the soil is essentially transparent and the field produced by a single line conductor can easily be computed. Indeed, by symmetry, in cylindrical coordinates with the axis on the conductor, the field is along the polar angle unit vector $\hat{\boldsymbol{\theta}}$ ($\boldsymbol{B} = B_\theta \hat{\boldsymbol{\theta}}$) and is constant at a given distance R from the conductor. Form the Ampere law, the field can then be expressed as:

$$B_\theta = \frac{\mu_0 I}{2\pi R} \tag{7.29}$$

with I the current in the conductor.

The total fields can be computed at any location by summing the contribution of the three conductors, taking into account the phase of the current in each conductor:

$$[I_{\mathrm{a}}, I_{\mathrm{b}}, I_{\mathrm{c}}] = I_{\mathrm{L}}[e^{-j\alpha}, 1, e^{j\alpha}] \tag{7.30}$$

with I_{L} the RMS line current, $I_{\mathrm{a,b,c}}$ the three phase currents phasors and $\alpha = 2\pi/3$, the phase difference between the line currents. The result is a complex vector that represents an elliptically polarized magnetic field.

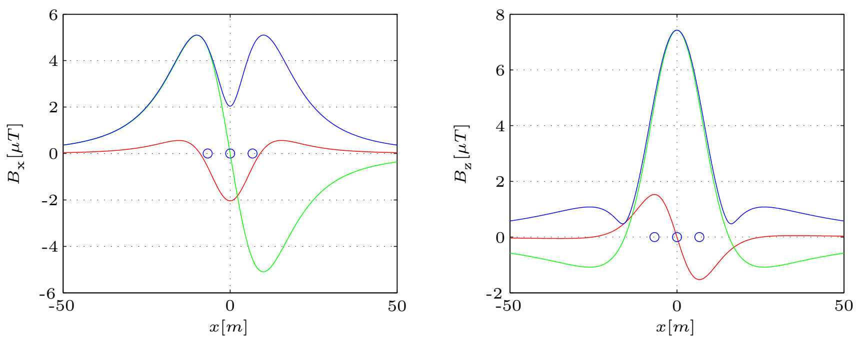

(a) (b)

Figure 7.9: *Horizontal (B_{x}) and vertical (B_{z}) magnetic induction at ground level as a function of x, with $|x|$, the lateral distance distance to the line. Magnitude (blue), real (red) and imaginary (green) parts are shown. The x-coordinate of the line conductors are indicated by circles.*

We now consider a Cartesian axis system with the x-axis horizontal and perpendicular to the conductors, the z-axis vertical and the origin on the ground below the central cable. The conductors are then located at $(-D, y, H)$, $(0, y, H)$ and (D, y, H) respectively for phases a, b and c and the magnetic field has two (complex) components $B_{\rm x}$ and $B_{\rm z}$. Detectors are generally used close to the ground and we have therefore computed the field at ground level as a function of x with $|x|$ the lateral distance to the high voltage line. This is illustrated in Fig. 7.9 which shows that, as expected by symmetry, $B_{\rm x}$ is purely real (in phase with the central conductor current) and $B_{\rm z}$ is purely imaginary (in quadrature with the central conductor current) below the central conductor. Furthermore, the vertical component of the field is maximum below the central conductor while the horizontal component is maximum in the vicinity of the outer conductors.

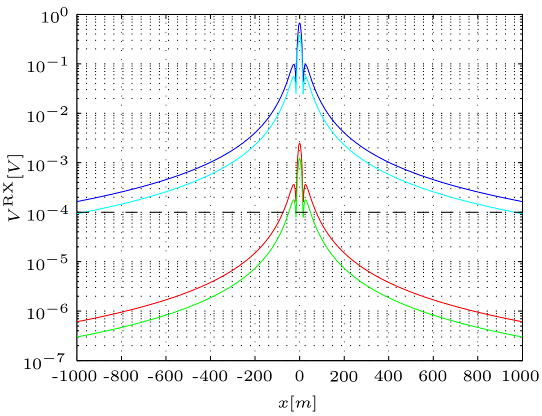

Figure 7.10: *Steady state amplitude for $V_{\rm coil}^{\rm RX}$ (red), $V_{\rm filt}^{\rm RX}$ (green), $V_{\rm amp}^{\rm RX}$ (blue) and corresponding amplitude of the slow-time signal $A_{\rm slow}$ (cyan) at ground level as a function of x, with $|x|$, the lateral distance distance to the line. The dashed black line shows a reference noise level of 0.1mV.*

Detectors are in general used with the head horizontal and are thus only sensitive to the vertical magnetic field. The induced voltage is then:

$$e_{\rm L}^{\rm RX} = j\omega N_{\rm RX}\pi r_{\rm RX}^2 B_{\rm z} \tag{7.31}$$

with $N_{\rm RX}$ and $r_{\rm RX}$ the number of turns and the radius of the RX coil. Considering a frequency of 60Hz, (7.21) can then be used to compute the slow-time response. This is illustrated in Fig. 7.10 which shows that the high voltage line can significantly affect the detector and that the response remains above the noise level (again assumed to be 0.1mV) up to a distance of one kilometer of the line. The coil voltage ($V^{\mathrm{RX}}_{\mathrm{coil}}$ — red curve) remains below $2mV$ and the steady state fast-time response reaches $0.5V$ only in a small area just below the line[8]. Hence little nonlinear effects are expected and simple filters can be used to efficiently mitigate the effect of the high voltage line without reducing the sensitivity to the targets (see Section 7.6.2). Note however that, for the line considered, the maximum field is about $8\mu T$ and this is still more than ten times below the maximum allowed magnetic field of $100\mu T$. Hence nonlinearities and reduction of target sensitivity may occur below high voltage power lines generating larger fields, closer to the allowed limit.

7.8.2 High-frequency fluorescent lamp

We have observed experimentally that fluorescent lamps with high frequency electronic ballast produce large fast-time signals. Signals around $1V$ where commonly measured. To check if this can be explained by our model, we have considered a TLD58W lamp with a length of $1.5m$ and a diameter of $2.54cm$ (one inch). The current flows in closed loop which we modeled as a horizontal rectangle of dimension $150 \times 1.5cm$. This does not take into account the current distribution inside the tube, as the current is assumed concentrated in the middle of the tube. Furthermore the current return wire is assumed horizontal and a few millimeters on the side of the tube. Other configurations are of course possible but this simple model should be sufficient to predict the order of magnitude of the response.

For this geometry , the induced voltage can easily be computed as:

$$e^{\mathrm{RX}}_{\mathrm{L}} = j\omega M I_{\mathrm{lamp}} \tag{7.32}$$

with M the mutual coupling coefficient between the lamp circuit and the RX coil. This coefficient can easily be computed by using the analytic expression of the vector potential of a circle [31, p. 273] and integrating it on the rectangular lamp circuit.

With a high frequency electronic ballast, the lamp typically works at frequencies above 20kHz, close to the sensitivity peak of the detector. As a test case, we have used the ballast described in [78] which works at $45kHz$ and generates a current of about $450mA$. The resulting response is illustrated in Fig. 7.11. One sees that the lamp can significantly affect

[8]For larger values, the displacement of the evaluation window may become large, which may significantly reduce the target response.

the detector and that the response remains above the noise level (again assumed to be 0.1mV) up to a distance of about 10m.

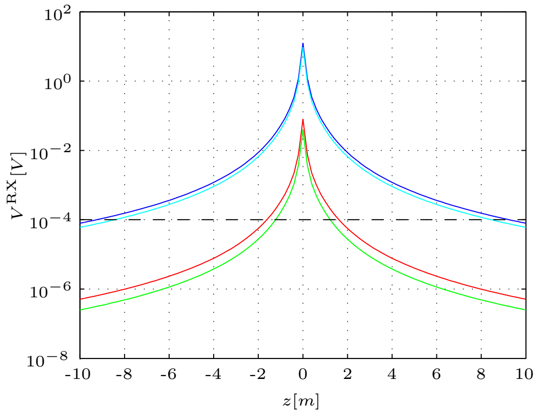

Figure 7.11: *Steady state amplitude for $V_{\text{coil}}^{\text{RX}}$ (red), $V_{\text{filt}}^{\text{RX}}$ (green), $V_{\text{amp}}^{\text{RX}}$ (blue) and corresponding amplitude of the slow-time signal A_{slow} (cyan) just below the lamp as a function of the vertical distance z to the lamp. The dashed black line shows a reference noise level of 0.1mV.*

CHAPTER 8

Conclusions and perspectives

The effect of the environment on EMI sensors has been investigated. More specifically, we have focused our attention on the response of magnetic soils and the corresponding *Volume of Influence*, on interactions between the head and water and on the effect of the EM background. In order to perform this analysis, a detailed detector model, including the coil and the electronics has first been developed. The voltage induced in the coil was rigorously established by resorting the quasi-static approximation of the reciprocity expression. This yields, in addition to the classical derivative of the magnetic flux, a contribution related to the incident electro quasi-static field. The latter contribution is required to understand the effect of water on the detector head.

In this chapter, we provide a summary of the important developments together with some conclusions. Finally, we propose a number of perspectives for further research.

Contents

8.1 Summary and Conclusions

8.1.1 Detector model

A complete model of the detector up to the generation of the slow-time signal has been developed in the first part of this thesis. This model allows us to compute the time-domain sensitivity maps which provide very useful information on the sensitivity of the detector to various targets as a function of their dynamic behavior (their impulse response). A detailed model is required for this purpose because the electronic modules such as the Receive (RX) filter or the dynamics of the amplifier play an important role. We have further used the model developed in the second part of this thesis to compute the effect of water or of the EM background on the detector. There also, the electronic modules play an important role. Furthermore, the physical mechanism by which water can affect a Metal Detector (MD) still had to be established. We have used our detailed model to validate our hypothesis, allowing not only for a qualitative validation but also a quantitative one.

The model includes the coils, the Transmit (TX) pulse generation, the RX filtering and amplification as well as the transformation from the fast-time signal to the slow-time signal through integration in the evaluation window. The slow-time processing (audio generation, background compensation, ...) was briefly mentioned in Section 2.8 but it has not been included in the model because it varies significantly from one detector to another. Further, the design of the audio generation is rather at the ergonomics level and must take into account the functioning of the human hearing, which falls outside the scope of this thesis. If required, those modules may be added without interference with the existing model as the processing happens at two different time scales, without any feedback.

The output of the model has been compared with measurements on the detector and an excellent matching has been shown. The detailed model is specific to the Schiebel detector but to a large extent, it highlights the functioning principle of most pulse MDs. The model should be easily adapted to other PI detectors and with some more work to Continuous Wave (CW) detectors as well. Furthermore, a number of functionalities present in newer detectors such as the use of variable pulse width or more complex evaluation windows to allow for soil compensation have been addressed in Sections 2.6 and 2.8.

A major achievement is the accurate coil model that has been developed. We have shown, by resorting to reciprocity that a real coil not only responds to a variation in the magnetic flux as classically assumed, but also to an Electro Quasi-Static (EQS) irrotational electric field. The two contributions have been called the magnetic and electric induced voltages respectively. The electrical contribution is related to the charge distribution that appears on a coil due to its parasitic capacitance and allowed us to explain the effect of water on the detector head. Furthermore, in the literature, the induced voltage is usually computed, assuming a perfectly shielded electronics and a connection through an ideal coaxial cable. This significantly simplifies the development but such a configuration is not representative of most MDs. We have therefore discussed the effect of an imperfectly shielded electronics and of the use of other connecting cables. We have shown that the results obtained for a perfectly shielded electronics and coaxial cable connections can be used in good approximation for other configurations.

To show that induced voltage can be split in an electric and a magnetic contribution, we had to rely on the Quasi-Static (QS) approximation and to derive the corresponding QS reciprocity expression. As the term QS approximation is used for various low frequency approximation in the literature, we have clarified, in. an appendix, what is precisely meant by the approximation used.

We have also shown that the real coil may be replaced by equivalent sources that produce the same field as the coil on a surface that may be chosen arbitrarily as long as it completely includes the detector and completely excludes the target and the soil. This allows for significant simplifications of the coil model as the detailed current and charge distribution is not required, especially if the target is at some distance from the detector.

More precisely, the induced voltage has been related to the current and charge distribution that would appear on the RX coil if a unit current was injected into it. The magnetic and electric contribution being related to the current and charge distribution respectively. The induced voltage may be introduced in the coil circuit model as a single voltage source. This is however not ideal because the relation between the external fields and the induced voltage is frequency dependent, yielding a convolution in the time-domain. We have then shown that the total induced voltage can be split into a number of contributions, yielding a voltage source for each inductor and for each capacitor. The relation between the external fields contribution and the induced voltage contribution is not frequency dependent anymore (except for a derivative that is easy to handle) yielding a more convenient circuit.

The required charge and current distribution has been computed from a detailed coil model in which each turn has been represented by an inductor and a capacitor has been introduced for each pair of turns. The Method of Auxiliary Sources (MAS) has been used to compute the turn-to-turn capacitance matrix. This requires a detailed knowledge of the winding geometry and of the material used, mainly the electrical permittivity of the casing. We had access to a detailed drawing of the wire geometry but we had no information on the electrical permittivity of the casing. We have therefore estimated this parameter to match the coil equivalent capacitance with the measured one. The obtained value is compatible with the kind of material that is expected to be used for the casing.

A simple model in which the coil is represented by a single inductor and a single capacitor inductor branch has also been implemented. The parameter of this model are available from measurements. They can also be derived from the detailed model. We have compared both models and they showed a good match in the frequency band of interest. Differences appear only at higher frequencies where the effect of the additional resonance modes of the detailed model become apparent. Therefore, the simple model is in general better suited to simulate the detector. Surprisingly, it is even more accurate than the detailed one because the detailed model shows high frequency oscillations that are not present in the measurements. The latter have been attributed to the skin effect, that could not be taken into account in the state-space model, and that is expected to yield stronger damping. Nevertheless, the detailed model is mandatory to estimate the current and the charge distribution on the coil. It can also be used to evaluate a new coil design without having to realize a prototype. It can then be used to estimate the resulting parameters for the simple model.

8.1.2 Soil response

The response of a magnetic soil has been investigated in Chapter 4. We have shown that under realistic conditions—negligible conductivity, low magnetic susceptibility—the soil response can be expressed as an integral on the soil volume of the magnetic susceptibility multiplied by the head sensitivity. Therefore, the sensitivity map helps to understand the soil response. As an illustration, the sensitivity map of a double-D head was presented and used to explain the partial soil compensation inherent in such a head design and to understand the limitations of that compensation.

This approach is both general and efficient. Indeed, when compared to available analytic solutions, it is much more general as it makes it possible to consider any coil shape and relative position, any soil inhomogeneity and relief and any head position and orientation. Further, when compared with generic numerical methods, our approach is much more efficient and makes it possible to compute the soil response for many different configurations within a reasonable time. The computation speed is further improved for heads which can be represented by line and circular segments for which the field can be calculated analytically. Additional efficiency is obtained by the introduction of dimensionless quantities which makes it possible to analyze a head design without having to specify its size. The head size only appears in the expressions relating the dimensionless quantities to their dimensional counterparts. Those expressions make it possible to assess efficiently the effect of head scaling.

In addition to the general expression, valid for any soil relief and inhomogeneity, we have also developed a simpler expression which is only valid for a homogeneous Half-Space (HS) but which does not require the Born approximation. Comparing both approaches on a HS configuration made it possible to establish an analytic expression for the error introduced by the Born approximation as a function of the soil magnetic susceptibility. In the light of susceptibility measurements of many soils found in the literature, this expression showed that for most soils of interest within the framework of mine clearance, the corresponding error is negligible.

Comparing numerical results obtained with the two models on a HS configuration also provided a cross-check for the validity of those models and their implementations. An additional validation was obtained in the case of concentric circular loops by comparing the numerical results with the available analytic solution.

Two important head characteristics, the zero equi-sensitivity surface and the sensitivity map, were visualized for a number of representative head designs. Those concepts may be very useful in practice to better understand the detector behavior. Another useful concept that may be derived from the model is the volume of sensitivity. This will be discussed in the next Section.

The heads were also compared with respect to their HS response. This shows that soil response is perfectly compensated for a quad head and that it is very-well compensated for a double-D coil. The variation of the HS response with the head height was investigated and this showed that it increases much more severely when the head approaches the soil for single coil heads than for double coils. This might be one of the reasons for which separate TX and RX coils are used with some Pulse Induction (PI) detectors.

Those results are interesting but further research is required for a complete head comparison. The target response should be taken into account. Indeed, a better soil compensation does not necessarily improve the overall detector performance because the better soil compensation might come at the expense of a reduced target sensitivity. The efficiency of the electronic soil compensation[1] should also be considered. Indeed, if that compensation is efficient enough, the head geometry should not be optimized to reduce the soil response but to increase the target sensitivity. Finally, head comparison was performed for flat and homogeneous soils. Real soils are much more complex and their relief and inhomogeneities should be taken into account. The model developed provides the right tool for this analysis. One could for example compare various heads for a sinusoidal soil relief or for a sinusoidal soil inhomogeneity. This would then highlight the kind of inhomogeneities or relief to which each head is the most sensitive.

8.1.3 Volume of influence

The concept of Volume of Influence (VoI) has been discussed in Chapter 5. Basically, the Volume of Influence (VoI) is the volume that produces a fraction α of the total soil response. It should not be confused with the volume in which a metallic target can be detected. The concept of VoI is not entirely new but, to the best knowledge of the authors, it has never been rigorously defined and quantified for Electromagnetic Induction (EMI) detectors. For such detectors, significant simplifications are possible to compute the response of most soils (those for which the response is dominated by the magnetic susceptibility, which in addition is small) and this allows the concept of VoI to be developed much further.

After showing that the basic and intuitive definition of the VoI has

[1] processing of the fast-time response

some limitations for heads with intrinsic soil compensation, we proposed a generalized definition in which the VoI is the union of a positive and a negative VoI, each being defined as in the basic case, but accounting only for the areas in which the sensitivity is positive or negative. We showed that this generalized definition can be used for all heads and that for heads with intrinsic soil compensation, it allows one to estimate the volume that should be homogeneous for a given efficiency of compensation.

Next, we showed that to yield a unique VoI, a constraint must be introduced. We have proposed two constraints, one yielding the *smallest VoI* and the other one yielding the *layer of influence*. We showed that those two specific VoI are very useful for a number of applications. For example, in the scope of mine action, if test lanes are built to evaluate EMI sensors for specific soils, the *layer of influence* allows the objective definition of the depth to which the actual soils must be removed and replaced by those specific test soils. Also, the *smallest VoI* is the volume of soil that should be characterized if the aim is to predict the response of a detector at a given location.

Then, the effect of soil inhomogeneity has been investigated. More precisely, we have considered a soil for which the magnetic susceptibility is in a range $[\chi_{\mathrm{min}}, \chi_{\mathrm{max}}]$ at each location and we have shown how a worst-case VoI (i.e. valid for the worst-case soils under consideration) can be obtained by increasing the fraction α taking into account the expected range of magnetic susceptibilities. Similarly, we have quantified the effect of soil inhomogeneity on the efficiency of the head soil compensation. This allowed us to translate a requirement on quality of the compensation in a worst-case situation into a response fraction α and, hence, to compute the corresponding VoI.

Further, visualizing the *smallest VoI* may help to understand the detector behavior. For example, in geophysical survey, it defines the soil region that can be investigated by the detector. Similarly, in the scope of mine action, it defines the soil region that may be at the origin of a false alarm. In the same context, it defines the volume of soil that should be homogeneous for a given efficiency of soil compensation. Therefore, the shape of the *smallest VoI* has been illustrated for a number of typical head geometries. It was noted that for small values of the response fraction α (below 0.9), the shape can be arbitrary. However for most applications, large values of the fraction α need to be considered. For such values, the shape of the *smallest VoI* becomes identical for most heads, only its size changes. A noticeable exception is the quad head, for which the shape of the *smallest VoI* is significantly different compared to the other heads considered in this chapter. This shape similarity has been explained by resorting to the far-field approximation of the magnetic field, for which only the dipolar moment of the coils is considered. The specific case of the quad head is then explained by the fact that one needs to account for the quadrupole moment, since the receiving coil has no dipolar moment.

Finally, the size of the VoI has been computed and compared for various heads and this yielded practical conclusions. For example, the *smallest VoI* is much larger for the double-D head than for the other heads considered and therefore, the compensation of the double-D head will be optimal only if the soil is homogeneous in a large region below the coil. We also noted that the size of the VoI strongly depends on the head height. This size becomes larger when the head is lifted above the ground. In addition to the size of the VoI, the study of some other head characteristics allows for a better understanding of the head behavior. For example, the compensation ratio (γ) is much larger for the double-D head than for the concentric head, and this explains why the former nearly perfectly compensates the response of a homogeneous soil while the latter only partly compensates the soil response.

8.1.4 Water effect

The influence of water on the head has been investigated in Chapter 6. More than ten years ago, a 'moisture problem' was reported with the Schiebel AN-19/2. This problem could be reproduced by Defence Research and Development Canada (DRDC) and mitigation means were found but the physical mechanism at the origin of the problem was not understood. Most modern metal detector coils are shielded and this solves the problem. The use of a shield however has some drawbacks. It increases the coil capacitance and this makes the Transmit (TX) current turn-off slower. Manufacturers are still trying to increase the sensitivity of detectors. However, as the detector can only listen to the target response after the TX current has decreased to a sufficiently small value, this capacitor increase may become the limiting factor to improve the sensitivity. The shield should then be optimized and this optimization requires a better understanding of the origin of the signals against which the detector must be shielded.

We therefore investigated this problem again in order to find a model that can predict the observed signals. We first reproduced the measurements that were performed by DRDC. This confirmed that a number of different phenomena occur. When the head is completely immersed, no water effect is observed. A positive response is however observed when the operator touches the water with his finger and the response seems to be amplified when moving the finger. When the head is lifted out of the water and large quantities of water are dripping, a large negative response is observed. The response is similar to that of a large metallic target and produces an alarm. When enough water has dripped and only a thin layer of water remains on the head[2], the polarity of the response reverses. This positive response is at the origin of the loss of sensitivity reported from the field.

To better understand the problem, we performed a number of additional measurements. We mainly investigated the effect of water conductivity by starting from distilled water and adding salt progressively. We found that the water conductivity has no effect on the response observed when touching the water but it has a major effect on all other phenomenons.

The negative response first observed when lifting the head out of the water disappears for very small ($< 25\mu S$) and very large conductivities ($> 7mS$). It is maximum for a conductivity of about $650\mu S$ representative of tap water. The moment at which the maximum deviation is observed is a function of the conductivity. For tap water, the maximum deviation is observed just after the head has been lifted out of the water. For higher conductivities, the maximum deviation occurs later, when water is no longer dripping from the head. This suggests that the water movement is not at the origin of the response.

The positive response observed after enough water has dripped from the head is maximum for distilled water. The effect diminishes with the conductivity and disappears for a conductivity of about $3mS$. Going towards lower conductivities than distilled water, we expect the response to reach a maximum for a given conductivity and then decrease to zero

[2]This layer is not necessarily continuous, it may break in smaller parts. It is however difficult to assess the exact state of the water layer when the largest response is observed. Similar effects were observed in the IPPTC trials [68] when lightly misting the head from a bottle sprayer. We also tried to moist the head with a sprayer but this did not yield any visible effect on the fast-time signal. This discrepancy may be due to the fact that in the IPPTC tests the slow-time signal was used whereas we used the fast-time signal. Using the slow-time signal may increase the sensitivity. We nevertheless used the fast-time signal because it conveys more information. This needs further investigation.

for even smaller conductivities. This could however not be tested because the lowest available conductivity was that of distilled water (about $25\mu S$).

Clearly, the observed responses are not due to eddy currents because the water conductivity is too small; especially for distilled water and the responses, in general, decrease with the conductivity. The first idea that usually comes to mind and that has often been mentioned to explain how water can affect the detector, is a capacitive effect. The diversity of phenomena observed is however surprising and difficult to explain by a capacitive effect alone.

To explain the phenomena observed, we first showed that, for most conductivities, water can be seen as a perfectly conducting shield for the Electro Quasi-Static (EQS) problem at hand. We then extended the coil circuit model to introduce this fictive 'shield' that appears when the head is immersed in water. This is done by introducing a number of turn-to-shield capacitors; the value of which are computed numerically, using the Method of Auxiliary Sources (MAS). The resulting circuit coil model was combined with the detector electronics model to compute the fast-time response for the head immersed in water. This showed that immersing the head in water has very little effect on the fast-time response. The predicted deviation was small enough to be compatible with the tests that showed no measurable effect.

We then searched for a model to explain the effect observed when touching the water with the head immersed in water. By chance, we found that this effect disappears when the operator is standing on a wooden chair. This led us to the idea that the effect is due to a connection between the coil casing and the electronics via the water, the operator body, the ground and the oscilloscope. We then introduced such a connection in the immersed head circuit model where it appears as an additional RC path. Similar simple circuit models have been developed to explain the other observed phenomena. A resistive connection between the TX and RX 'water shield' has been introduced to model the water film[3] appearing between the coils when lifting the head out of the water. Finally, to model the thin water layer remaining on the head when enough water has dripped, a resistor was introduced in the turn-to-shield connection in order to take into account the fact that a thin layer may not be considered as a PEC shield anymore.

[3]More precisely, the connection is through the bulk water and two water films; one between each coil and the bulk water.

In all cases, the value of the resistance introduced in the circuit-model is a critical parameter that significantly affects the response. The value of this resistance is difficult to compute because the current path and corresponding resistivity is not known. For example, for the resistor modeling the water film joining the coils when the head is lifted, the exact shape of the film is unknown. For the resistor modeling the ground connection appearing when touching the water, the resistance of the operator body and the water-finger contact resistor is difficult to estimate. We therefore varied the resistor to find the value that yields the largest response. This largest response was then compared to the measured response. For the four phenomena observed, the largest computed response was in good agreement with the measurements, showing the right polarity and the right shape. The magnitude of the response was however underestimated by a factor ranging from about two, for the response observed when touching the water, to about ten, for the response observed when lifting the head out of the water. We can not exclude that this underestimation might be due to the existence of not yet understood mechanisms that contribute to the response. It is however also possible that all important mechanisms have been found and that the underestimation of the response magnitude is simply due to inaccuracies in the detector parameters, mainly the coil-to-shield capacitance.

As just mentioned, the value of the additional resistor introduced in the model was not computed from the water geometry. Therefore, the effect of water conductivity on the response can not be derived quantitatively from the circuit models. We could however explain most of the observed effects of water conductivity qualitatively. For example the decrease of the response of a thin water layer on the head, observed when the water conductivity increases can be explained by noting that the water layer yielding the 'optimal' resistance becomes unrealistically thin. The water layer is thus expected to break before the 'optimal' thickness is reached, yielding a smaller response because only part of the coil contributes to the response and the corresponding resistor is further 'sub-optimal'. Similarly, for the response observed when the head is lifted and large quantities of water are dripping, the 'optimal' thickness for the film linking the coils is also getting unrealistically small for large conductivities. Note that in that case, the 'optimal' resistance may be reached by the water layer on the plastic spokes between the coils alone. This could explain why the largest response is observed later for large conductivities, at a moment when water is not dripping from the head anymore. Even for the smaller water layer, located only on the plastic spokes, the 'optimal' thickness will become unrealistically small for the largest conductivities. This explains why the response is observed later and then disappears for increasing conductivities. Finally, when touching the water, the variation of finger-water contact resistor may explain the variation of the response observed when moving the finger.

The circuit model for the thin water layer case was shown to have some limitations, mainly because the PEC shield model becomes inaccurate. Furthermore, the effect of a thin water layer is the most important from a practical point of view. It is indeed at the origin of the loss of sensitivity reported from the field. Besides, this effect is the only one that is expected to occur in normal use (the head can get moist, for example in contact with wet grass but is very seldom used in water). Due to its importance and to the just mentioned limitations of the corresponding circuit model, we have developed an alternative field-level model in which the field scattered by the water layer is explicitly computed. The scattered field is EQS in nature and according to the simple model usually used, such fields do not induce any voltage in the coil. The more accurate model that we have developed in Chapter 2 and specifically, the expression (2.58) was thus needed to compute the voltage induced by the scattered electric field.

To keep a tractable model, we have considered an ellipsoidal shaped water layer and used the corresponding analytic solution. With this model, the critical parameter governing the dynamic of the response is the depolarization factor which is related to the elongation of the ellipsoid. The exact water geometry is not known and we have therefore computed the response as a function of the ellipsoid small axis length which corresponds to the thickness of the water layer. The response corresponding to the 'optimal' thickness was then compared to the measurements, showing a good agreement. Indeed, the computed response has the right polarity and the right shape but its magnitude is underestimated by a factor of about five for tap water. As for the circuit-model, the underestimation may be due to model inaccuracies, mainly errors in the coil turn-to-shield capacitance, and to the water layer that is not ellipsoidal as assumed.

With the field-level model, the effect of water conductivity can be computed quantitatively. The result shows however some discrepancy with the measurements. It does not decrease for large conductivities, but as for the circuit model this may be explained by noting that ellipsoid yielding the largest response become unrealistically thin. In addition, the model predicts a decrease of the response for small conductivities and this decrease was not observed in the measurements. We expect that such a decrease really exists for conductivities lower than that of distilled water and that were not available for the measurements. There is nevertheless a problem with the model because it predicts a large decrease of the response for conductivities that were used for the measurements and this decrease was not observed. The reason for this discrepancy might be that, for the lowest conductivities, the higher order modes that were neglected in the model, start to dominate the response. This issue needs further investigation.

8.1.5 Electromagnetic background influence

The influence of the Electromagnetic (EM) background has been investigated in Chapter 7. We have shown[4] that the EM background may affect the detector from frequencies below $1Hz$ to about $20MHz$ with a sensitivity peak around $100kHz$. For the maximum allowed fields, the effect may be very severe; significantly lowering the usable sensitivity or even preventing the normal functioning of the detector. In most places however, the fields are much lower than the maximum value allowed and the effect on the detector is much less severe. It is however not uncommon that the external field reduces the maximum usable sensitivity. It is then the operator who should decide if the usable sensitivity is high enough to meet the detection requirements in a particular situation.

There exists many sources of radiation in the critical frequency band, such as high voltage power lines, AM broadcasting antennas (short, medium and long waves), aircraft beacons, electronic fluorescent lamps, electrical drives and computer screens. Two sources have been studied in more details as test cases; high voltage power lines, because they are well-known to affect the detector, and fluorescent lamps with a high frequency electronic ballast because they were the main disturbing source during our measurements. We have shown that even though the frequency used is quite low, high voltage power lines can significantly affect the detector because large magnetic fields are produced. For the line considered, perturbations are possible up to a distance of about one kilometer. In contrast, fluorescent lamps produce much lower field but the frequency used by the electronic ballast is above 20kHz; close to the

[4]Recall that the numerical results have been obtained using the Schiebel state-space model. However, similar results are expected for many PI detectors.

sensitivity peak of the detector. For the configuration considered, the detector could be affected by the lamp at distances up to ten meters.

We have shown that nonlinear effects may yield very complex responses. In most cases however, the fast-time response remains linear. Even then, rigorously speaking, a complete time-domain simulation is required and this is not efficient. We have however shown that the fast-time response can efficiently be computed as the sum of a steady state and transient contribution that can be computed from the listening-phase transfer function without having to perform a time-domain simulation.

We have also shown that the slow-time response can be seen as a sampled version of the (filtered) fast-time steady state response. The time interval between two samples may however vary because the external field may affect the location of the evaluation window. If the external fields are small enough, regular sampling can be assumed, which significantly simplifies the problem. The magnitude of the external field for which the regular sampling assumption is valid has been established. This limit is a decreasing function of the frequency. When regular sampling can be assumed, the slow-time response to an external sinusoidal is then a discrete sinusoid. The amplitude and phase of that sinusoid can be computed from the listening-phase fast-time transfer function and from the fast-to-slow-time transfer function. The frequency of the discrete sinusoid is in general different from that of the external field due to the aliasing. More precisely, the whole electromagnetic spectrum is projected between zero and the Nyquist frequency ($\nu_{\mathrm{TX}}/2$ with ν_{TX} the Pulse Repetition Frequency (PRF).)

As already mentioned, large external fields may affect significantly the location of the evaluation window. If the displacement is significant when compared to the time constant of the target, this may significantly affect the target response. Depending on the phase of the external field with respect to the TX pulse, the displacement of the evaluation window may be positive or negative. As the detector is asynchronous with the external field, the phase will be different for each pulse and positive and negative displacements will occur. Due to the asymmetry of the exponential decay, positive displacements will however be larger and this will, on average, reduce the target response. In the extreme case, for fields yielding a fast-time response larger than the evaluation window threshold, the evaluation window may not be triggered for some pulses and this may jeopardize the normal functioning of the detector. In summary, large external fields not only require an operator to use a lower sensitivity, but it also reduces the target response. Those problems may be avoided by choosing the minimum available detector sensitivity large enough such that fields yielding a large reduction of the target response, also produce a very noisy audio signal. The operator will then notice that the detector is unusable in the prevailing environment.

A number of counter-measures have been discussed:

- A differential head has little sensitivity to external fields but this is not always the optimal solution because the target sensitivity of such a head is also reduced.

- For low frequencies, a second evaluation window may be used after some delay from the first one to estimate the external field contribution to the response which can then be canceled.

- Slow-time filtering can be used to reduce the response of the external field. Low slow-time frequencies can however hardly be filtered because this would also reduce the target response. The frequency limit is related to the scanning speed.

- The energy of the spectrum aliased in the critical frequency band, that can not be filtered by the slow-time processing, is influenced by the PRF. In this context, increasing the PRF is beneficial. Optimizing the PRF according to the EM environment to prevent the dominant frequencies from falling in the critical frequency band is even better.

- For low frequencies, pulses with alternating polarity may be efficient. The resulting modulation increases the frequency of the disturbing slow-time signal and this makes efficient slow-time filtering easier. Choosing the PRF according to frequency of the external field may yield an even more efficient filtering. This is the principle of some methods implemented in detectors to mitigate the effect of high voltage power lines. The PRF is then adapted to the line frequency (50Hz and 60Hz).

The internal processing implemented in detectors is in general not known but it seems that most of the counter-measures discussed are implemented in some detectors. The use of an extra evaluation window is discussed in a patent [47]. The PRF was measured for three detectors (the Schiebel AN-19/2 and two Vallon detectors). The adaptation of the PRF to mitigate the effect of power lines was observed for the Vallon ML1620 which has a switch to select 50 or 60Hz. The PRF is clearly increasing from the Schiebel AN-19/2 to the Vallon ML1620 and further increased for the newer Vallon VMH3. This last detector further allows to choose amongst a large number of PRFs. The PRF can also automatically be optimized according to the prevailing EM background.

The interaction with jammers requires further investigation. We have suggested that they may affect the detector at frequencies above $20MHz$ as a result of coil or cable resonances and nonlinear effects at the input side of the amplifier. More precisely, the saturation of the clipping diodes in the filter and conditioning network may affect dramatically the detector. In the worst case, the detector may stop working without any warning to the user. This is a critical issue and we are not aware of any counter-measures implemented in modern detectors. A simple solution might be to use a dedicated sensor that alerts the user about the presence of a critical EM background.

8.2 Perspectives

In Chapter, 4, we have developed a model that allows one to compute the response of a magnetic soil with an arbitrary relief and arbitrary inhomogeneities of the magnetic susceptibility. This model was used to compute a number of useful characteristics of typical detector heads. For example, the VoI was computed and the problem of soil inhomogeneities was addressed in that context. However, a more general analysis of the effects of soil inhomogeneities was not performed. We believe that the model developed may be quite useful in that context. It could be used to compute the response of soils with relevant inhomogeneities or relief. One could for example consider a harmonic variation of the magnetic susceptibility. The model would then yield the soil response as a function of the amplitude and direction (x, y or z) of the harmonic variation considered. A statistical approach based on a random susceptibility distribution is also possible. This could provide interesting conclusions on the effectiveness of the head intrinsic soil compensation for more realistic soils than a homogeneous Half-Space (HS). The worst harmonic soil (the one providing the largest response) could also be defined. A similar investigation could be performed to assess the effect of soil relief. One could then consider a homogeneous soil with a harmonic relief. Finally, a 3D numerical code could be used to investigate specific soils for which the model accuracy may decrease. This would be the case for soils with an exceptionally high magnetic susceptibility, for soils with localized highly magnetic stones or for soils with an exceptionally high conductivity.

In Chapter 6, we have proposed a number of models to explain the various phenomena observed when the head is interacting with water. The models predict responses which are in good agreement with the measurements. The predicted responses are however smaller than the measured ones, by a factor ranging from two to ten. Further research would therefore be useful to investigate the origin of this discrepancy and to further investigate the accuracy of the proposed models.

In Chapter 7, we have investigated the influence of the EM background on the detector. The influence of nonlinear effects that may occur for large fields, has been briefly addressed. However, the quantitative results were obtained assuming that no nonlinear effects come into play. A further investigation of the effects of nonlinearities could provide new interesting and useful results. This could for example yield a better understanding of the effect that jammers may have on detectors. This investigation might require the use of a more accurate model of the RX amplifier, valid for higher frequencies, and better taking into account the behavior of the amplifier when it recovers from saturation.

Appendices

APPENDIX A

Circuit state-space model

The objective is to obtain a state-space representation [79, Section 2.5.1] of an electric circuit composed of coupled inductors, capacitors, resistors as well as voltage and current sources. The state-space equations can be written as:

$$\frac{\mathrm{d}\underline{X}}{\mathrm{d}t} = \underline{\underline{A}}\,\underline{X} + \underline{\underline{B}}\,\underline{U} \tag{A.0.1}$$

$$\underline{Y} = \underline{\underline{C}}\,\underline{X} + \underline{\underline{D}}\,\underline{U} \tag{A.0.2}$$

with $\underline{X}$ the state vector, $\underline{U}$ the input vector, $\underline{Y}$ the output vector and $\underline{\underline{A}}$, $\underline{\underline{B}}$,$\underline{\underline{C}}$, $\underline{\underline{D}}$ are the state-space (constant) matrices. With such a description, programs such as Matlab® can be used to analyze the circuit by computing impulse or step responses, Bode curves, pole and zero maps etc.

The state vector contains the current in the inductors and the voltage across the capacitors: $\underline{X} = [\underline{V}_{\mathrm{C}}; \underline{I}_{\mathrm{L}}]$. The input vector contains the voltage and current sources: $\underline{U} = [\underline{V}_{\mathrm{s}}; \underline{I}_{\mathrm{s}}]$. The outputs are the voltages at nodes of interest or the currents through the branches of interest.

To compute the state-space matrices ($\underline{\underline{A}}$, $\underline{\underline{B}}$, $\underline{\underline{C}}$ and $\underline{\underline{D}}$), the circuit is first described by a list of resistors, capacitors, inductors (and mutual coupling between the inductors), voltage sources, current sources, short circuits[1] together with the two nodes to which they are connected. The circuit equations are then introduced to compute the circuit unknowns $\underline{Z} = [\underline{V}_{\mathrm{n}}; \underline{I}_{\mathrm{C}}; \underline{I}_{\mathrm{Vs}}; \underline{I}_{\mathrm{cc}}]$ with $\underline{V}_{\mathrm{n}}$ the node voltages, $\underline{I}_{\mathrm{C}}$, the current through the capacitances, $\underline{I}_{\mathrm{Vs}}$, the current through the voltage sources and $\underline{I}_{\mathrm{cc}}$ the current through the short-circuits. Any element of the unknown vector $\underline{Z}$ can be used as output[2].

[1] which are useful to connect two circuit parts or, as it will become apparent below, to use the currents through a circuit branch as output.

[2] Hence, as already mentioned, short-circuits can be introduced in a branch to get the corresponding current as output

The circuit equations used are the Kirchoff current equations which state that at each node, the sum of the currents is zero. Those equations can easily be expressed as a linear constraint on the unknown $\underline{Z}$, the state vector $\underline{X}$ and the input vector $\underline{U}$:

$$\underline{\underline{K}}_{\mathrm{Z}}\underline{Z} + \underline{\underline{K}}_{\mathrm{X}}\underline{X} + \underline{\underline{K}}_{\mathrm{U}}\underline{U} = 0 \tag{A.0.3}$$

where the matrices $\underline{\underline{K}}_{\mathrm{Z}}$, $\underline{\underline{K}}_{\mathrm{X}}$ and $\underline{\underline{K}}_{\mathrm{U}}$ have one row for each node except the first one[3]. Indeed, for each capacitor, each source and each short-circuit branch, the corresponding current is included in $\underline{Z}$ and for each node connected to such a branch, the corresponding element of $\underline{\underline{K}}_{\mathrm{Z}} = 1$ if the current enters the node and $\underline{\underline{K}}_{\mathrm{Z}} = -1$ if the current flows out of the node. Similarly, for each inductor, the corresponding current is included in $\underline{X}$ and this yields two contributions (+1 and -1) to $\underline{\underline{K}}_{\mathrm{X}}$. Similarly again, for each current source, the corresponding current is included in $\underline{U}$ and this yields two contributions to $\underline{\underline{K}}_{\mathrm{U}}$. Finally, for each resistor, the current is $(V_{\mathrm{i}} - V_{\mathrm{j}})/R$ and as the node voltages V_{i} and V_{j} are included in $\underline{Z}$, this yields 4 contributions $\pm 1/R$ to $\underline{\underline{K}}_{\mathrm{Z}}$.

In addition, a number of constraints must be satisfied. The voltage must be set to zero for a reference node (e.g. choosing node 1 as reference, $V_{\mathrm{n}}^{1} = 0$). For a voltage source $V_{\mathrm{s}}^{\mathrm{k}}$ between nodes i and j, the node voltages are related by $V_{\mathrm{n}}^{\mathrm{j}} - V_{\mathrm{n}}^{\mathrm{i}} = V_{\mathrm{s}}^{\mathrm{k}}$. Similarly, for a short-circuit, the node voltages are related by $V_{\mathrm{n}}^{\mathrm{j}} - V_{\mathrm{n}}^{\mathrm{i}} = 0$. Finally, for a capacitor, node voltages are related by $V_{\mathrm{n}}^{\mathrm{j}} - V_{\mathrm{n}}^{\mathrm{i}} = V_{\mathrm{c}}^{\mathrm{k}}$ with $V_{\mathrm{C}}^{\mathrm{k}}$ the voltage difference across the k^{th} capacitor. The node voltages $V_{\mathrm{n}}^{\mathrm{k}}$ are part of $\underline{Z}$, the source voltages $V_{\mathrm{s}}^{\mathrm{k}}$ are part of $\underline{U}$ and the voltage difference across the capacitors $V_{\mathrm{C}}^{\mathrm{k}}$ are part of $\underline{X}$. Therefore, the constraint can easily be expressed as a linear equation:

$$\underline{\underline{C}}_{\mathrm{Z}}\underline{Z} + \underline{\underline{C}}_{\mathrm{X}}\underline{X} + \underline{\underline{C}}_{\mathrm{U}}\underline{U} = 0 \tag{A.0.4}$$

where the matrices $\underline{\underline{C}}_{\mathrm{Z}}$, $\underline{\underline{C}}_{\mathrm{X}}$ and $\underline{\underline{C}}_{\mathrm{U}}$ have one row per constraint.

Combining (A.0.3) and (A.0.4) yields:

$$\underline{\underline{E}}_{\mathrm{Z}}\underline{Z} + \underline{\underline{E}}_{\mathrm{X}}\underline{X} + \underline{\underline{E}}_{\mathrm{U}}\underline{U} = 0 \tag{A.0.5}$$

where the matrices $\underline{\underline{E}}_{\mathrm{x}}$ are obtained by the concatenation of the corresponding matrices $\underline{\underline{K}}_{\mathrm{x}}$ and $\underline{\underline{C}}_{\mathrm{x}}$. For a non-degenerate circuit, the matrix $\underline{\underline{E}}_{\mathrm{Z}}$ is square and invertible. This allows to compute the unknown vector:

$$\underline{Z} = \underline{\underline{F}}_{\mathrm{X}}\underline{X} + \underline{\underline{F}}_{\mathrm{U}}\underline{U} \tag{A.0.6}$$

[3]The Kirchoff current equations are not independent; one is superfluous and we therefore do not include the equation for the first node in (A.0.3).

with $\underline{\underline{F}}_{\mathrm{X}} = -\underline{\underline{E}}_{\mathrm{Z}}^{-1}\underline{\underline{E}}_{\mathrm{X}}$ and $\underline{\underline{F}}_{\mathrm{U}} = -\underline{\underline{E}}_{\mathrm{Z}}^{-1}\underline{\underline{E}}_{\mathrm{U}}$

The state-space equation for the ith capacitor is:

$$\frac{\mathrm{d}V_{\mathrm{C}}^{\mathrm{i}}}{\mathrm{d}t} = \frac{I_{\mathrm{C}}^{\mathrm{i}}}{C_{\mathrm{i}}} \tag{A.0.7}$$

with C_{i} the capacitance of the capacitor, $V_{\mathrm{C}}^{\mathrm{i}}$ the voltage difference across it and $I_{\mathrm{C}}^{\mathrm{i}}$ the current flowing into it (the direction of the positive capacitor voltage is chosen opposite to the direction of the positive branch current). As the capacitor currents are part of $\underline{Z}$, according to (A.0.6), we may write:

$$\underline{I}_{\mathrm{C}} = \underline{\underline{F}}_{\mathrm{CX}}\underline{X} + \underline{\underline{F}}_{\mathrm{CU}}\underline{U} \tag{A.0.8}$$

where $\underline{\underline{F}}_{\mathrm{CX}}$ and $\underline{\underline{F}}_{\mathrm{CU}}$ are parts of $\underline{\underline{F}}_{\mathrm{X}}$ and $\underline{\underline{F}}_{\mathrm{U}}$ respectively. Hence the state-space equations for the capacitors may be written:

$$\frac{\mathrm{d}\underline{V}_{\mathrm{C}}}{\mathrm{d}t} = \underline{\underline{A}}_{\mathrm{C}}\underline{X} + \underline{\underline{B}}_{\mathrm{C}}\underline{U} \tag{A.0.9}$$

with $\underline{\underline{A}}_{\mathrm{C}} = \underline{\underline{C}}^{-1}\underline{\underline{F}}_{\mathrm{CX}}$ and $\underline{\underline{B}}_{\mathrm{C}} = \underline{\underline{C}}^{-1}\underline{\underline{F}}_{\mathrm{CU}}$ with $\underline{\underline{C}}$ a diagonal matrix with C_{i} the ith diagonal element.

On the other hand, the state-space equations for the inductors are:

$$\frac{\mathrm{d}\underline{I}_{\mathrm{L}}}{\mathrm{d}t} = \underline{\underline{M}}^{-1}\left(\underline{V}_{\mathrm{L}}^{\mathrm{in}} - \underline{V}_{\mathrm{L}}^{\mathrm{out}}\right) \tag{A.0.10}$$

with $\underline{\underline{M}}$ the mutual inductance matrix and $\underline{V}_{\mathrm{L}}^{\mathrm{in}}$ and $\underline{V}_{\mathrm{L}}^{\mathrm{out}}$ the node voltage respectively at the (current) entry and exit nodes of the inductors. As those voltages are part of $\underline{Z}$, according to (A.0.6), we may write:

$$\underline{V}_{\mathrm{L}}^{\mathrm{in/out}} = \underline{\underline{F}}_{\mathrm{LX}}^{\mathrm{in/out}}\underline{X} + \underline{\underline{F}}_{\mathrm{LU}}^{\mathrm{in/out}}\underline{U} \tag{A.0.11}$$

where $\underline{\underline{F}}_{\mathrm{LX}}^{\mathrm{in/out}}$ and $\underline{\underline{F}}_{\mathrm{LU}}^{\mathrm{in/out}}$ are obtained by concatenating the appropriate lines of $\underline{\underline{F}}_{\mathrm{X}}$ and $\underline{\underline{F}}_{\mathrm{U}}$; one for each inductor. Hence the state-space equations for the inductances may be written:

$$\frac{\mathrm{d}\underline{I}_{\mathrm{L}}}{\mathrm{d}t} = \underline{\underline{A}}_{\mathrm{L}}\underline{X} + \underline{\underline{B}}_{\mathrm{L}}\underline{U} \tag{A.0.12}$$

with $\underline{\underline{A}}_{\mathrm{L}} = \underline{\underline{M}}^{-1}(\underline{\underline{F}}_{\mathrm{LX}}^{1} - \underline{\underline{F}}_{\mathrm{LX}}^{0})$ and $\underline{\underline{B}}_{\mathrm{L}} = \underline{\underline{M}}^{-1}(\underline{\underline{F}}_{\mathrm{LU}}^{\mathrm{in}} - \underline{\underline{F}}_{\mathrm{LU}}^{\mathrm{out}})$.

Finally, the state-space matrices $\underline{\underline{A}}$ and $\underline{\underline{B}}$ can be obtained by concatenation: $\underline{\underline{A}} = \left[\underline{\underline{A}}_{\mathrm{C}}; \underline{\underline{A}}_{\mathrm{L}}\right]$ and $\underline{\underline{B}} = \left[\underline{\underline{B}}_{\mathrm{C}}; \underline{\underline{B}}_{\mathrm{L}}\right]$. On the other hand, as the outputs are part of $\underline{Z}$, $\underline{\underline{C}}$ and $\underline{\underline{D}}$ are obtained, according to (A.0.6), by choosing the appropriate parts of $\underline{\underline{F}}_{\mathrm{X}}$ and $\underline{\underline{F}}_{\mathrm{U}}$ respectively.

APPENDIX B

Maxwell equations

B.1 Formulas of Vector Analysis

$$\boldsymbol{a} \times \boldsymbol{b} \cdot \boldsymbol{c} = \boldsymbol{a} \cdot \boldsymbol{b} \times \boldsymbol{c} \tag{B.1.1}$$

$$\nabla \times (\phi \boldsymbol{a}) = \nabla \phi \times \boldsymbol{a} + \phi \nabla \times \boldsymbol{a} \tag{B.1.2}$$

$$\nabla \cdot (\phi \boldsymbol{a}) = \nabla \phi \cdot \boldsymbol{a} + \phi \nabla \cdot \boldsymbol{a} \tag{B.1.3}$$

$$\nabla \cdot (\boldsymbol{A} \times \boldsymbol{B}) = (\nabla \times \boldsymbol{A}) \cdot \boldsymbol{B} - (\nabla \times \boldsymbol{B}) \cdot \boldsymbol{A} \tag{B.1.4}$$

B.2 Full wave

In the frequency domain, assuming an $e^{j\omega t}$ time dependence (which is suppressed), the frequency domain Maxwell equations are [31, Chapter 1]:

$$\nabla \times \boldsymbol{E} = -j\omega \boldsymbol{B} \tag{B.2.5a}$$
$$\nabla \times \boldsymbol{H} = \boldsymbol{J} + j\omega \boldsymbol{D} \tag{B.2.5b}$$
$$\nabla \cdot \boldsymbol{D} = \rho \tag{B.2.5c}$$
$$\nabla \cdot \boldsymbol{B} = 0 \tag{B.2.5d}$$

with $\boldsymbol{E}$, $\boldsymbol{D}$, $\boldsymbol{H}$ and $\boldsymbol{B}$, respectively the electric, displacement, magnetic and induction fields. Furthermore $\boldsymbol{J}$ is the electric current distribution and ρ is the corresponding electrical charge distribution. For convenience, we will refer to the individual Maxwell equations by the law from which they derive—although the original law is usually less general. That is, by order of appearance, Faraday, Ampere, electric and magnetic Gauss law.

The charges are related to the currents through the continuity equations:

$$\nabla \cdot \boldsymbol{J} = -j\omega\rho \tag{B.2.6}$$

The fields are further related by the constitutive equations which for a linear and isotropic medium are:

$$\boldsymbol{D} = \epsilon \boldsymbol{E} \tag{B.2.7a}$$
$$\boldsymbol{B} = \mu \boldsymbol{H} \tag{B.2.7b}$$
$$\boldsymbol{J} = \sigma \boldsymbol{E} + \boldsymbol{J}_{\mathrm{s}} \tag{B.2.7c}$$

with $\boldsymbol{J}_{\mathrm{s}}$, the impressed current source distribution[1], ϵ, μ and σ the constitutive parameters of the medium; respectively the electric permittivity, the magnetic permeability and the electric conductivity. For an anisotropic medium, the tensors $\overline{\boldsymbol{\epsilon}}$, $\overline{\boldsymbol{\mu}}$ and $\overline{\boldsymbol{\sigma}}$ may be used instead of their scalar counterparts in (B.2.7).

The impressed current source distribution ($\boldsymbol{J}_{\mathrm{s}}$) and the corresponding charge distribution ($\rho_{\mathrm{s}} = j\nabla \cdot \boldsymbol{J}_{\mathrm{s}}/\omega$) may be used instead of their total counterpart ($\boldsymbol{J}$ and ρ) in the Maxwell equations if the constitutive relation (B.2.7a) is also modified as follows:

$$\boldsymbol{D} = \epsilon_{\sigma} \boldsymbol{E} \tag{B.2.8}$$

with

$$\epsilon_{\sigma} = \epsilon + \frac{\sigma}{j\omega} \tag{B.2.9}$$

The fields may be related to scalar and vector potentials by the following relations:

$$\boldsymbol{E} = -\nabla \phi - j\omega \boldsymbol{A} \tag{B.2.10a}$$
$$\boldsymbol{B} = \nabla \times \boldsymbol{A} \tag{B.2.10b}$$

with ϕ, the scalar electric potential and $\boldsymbol{A}$, the vector magnetic potential.

B.3 Low-frequency approximations

It is well-known that the Maxwell equations simplify at low frequency. In simple terms, at low frequency, the fields can be computed as in the static regime and one therefore speaks about the Quasi-Static (QS) approximation. Actually it is not true that both the electrical and the magnetic fields may be computed as in the static regime. To be more precise, one must consider two QS approximations [50, Chapters 3, 4

[1]The term ‘impressed’ is used to make the distinction with the total current distribution $\boldsymbol{J}$ which also includes the induced current distribution $\sigma\boldsymbol{E}$.

and 8]; the Magneto Quasi-Static (MQS) and the EQS approximations. In the first case, it is the magnetic field that can be computed as in the static case and in the second case, it is the electric field.

B.3.1 EQS approximation

The prototypical example of an EQS problem is a capacitor composed of two parallel metallic plates excited by a voltage source. For an EQS problem, the electric field can be computed as static. This yields the following EQS Maxwell equations:

$$\nabla \times \boldsymbol{E} = 0 \tag{B.3.11a}$$

$$\nabla \cdot \boldsymbol{D} = \rho \tag{B.3.11b}$$

Note that we consider a low frequency and not a static regime (i.e. $\omega \sim 0$ but $\neq 0$). Therefore, the charge distribution varies harmonically with the time. This is only possible if a current distribution exists. This current will generate a magnetic field that can be computed in a second step, after the electric field has been computed according to:

$$\nabla \times \boldsymbol{H} = \boldsymbol{J} + j\omega \boldsymbol{D} \tag{B.3.12a}$$

$$\nabla \cdot \boldsymbol{B} = 0 \tag{B.3.12b}$$

which can be interpreted as a MQS problem (see below) for the total current $\boldsymbol{J} + j\omega\boldsymbol{D}$.

This magnetic field is usually quite small for an EQS problem but claiming that is negligible may not be accurate because we have nothing to compare it with. It may be barely measurable, of little interest for many applications but it may still be needed for some applications. For example, the voltage induced by an external EQS field in the capacitor can be computed by resorting to reciprocity as we did in Section 2.4 for a coil. The induced voltage may then be computed according to (2.39) in which products $\boldsymbol{E} \times \boldsymbol{H}$ appear. Using $\boldsymbol{H} = 0$ would yield a zero induced voltage for any external field, which is obviously absurd. On the contrary, using the magnetic field computed from (B.3.12) yields the right result.

Once the magnetic field is known, it is possible to check the accuracy of the EQS approximation. Indeed, it is possible to compute the electric field resulting from the term $j\omega\boldsymbol{B}$ in the Faraday law. If this electric field is small *compared* to the EQS electric field produced by the charge distribution itself, then the EQS approximation is accurate.

When conductors are present in the problem, the induced charges and current distribution is unknown. This is however not an issue, because as for the full-wave equations, the impressed current source distribution ($\boldsymbol{J}_\mathrm{s}$) and the corresponding charge distribution ($\rho_\mathrm{s} = j\nabla \cdot \boldsymbol{J}_\mathrm{s}/\omega$) may be used instead of their total counterpart ($\boldsymbol{J}$ and ρ) if permittivity ϵ is replaced by ϵ_σ which includes the conductivity.

B.3.2 MQS approximation

The prototypical example of a MQS problem is a loop excited by a current source. In simple terms, for a MQS problem, the magnetic field can be computed as in the static case. This however only makes sense if the current is solenoidal[2] which is rigorously speaking not the case for the example of the loop. Indeed, a charge distribution is needed on the conductor boundary to 'guide the current along the wire' by producing a total electric field directed along the wire. This charge can only be produced by a divergent current but for a MQS problem the divergent current needed to produce the required electric field through the corresponding charge distribution is small and can be neglected *when compared to* the solenoidal current distribution. Or more precisely, it is the magnetic field produced by the divergent current that may be neglected *compared to* the magnetic field produced by the solenoidal current. This condition may be used as criteria to decide if a problem is a MQS one.

To define a MQS problem, we have thus to first split the current distribution into a solenoidal and a divergent contribution:

$$\boldsymbol{J} = \boldsymbol{J}_0 + \boldsymbol{J}_1 \tag{B.3.13}$$

with $\boldsymbol{J}_0$ and $\boldsymbol{J}_1$ respectively the solenoidal and divergent contribution and we must check that the magnetic field produced by $\boldsymbol{J}_1$ is negligible *with respect* to the one produced by $\boldsymbol{J}_0$. The MQS Maxwell equations can than be written as::

$$\nabla \times \boldsymbol{H} = \boldsymbol{J}_0 \tag{B.3.14a}$$
$$\nabla \cdot \boldsymbol{B} = 0 \tag{B.3.14b}$$

[2]Indeed, taking the rotational of (B.2.5b) for $\omega = 0$ yields zero for the left hand side (l.h.s.) but not for the right hand side (r.h.s.) if a general current such that $\nabla \cdot \boldsymbol{J} \neq 0$ is used.

The electric field can then be computed in second step if needed, according to:

$$\nabla \times \boldsymbol{E} = -j\omega \boldsymbol{B} \tag{B.3.15a}$$

$$\nabla \cdot \boldsymbol{D} = \rho \tag{B.3.15b}$$

which makes use of the magnetic field obtained in the first step by solving (B.3.14). This electric field has no static counterpart, unless magnetic currents are considered. Note that $\boldsymbol{J}_1$ is usually a contribution which is induced into conductors to satisfy the boundary conditions. This current distribution is thus in general unknown. This is however not an issue because, again, the impressed charge distribution ρ_s (which is known and usually null for MQS problems) may be used instead of ρ) if the permittivity ϵ is replaced by ϵ_σ which includes the conductivity in (B.3.15b).

Things are however more complex for the current $\boldsymbol{J}_0$. Indeed, there also, the (solenoidal) currents induced in the conductors is in general unknown. However, using ϵ_σ instead of ϵ in (B.3.14a) is in general not possible because the resulting $j\omega\boldsymbol{D}$ is not negligible anymore as it now includes the real currents induced in the conductors. This actually results in a diffusion problem which yields the well-known skin effect that has no static counterpart. To use the MQS approximation, it is thus in general necessary to know the current distribution, including the induced currents from the onset. More precisely, it is the solenoidal contribution $\boldsymbol{J}_0$ that must be known. The divergent contribution $\boldsymbol{J}_1$ and the corresponding charge distribution can be computed using the MQS equations.

A noticeable exception of a MQS problem for which the currents may be unknown is the scattering by a Perfect Electric Conductor (PEC) body. The magnetic field inside the PEC is then known to be null. No diffusion equation must be solved and the current distribution on the PEC surface is not needed to compute the magnetic field. This current can be computed in a second step if needed. The problem is actually equivalent to a perfectly magnetic body in which no current flows.

Note that in [50, Section 10.5] the term $\sigma\boldsymbol{E}$ is introduced in (B.3.14a) and this is still called an MQS problem, although a coupling between the magnetic and the electric field has been introduced. The resulting magnetic field is completely different from its static counterpart. We therefore find the qualifier 'quasi-static' confusing in that context. On the contrary, when the current distribution is known, the conductor can be replaced by those equivalent currents and the magnetic field can then be computed as in the static case. The term MQS is then clearly adequate.

B.3.3 QS approximation

A QS field may be obtained by combining an EQS solution with a MQS one. In some cases, the space can still be split in an EQS and a MQS region. The corresponding approximation can then be used in each region. This leaves the problem to define the boundaries of the regions and to ensure that the boundary conditions are fulfilled at the interface. Furthermore, there may be regions where the EQS and MQS fields have the same order of magnitude. Neither the MQS nor the EQS approximation may then be used to compute the total fields. We will therefore derive approximated field equations that are valid for the general QS case and we will discuss the underlying assumptions.

Another approximation commonly called the 'QS approximation' in the literature is obtained by neglecting time derivative terms in the equations governing the scalar and vector potentials. To make the distinction with our QS approximation, we will call it the 'Potential Quasi-Static (PQS) approximation'. This approximation yields equations for the potentials that are identical to their static counterpart. We could however not find the corresponding QS field equations in the literature and those equations are not straightforward to derive. We will however show in Section B.3.6 that the PQS approximation is a specific case of our QS approximation. Our derivation thus yields, as a side product, the QS field equations corresponding the QS potential approximation. It is further more general, providing for more flexibility, and may therefore allow for simpler solutions to some problems.

To get the QS approximation of the Maxwell equations, we again start by splitting the currents into a solenoidal $\boldsymbol{J}_0$ and a divergent $\boldsymbol{J}_1$ contribution. Note that such a decomposition is not unique and that a good choice must be made to get a valid QS approximation. This will be discussed in Section B.3.9.

We then define $\boldsymbol{E}_0$, the EQS electric field corresponding to the charge distribution and $\boldsymbol{H}_0$, the MQS magnetic field corresponding to $\boldsymbol{J}_0$. By definition, they obey the following equations:

$$\nabla \times \boldsymbol{E}_0 = 0 \tag{B.3.16a}$$
$$\nabla \cdot \boldsymbol{D}_0 = \rho \tag{B.3.16b}$$
$$\nabla \times \boldsymbol{H}_0 = \boldsymbol{J}_0 \tag{B.3.16c}$$
$$\nabla \cdot \boldsymbol{B}_0 = 0 \tag{B.3.16d}$$

We now search a solution for the fields that can be expressed as:

$$\boldsymbol{E} = \boldsymbol{E}_0 + \boldsymbol{E}_1 \tag{B.3.17a}$$
$$\boldsymbol{H} = \boldsymbol{H}_0 + \boldsymbol{H}_1 \tag{B.3.17b}$$
$$\tag{B.3.17c}$$

and we call $(\boldsymbol{E}_0, \boldsymbol{H}_0)$ and $(\boldsymbol{E}_1, \boldsymbol{H}_1)$ respectively the order zero and the order one contributions.

Introducing this decomposition in (B.2.5), one gets the following expression for the order one contribution:

$$\nabla \times \boldsymbol{E}_1 = -j\omega \boldsymbol{B}_0 - j\omega \boldsymbol{B}_1 \tag{B.3.18a}$$
$$\nabla \cdot \boldsymbol{D}_1 = 0 \tag{B.3.18b}$$
$$\nabla \times \boldsymbol{H}_1 = \boldsymbol{J}_1 + j\omega \boldsymbol{D}_0 + j\omega \boldsymbol{D}_1 \tag{B.3.18c}$$
$$\nabla \cdot \boldsymbol{B}_1 = 0 \tag{B.3.18d}$$

We now assume that the terms $\boldsymbol{B}_1$ and $\boldsymbol{D}_1$ may be neglected in (B.3.18). This is the QS assumption. This does not necessarily imply that they are negligible compared to the other terms of the *same* equation. It only means that their contribution to the total fields is negligible *compared* to the other contributions. For example, for an EQS problem, $\boldsymbol{B}_0$ is null and $\boldsymbol{B}_1$ is thus not negligible with respect to $\boldsymbol{B}_0$ in (B.3.18a). However, $\boldsymbol{E}$ has another contribution through the charge distribution and both the charge distribution and $\boldsymbol{B}_1$ are related to $\boldsymbol{J}_1$ and it is still possible that the contribution to $\boldsymbol{E}$ related to $\boldsymbol{J}_1$ through the charges dominates its contribution through $\boldsymbol{B}_1$. The QS assumptions will be further discussed in Section B.3.7.

Introducing the QS assumption in (B.3.18) yields:

$$\nabla \times \boldsymbol{E}_1 = -j\omega \boldsymbol{B}_0 \tag{B.3.19a}$$
$$\nabla \cdot \boldsymbol{D}_1 = 0 \tag{B.3.19b}$$
$$\nabla \times \boldsymbol{H}_1 = \boldsymbol{J}_1 + j\omega \boldsymbol{D}_0 \tag{B.3.19c}$$
$$\nabla \cdot \boldsymbol{B}_1 = 0 \tag{B.3.19d}$$

One sees that the order 1 equations for the magnetic field and for the electric field are also uncoupled; as the order 0 equations. The equations for the magnetic field can further be interpreted as the MQS equations for the total electric currents $\boldsymbol{J}_1^{\text{tot}} = \boldsymbol{J}_1 + j\omega\boldsymbol{D}_0$ (which is indeed solenoidal as required for an MQS problem). The equations for the electric field can be interpreted as a generalized EQS problem but this requires one to introduce magnetic currents[3] $\boldsymbol{M}$ in the Maxwell equations. The sources for the generalized EQS field are then the charge distribution ρ and the solenoid magnetic current $\boldsymbol{M}_0 = j\omega\boldsymbol{B}_0$.

One can easily check that the EQS and MQS approximations are special cases of the general QS equations. The first are obtained for $\boldsymbol{J}_0 = 0$ and the second for $\boldsymbol{J}_1 = 0$. For a EQS problem, $\boldsymbol{E}_1$ and $\boldsymbol{H}_0$ are null and the dominant fields are $\boldsymbol{E}_0$ and $\boldsymbol{H}_1$. For a MQS problem, $\boldsymbol{H}_1$ and $\boldsymbol{E}_0$ are null and the dominant fields are $\boldsymbol{H}_0$ and $\boldsymbol{E}_1$. For a general QS problem consisting of the sum of a MQS and an EQS problem, none of the contributions is null and the dominant fields may vary from point to point. Therefore, to ensure that the dominant contribution is always taken into account in field computation, both the order zero and the order one term must be taken into account.

Combining the two contributions yields the following equations for the total QS fields:

$$\nabla \times \boldsymbol{E} = -j\omega\boldsymbol{B}_0 \tag{B.3.20a}$$
$$\nabla \cdot \boldsymbol{D} = \rho \tag{B.3.20b}$$
$$\nabla \times \boldsymbol{H} = \boldsymbol{J} + j\omega\boldsymbol{D}_0 \tag{B.3.20c}$$
$$\nabla \cdot \boldsymbol{B} = 0 \tag{B.3.20d}$$

which shows that the QS magnetic field is independent of the chosen current decomposition. Indeed, $\boldsymbol{D}_0$ is only a function of the charge distribution, which is a physical parameter. This distribution is the same for all possible current decomposition. The electrical field however is a function of the current decomposition, through the term $\boldsymbol{B}_0$, which is a function of $\boldsymbol{J}_0$ and thus dependent on the chosen current decomposition. To make this dependency more apparent, we take the rotational

[3] Magnetic currents do not exist physically but they allow to get symmetric equations and are further needed in the surface equivalence principle to replace a volume by a surface distribution of currents. Electrical and magnetic currents are then needed in general.

of (B.3.20a). Then using (B.3.16c), this yields:

$$\nabla \times \frac{\nabla \times \boldsymbol{E}}{\mu} = -j\omega \boldsymbol{J}_0 \tag{B.3.21}$$

B.3.4 Field power series expansion

The QS equations may be written in the following compact form:

$$\nabla \times \boldsymbol{E}_{\mathrm{i}} = -j\omega \boldsymbol{B}_{\mathrm{i}-1} \tag{B.3.22a}$$
$$\nabla \times \boldsymbol{H}_{\mathrm{i}} = \boldsymbol{J}_{\mathrm{i}} + j\omega \boldsymbol{D}_{\mathrm{i}-1} \tag{B.3.22b}$$
$$\nabla \cdot \boldsymbol{D}_{\mathrm{i}} = \rho_{\mathrm{i}} \tag{B.3.22c}$$
$$\nabla \cdot \boldsymbol{B}_{\mathrm{i}} = 0 \tag{B.3.22d}$$

The continuity equation then is given by:

$$\nabla \cdot \boldsymbol{J}_{\mathrm{i}} = -j\omega \rho_{\mathrm{i}-1} \tag{B.3.23}$$

with the convention that the quantities are null for negative indices. Recall that the only current source terms are $\boldsymbol{J}_0$ and$\boldsymbol{J}_1$ and, as $\nabla \cdot \boldsymbol{J}_0 = 0$, the only charge source term is ρ_0. In other words, the current distributions are null for $i > 1$ and the charge distributions are null for $i > 0$.

This notation suggests that (B.3.22) is a series development of the exact fields and that the QS approximation is obtained by truncating the series at the first order. One can show that this is indeed the case by considering a fictious current frequency dependency:

$$\boldsymbol{J}_{\mathrm{f}}(\omega') = \boldsymbol{J}_0 + \frac{\omega'}{\omega}\boldsymbol{J}_1 \tag{B.3.24}$$

which is obviously equal to the physical current distribution at the frequency of interest: $\boldsymbol{J}_{\mathrm{f}}(\omega) = \boldsymbol{J}(\omega)$. Those currents then produce frequency dependent fields in ω' which are also equal to the real fields at the frequency of interest. The fields can then be expressed in a power series of ω'. For the electrical field, this yields:

$$\boldsymbol{E}(\omega', \boldsymbol{r}) = \boldsymbol{E}_0(\boldsymbol{r}) + (\frac{\omega'}{\omega})\boldsymbol{E}_1(\boldsymbol{r}) + (\frac{\omega'}{\omega})^2\boldsymbol{E}_2(\boldsymbol{r}) + ... \tag{B.3.25}$$

The searched for physical fields are then:

$$\boldsymbol{E}(\omega, \boldsymbol{r}) = \boldsymbol{E}_0(\boldsymbol{r}) + \boldsymbol{E}_1(\boldsymbol{r}) + \boldsymbol{E}_2(\boldsymbol{r}) + ... \tag{B.3.26}$$

Such a power series development was also introduced in [80, Chapter 13] but the notion of fictious frequency dependency was not mentioned. The use of a fictious frequency dependency for the current is mandatory for our discussion because the real current frequency dependence may be much more complex and the development would then need much more terms to be accurate. This problem is related to the fact that the QS approximation is in general not valid inside conductors.When conductors are present, they must be replaced by an equivalent current distribution to use the QS approximation. See Section B.3.8 for more details.

Plugging (B.3.24), (B.3.25) and a similar development for the magnetic field in the Maxwell equations and equating the coefficients of the same power on both sides then immediately yields (B.3.22). Hence, as already mentioned, this series expansion yields another interpretation of the QS fields. They are obtained by truncating the expansion to the first order in ω'. The higher order terms are then interpreted as propagation contributions.

B.3.5 Potential power series expansion

The fields appearing in the power series expansion can be related to potentials as follows:

$$\boldsymbol{E}_{\mathrm{i}} = -\nabla\phi_{\mathrm{i}} - j\omega\boldsymbol{A}_{\mathrm{i}-1} \tag{B.3.27a}$$

$$\boldsymbol{B}_{\mathrm{i}} = \nabla\times\boldsymbol{A}_{\mathrm{i}} \tag{B.3.27b}$$

with the convention that the quantities are null for negative indexes.

Introducing (B.3.27b) in (B.3.22b) and (B.3.27a) in (B.3.22c) yields the following equations for the potentials:

$$\nabla\times\frac{\nabla\times\boldsymbol{A}_{\mathrm{i}}}{\mu} = \boldsymbol{J}_{\mathrm{i}} + j\omega\boldsymbol{D}_{\mathrm{i}-1} \tag{B.3.28a}$$

$$\nabla\cdot(\epsilon\nabla\phi_{\mathrm{i}}) = -\rho_{\mathrm{i}} - j\omega\nabla\cdot\left(\epsilon\boldsymbol{A}_{\mathrm{i}-1}\right) \tag{B.3.28b}$$

Which are static uncoupled equations for the potentials. To completely define the vector potential, one must further define the gauge equation. We consider the Coulomb ($\nabla\cdot(\epsilon\boldsymbol{A}_{\mathrm{i}}) = 0$) and Lorentz gauge ($\nabla\cdot(\epsilon\boldsymbol{A}_{\mathrm{i}}) = -j\omega\epsilon^2\mu\phi_{\mathrm{i}-1}$). They yield the following equations for the scalar potential:

$$\nabla\cdot(\epsilon\nabla\phi_{\mathrm{i}}) = -\rho_{\mathrm{i}} \tag{B.3.29a}$$

$$\nabla\cdot(\epsilon\nabla\phi_{\mathrm{i}}) = -\rho_{\mathrm{i}} - \omega^2\epsilon^2\mu\phi_{\mathrm{i}-2} \tag{B.3.29b}$$

In both cases, the order one scalar potential has no sources and we may choose $\phi_1 = 0$. With the Coulomb gauge all higher order scalar potentials are also null. The power series expansion for the potentials are thus:

$$\boldsymbol{A} = \boldsymbol{A}_0 + \boldsymbol{A}_1 + \cdots \tag{B.3.30a}$$

$$\phi = \phi_0 + 0 + \cdots \tag{B.3.30b}$$

Where the scalar potential expansion only includes the zeroth order term if the Coulomb gauge is used.

B.3.6 PQS approximation

Another approximation often used and that is also called the QS approximation in the literature is obtained by neglecting the propagation term in the wave equation for the potentials. This approximation will be called the PQS approximation to avoid confusion with our QS approximation discussed above.

For a homogeneous medium and under the Lorentz gauge:

$$\nabla \cdot \boldsymbol{A} + j\omega\epsilon\mu\phi = 0 \tag{B.3.31}$$

the potential wave equations are:

$$\triangle \boldsymbol{A} + k^2 \boldsymbol{A} = -\mu \boldsymbol{J} \tag{B.3.32a}$$

$$\triangle \phi + k^2 \phi = -\frac{\rho}{\epsilon} \tag{B.3.32b}$$

with $k = \omega\sqrt{\epsilon\mu}$ the wave number and $\triangle \equiv \nabla^2$, the Laplacian operator.

Neglecting the terms in k^2 yields:

$$\triangle \boldsymbol{A} = -\mu \boldsymbol{J} \tag{B.3.33a}$$

$$\triangle \phi = -\frac{\rho}{\epsilon} \tag{B.3.33b}$$

which shows that under this approximation, the potentials (and not the fields) are computed as in the static regime.

The corresponding equations for the fields can be obtained by first expressing the fields as a function of the potential according to (B.2.10) and then computing $\nabla \times \boldsymbol{E}$, $\nabla \times \boldsymbol{H}$, $\nabla \cdot \boldsymbol{D}$ and $\nabla \cdot \boldsymbol{B}$. This yields:

$$\nabla \times \boldsymbol{E} = -j\omega \boldsymbol{B} \tag{B.3.34a}$$

$$\nabla \times \boldsymbol{H} = \boldsymbol{J} - j\omega\epsilon\nabla\phi \tag{B.3.34b}$$

$$\nabla \cdot \boldsymbol{D} = \rho - \omega^2\epsilon^2\mu\phi \tag{B.3.34c}$$

$$\nabla \cdot \boldsymbol{B} = 0 \tag{B.3.34d}$$

where we used the gauge equation (B.3.31) to obtain (B.3.34b) and (B.3.34c). To obtain (B.3.34b), we further used the development for the vector Laplacian operator $\triangle \boldsymbol{A} = \nabla\nabla \cdot \boldsymbol{A} - \nabla \times \nabla \times \boldsymbol{A}$.

To relate those equations to our QS approximation, we first note that according to (B.3.27a) $\boldsymbol{E}_0 = -\nabla\phi_0$ and that the equation for ϕ_0 (B.3.28b) is the same as that for ϕ in the PQS approximation. The term $-\nabla\phi$ appearing in (B.3.34) is thus identical to the term $\boldsymbol{E}_0$ appearing in our QS approximation.

Comparing (B.3.34c) with (B.3.20b) shows that the two approximations can not be the same unless the term $\omega^2\epsilon^2\mu\phi$ is neglected. The equations (B.3.34) and (B.3.20) are then identical if the following current decomposition is used:

$$\boldsymbol{J}_0 = \boldsymbol{J} - j\omega\epsilon\nabla\phi = \boldsymbol{J} + j\omega\boldsymbol{D}_0 \tag{B.3.35a}$$

$$\boldsymbol{J}_1 = j\omega\epsilon\nabla\phi = -j\omega\boldsymbol{D}_0 \tag{B.3.35b}$$

Indeed, according to (B.3.19c), the source for $\boldsymbol{B}_1$ is null and the total magnetic induction is then $\boldsymbol{B} = \boldsymbol{B}_0$.

The origin of the extra term $\omega^2\epsilon^2\mu\phi$ can be further understood by noting that, according to (B.3.33), the PQS approximation can also be interpreted as the result of truncating the power series expansion for the potentials (under the Lorenz gauge) at the first order. This is not equivalent to truncating the fields to the first order because the electric field computed from the potentials then includes the term $-j\omega\boldsymbol{A}_1$ which is a second order contribution to the field.

To summarize, neglecting the term $\omega^2\epsilon^2\mu\phi$, the PQS approximation is a specific case of our approximation which is obtained if we choose for the solenoidal current the sum of the current and the displacement current *computed from the EQS field*. Our approximation allows for other choices that may be more easy to handle. In addition, it is applicable to inhomogeneous media whereas the PQS approximation is easily obtained for a homogeneous medium but it is more difficult (though possible) to extend it to inhomogeneous cases. Finally, when the PQS approximation is presented, to the best knowledge of the author, no equations are provided for the fields. Such field equations are however very useful for some applications[4] and establishing them is not straightforward. With our approximation, equation for the fields are provided. As a specific case, with the appropriate choice of current decomposition, our development provides the equation for the fields corresponding to the PQS approximation.

B.3.7 QS approximation assumptions

We recall that the QS approximation was obtained by neglecting the terms $\boldsymbol{B}_1$ and $\boldsymbol{D}_1$ in (B.3.18). Solving the QS equations yields an approximation for the neglected terms and we can then use this approximation to estimate the contribution of the neglected terms to the fields. If this contribution is negligible *compared to* to the fields obtained using the QS approximation, then this approximation is valid. This provides a practical means to check if the used QS approximation is valid for a given problem. Note that a negative check result does not necessarily imply that a QS approximation can not be used to solve the problem. It may also indicate that the chosen current decomposition is not appropriate. See Section B.3.9 for more details.

We now assess the relative contribution of the neglected terms to the total field:

- $\boldsymbol{D}_1$ only contributes to $\boldsymbol{H}$. To assess its relative contribution, we take the rotational of the sum of (B.3.18c) and (B.3.16c). This yields:
$$\nabla \times \left(\frac{\nabla \times \boldsymbol{H}}{\epsilon} \right) = \nabla \times \frac{\boldsymbol{J}}{\epsilon} + \omega^2 \boldsymbol{B} \tag{B.3.36}$$
in which the contribution of $\boldsymbol{D}_1$ is $\omega^2 \boldsymbol{B}$. This shows that the current $\boldsymbol{J}$ produces two contribution to $\boldsymbol{H}$. One direct contribution and one due to $\boldsymbol{D}_1$ through $\boldsymbol{B}$. This contribution appears with the second power of the frequency and is a propagation term. This term is negligible at low frequency. The corresponding error is identical to the error introduced by using the MQS approximation to compute the magnetic field of a solenoidal current.

[4]See for example the derivation of the QS reciprocity relation (C.4.13) which is very powerful to compute the voltage induced in a real loop

- $\boldsymbol{B}_1$ only contributes to $\boldsymbol{E}$. The total source for $\boldsymbol{E}$ is not only $\boldsymbol{B}_0 + \boldsymbol{B}_1$ but also the charge corresponding to $\boldsymbol{J}_1$. Therefore, the fact that the effect of $\boldsymbol{B}_1$ can be neglected does *not* imply that $\boldsymbol{B}_1 \ll \boldsymbol{B}_0$. It is sufficient that the contribution of $\boldsymbol{E}$ related to $\boldsymbol{J}_1$ through the charges dominates its contribution through $\boldsymbol{B}_1$. This is usually the case at low frequency because to produce a given charge distribution, one can find a divergent current that produces a much smaller contribution to the electric fields (the term $-j\omega\boldsymbol{A}_1$) than the charges themselves (the term $-\nabla\phi_0$).

In summary, the QS approximation is valid if:

- *The current $\boldsymbol{J}$ produces a much smaller contribution to the magnetic field through $\boldsymbol{B}$ (the term $\omega^2\boldsymbol{B}$) than its direct contribution.* (Assumption QS1)
- *The divergent current $\boldsymbol{J}_1$ produces a much smaller contribution to the electric fields (the term $-j\omega\boldsymbol{A}_1$) than the charges themselves (the term $-\nabla\phi_0$).* (Assumption QS2)

The second condition can always be fulfilled with an appropriate choice of current decomposition. Indeed, this assumption comes from the fact that $\boldsymbol{B}_1$ has been neglected in (B.3.18a) and using the decomposition (B.3.35), $\boldsymbol{B}_1 = 0$ removing the need for neglecting it.

B.3.8 Validity of the QS approximation

The validity of the QS approximation can be checked analytically for a homogeneous medium and for the PQS approximation (which, as we have shown, is a specific QS approximation for the current decomposition (B.3.35)).

The exact solution for the magnetic potential for a unit current dipole located at the origin and directed along an arbitrary direction $\hat{\boldsymbol{d}}$ is:

$$\boldsymbol{A}(\boldsymbol{r}) = -\frac{\mu e^{jkR}}{4\pi R}\hat{\boldsymbol{d}} \tag{B.3.37}$$

with $R = |\boldsymbol{r}|$ the distance between the field point $\boldsymbol{r}$ and the origin. The corresponding QS approximation is obtained for $k = 0$. The approximation is thus accurate if $|kR| \ll 1$ or equivalently, if $R \ll |\lambda|$ with $\lambda = \frac{1}{\sqrt{\epsilon\mu\nu}}$. For 300kHz which is above the bandwidth of the MDs, the wavelength in free space is 1km. The volume of interest around the detector (say a sphere of about 1m) is thus always in the near field and

QS approximation is always valid for a free space environment. For soils, the relative magnetic permeability remains around 1 but the electrical permittivity may rise up to 40 for extremely wet soils [81, Fig. 20]. The wavelength is then reduced by a factor 7 and the QS approximation remains valid in the volume of interest; at least for a homogeneous medium. For an inhomogeneous medium, no analytic solution exists, but due to the large margin available for homogeneous media, we expect an accurate QS approximation for all types of soil.

Care should however be taken in the presence of conductors. Indeed, a general QS problem is a mix of an EQS and an MQS problem. The remarks related to the presence of conductors mentioned in Sections B.3.1 and B.3.2 thus hold. The charge induced in the conductors and the corresponding current distribution $\boldsymbol{J}_1$ can in general be estimated under the QS approximation. For this, the fields may first be computed using ϵ_σ, which includes the conductivity, instead of ϵ. The charge and current distribution can then be computed from the resulting electric field. Indeed, for a good choice of current decomposition (for example (B.3.35)), the assumption QS2 remains valid when ϵ is replaced by ϵ_σ. This is not true for the assumption QS1 which is in general not valid anymore when the conductivity is included in the permittivity because the induced eddy currents produce a significant magnetic field. This is at the origin of the skin effect. The importance of this effect can be quantified using the analytic solution (B.3.37). When the conductivity is taken into account, the wavenumber becomes complex and the fields are exponentially attenuated inside the conductor with a characteristic distance equal to the skin depth (2.5). For copper, this yields $660\mu m$ at 10kHz. Hence at the frequencies used by the MD and for typical object dimensions in the order of centimeters, the solenoidal current distribution $\boldsymbol{J}_0$ in the conductors can not be estimated under the QS approximation. It must be known before using the QS approximation. For thin conductors, the exact distribution is in general not critical if the fields must not be computed in the immediate vicinity of the conductor. A simple distribution can then be assumed. This is illustrated in Chapter 2 where a circuit model is used to analyze a coil. Using a circuit model, the conducting structure is further split into smaller parts (turns for the coil example). It is then only necessary to know the current distribution in each part up to a multiplicative factors. Those factors are then computed by solving the circuit equations.

As already mentioned, PEC conductors are in general not an issue because the fields are then null inside the conductors and they do not need to be computed. The presence of the conductor is then translated into boundary conditions on its surface.

B.3.9 Choice of current decomposition

There are many ways in which a current can be split into a solenoidal and a divergent contribution and a good decomposition should be chosen. A good decomposition is one for which the QS assumptions are valid. More precisely, as we already mentioned, according to (B.3.20), the current decomposition has no influence on the resulting QS magnetic field; it only influences the resulting QS electric field. Therefore, the choice of the current decomposition may only have an effect on validity the second QS assumption which states that 'the divergent current $\boldsymbol{J}_1$ produces a much smaller contribution to the electric fields (the term $-j\omega\boldsymbol{A}_1$) than the charges themselves (the term $-\nabla\phi_0$)'. As already discussed, this assumption is always satisfied for the current decomposition (B.3.35) which is thus always a good choice. This decomposition may however yield a complicated solenoidal current $\boldsymbol{J}_0$. Other choices may thus also be useful.

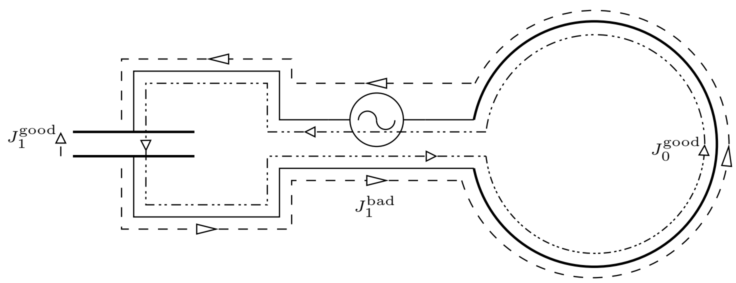

Figure B.1: *Two possible current decompositions $\boldsymbol{J} = \boldsymbol{J}_0 + \boldsymbol{J}_1$. A good one and a bad one. $\boldsymbol{J}_1^{\text{bad}}$ is clearly a bad choice because it is a large current that flows on a large loop. The contribution of the corresponding magnetic vector potential to the electric field $-j\omega\boldsymbol{A}_1$ will therefore not be negligible when compared to contribution of the electric charges $-\nabla\phi_0$, especially at some distance from the capacitor plates (where most charges are located) and close to the loop (where the current $\boldsymbol{J}_1^{\text{bad}}$ flows). In contrast, the current $\boldsymbol{J}_1^{\text{good}}$ is much more localized and it is further localized between the capacitor plates, where the term $-\nabla\phi_0$ is large.*

Two possible decomposition are is illustrated in Fig. B.1 for a QS problem composed of a capacitor and a loop excited with a voltage source. The real sources are located inside the voltage source. The total resulting current is $\boldsymbol{J}_1^{\text{bad}}$. This current yields a possible current decomposition with $\boldsymbol{J}_0^{\text{bad}} = 0$. This is however a bad decomposition because, around the loop, the dominant electric field is $j\omega\boldsymbol{A}$ and as $\boldsymbol{J}_1^{\text{bad}}$ includes the total current, this field is clearly not negligible compared to the field produced by the electric charge which is concentrated on the capacitor. The decomposition $\boldsymbol{J} = \boldsymbol{J}_0^{\text{good}} + \boldsymbol{J}_1^{\text{good}}$ is a much better as which the QS approximation is expected to be valid at low frequencies. Note that the decomposition (B.3.35), which is always a good one, is similar to $\boldsymbol{J}_{0/1}^{\text{good}}$ but the currents spread out between the capacitor plates.

APPENDIX C

Reciprocity

In this section we derive various reciprocity expressions, first the exact full-wave expression, then a number of low frequency approximations. Reciprocity is usually expressed in the frequency domain and it allows to relate the fields and sources pertaining to two configurations called 'states'. Several reciprocity expressions exist[31, 41, 35, 42, 43] and vary in their generality. For example [43] allows consideration of different media in the two states and therefore includes a contrast term whereas [41] assumes the same medium in both states. We could however not find a general derivation of the reciprocity expression, including the low frequency approximations. A coherent derivation, including the link between the various approximations, is therefore presented in this Appendix.

C.1 Full-wave Reciprocity

We consider two states A and B for which the sources and the fields are respectively ($\boldsymbol{J}^{\mathrm{A|B}}$ and ($\boldsymbol{E}^{\mathrm{A|B}}$, $\boldsymbol{H}^{\mathrm{A|B}}$). The most general expression of reciprocity between states A an B in volume $\mathcal{V}_{\mathrm{r}}$ bounded by surface $\mathcal{S}_{\mathrm{r}}$ is obtained by integrating $\nabla \cdot \left(\boldsymbol{E}^{\mathrm{A}} \times \boldsymbol{H}^{\mathrm{B}} - \boldsymbol{E}^{\mathrm{B}} \times \boldsymbol{H}^{\mathrm{A}}\right)$ on the volume $\mathcal{V}_{\mathrm{r}}$. Two expressions are obtained for this integral. The first is obtained directly using the Gauss theorem and the second by using the vector identity (B.1.4) and the Maxwell equations. Both expressions must be equal and this yields:

$$B^{\mathrm{EH}}_{\mathcal{S}_{\mathrm{r}}} = S^{\mathrm{J}}_{\mathcal{V}_{\mathrm{J}}} + j\omega\left(C^{\mathrm{e}}_{\mathcal{V}_{\chi_{\mathrm{e}}}} + C^{\mathrm{m}}_{\mathcal{V}_{\chi_{\mathrm{m}}}}\right) \tag{C.1.1}$$

where B, S and C are respectively the boundary, the source and the contrast contribution. The subscript indicates the volume or surface on which the corresponding term is computed. The superscript 'EH' appearing in the boundary term indicates that electrical and magnetic fields are involved in the expression. The superscript (J) appearing in the source term indicates that it is related to the electrical current[1]. The superscript appearing in the contrast term indicates whether it is an electrical (e) or magnetic (m) contrast. $\mathcal{V}_\mathrm{J}$, $\mathcal{V}_{\chi_\mathrm{e}}$, $\mathcal{V}_{\chi_\mathrm{m}}$ are the part of $\mathcal{V}_\mathrm{r}$ in which the electrical current, the electrical and magnetic contrasts are respectively located.

We now detail each term:

$$B^{\mathrm{EH}}_{\mathcal{S}_\mathrm{r}} = \oint_{\mathcal{S}_\mathrm{r}} \Big(\boldsymbol{E}^\mathrm{A} \times \boldsymbol{H}^\mathrm{B} - \boldsymbol{E}^\mathrm{B} \times \boldsymbol{H}^\mathrm{A}\Big) \cdot \mathrm{d}\boldsymbol{S} \tag{C.1.2}$$

$$S^{\mathrm{J}}_{\mathcal{V}_\mathrm{J}} = -\int_{\mathcal{V}_\mathrm{J}} \Big(\boldsymbol{E}^\mathrm{A} \cdot \boldsymbol{J}^\mathrm{B} - \boldsymbol{E}^\mathrm{B} \cdot \boldsymbol{J}^\mathrm{A}\Big)\mathrm{d}V \tag{C.1.3}$$

$$C^{\mathrm{e}}_{\mathcal{V}_{\chi_\mathrm{e}}} = -\int_{\mathcal{V}_{\chi_\mathrm{e}}} \chi_\mathrm{e}\boldsymbol{E}^\mathrm{A} \cdot \boldsymbol{E}^\mathrm{B}\mathrm{d}V \tag{C.1.4}$$

$$C^{\mathrm{m}}_{\mathcal{V}_{\chi_\mathrm{m}}} = \int_{\mathcal{V}_{\chi_\mathrm{m}}} \chi_\mathrm{m}\boldsymbol{H}^\mathrm{A} \cdot \boldsymbol{H}^\mathrm{B}\mathrm{d}V \tag{C.1.5}$$

where $\chi_\mathrm{e} = \epsilon^\mathrm{B} - \epsilon^\mathrm{A}$ and $\chi_\mathrm{m} = \mu^\mathrm{B} - \mu^\mathrm{A}$ are respectively the electrical and magnetic contrast. The development can easily be generalized to non-isotropic media for which the electric permittivity and magnetic susceptibility become tensors ($\overline{\boldsymbol{\epsilon}}$ and $\overline{\boldsymbol{\mu}}$). The contrast term then becomes the tensors $\overline{\boldsymbol{\chi}}_\mathrm{e} = \overline{\boldsymbol{\epsilon}}^\mathrm{B} - \left(\overline{\boldsymbol{\epsilon}}^\mathrm{A}\right)'$ and $\overline{\boldsymbol{\chi}}_\mathrm{m} = \overline{\boldsymbol{\mu}}^\mathrm{B} - \left(\overline{\boldsymbol{\mu}}^\mathrm{A}\right)'$ where the prime symbol indicate a transposition. Furthermore the integrand of (C.1.4) and (C.1.5) then become $\sum_{i,j} E^\mathrm{A}_\mathrm{i}\chi^{\mathrm{i,j}}_\mathrm{e}E^\mathrm{B}_\mathrm{j}$ and $\sum_{i,j} H^\mathrm{A}_\mathrm{i}\chi^{\mathrm{i,j}}_\mathrm{h}H^\mathrm{B}_\mathrm{j}$ respectively. This shows that the contrast term disappears only if the same medium appears in the two states and if this medium is reciprocal. This last condition means that the constitutive parameters are either scalar or tensorial and symmetrical.

C.2 EQS reciprocity

When a scalar potential exists, $\boldsymbol{E}_0 = -\nabla\phi_0$, a reciprocity relation may be obtained by proceeding as for the full-wave case but with $\nabla \cdot \Big(\phi^\mathrm{A}_0\boldsymbol{D}^\mathrm{B}_0 - \phi^\mathrm{B}_0\boldsymbol{D}^\mathrm{A}_0\Big)$, where $\boldsymbol{D}^{\mathrm{A|B}}_0$ and $\phi^{\mathrm{A|B}}_0$ are respectively the displacement field and static potential corresponding to the static charge distribution $\rho^{\mathrm{A|B}}$. The subscript '0' has been introduced to emphasis that

[1]Magnetic currents may be introduced in the Maxwell equations. An additional term $S^{\mathrm{M}}_{\mathcal{V}_\mathrm{M}} = \int_{\mathcal{V}_\mathrm{M}} (\boldsymbol{H}^\mathrm{A} \cdot \boldsymbol{M}^\mathrm{B} - \boldsymbol{H}^\mathrm{B} \cdot \boldsymbol{M}^\mathrm{A})\mathrm{d}V$ then appears in the reciprocity expression.

the reciprocity expression is only valid for EQS fields or more generally for the order zero electric field appearing in our QS approximation (see Appendix B.3.7).

Using the vector identity (B.1.3), one finds:

$$B^{\phi}_{\mathcal{S}_\mathrm{r}} = S^{\rho}_{\mathcal{V}_\rho} + C^{\mathrm{e}_0}_{\mathcal{V}_{\chi_\mathrm{e}}} + D^{\epsilon}_{\mathcal{S}_{\triangle\epsilon}} \tag{C.2.6}$$

where

$$B^{\phi}_{\mathcal{S}_\mathrm{r}} = \oint_{\mathcal{S}_\mathrm{r}} \left(\phi^\mathrm{A}_0 \boldsymbol{D}^\mathrm{B}_0 - \phi^\mathrm{B}_0 \boldsymbol{D}^\mathrm{A}_0\right) \cdot \mathrm{d}\boldsymbol{S} \tag{C.2.7}$$

$$S^{\rho}_{\mathcal{V}_\rho} = \int_{\mathcal{V}_\rho} \left(\phi^\mathrm{A}_0 \rho^\mathrm{B} - \phi^\mathrm{B}_0 \rho^\mathrm{A}\right) \mathrm{d}V \tag{C.2.8}$$

$$D^{\epsilon}_{\mathcal{S}_{\triangle\epsilon}} = \oint_{\mathcal{S}_{\triangle\epsilon}} \left(\phi^\mathrm{A}_0 \rho^\mathrm{B}_\mathrm{s,eq} - \phi^\mathrm{B}_0 \rho^\mathrm{A}_\mathrm{s,eq}\right) \mathrm{d}S \tag{C.2.9}$$

and the contrast term is identical to its the full-wave counterpart (C.1.4) except that, as is indicated by the subscript 0, $\boldsymbol{E}_0$ must be used instead of $\boldsymbol{E}$. For the boundary term, the superscript 'ϕ' indicates that the scalar potential is involved and for the source term, the superscript 'ρ' indicates that an electrical charge distribution is involved. The new term D appears when the electrical permittivity presents discontinuities on $\mathcal{S}_\epsilon$. Indeed, when this is the case, a thin layer around that discontinuity surface must be excluded before the Green's theorem may be applied. The corresponding additional surface term yields $D^{\epsilon}_{\mathcal{S}_\epsilon}$ where $\rho_\mathrm{s,eq} = \left(\boldsymbol{D}^+_0 - \boldsymbol{D}^-_0\right) \cdot \hat{\boldsymbol{n}}$. This term can be interpreted as the contribution of an equivalent surface charge distribution $\rho_\mathrm{s,eq}$ appearing at the interface when the dielectric medium is replaced by equivalent electrical dipoles.

C.3 MQS reciprocity

The MQS reciprocity expression is obtained as its full-wave counterpart, but starting with $-\nabla\cdot\left(\boldsymbol{A}^\mathrm{A}_0 \times \boldsymbol{H}^\mathrm{B}_0 - \boldsymbol{A}^\mathrm{B}_0 \times \boldsymbol{H}^\mathrm{A}_0\right)$, where $\boldsymbol{A}^{\mathrm{A|B}}_0$ is the vector potential related to the static current sources $\boldsymbol{J}^{\mathrm{A|B}}_0$. The subscript '0' has been introduced to emphasis that the reciprocity expression is only valid for MQS fields or more generally for the order zero magnetic fields and potentials appearing in our QS approximation (see Appendix B.3.7).

One then finds:

$$B^{\mathrm{A}}_{\mathcal{S}_\mathrm{r}} = S^{\mathrm{J}_0}_{\mathcal{V}_\mathrm{J}} + C^{\mathrm{m}_0}_{\mathcal{V}_{\chi_\mathrm{m}}} \tag{C.3.10}$$

$$B^{\mathrm{A}}_{\mathcal{S}_\mathrm{r}} = -\oint_{\mathcal{S}_\mathrm{r}} \left(\boldsymbol{A}^{\mathrm{A}}_0 \times \boldsymbol{H}^{\mathrm{B}}_0 - \boldsymbol{A}^{\mathrm{B}}_0 \times \boldsymbol{H}^{\mathrm{A}}_0\right) \cdot \mathrm{d}\boldsymbol{S} \tag{C.3.11}$$

$$S^{\mathrm{J}_0}_{\mathcal{V}_\mathrm{J}} = \int_{\mathcal{V}_\mathrm{J}} \left(\boldsymbol{A}^{\mathrm{A}}_0 \cdot \boldsymbol{J}^{\mathrm{B}}_0 - \boldsymbol{A}^{\mathrm{B}}_0 \cdot \boldsymbol{J}^{\mathrm{A}}_0\right) \mathrm{d}V \tag{C.3.12}$$

and the contrast term is identical to its the full-wave counterpart (C.1.5) except that, as is indicated by the subscript 0, $\boldsymbol{H}_0$ is used instead of $\boldsymbol{H}$. For the boundary term, the superscript 'A' indicates that the magnetic vector potential is involved and for the source term, the superscript 'J_0' indicates that static electrical currents are involved.

C.4 QS reciprocity

The QS reciprocity expression is an approximation of the full-wave reciprocity expression obtained by introducing the power series development for the various fields (B.3.25) in the full-wave reciprocity (C.1.1), expressing the fields as functions of the potentials according to (B.3.27a) and limiting the development to the first order in ω'. The QS reciprocity is thus not obtained by introducing the QS approximation of the fields in the full-wave reciprocity. Doing so would yield additional terms such as $\boldsymbol{E}^{\mathrm{A}}_1 \times \boldsymbol{H}^{\mathrm{B}}_1$. The difference is however quite limited because those second order extra terms will in general yield very small contributions. They are further rigorously null for the current decomposition (B.3.35).

The QS reciprocity can be written as:

$$B^{\mathrm{QS}}_{\mathcal{S}_\mathrm{r}} = S^{\mathrm{J,QS}}_{\mathcal{V}_\mathrm{J}} + j\omega \left(C^{\mathrm{e}_0}_{\mathcal{V}_{\chi_\mathrm{e}}} + C^{\mathrm{m}_0}_{\mathcal{V}_{\chi_\mathrm{m}}}\right) \tag{C.4.13}$$

where the superscript 'QS' indicates that the 'QS' approximation of the corresponding full-wave term is used.

When introducing the field power series developments in the full-wave reciprocity, one obtains terms:

$$\oint_{\mathcal{S}} \left(\boldsymbol{E}^{\mathrm{A}}_\mathrm{i} \times \boldsymbol{H}^{\mathrm{B}}_\mathrm{j}\right) \cdot \mathrm{d}\boldsymbol{S} \tag{C.4.14}$$

and

$$\int_{\mathcal{V}} \left(\boldsymbol{E}^{\mathrm{A}}_\mathrm{i} \cdot \boldsymbol{J}^{\mathrm{B}}_\mathrm{j}\right) \mathrm{d}V \tag{C.4.15}$$

Those integrals are computed hereunder. Using (C.4.22a)-(C.4.22c), to compute QS approximation of the boundary term, one finds:

$$B_{\mathcal{S}_\mathrm{r}}^{\mathrm{QS}} = J_{\mathcal{S}_\mathrm{r}} + j\omega\left(B_{\mathcal{S}_\mathrm{r}}^{\phi} + B_{\mathcal{S}_\mathrm{r}}^{\mathrm{A}_0}\right) \tag{C.4.16}$$

where

$$J_{\mathcal{S}_\mathrm{r}} = \oint_{\mathcal{S}} \left(\phi_0^{\mathrm{A}}\boldsymbol{J}^{\mathrm{B}} - \phi_0^{\mathrm{B}}\boldsymbol{J}^{\mathrm{A}}\right)\cdot \mathrm{d}\boldsymbol{S} \tag{C.4.17}$$

where we recall that $\boldsymbol{J}^{\mathrm{A|B}}$ is the total current that we have defined as $\boldsymbol{J}^{\mathrm{A|B}} = \boldsymbol{J}_0^{\mathrm{A|B}} + j\omega\boldsymbol{J}_1^{\mathrm{A|B}}$

Similarly, using (C.4.26a)-(C.4.26c) to compute the QS approximation of the source term, one finds:

$$S_{\mathcal{V}_\mathrm{J}}^{\mathrm{J,QS}} = J_{\mathcal{S}_\mathrm{r}} + j\omega\left(S_{\mathcal{V}_\mathrm{J}}^{\mathrm{J}_0} + S_{\mathcal{V}_\rho}^{\rho}\right) \tag{C.4.18}$$

where $S_{\mathcal{V}_\mathrm{J}}^{\mathrm{J}_0}$ and $S_{\mathcal{V}_\rho}^{\rho}$ are identical to the MQS and EQS source terms (C.3.12) and (C.2.8).

The contrast term is identical to the sum of the EQS and the MQS contrast terms. Note that this is not the case for the boundary and source terms which, in addition to the sum of their EQS and MQS counterparts also include a term $J_{\mathcal{S}_\mathrm{r}}$. As this additional term is equal for both the source and boundary terms, the QS reciprocity expression is consistent with the QS and MQS reciprocity expression. This provides a consistency check for the various reciprocity expressions that we have established.

C.4.1 Computation of $\oint_{\mathcal{S}}\left(\boldsymbol{E}_\mathrm{i}^{\mathrm{A}} \times \boldsymbol{H}_\mathrm{j}^{\mathrm{B}}\right)\cdot \mathrm{d}\boldsymbol{S}$

Using (B.3.27), we get:

$$\boldsymbol{E}_\mathrm{i}^{\mathrm{A}} \times \boldsymbol{H}_\mathrm{j}^{\mathrm{B}} = -\nabla\phi_\mathrm{i}^{\mathrm{A}} \times \boldsymbol{H}_\mathrm{j}^{\mathrm{B}} - j\omega\boldsymbol{A}_{\mathrm{i-i}}^{\mathrm{A}} \times \boldsymbol{H}_\mathrm{j}^{\mathrm{B}} \tag{C.4.19}$$

integrating the first term on $\mathcal{S}$, using the vector identity (B.1.2) in which the l.h.s. is null (the integral of a rotational on a closed surface is null), one gets:

$$-\oint_{\mathcal{S}}\left(\nabla\phi_\mathrm{i}^{\mathrm{A}} \times \boldsymbol{H}_\mathrm{j}^{\mathrm{B}}\right)\cdot \mathrm{d}\boldsymbol{S} = \oint_{\mathcal{S}} \phi_\mathrm{i}^{\mathrm{A}}\nabla \times \boldsymbol{H}_\mathrm{j}^{\mathrm{B}}\cdot \mathrm{d}\boldsymbol{S} = \oint_{\mathcal{S}} \phi_\mathrm{i}^{\mathrm{A}}\left(\boldsymbol{J}_\mathrm{j}^{\mathrm{B}} + j\omega\boldsymbol{D}_{\mathrm{j-1}}^{\mathrm{B}}\right)\cdot \mathrm{d}\boldsymbol{S} \tag{C.4.20}$$

and hence,

$$\oint_{\mathcal{S}} \left(\boldsymbol{E}_{\mathrm{i}}^{\mathrm{A}} \times \boldsymbol{H}_{\mathrm{j}}^{\mathrm{B}}\right) \cdot \mathrm{d}\boldsymbol{S} = \\ \oint_{\mathcal{S}} \phi_{\mathrm{i}}^{\mathrm{A}} \left(\boldsymbol{J}_{\mathrm{j}}^{\mathrm{B}} + j\omega \boldsymbol{D}_{\mathrm{j-1}}^{\mathrm{B}}\right) \cdot \mathrm{d}\boldsymbol{S} - j\omega \oint_{\mathcal{S}} \boldsymbol{A}_{\mathrm{i-i}}^{\mathrm{A}} \times \boldsymbol{H}_{\mathrm{j}}^{\mathrm{B}} \cdot \mathrm{d}\boldsymbol{S} \quad \text{(C.4.21)}$$

We recall that $\phi_1 = 0$ and that coefficients corresponding to negative order are null (see Appendix B.3.7). The lower order terms are then:

$$\oint_{\mathcal{S}} \left(\boldsymbol{E}_0^{\mathrm{A}} \times \boldsymbol{H}_0^{\mathrm{B}}\right) \cdot \mathrm{d}\boldsymbol{S} = \oint_{\mathcal{S}} \phi_0^{\mathrm{A}} \boldsymbol{J}_0^{\mathrm{B}} \cdot \mathrm{d}\boldsymbol{S} \quad \text{(C.4.22a)}$$

$$\oint_{\mathcal{S}} \left(\boldsymbol{E}_0^{\mathrm{A}} \times \boldsymbol{H}_1^{\mathrm{B}}\right) \cdot \mathrm{d}\boldsymbol{S} = \oint_{\mathcal{S}} \phi_0^{\mathrm{A}} \left(\boldsymbol{J}_1^{\mathrm{B}} + j\omega \boldsymbol{D}_0^{\mathrm{B}}\right) \cdot \mathrm{d}\boldsymbol{S} \quad \text{(C.4.22b)}$$

$$\oint_{\mathcal{S}} \left(\boldsymbol{E}_1^{\mathrm{A}} \times \boldsymbol{H}_0^{\mathrm{B}}\right) \cdot \mathrm{d}\boldsymbol{S} = -j\omega \oint_{\mathcal{S}} \boldsymbol{A}_0^{\mathrm{A}} \times \boldsymbol{H}_0^{\mathrm{B}} \cdot \mathrm{d}\boldsymbol{S} \quad \text{(C.4.22c)}$$

C.4.2 Computation of $\int_{\mathcal{V}} \left(\boldsymbol{E}_{\mathrm{i}}^{\mathrm{A}} \cdot \boldsymbol{J}_{\mathrm{j}}^{\mathrm{B}}\right) \mathrm{d}V$

Using (B.3.27), we get:

$$\boldsymbol{E}_{\mathrm{i}}^{\mathrm{A}} \cdot \boldsymbol{J}_{\mathrm{j}}^{\mathrm{B}} = -\nabla \phi_{\mathrm{i}}^{\mathrm{A}} \cdot \boldsymbol{J}_{\mathrm{j}}^{\mathrm{B}} - j\omega \boldsymbol{A}_{\mathrm{i-1}}^{\mathrm{A}} \cdot \boldsymbol{J}_{\mathrm{j}}^{\mathrm{B}} \quad \text{(C.4.23)}$$

integrating the first term on $\mathcal{V}$, using the vector identity (B.1.3) and Gauss theorem, one gets:

$$\int_{\mathcal{V}} \left(\nabla \phi_{\mathrm{i}}^{\mathrm{A}} \cdot \boldsymbol{J}_{\mathrm{j}}^{\mathrm{B}}\right) \mathrm{d}V = \oint_{\mathcal{S}} \phi_{\mathrm{i}}^{\mathrm{A}} \boldsymbol{J}_{\mathrm{j}}^{\mathrm{B}} \cdot \mathrm{d}\boldsymbol{S} + j\omega \int_{\mathcal{V}} \phi_{\mathrm{i}}^{\mathrm{A}} \rho_{\mathrm{j-1}}^{\mathrm{B}} \mathrm{d}V \quad \text{(C.4.24)}$$

and hence,

$$\int_{\mathcal{V}} \left(\boldsymbol{E}_{\mathrm{i}}^{\mathrm{A}} \cdot \boldsymbol{J}_{\mathrm{j}}^{\mathrm{B}}\right) \mathrm{d}V = \\ -\oint_{\mathcal{S}} \phi_{\mathrm{i}}^{\mathrm{A}} \boldsymbol{J}_{\mathrm{j}}^{\mathrm{B}} \cdot \mathrm{d}\boldsymbol{S} - j\omega \int_{\mathcal{V}} \phi_{\mathrm{i}}^{\mathrm{A}} \rho_{\mathrm{j-1}}^{\mathrm{B}} \mathrm{d}V - j\omega \int_{\mathcal{V}} \boldsymbol{A}_{\mathrm{i-1}}^{\mathrm{A}} \cdot \boldsymbol{J}_{\mathrm{j}}^{\mathrm{B}} \mathrm{d}V \quad \text{(C.4.25)}$$

We recall that $\phi_1 = 0$ and that coefficients corresponding to negative order are null. The lower order terms are then:

$$\int_{\mathcal{V}} \left(\boldsymbol{E}_0^{\mathrm{A}} \cdot \boldsymbol{J}_0^{\mathrm{B}}\right) \mathrm{d}V = -\oint_{\mathcal{S}} \phi_0^{\mathrm{A}} \boldsymbol{J}_0^{\mathrm{B}} \cdot \mathrm{d}\boldsymbol{S} \tag{C.4.26a}$$

$$\int_{\mathcal{V}} \left(\boldsymbol{E}_0^{\mathrm{A}} \cdot \boldsymbol{J}_1^{\mathrm{B}}\right) \mathrm{d}V = -\oint_{\mathcal{S}} \phi_0^{\mathrm{A}} \boldsymbol{J}_1^{\mathrm{B}} \cdot \mathrm{d}\boldsymbol{S} - j\omega \int_{\mathcal{V}} \phi_0^{\mathrm{A}} \rho_0^{\mathrm{B}} \mathrm{d}V \tag{C.4.26b}$$

$$\int_{\mathcal{V}} \left(\boldsymbol{E}_1^{\mathrm{A}} \cdot \boldsymbol{J}_0^{\mathrm{B}}\right) \mathrm{d}V = -j\omega \int_{\mathcal{V}} \boldsymbol{A}_0^{\mathrm{A}} \cdot \boldsymbol{J}_0^{\mathrm{B}} \mathrm{d}V \tag{C.4.26c}$$

C.5 Circuit reciprocity

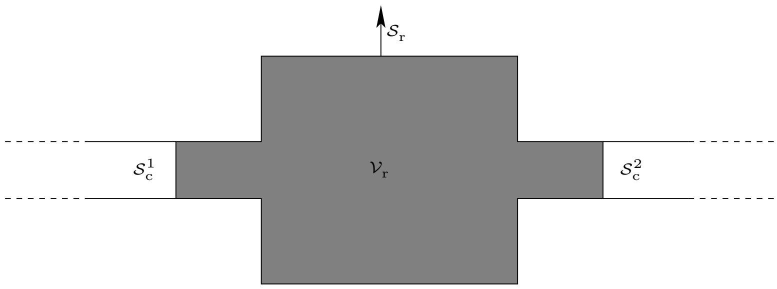

Figure C.1: *Perfectly shielded two-port network used to derive circuit from general field reciprocity. Reciprocity is expressed inside volume $\mathcal{V}_{\mathrm{r}}$ which is bounded by $\mathcal{S}_{\mathrm{r}}$ and which contains no source. $\mathcal{S}_{\mathrm{c}}^1$ and $\mathcal{S}_{\mathrm{c}}^1$ are parts of $\mathcal{S}_{\mathrm{r}}$ and are the transverse sections of the coaxial cable respectively at port 1 and 2. The elements outside $\mathcal{S}_{\mathrm{r}}$ does not need to be specified to apply reciprocity. In practice, voltage sources, current sources, loads or other circuits will be connected to the outgoing cables.*

For a linear circuit with p access ports, the following reciprocity can be used [82, Equ. 8.13]:

$$\sum_{i=1}^{p} V_{\mathrm{i}}^{\mathrm{A}} I_{\mathrm{i}}^{\mathrm{B}} = \sum_{i=1}^{p} V_{\mathrm{i}}^{\mathrm{B}} I_{\mathrm{i}}^{\mathrm{A}} \tag{C.5.27}$$

with $V_{\mathrm{i}}^{\mathrm{A|B}}$ the voltage at port i in states $A|B$ and $I_{\mathrm{i}}^{\mathrm{A|B}}$ the corresponding current. The sign convention is arbitrary as long as the same convention is used on both sides.

This expression can be derived directly from the general full-wave reciprocity expression (C.1.1) for a perfectly-shielded circuit for which the ports are connected with the external world with coaxial cables. This is illustrated in Fig. C.1 for a two-port system. There are no sources inside the circuit and the material inside the circuit remains unchanged for the two states. Therefore, only the boundary $B^{\mathrm{EH}}_{\mathcal{S}_\mathrm{r}}$ term remains in (C.1.1). Furthermore, at the frequencies of interest, only the Transverse Electromagnetic (TEM) mode propagates in a coaxial cable, the other modes being attenuated exponentially with a characteristic length of the order of the radius of the coaxial cable. Therefore, assuming that $\mathcal{S}^\mathrm{i}_\mathrm{c}$ is located at more than a cable radius from the cable connectors, only the TEM mode is present at $\mathcal{S}^\mathrm{i}_\mathrm{c}$ and the transverse electric field derives from a scalar potential $\boldsymbol{E} = -\nabla\phi$ [44, Section 10]. Introducing this electric field in $B^{\mathrm{EH}}_{\mathcal{S}_\mathrm{r}}$ then[2] yields (C.5.27).

C.6 Remarks

When applying reciprocity, one should keep in mind that:

- The reciprocity theorem is based on the harmonic Maxwell equations, which assume an $e^{j\omega t}$ time dependence for the fields and the sources, and are only valid for a linear time-invariant medium. However, the Maxwell equations are only used inside the volume considered $\mathcal{V}_\mathrm{r}$. Hence, inside that volume, the medium must be linear time-invariant but no restriction exists on the medium outside $\mathcal{V}_\mathrm{r}$. Obviously, the presence of nonlinear or time-variant medium outside $\mathcal{V}_\mathrm{r}$ may render the calculation of the fields on $\mathcal{S}_\mathrm{r}$ more complicated but, as such, this does not invalidate the reciprocity expression.

- With the general reciprocity expressions presented, the medium inside $\mathcal{V}_\mathrm{r}$ does not need to be reciprocal (i.e. constitutive parameters $\overline{\boldsymbol{\epsilon}}$, $\overline{\boldsymbol{\mu}}$ and $\overline{\boldsymbol{\sigma}}$ are symmetrical tensors or scalar). If the medium is not reciprocal, a reciprocity expression still exists but contrast terms (C.1.4) and (C.1.5) must be taken into account, even if the same medium is used in the two states considered (see discussion at the end of Section (C.1).

[2]The reasoning is similar to the one used to obtain (2.35) from (2.33).

- In the full-wave source term $S^{\mathrm{J}}_{\mathcal{V}_{\mathrm{J}}}$, we may either use the impressed sources $\boldsymbol{J}_{\mathrm{s}}$ solely or the total current $\boldsymbol{J} = \boldsymbol{J}_{\mathrm{s}} + \sigma\boldsymbol{E}$. In the first case, the conductivity must be included in ϵ which then becomes $\epsilon_\sigma = \epsilon + \frac{\sigma}{j\omega}$. When the total current is used, conductivity does not appear in the Maxwell equations and, therefore, no restrictions exist on the conductivity. It may be nonlinear or time-variant. On the contrary, when the impressed current is used, the conductivity appears in ϵ_σ and it should be linear. If non-reciprocal, the conductivity will then contribute to the contrast term.

- Nonlinear or time-variant elements are often present in electronic circuits (diodes, transistors, ...). To apply reciprocity, one may thus either choose the volume $\mathcal{V}_{\mathrm{r}}$ to exclude the electronics or consider the currents in the nonlinear or time-varying components as sources. This is only possible if the external fields have no significant effect on those currents, as will be the case, for example, for an electronic current source.

- In the QS source term $S^{\mathrm{J,QS}}_{\mathcal{V}_{\mathrm{J}}}$ one must in general use the total current; at least for J_0. It is not possible, as in the full-wave case, to consider only the current source distribution and to take into account the induced currents by using ϵ_σ in place of ϵ. Indeed, as discussed in Section B.3.8, the QS assumption is not valid inside conductors at the frequency used by MD. The QS approximation may then only be used if the conductor has first been replaced by equivalent currents.

APPENDIX D

Soil response

D.1 TX current in presence of soil

The TX current may be different in free space and in presence of soil. This effect is dependent on the TX coil driver circuit. For an ideal current source, the TX current is unaffected by the presence of the soil. However, for other sources, the TX current varies with the soil properties as well as with the sensor height and orientation. It is then necessary to relate the TX current in the presence of soil to its free space counterpart, which can be measured and used as a detector characteristic.

In Chapter 4, we could use I_{TX} to denote the TX current without ambiguity because it was always the current in the presence of soil that was meant. We will now denote the TX current in the presence of soil and its free space counterpart by $I_{\mathrm{TX(as)}}$ and $I_{\mathrm{TX(fs)}}$, respectively.

To compute the TX current, let us consider that the electronics can be modeled by its Thevenin equivalent circuit composed of an ideal voltage source V_{TX} and a series impedance $Z^{\mathrm{el}}_{\mathrm{TX}}$ which can both be estimated by simple measurements on the detector. The coil can also be represented by its Thevenin equivalent circuit composed of an ideal voltage source $e^{\mathrm{soil}}_{\mathrm{TX}}$ and a series impedance $Z^{\mathrm{coil}}_{\mathrm{TX}}$. $Z^{\mathrm{coil}}_{\mathrm{TX}}$ can be estimated by simple measurements on the coil and $e^{\mathrm{soil}}_{\mathrm{TX}}$, which is the voltage induced by the soil in the TX coil[1], can be computed using (4.11). For this purpose, the sensitivity of a fictious monostatic head (in which the TX coil of the physical head is used both for transmission and reception) must be used; it can be obtained by replacing RX by TX in (4.12).

Note that $I_{\mathrm{TX(as)}}$, which is still to be determined, appears in (4.11). We therefore first compute the normalized soil response:

$$\check{e}^{\mathrm{soil}}_{\mathrm{TX}} = e^{\mathrm{soil}}_{\mathrm{TX}} / I_{\mathrm{TX(as)}} \tag{D.1.1}$$

[1]For a two-coil head, the Thevenin equivalent of the Receive (RX) coil as well as the coupling between the TX and RX coils must be taken into account. As this generalization is straightforward, it will not be further discussed.

We also define the total TX impedance:

$$Z_{\mathrm{TX}} = Z_{\mathrm{TX}}^{\mathrm{el}} + Z_{\mathrm{TX}}^{\mathrm{coil}} \tag{D.1.2}$$

According to the Thevenin equivalent circuit, we have:

$$I_{\mathrm{TX(as)}} = \frac{V_{\mathrm{TX}} - \check{e}_{\mathrm{TX}}^{\mathrm{soil}} I_{\mathrm{TX(as)}}}{Z_{\mathrm{TX}}} \tag{D.1.3}$$

which immediately gives the following TX current:

$$I_{\mathrm{TX(as)}} = \frac{V_{\mathrm{TX}}}{Z_{\mathrm{TX}} + \check{e}_{\mathrm{TX}}^{\mathrm{soil}}} \tag{D.1.4}$$

In practice, $\check{e}_{\mathrm{TX}}^{\mathrm{soil}}$ is often much smaller than Z_{TX} and $I_{\mathrm{TX(as)}} \backsimeq I_{\mathrm{TX(fs)}} = V_{\mathrm{TX}}/Z_{\mathrm{TX}}$. In case of doubt, (D.1.4) can be used to check whether, for a given soil and detector, $I_{\mathrm{TX(as)}}$ can be replaced accurately by $I_{\mathrm{TX(fs)}}$ in (4.11) to compute the soil response.

D.2 Mutual induction coefficient

Here, we relate the mutual induction coefficient between the $\widehat{\mathrm{TX}}$ coil (the mirror of the TX coil) and the RX coil to the head sensitivity.

For this purpose, we first apply reciprocity (C.3.10) to the HS configuration illustrated in Fig. 4.1 (b) in the air volume $\mathcal{V}_{\mathrm{a}}$ with the following two states:

- $\Sigma_{\widehat{\mathrm{TX}}}^{(\mathrm{fs})}$ for which the mirrored TX coil is carrying current I_{TX} in free space
- $\Sigma_{\mathrm{RX}}^{(\mathrm{fs})}$ for which the RX coil is carrying current I_{RX} in free space

This yields:

$$\int_{\mathcal{S}_{\mathrm{as}}} \left(\boldsymbol{A}_{\widehat{\mathrm{TX}}}^{(\mathrm{fs})} \times \boldsymbol{H}_{\mathrm{RX}}^{(\mathrm{fs})} - \boldsymbol{A}_{\mathrm{RX}}^{(\mathrm{fs})} \times \boldsymbol{H}_{\widehat{\mathrm{TX}}}^{(\mathrm{fs})} \right) \cdot \mathrm{d}\boldsymbol{S} = I_{\mathrm{RX}} \int_{\mathcal{C}_{\mathrm{RX}}} \hat{\boldsymbol{\ell}}_{\mathrm{RX}} \cdot \boldsymbol{A}_{\widehat{\mathrm{TX}}}^{(\mathrm{fs})} \mathrm{d}\ell \tag{D.2.5}$$

where $\mathcal{S}_{\mathrm{as}}$ is the air-soil interface for which the positive normal has been defined to point up. The r.h.s. of the above equation was obtained from the r.h.s. of (C.3.10) by noting that the first term of the volume integral is null because the permeability is the same for both states, the second term is null because in the first state ($\Sigma^{(\mathrm{fs})}_{\widehat{\mathrm{TX}}}$) there is no current in the volume considered (the upper HS) and the last term degenerates in a contour integral because the current is localized on $\mathcal{C}_{\mathrm{RX}}$. A direct application of reciprocity yields a surface integral on $\mathcal{S}_{\mathrm{air}}$ instead of $\mathcal{S}_{\mathrm{as}}$ and an opposite sign for the r.h.s. term. The above equation can then be obtained by noting that only $\mathcal{S}_{\mathrm{as}}$ contributes to the surface integral and that the positive normal of $\mathcal{S}_{\mathrm{as}}$ and $\mathcal{S}_{\mathrm{air}}$ are in opposite directions on that surface.

By symmetry, the currents, fields and potentials of the mirrored coil are related to the original one as follows:

$$\begin{aligned} \boldsymbol{J}_{\widehat{\mathrm{TX}}}(x,y,z) &= \pm \boldsymbol{J}_{\mathrm{TX}}(x,y,-z) \\ \boldsymbol{A}_{\widehat{\mathrm{TX}}}(x,y,z) &= \pm \boldsymbol{A}_{\mathrm{TX}}(x,y,-z) \\ \boldsymbol{H}_{\widehat{\mathrm{TX}}}(x,y,z) &= \mp \boldsymbol{H}_{\mathrm{TX}}(x,y,-z) \end{aligned} \tag{D.2.6}$$

where the upper sign is valid for x and y coordinates and the lower sign is valid for the z coordinate.

Therefore, on $\mathcal{S}_{\mathrm{as}}$ where $z = 0$ and $\hat{\boldsymbol{n}} = \hat{\boldsymbol{z}}$, $\boldsymbol{A}^{(\mathrm{fs})}_{\widehat{\mathrm{TX}}} \times \hat{\boldsymbol{n}} = \boldsymbol{A}^{(\mathrm{fs})}_{\mathrm{TX}} \times \hat{\boldsymbol{n}}$ and $\boldsymbol{H}^{(\mathrm{fs})}_{\widehat{\mathrm{TX}}} \times \hat{\boldsymbol{n}} = -\boldsymbol{H}^{(\mathrm{fs})}_{\mathrm{TX}} \times \hat{\boldsymbol{n}}$ and (D.2.5) becomes:

$$\int_{\mathcal{S}_{\mathrm{as}}} \left(\boldsymbol{A}^{(\mathrm{fs})}_{\mathrm{TX}} \times \boldsymbol{H}^{(\mathrm{fs})}_{\mathrm{RX}} + \boldsymbol{A}^{(\mathrm{fs})}_{\mathrm{RX}} \times \boldsymbol{H}^{(\mathrm{fs})}_{\mathrm{TX}} \right) \cdot \mathrm{d}\boldsymbol{S} = I_{\mathrm{RX}} \int_{\mathcal{C}_{\mathrm{RX}}} \boldsymbol{A}^{(\mathrm{fs})}_{\widehat{\mathrm{TX}}} \cdot \mathrm{d}\boldsymbol{\ell} \tag{D.2.7}$$

The first term of the l.h.s. can be further developed by applying again reciprocity in the soil volume $\mathcal{V}_{\mathrm{soil}}$ between the following states:

- $\Sigma^{(\mathrm{fs})}_{\mathrm{TX}}$ for which the TX coil is carrying a current I_{TX} and is in free space and
- $\Sigma^{(0)}_{\mathrm{RX}}$ for which the RX coil is carrying a current I_{RX} in a fictitious medium for which $\mu = 0$. For that medium, $\boldsymbol{H}^{(0)}_{\mathrm{RX}} = \boldsymbol{H}^{(\mathrm{fs})}_{\mathrm{RX}}$ and $\boldsymbol{A}^{(0)}_{\mathrm{RX}} = 0$.

This yields

$$\int_{\mathcal{S}_{\mathrm{as}}} \boldsymbol{A}^{(\mathrm{fs})}_{\mathrm{TX}} \times \boldsymbol{H}^{(\mathrm{fs})}_{\mathrm{RX}} \cdot \mathrm{d}\boldsymbol{S} = \mu_0 \int_{\mathcal{V}_{\mathrm{soil}}} \boldsymbol{H}^{(\mathrm{fs})}_{\mathrm{TX}} \cdot \boldsymbol{H}^{(\mathrm{fs})}_{\mathrm{RX}} \mathrm{d}V \tag{D.2.8}$$

where we used the fact that only $\mathcal{S}_{\mathrm{as}}$ contributes to the surface integral on $\mathcal{S}_{\mathrm{soil}}$ and that the positive normal of $\mathcal{S}_{\mathrm{as}}$ and $\mathcal{S}_{\mathrm{soil}}$ are identical on that surface.

The second term of the l.h.s. of (D.2.7) can be obtained as the first one by interchanging 'RX' and 'TX'. Therefore, according to (D.2.8), both terms are equal. According to (4.18), the r.h.s. of (D.2.7) is equal to $I_{\mathrm{TX}} I_{\mathrm{RX}} M_{\widehat{\mathrm{TX}},\mathrm{RX}}$ where $M_{\widehat{\mathrm{TX}},\mathrm{RX}}$ is the mutual induction coefficient between the mirrored TX coil and the RX coil.

One finally gets the following expression for the mutual induction coefficient:

$$M_{\widehat{\mathrm{TX}},\mathrm{RX}} = 2\mu_0 \int_{\mathcal{V}_{\mathrm{s}}} S \mathrm{d}V \tag{D.2.9}$$

with S defined in (4.12).

D.3 Far field approximation of sensitivity

We consider a head composed of two horizontal coils which have non-vanishing magnetic moments m_{TX} and m_{RX} both along the vertical direction. Far away from the head, the distance between the coils can be neglected and the fields may be approximated by that of two collocated magnetic dipoles. Introducing the magnetic field of a dipole [46, Equ. 11.7] in (4.12) yields:

$$S^{\mathrm{FF}}(\boldsymbol{R}) = \frac{1}{16\pi^2} \frac{m_{\mathrm{TX}} m_{\mathrm{RX}}}{I_{\mathrm{TX}} I_{\mathrm{RX}}} \frac{1 + 3\cos^2\theta}{R^6} \tag{D.3.10}$$

where $\boldsymbol{R}$ is the vector from the common location of the TX and RX dipoles to the field point, R is its norm and θ the angle between that vector and the common dipoles direction.

APPENDIX E

Publications

E.1 Journal papers

1. P. Druyts, C. Craeye, and M.Acheroy. Volume of influence for magnetic soils and electromagnetic induction sensors. IEEE transactions on geoscience and remote sensing, 48(10):3686–3697, October 2010.

2. P. Druyts, Y. Das, C. Craeye, and M.Acheroy. Modeling the response of electromagnetic induction sensors to inhomogeneous magnetic soils with arbitrary relief. IEEE transactions on geoscience and remote sensing, 47(1)(8):2627–2638, August 2009.

3. I. van den Bosch, S. Lambot, P. Druyts, I. Huynen, and M. Acheroy. Buried target signature extraction from ground-penetrating radar signal measurements and simulations. Near Surface Geophysics, 4(1):31-38, February 2006.

4. I. van den Bosch, S. Lambot, I. Huynen, M. Acheroy, and P. Druyts. Accurate and efficient modeling of monostatic GPR signal of dielectric targets buried in stratified media. Journal of Electromagnetic Waves and Applications, 20(3):283–290, 2006.

5. S. Lambot, I. van den Bosch, B. Stockbroeckx, P. Druyts, M. Vanclooster, and E. C. Slob. Frequency dependence of the soil dielectric properties derived from ground-penetrating radar signal inversion. Subsurface Sensing Technologies and Applications, 6(1):73–87, January 2005.

6. Stephane Pigeon, Pascal Druyts, and Patrick Verlinde. Applying logistic regression to the fusion of the nist'99 1-speaker submissions. Digital Signal Processing, 10(1-3):237–248, July 2000.

E.2 Book chapters

1. Pascal Druyts, Yann Yvinec, and Marc Acheroy. A framework to relate soil properties to soil classes based on performance of metal detectors and dual sensors. In Y. Baudoin and Maki K. Habib, editors,Using Robots in Hazardous Environments, chapter 8, pages 189-218. Woodhead Publishing Limited, 2011.

E.3 Conference proceedings

1. Y. Yvinec, P. Druyts, and Yves Dupont. Simulator Of Magnetometer And Gradiometer To Evaluate Detection And Classification Algorithms. In Poster for the 7th International Marine Electromagnetics Conference (MARELEC 2011), San Diego, USA, June 2011.
2. F. Gabriel, F. De Belie, P. Druyts, and X. Neyt. Sensorless drive of surface mounted permanent-magnet brushless DC machines with concentrated windings based on inductance measurements. In IEEE International Conference on Power Electronics (ICPE'11) - ECCE Asia, Jeju, Korea, May 2011.
3. F. Gabriel, F. De Belie, P. Druyts, and X. Neyt. Strategy to detect and prevent the current zero-crossing for inverter powered drives. In IEEE International Conference on Electrical Machines (ICEM'10), Rome, Italy, September 2010
4. Y. Yvinec and P. Druyts. A Simple Protocol For A Double-Blind Test On An Explosives/Drugs Long-Range Detector. In International conference dedicated to: Hazardous Materials: Issues Of Detection And Disposal, Koscierzyna, Poland, May 2010.
5. F. Gabriel, F. De Belie, P. Druyts, X. Neyt, J.A. Melkebeek, and M. Acheroy. Compensating the influence of the stator resistor and inverter nonlinearities in signal-injection based sensorless strategies. In IEEE Vehicle Power and Propulsion Conference (VPPC'09), pages 283-290, Dearborn, USA, September 2009.
6. Yann Yvinec, Pascal Druyts, and Marc Acheroy. A simple metal detector model to predict the probability of detection in landmine detection. In Proc. of The UXO/Countermine/Range Forum 2009, Orlando, USA, August 2009.

7. X. Neyt, P. Druyts, M. Acheroy, and J. G. Verly. Structured covariance matrix estimation for the range-dependent problem in STAP. In Proceedings of the 4th IASTED International Conference on Antennas, Radar, and Wave Propagation, Montreal, Canada, May 2007.

8. Pascal Druyts, Christophe Craeye, and Marc Acheroy. Comparing two methods to solve the layered sphere problem, application to electromagnetic induction sensors. In Proc. of The first European Conference on Antennas and Propagation (EUCAP2006), Nice, France, November 2006.

9. I. van den Bosch, P. Druyts, M. Acheroy, and I. Huynen. Numerical Parametric Study of Buried Target Ground-Penetrating Radar Signature. In Proceedings of SPIE Defence and Security Symposium, Orlando, FL, USA, April 2006.

10. Pascal Druyts, Yogadhish Das, Christophe Craeye, and Marc Acheroy. Effect of the soil on the metal detector signature of a buried mine. In Proc. SPIE Defence and Security Symposium, Orlando, FL, USA, April 2006.

11. I. van den Bosch, P. Druyts, M. Acheroy, and I. Huynen. Frequency and Time-Domain Error in Buried Target Radar Signature Extraction. In Proceedings of the Progress in Electromagnetics Research Symposium (PIERS), pages 251–255, Cambridge, MA, USA, March 2006.

12. I. van den Bosch, P. Druyts, S. Lambot, I. Huynen, and M. Acheroy. Accurate and efficient modeling of monostatic GPR signal of dielectric targets embedded in stratified media. In Proceedings of the Progress in Electromagnetics Research Symposium (PIERS), pages 251–255, Hangzhou, Zhejiang, China, August 2005.

13. I. van den Bosch, S. Lambot, M. Acheroy, I. Huynen, and P. Druyts. Accounting for Multiple Reflections and Antenna Radiation Pattern in GPR Signal Modeling and Experimental Validation. In S. Lambot, A. G. Gorriti, editor, Proceedings of the Third International Workshop on Advanced Ground-Penetrating Radar, pages 135–140, TU Delft, The Netherlands, May 2005.

14. Pascal Druyts. Modeling a metal detector. In Y. Baudoin and P. Kopacek, editors, Proceedings of the International IARP Workshop on Robotics and Mechanical assistance in Humanitarian Demining and similar risky interventions, Royal Military Academy, Brussels, June 2004.

15. Pascal Druyts, Armin Merz, Markus Peichl, and Gunnar Triltzsch. HOPE : a hand-held multi-sensor (MD, GPR, MWR) mine detector prototype with imaging capabilities. In Proceedings of Progress in Electromagnetics Research Symposium (PIERS2003), Singapore, January 2003.

16. Pascal Druyts, Armin Merz, Markus Peichl, and Gunnar Triltzsch. HOPE : raising the reliability of mine detection through an innovative a hand-held multi-sensor (MD, GPR, MWR) mine detector prototype with imaging capabilities. In Proceedings of the 3rd European-American Workshop on Reliability of NDE and Demining, Berlin, Germany, September 2002.

17. Charles Beumier, Pascal Druyts, Yann Yvinec, and Marc Acheroy. Real-time optical position monitoring using a reference bar. In Signal Processing and Communications (SPC2000), pages 468–473, Marbella, Spain, September 2000.

18. Pascal Druyts, Lionel Merlat, and Marc Acheroy. Modeling considerations for imaging with a standard metal detector. In Abinash C. Dubey, James F. Harvey, J. Thomas Broach, and Regina E. Dugan, editors, Proceedings of SPIE Detection and Remediation Technologies for Mines and Minelike Targets V, volume 4038, pages 1431–1451, Orlando, FL, USA, August 2000.

19. Charles Beumier, Pascal Druyts, Yann Yvinec, and Marc Acheroy. Motion estimation of a hand-held mine detector. In Signal Processing Symposium, Hilvarenbeek, The Netherlands, March 2000.

20. Pascal Druyts, Yann Yvinec, and Marc Acheroy. Image processing tools for semi-automatic minefield detection. In 2nd International Symposium on Operationalization of Remote Sensing (ORS99), ITC-Enschede (The Netherlands), 1999.

21. P. Verlinde, P. Druyts, G. Chollet, and M. Acheroy. A multi-level data fusion approach for gradually upgrading the performances

of identity verification systems. In B. Dasarathy, editor, Sensor Fusion: Architectures, Algorithms, and Applications III, volume 3719, Orlando, FL, USA, 1999. SPIE Press.

22. P. Verlinde, P. Druyts, G. Chollet, and M. Acheroy. Applying bayes based classifiers for decision fusion in a multi-modal indentity verification system. In International Symposium on Pattern Recognition In Memoriam Prof Pierre Devijver, Royal Higher Institute for Defense Dreve St-Anna 90 B-1020 Brussels (Belgium), 1999.

23. Pascal Druyts, Wim Mees, Dirk Borghys, Youssef Ouaghli, Christiaan Perneel, Marc Acheroy, and J-L Valero. Sahara - semi-automatic help for aerial region analysis, 'system description and final evaluation'. In Third NATO/IRIS Joint Symposium, Quebec City, Quebec, 1998.

24. Pascal Druyts, Yann Yvinec, and Marc Acheroy. Usefulness of semi-automatic tools for airborne minefield detection. In Clawar 98 -First International Symposium, pages 241–248, Brussels, 1998.

25. Pascal Druyts and Marc Acheroy. A modular multi layer perceptron (mmlp) to identify objects composed of characteristic subparts. In Dagli, Akay, Fernandez, Erosy, and Smith, editors, annie'97, University ouf Missouri-Rolla, 1997. ASME Press.

26. Pascal Druyts and Marc Acheroy. A modular multi layer perceptron (mmlp) to identify objects composed of characteristic subparts. In Internal Report - full version of annie 97 paper, 1997.

27. Pascal Druyts, Wim Mees, Dirk Borghys, Christiaan Perneel, Marc Acheroy, and J-L Valero. Sahara - semi-automatic help for aerial region analysis. In Joint Workshop 'Sensors and Mapping from Space' of The International Society for Photogrametry and Remote Sensing (ISPRS), volume 17, pages 267–274, Hannover, Germany, 1997.

28. Pascal Druyts and Christian Perneel. A complete scheme for short range identification of armoured vehicle on ir images. In Defence Optics 96, Brussels, 1996. Promoptica.

Bibliography

[1] D. Guelle, A. Smith, A. Lewis, and T. Bloodworth, *Metal Detector Handbook for Humanitarian Demining*. European Commission, 2003. [Online]. Available: http://www.itep.ws/pdf/metal_detector_handbook.pdf [Accessed: June 2011]

[2] G. Edwards, *Treasure Hunting with Metal Detectors*. Jones Harvest Pub, 2007.

[3] D. M. Jones, *Geophysical Survey in Archaeological Field Evaluation*. English Heritage Publishing, April 2008. [Online]. Available: http://www.helm.org.uk/upload/pdf/GeophysicsGuidelines.pdf [Accessed: June 2011]

[4] R. T. Roberts, "The history of metal detectors," *Western and Eastern Treasures*, p. 26, September 1999. [Online]. Available: http://www.howmetaldetectorswork.com/page14/page10/page10.html [Accessed: September 2011]

[5] E. S. Grosvenor and M. Wesson, *Alexander Graham Bell: The Life and Times of the Man who Invented the Telephone*. Harry Abrams, 1997.

[6] B. B. M. Graves, A. Smith, *Approaches to Foreign Body Detection in Foods, Trends in Food Science and Technology*. Colin King, 1998.

[7] C. Bruschini, "A multidisciplinary analysis of frequency domain metal detectors for humanitarian demining," Ph.D. dissertation, Vije Universiteit Brussel, Brussels, Belgium, 2002.

[8] A. M. Lewis, T. J. Bloodworth, D. M. Guelle, F. R. Littmann, A. Logreco, and M. A. Pike, "Systematic test and evaluation of metal detectors (STEMD) — interim report laboratory tests italy," JRC, Joint Research Centre of the European Commission, Tech. Rep. EUR22536EN, December 2006. [Online]. Available: www.itep.ws/pdf/STEMD_Interim_Lab.pdf [Accessed: June 2011]

[9] Y. Das, J. E. McFee, and R. H. Chesney, "Time domain response of a sphere in the field of a coil: Theory and experiment," *IEEE*

Transactions on Geoscience and Remote Sensing, vol. GE-22, no. 4, pp. 360–367, July 1984.

[10] Y. Das, J. E. McFee, J. Toews, and G. C. Stuart, "Analysis of an electromagnetic induction detector for real-time location of buried objects," *IEEE Transactions on Geoscience and Remote Sensing*, vol. 28, no. 3, pp. 278–288, May 1990.

[11] Y. Das and J. E. McFee, "A simple analysis of the electromagnetic response of buriedconducting objects," *IEEE Transactions on Geoscience and Remote Sensing*, vol. 29, no. 2, pp. 342–344, March 1991.

[12] T. M. Grzegorczyk, B. Zhang, J. A. Kong, B. E. Barrowes, and K. O'Neill, "Electromagnetic induction from highly permeable and conductive ellipsoids under arbitrary excitation: application to the detection of unexploded ordnances," *IEEE Transactions on Geoscience and Remote Sensing*, vol. 46, no. 4, pp. 1164–1176, April 2008.

[13] P. P. Silvester and D. Omeragic, "Sensitivity of metal detectors to spheroidal targets," *IEEE Transactions on Geoscience and Remote Sensing*, vol. 33, no. 6, pp. 1331–1335, November 1995.

[14] F. Shubitidze, K. O'Neill, I. Shamatava, K. Sun, and K. D. Paulsen, "Fast and accurate calculation of physically complete EMI response by a heterogeneous metallic object," *IEEE Transactions on Geoscience and Remote Sensing*, vol. 43, no. 8, pp. 1736–1750, August 2005.

[15] J. L. Stalnaker, M. E. Everett, A. Benavides, and C. J. Pierce, "Mutual induction and the effect of host conductivity on the em induction response of buried plate targets using 3-D finite-element analysis," *IEEE Transactions on Geoscience and Remote Sensing*, vol. 44, no. 2, pp. 251–259, February 2006.

[16] N. Geng, C. E. Baum, and L. Carin, "On the low-frequency natural response of conducting and permeable targets," *IEEE Transactions on Geoscience and Remote Sensing*, vol. 37, no. 1, pp. 347–359, January 1999.

[17] A. Smith, "Type 72 anti-personnel blast mine." [Online]. Available: http://www.nolandmines.com/minestype72ap.htm [Accessed: June 2011]

[18] Geneva International Centre for Humanitarian Demining, *Metal Detectors and PPE Catalogue.* GIHCD, 2005. [Online]. Available: http://www.gichd.org/fileadmin/pdf/publications/PPE-Cat-Archives/MetalDetectors-PPE-Catalogue-2005.pdf [Accessed: June 2011]

[19] Jane's, "Jane's mines and mine clearance," February 2011. [Online]. Available: http://articles.janes.com/articles/Janes-Mines-and-Mine-Clearance/Guartel-WD-100-Cable-Detector-United-Kingdom.html [Accessed: June 2011]

[20] ——, "Jane's explosive ordnance disposal," November 2010. [Online]. Available: http://articles.janes.com/articles/Janes-Explosive-Ordnance-Disposal/Ebinger-EBEX-420-DR-wire-locator-Germany.html [Accessed: June 2011]

[21] J. R. Wait and R. H. Ott, "On calculating transient electromagnetic fields of a small current-carrying loop over a homogeneous earth," *Pure and Applied Geophysics*, vol. 95, no. 1, pp. 157–162, December 1972.

[22] T. Lee and R. Lewis, "Transient EM response of a large loop on a layered ground," *Geophysical Prospecting*, vol. 22, no. 3, pp. 430–444, September 1974.

[23] C. Gaudin, C. Sigrist, and C. Bruschini, "Metal detectors for humanitarian demining: a patent search and analysis," Vrije Universiteit Brussel, Brussels, Belgium," EUDEM2 Technology Survey Report, November 2003. [Online]. Available: http://www.eudem.vub.ac.be/publications/files/MDPatentSearch/v1.1/patent_search/Documents/final_reportv1.1.pdf [Accessed: June 2011]

[24] Y. Das, "A preliminary investigation of the effects of soil electromagnetic properties on metal detectors," in *Proc. SPIE Conference on Detection and Remediation Technologies for Mines and Mine-like Targets IX, 5415*, Orlando, FL, USA, April 2004, pp. 677–690.

[25] ——, "Effects of soil electromagnetic properties on metal detectors," *IEEE Transaction on Geoscience and Remote Sensing*, vol. 44, no. 6, pp. 1444–1453, June 2006.

[26] S. D. Billings, L. R. Pasion, D. W. Oldenburg, and J. Foley, "The influence of magnetic viscosity on electromagnetic sensors," in *EUDEM-SCOT2 2003, International Conference on Requirements and Technologies for the Detection, Removal and Neutralization of Landmines and UXO*, Brussels, Belgium, September 2003.

[27] J. D. Toews, "Soil-properties measurement system. Schiebel, PC and National Instruments PXI hardware," Technical Memorandum, Defence R&D Canada – Suffield, Tech. Rep. TM 2006-142, October 2006. [Online]. Available: http://pubs.drdc.gc.ca/PDFS/unc71/p526384.pdf [Accessed: June 2011]

[28] C. R. Sullivan, "Optimal choice for number of strands in a litz-wire transformer winding," *IEEE Transactions on Power Electronics*, vol. 14, no. 2, pp. 283–291, March 1999.

[29] A. Massarini, M. K. Kazimierczuk, and G. Grandi, "Lumped parameter models for single- and multiple-layer inductors," in *Proceedings of PESC'96*, Baveno, Italy, June 1996, pp. 295–301.

[30] G. Grandi, M. K. Kazimierczuk, A. Massarini, and U. Reggiani, "Stray capacitances of single-layer solenoid air-core inductors," *IEEE Transactions on Industry Applications*, vol. 35, no. 5, pp. 1162–1168, October 1999.

[31] J. A. Stratton, *Electromagnetic theory*, I. S. in Physics, Ed. McGraw-Hill Book Company, 1941.

[32] G. Crotti and D. Giordano, "Evaluation of frequency behavior of coils for reference magnetic field generation," *IEEE Transactions on Instrumentation and Measurement*, vol. 54, no. 2, pp. 718–721, April 2005.

[33] R. F. Harrington, *Field Computation by Moment Methods.* New York: MacMillan, 1968.

[34] F. Shubitidze, K. O'Neill, S. A. H. K. Sun, and K. D. Paulsen, "Application of the method of auxiliary sources to the wide-band electromagnetic induction problem," *IEEE Transactions on Geoscience and Remote Sensing*, vol. 40, no. 4, pp. 928–942, April 2002.

[35] R. F. Harrington, *Time-Harmonic Electromagnetic Fields.* Wiley-IEEE Press, 2001.

[36] P. Yla-Oijala and M. Taskinen, "Application of combined field integral equation for electromagnetic scattering problems," in *Proc. XXVIIth URSI General Assembly*, Maastricht, 2002.

[37] ——, "Calculation of CFIE impedance matrix elements with RWG and n×RWG functions," *IEEE Transactions on Antennas and Propagation*, vol. 51, no. 8, pp. 1837–1846, Augusts 2003.

[38] P. Ylä-Oijala, M. Taskinen, and J. Sarvas, "Surface integral equation method for general composite metallic and dielectric structures with junctions," *Progress In Electromagnetics Research*, vol. 52, pp. 81–108, 2005.

[39] J.-F. Lee, R. Lee, and R. J. Burkholder, "Loop star basis functions and a robust preconditioner for EFIE scattering problems," *IEEE Transactions on Antennas and Propagation*, vol. 51, no. 8, pp. 1855–1863, Augustus 2003.

[40] W. C. Chew, J.-M. Jin, E. Michielssen, and J. Song, *Fast and Efficient Algorithms in Computational Electromagnetics.* Norwood, MA 02062: Artech House, 2001.

[41] A. F. Peterson, S. L. Ray, and R. Mittra, *Computational Methods for Electromagnetics*, ser. IEEE/OUP Series on Electromagnetic Wave Theory. New York: IEEE Press, 1998.

[42] J. van der Kruk, E. C. Slob, J. T. Fokkema, and P. M. van den Berg, "General framework for describing electrical and electromagnetic exploration methods," in *Expanded Abstracts with Author's Biographies Volume 1, Society of Exploration Geophyisicists International Exposition and Sixty-Seventh Annual Meeting*, Dallas, Texas, USA, November 1997, pp. 374–377.

[43] J. van der Kruk, "Three-dimensional imaging of multicomponent ground-penetrating radar data," Ph.D. dissertation, Delft University of Technology, Delft, The Netherlands, 2001.

[44] S. J. Orfanidis, *Electromagnetic Waves and Antennas.* Rutgers University, 2010. [Online]. Available: http://www.ece.rutgers.edu/~orfanidi/ewa/ [Accessed: June 2011]

[45] Y. Das and J. E. McFee, “Limitations in identifying objects from their time-domain electromagnetic induction response,” in *Proc. SPIE Conference on Detection and Remediation Technologies for Mines and Mine-like Targets VII, 4742*, Orlando, FL, USA, April 2002, pp. 776–789.

[46] C. E. Baum, *Detection and Identification of Visually Obscured Targets*, C. E. Baum, Ed. Taylor and Francis, 1998.

[47] B. H. Candy, “Pulse induction time domain metal detector,” Patent US5 576 624, November, 1996.

[48] R. L. Van Dam, J. M. H. Hendrickx, J. B. J. Harrison, B. Borchers, D. I. Norman, S. Ndur, C. Jasper, P. Niemeyer, R. Nartey, D. Vega, L. Calvo, and J. E. Simms, “Spatial variability of magnetic soil properties,” in *Detection and Remediation Technologies for Mines and Minelike Targets IX, 5415*, Orlando, FL, USA, 2004, pp. 665–676.

[49] R. L. Van Dam, J. M. H. Hendrickx, J. B. J. Harrison, and B. Borchers, “Conceptual model for prediction of magnetic properties in tropical soils,” in *Detection and Remediation Technologies for Mines and Minelike Targets X, 5794*, Orlando, FL, USA, 2005, pp. 177–187.

[50] H. A. Haus and J. R. Melcher, *Electromagnetic Fields and Energy.* MIT Hypermedia Teaching Facility, 1998. [Online]. Available: http://web.mit.edu/6.013_book/www/index.html [Accessed: June 2011]

[51] Y. Das, “Electromagnetic induction response of a target buried in conductive and magnetic soil,” in *Proc. SPIE Conference on Detection and Remediation Technologies for Mines and Mine-like Targets X, 5794*, Orlando, FL, USA, June 2005, pp. 263–274.

[52] ——, “Time-domain response of a metal detector to a target buried in soil with frequency-dependent magnetic susceptibility,” in *Proc. SPIE Conference on Detection and Remediation Technologies for Mines and Mine-like Targets XI, 6217*, Orlando, FL, USA, April 2006.

[53] P. Druyts, Y. Das, C. Craeye, and M. Acheroy, "Effect of the soil on the metal detector signature of a buried mine," in *Proc. SPIE Defence and Security Symposium*, Orlando, FL, USA, April 2006.

[54] C. Bruschini, "On the low frequency EMI response of coincident loops over a conductive and permeable soil and corresponding background reduction schemes," *IEEE Transaction on Geoscience and Remote Sensing*, vol. 42, no. 8, pp. 1706–1719, Augutsus 2004.

[55] C. Moreland, "Coil basics," Geotech, Tech. Rep., 2006. [Online]. Available: http://www.geotech1.com/pages/metdet/info/coils.pdf [Accessed: June 2011]

[56] D. Guelle, M. Gaal, M. Bertovic, C. Mueller, M. Scharmach, and M. Pavlovic, "South-east europe interim report field trial croatia (continuation of the ITEP-project systematic test and evaluation of metal detectors - STEMD) 25 september – 18 october 2006," BAM, Bundesanstalt für Materialforschung und prüfung, Tech. Rep., March 2007. [Online]. Available: www.itep.ws/pdf/STEMD_Interim_Croatia_final.pdf [Accessed: June 2011]

[57] D. M. Guelle, A. M. Lewis, M. A. Pike, A. Carruthers, and S. M. Bowen, "Systematic test and evaluation of metal detectors (STEMD). interim report field trial lao, 27 september–5 november 2004," JRC, Joint Research Centre of the European Commission, Tech. Rep. S.P.I05.24, March 2005. [Online]. Available: www.itep.ws/pdf/STEMD_Interim_Laos_final_Small.pdf [Accessed: June 2011]

[58] D. M. Guelle, A. M. Lewis, M. A. Pike, and C. Craill, "Systematic test and evaluation of metal detectors (STEMD). interim report field trial mozambique, 12 april–5 may 2005," JRC, Joint Research Centre of the European Commission, Tech. Rep. EUR21886EN, November 2005. [Online]. Available: www.itep.ws/pdf/Interim_Final_Moz160108_web_optimized.pd [Accessed: June 2011]

[59] R. L. Van Dam, J. B. J. Harrison, J. M. H. Hendrickx, D. A. Hirschfeld, R. E. North, J. E. Simms, and Y. Li, "Mineralogy of magnetic soils at a UXO remediation site in kaho'olawe hawaii," in *18th Annual Symposium on the Application of Geophysics to Engineering and Environmental Problems*, Atlanta, USA, April 2005.

[60] B. A. Auld and J. C. Moulder, "Review of advances in quantitative eddy current nondestructive evaluation," *Journal of Nondestructive Evaluation*, vol. 18, no. 1, pp. 3–36, March 1999.

[61] W. C. Chew, *Waves and Fields in Inhomogeneous Media*. Van Nostrand Reinhold, 1990.

[62] S. F. Gruber and J. D. Norgard, "Dielectric oblate spheroidal model of buried landmines," in *Proc. SPIE Conference on Detection and Remediation Technologies for Mines and Mine-like Targets VI, 4394*, Orlando, FL, USA, April 2001, pp. 1316–1324.

[63] P. P. Silvester and D. Omeragic, "Sensitivity maps for metal detector design," *IEEE Transactions on Geoscience and Remote Sensing*, vol. 34, no. 3, pp. 788–792, May 1996.

[64] L. K. Urankar, "Vector potential and magnetic field of current-carrying finite arc segment in analytic form, part I: Filament approximation," *IEEE Transactions on Magnetics*, vol. 16, no. 5, pp. 1283–1288, September 1980.

[65] T. Tsange, *Classical Electrodynamics*. World Scientific Publishing Company, 1997.

[66] CEN workshop 7, "CEN workshop agreement, humanitarian and evaluation, metal detectors," CEN, European Committee for Standardization, Tech. Rep. CWA14747:2003, June 2003.

[67] H. Bolvin, A. Chambarela, and A. Chanzyb, "Three-dimensional numerical modeling of a capacitance probe. application to measurement interpretation," *Soil Science Society of America Journal*, vol. 68, pp. 440–446, March 2004.

[68] Y. Das, J. D. Toews, K. Russell, and S. Lewis, "Results of in-air testing of metal detectors," Technical Report, Defence R&D Canada – Suffield, Tech. Rep. TR-2000-185, December 2000. [Online]. Available: http://cradpdf.drdc-rddc.gc.ca/PDFS/zbd90/p515588.pdf [Accessed: June 2011]

[69] R. Becker, *Electromagnetic Fields and Interactions*. Dover Publications, 1981.

[70] McGraw-Hill, *McGraw-Hill Dictionary of Scientific and Technical Terms*. McGraw-Hill, 2003. [Online]. Available: http://encyclopedia2.thefreedictionary.com/depolarization+factor [Accessed: June 2011]

[71] T. B. Jones, *Electromechanics of Particles*. Cambridge University Press, 1995.

[72] R. Fitzpatrick, *Advanced Classical Electromagnetism*. The University of Texas at Austin, 2002. [Online]. Available: http://farside.ph.utexas.edu/teaching/jk1/lectures/node36.html [Accessed: June 2011]

[73] International Commission on Non-Ionizing Radiation Protection, "Guidelines for limiting exposure to time-varying electric, magnetic, and electromagnetic fields (up to 300 GHz)," *Health Physics*, vol. 74, no. 4, pp. 494–522, April 1998.

[74] R. Mancini, "Op amp noise theory and applications," in *Op Amps for Everyone*. Texas Instruments, 2002.

[75] ICNIRP, "Exposure to high frequency electromagnetic fields, biological effects and health consequences (100 kHz-300 GHz)," International Commission on Non-Ionizing Radiation Protection, Tech. Rep., 2009.

[76] C. Bornkessel, "Exposure of the general public to RF electromagnetic fields," in *Workshop Acute Health Impairment*, December 2006.

[77] DMD & Associates Ltd., "Effects of high voltage transmission line in proximity of highways," BC Ministry of Transportation, Tech. Rep., September 2005. [Online]. Available: http://www.th.gov.bc.ca/publications/eng_publications/electrical/transmission_line_study.pdf [Accessed: June 2011]

[78] J. H. G. Op het Veld, "HF-TL ballast with UBA2021 for TLD58W lamp, AN98099," Application note, Philips semiconductors, Tech. Rep., 1999. [Online]. Available: http://www.zlgmcu.com/nxp/lighting/applications/hf-tl_uba2021_tld58w.pdf [Accessed: June 2011]

[79] K. Dutton, S. Thompson, and B. Barraclough, *The Art of Control Engineering.* Pearson Education Limited, April 1997.

[80] J. G. Van Bladel, *Electromagnetic Fields (2^{nd} Edition).* Wiley-IEEE Press, 2007.

[81] G. Cross, "Soil properties and GPR detection of landmines. a basis for forecasting and evaluation of gpr performance," Contract Report, Defence R&D Canada – Suffield, Tech. Rep. CR 2000-091, October 1999. [Online]. Available: http://cradpdf.drdc-rddc.gc.ca/PDFS/unc92/p514145.pdf [Accessed: June 2011]

[82] T. S. K. V. Iyer, *Circuit Theory.* Tata McGraw-Hill, 1985.